

**Establishing a Fluid-Structure Interaction  
Platform for Investigating  
Infant Cardiopulmonary Resuscitation**



**Samar Ali Jaber Shaabeth**

M.Sc., Al Nahrain University, 2006

B.Sc., Al Nahrain University, 2004

Thesis Submitted in Partial Fulfilment of the  
Requirements for the Degree of  
Doctor of Philosophy

in

Medical Engineering  
School of Engineering

**CARDIFF UNIVERSITY**

June 2018

## Abstract

Improved knowledge of blood flow during CPR will provide a platform to understand how to optimise chest compression strategies, to maximise the success of this life-critical intervention. Modelling the human circulatory system remains, however, a very difficult and challenging task because of its complexity and heterogeneity, both geometrically and functionally. The work in this thesis presents the simulation process developed for subject-specific blood flow modelling of porcine left ventricle during a simulated CPR compression.

The building of the process chain required for the computations was described. The workflow consists of the fine segmentation of porcine CT data, extraction and processing of the 3D geometrical model, generation of high-quality controlled surface and volume meshes, definition of appropriate physical models, setting of realistic boundary conditions, and finally evaluation of the simulations. Aspects involving the computational stability and material characterisations essential for reliable computations were presented. Further, the integration of the individual steps into ANSYS including automation of the process, optimisation and the individualisation of the simulations, indispensable for a clinical implementation of such a subject-specific system, were described.

Subject-specific model velocity profile of the blood flow from the outlet gave a similar velocity profile and magnitude expected from a first compression of the left ventricle in a resting state. Moreover, the velocity obtained from the experimental validation model agreed relatively well with that of the computational model giving the proposed model validity to be used in the investigation of the LV blood flow during compression. The simulated blood viscosity profile agreed strongly with the literature blood non-Newtonian profile.

The experimental results of the present physical model agreed relatively well with the data from the computational model regarding the deformation of the structural part along with the velocity magnitude. Despite the fact that the biaxial data showed that the stiffness of the 3D printed material was found to be lower than the tissue in the very low strain rate, the preliminary FSI model material loading during the simulation was more significant for the choice of the hyperelastic material model.

The outcomes of this research achieved the aim of implementing a fully coupled FSI method for the design and optimization of a porcine infant left ventricle during a simulated CPR compression. This model is considered a platform for investigating infant CPR chest compression efficacy.

## **Acknowledgements**

The work in this thesis was achieved with the support of many people that I would like to express my sincere gratitude to.

I would like to express my genuine gratitude to my Iraqi sponsor who provided me an opportunity to join the Higher Committee of Education Development in Iraq (HCED) scholarship program. Without their and Cardiff University's support it would not be possible to conduct this research.

I would like to express my sincere gratitude to my supervisors, Dr. Peter S. Theobald and Dr. Michael D. Jones, for their motivation, continuous support of my Ph.D. study, and immense knowledge. Their guidance helped me in my research and writing of this thesis.

Besides my supervisors, I would like to thank the School of Engineering research office staff for their encouragement and support through all the years of my Ph.D. I also would like to thank the Mechanical and Civil laboratories' technicians who offered their assistance whenever needed through the experimental aspect of my work. I would like to acknowledge Dr. Richard Johnston's for imaging the porcine heart CT imaging and allowing me to use Swansea University laboratory for the porcine heart preparation process.

Every step of my academic progress and personal achievements would not be possible without the support, prayers, and faith of my parents.

This work would never be completed without the patience, constant encouragement and support of my beloved husband and soul mate Hassanain, to you and to Mayan I dedicate every accomplishment in my life.

## Table of Contents

Declaration .....	ii
Abstract .....	iii
Acknowledgements .....	iv
Table of Contents .....	v
List of Tables .....	viii
List of Figures .....	ix
List of Acronyms .....	xx
List of Nomenclature .....	xxii
Preface Image .....	xxiv
<b>Chapter 1. Introduction .....</b>	<b>1</b>
1.1. Motivation for the Study .....	1
1.2. The Goal of the Present Study .....	3
1.3. Thesis Layout .....	4
1.3.1. Chapter Two- Literature Review .....	4
1.3.2. Chapter Three – Materials and Methods .....	5
1.3.3. Chapter Four – Results and Discussion .....	5
1.3.4. Chapter Five _ Technical Achievements and Limitations .....	6
1.3.5. Chapter Six – Conclusions and Future Work .....	6
<b>Chapter 2. Literature Review .....</b>	<b>7</b>
2.1. Chapter Overview .....	7
2.2. Heart and Blood Circulation .....	8
2.3. Paediatric Cardiopulmonary Resuscitation (CPR) Overview .....	12
2.3.1. Theories of Blood Flow Mechanism during CPR .....	14
2.3.2. Effective Method of Chest Compression .....	16
2.3.3. CPR Procedure, Regulations, and Improvements .....	17
2.4. Cardiovascular (Fluid and/or Structure) modelling .....	22
2.4.1. Animal Studies in Cardiac Modelling .....	24
2.4.2. Infant vs Adult .....	29
2.5. System Coupling .....	31
2.5.1. Cardiovascular System Coupling Models .....	34
2.5.2. Governing Equations and Material Models .....	39
2.5.3. Meshing .....	43
2.5.4. 3D Printed Material Properties .....	47
Material Characterisation .....	50
Mathematical models of material behaviour .....	51
3D printed material characteristics for FE analysis .....	53
<b>Chapter 3. Materials and Methods .....</b>	<b>63</b>
3.1. Chapter Overview .....	63
3.2. Preliminary Computational Model .....	64
3.2.1. Two-Way FSI .....	64
Geometry and Material .....	65
Meshing and Elements Configurations .....	67
3.2.2. Material Characterisation .....	69

Characterising Uniaxial Tension and Compression .....	70
Characterising Planar Tension Behaviour .....	72
Characterising Biaxial Behaviour.....	76
Material Model Calibration.....	79
3.2.3. Computational Model Parametric Adjustments .....	81
Transient Structural (FE).....	81
Fluent (CFD).....	82
System Coupling (FSI) .....	85
3.2.4. Release (Filling) Stage FSI .....	85
3.3. Computational model validation.....	87
3.3.1. Validation Rig Design .....	87
3.3.2. 3D Printed Geometry Design .....	89
3.4. Subject-Specific Computational Model .....	90
3.4.1. Model Geometry.....	90
3.4.2. Porcine Left Ventricle Computational Workflow .....	91
3.4.3. Porcine Heart CT Scanning .....	92
3.4.4. Image Reconstruction and Initial Meshing .....	94
3.4.5. Mechanical Simulation Process .....	98
Transient Structural Settings .....	100
Fluent CFD Setting.....	101
System Coupling Setting.....	104
<b>Chapter 4. Results and Discussion.....</b>	<b>106</b>
4.1. Chapter Overview.....	106
4.2. Preliminary Model.....	107
4.2.1. Material Characterisation Results .....	107
Tensile test.....	107
Planar Test.....	109
Equibiaxial Test.....	111
4.2.2. Material Model Parametric Optimisation .....	112
4.2.3. Material Testing Computational Validation.....	116
Tensile test.....	117
Planar Shear .....	118
Equibiaxial test.....	121
4.2.4. Post-CFD results and Discussion .....	124
Velocity Profile and Distribution.....	125
Pressure Gradient and Wall Shear .....	133
4.2.5. Transient Structural Results and Discussion.....	141
4.2.6. Preliminary Model Validation .....	148
4.3. Subject-specific Model.....	153
4.3.1. FE and post-CFD data.....	153
Post CFD Pressure Distribution.....	154
Post CFD Velocity Distribution .....	161
4.3.2. Structural Computational Data.....	180
<b>Chapter 5. Technical Achievements and Limitations .....</b>	<b>198</b>
5.1. Chapter Overview.....	198
5.2. Model mesh and Mapping Quality .....	199

5.2.1. Mesh Sensitivity Study.....	199
5.2.2. Mapping Summary.....	204
Preliminary Model Mapping Summary.....	204
Subject-Specific Model Mapping Summary.....	206
5.3. Computational Achievements.....	210
5.4. Computational Model Limitations.....	212
<b>Chapter 6. Conclusion, Future Work and Research Contributions .....</b>	<b>214</b>
6.1. Conclusion.....	214
6.2. Future Work.....	216
6.2.1. Computational research needs .....	216
6.2.2. Experimental research needs .....	218
6.2.3. Prospective Simulations .....	219
6.3. Research Contributions .....	220
<b>References.....</b>	<b>221</b>
<b>Appendix A. Simulation Quality Assurance.....</b>	<b>233</b>
<b>Appendix B. Arduino UNO Technical Specifications.....</b>	<b>245</b>
<b>Appendix C. Arduino Sensor Code .....</b>	<b>250</b>
<b>Appendix D. Nickel-Plated Brass Non-Return Valves Datasheet .....</b>	<b>254</b>
<b>Appendix E. Turbine Flow Rate Sensor Data sheet.....</b>	<b>255</b>
<b>Appendix F. PolyJet Materials Data Sheet.....</b>	<b>257</b>
<b>Appendix G. Research Contributions.....</b>	<b>259</b>

## List of Tables

<i>Table 2-1 Paediatric phases of CA and resuscitation interventions CA, cardiac arrest; BLS, basic life support; ALS, advanced life support; CPR, cardiopulmonary resuscitation (Ornato and Peberdy, 2005).....</i>	<i>13</i>
<i>Table 2-2 Various non-Newtonian constitutive equations have been used to mimic the blood rheology (Doost et al., 2016).....</i>	<i>41</i>
<i>Table 3-1 Geometry information of the preliminary model computational design .....</i>	<i>67</i>
<i>Table 3-2 Dehydration solution concentration.....</i>	<i>93</i>
<i>Table 3-3 Left ventricle subject-specific model geometry information .....</i>	<i>100</i>
<i>Table 5-1 Results of dimensionless velocity, pressure, and wall shear and corresponding relative error (%) obtained at transitions between the different mesh element sizes in the idealized model.....</i>	<i>200</i>

## List of Figures

- Figure 2-1 Human heart and cardiac circulation diagram (Pearson Education, 2010).  
 (A) Representing the major cardiac structure of the heart compartments, valves, and connecting vessels.(B) represent the external view of the left ventricle (Drake et al., 2010). ..... 9
- Figure 2-2 Cardiac Cycle: Systole with isovolumetric contraction (I) and ejection (IIa and IIb) phases; Diastole with isovolumetric relaxation (III) and filling (IVa and IVb) phases (Silbernagl and Lang, 2000) ..... 10
- Figure 2-3 Three-dimensional flow in the ventricles and projections of the streamlines in the long-axis plane. As the mitral and tricuspid valves open, intake jets initially form during the filling process accompanied by a ring vortex after one quarter of a cardiac cycle. These occur to balance out the deceleration of the intake jet in the fluid at rest. As the diastole continues, because of the motion of the cardiac myocardium, the ring vortex increases in size. (Oertel and Kritttian, 2012) ..... 11
- Figure 2-4 Hand-positioning during lateral grabbing of an infant, depicted to scale. Positions of the anterior displacement points are depicted by the two faint yellow bars. Positions of the posterior displacement points are depicted by the faint red bar. (The anatomic structures include paired sixth rib (orange), sixth vertebral body (dark blue), inter-vertebral disks (light purple), rib head cartilage apophyses (cyan), transverse process cartilage apophyses (dark purple), vertebral synchondroses cartilage (magenta), and anterior costal cartilage (green). (Tsai et al., 2012).. 20
- Figure 2-5 A) Division of regions for the ALE Lagrange-Euler formulation of the flow-structure coupling for the human ventricle (Oertel and Kritttian, 2012), B) Position of the measurement planes. Aortic orifice (AO) as the outlet and Mitral orifice (MO) as inlet. (Espa et al., 2012)..... 24
- Figure 2-6 Internal view of the porcine (A) and human (B) left ventricle, showing its inlet, outlet and apical trabecular component parts. The fine criss-crossing left ventricular trabeculations of the human heart are replaced by much coarser muscles in the pig. The greater thickness of the porcine left ventricular free wall compared with that of man is indicated (between closed arrows). The mitral valve and its paired papillary muscle attachments are structurally very similar in man and pig. (Crick et al., 1998)..... 26
- Figure 2-7 Four chamber sections of the porcine (A) and human (B) heart illustrating the differences in the morphological proportions of atrial and ventricular chambers. In the porcine heart the greater proportion of the section is taken up by the left chambers, especially the left ventricle, which means that the interventricular septum is situated more to the right of the heart. This also means the apex is composed entirely of left ventricular musculature, unlike the apex of the human heart. In the human heart, the left chambers are less dominant, and as a result, the interventricular septum occupies a more central position within the section. TV, leaflets of tricuspid valve; MV, leaflets of mitral valve; IVS, interventricular septum (Crick et al., 1998). ..... 27
- Figure 2-8 Infant heart with a slightly 'bulky' left ventricle was subsequently perfusion-fixed with formalin. The heart was then cut in a left ventricular outflow tract view which did not demonstrate any outflow tract pathology. (Matshes and Trevenen, 2011) ..... 28



Figure 2-9 A) Infant heart had an unremarkable external morphology. The apical half of the heart was removed, and the remainder of the heart was dissected along the pathway of blood flow in continuity with the lungs and great vessels. The apical half of the heart was then serially sectioned. B) These contiguous sections of the heart represent serial sections from the heart demonstrated in Figure 2-8. Regardless of the plane of the section selected for evaluation, the myocardium should be thoroughly assessed for pathology (Matshes and Trevenen, 2011). .....	28
Figure 2-10 Execution Sequence Diagram for the System Coupling Service and Co-Simulation Participant, synchronization points are shown in dark grey. (ANSYS, 2018).....	32
Figure 2-11 Processing Details for the System Coupling Service and Co-Simulation Participants. Secondary synchronization points: Data Transfer and Solve, both shown in light grey. (ANSYS, 2018).....	33
Figure 2-12 Flow chart for the LV simulation procedure illustrating the conditions for the simulation convergence during the entire simulation. (Arefin and Morsi, 2014). .....	35
Figure 2-13 ANSYS FLUENT available solvers (2016).....	37
Figure 2-14 Subject-specific simulation workflow (Hazer et al., 2006b, Hazer et al., 2006a). (A) The workflow representing the resulting file types in each step, (B) image-based abdominal aortic model workflow.....	38
Figure 2-15 The apparent viscosity of different non-Newtonian models versus the shear rate. the viscosity is higher than the Newtonian viscosity in the range of shear rate less than $10^2 \text{ s}^{-1}$ and it reaches the Newtonian viscosity for the shear rate higher than $10^3 \text{ s}^{-1}$ (Doost et al., 2016) .	42
Figure 2-16 Mesh of the sphere with different number of elements: a) 3034, b) 88, c) 16, d) 8.(Krutilek and Raida, 2015).....	44
Figure 2-17 An ellipsoidal geometry was used for the mechanical test cases with hexahedra and tetrahedral (Oliveira and Sundnes, 2016) .....	45
Figure 2-18 Mesh parameters. On the left are the orthogonal quality vectors and on the right is skewness cell description (ANSYS, 2018).....	46
Figure 2-19 Time step effect on ANSYS transient simulation. Decreasing the $\Delta t$ increase the iteration step behaviour of the variable of interest. (ANSYS, 2018).....	47
Figure 2-20 Experimental Parameters describing the selected parameters (X-Y Orientation, Z Orientation, and Part Spacing), and the rationale for their selection (i.e., hypothesized effect) (Barclift and Williams, 2012) .....	49
Figure 2-21 a) Elasto-plastic stiffness curve (not to scale). b) Elastomeric stiffness curve (not to scale) (Pearson and Pickering, 2001) .....	51
Figure 2-22 Material testing techniques. (A) Test Methods for determining material properties, (B) Superposition of hydrostatic stresses (Pearson and Pickering, 2001) .....	54
Figure 2-23 Pure shear testing rig. (A) illustrates a small region at the central part of a rectangular sheet of material stretched along a parallel pair of clamped edges, (B) Experimental arrangement for pure shear (Moreira and Nunes, 2013) .....	56
Figure 2-24 Planar shear testing. (A) Test rig for planar tension tests: specimen, tensile and vision system (Palmieri et al., 2009), (B) Strain maps of the three different specimen. Principal strains on plane are plotted for three different values of load (Palmieri et al., 2009).....	58

Figure 2-25 Contour maps of (A) von-Mises stress (MPa) superimposed on real deformed shapes of the specimens, (B) Green-Lagrange strains EXX, EYY.(Avanzini and Battini, 2016) .....	61
Figure 2-26 Schematic and detailed view of the planar equibiaxial testing apparatus for determining target value of material properties. (Cosola et al., 2008) .....	62
Figure 3-1 FSI workflow flowchart representing the forces and displacements transferred between the two operating solvers (CFD and Mechanical) .....	65
Figure 3-2 Model geometry with boundary zones (A) Structural geometry with shell solid of 1mm thickness (B) Fluid region with surfaces name selection. Mesh with parts colour showing 2 perpendicular sections with 0.8 mm element size. (C) Structural Shell mesh (D) Fluid region mesh.....	69
Figure 3-3 Material model computational validation process from experimental data .....	70
Figure 3-4 Tensile test specimens with modified geometry to avoid slipping. Left images represents the patterned end geometrical modifications with different aspect views. The right images represent the beaded end geometrical modification to the standard tensile test specimen. ....	71
Figure 3-5 Tensile test measurement using video-extensometer. (A) The virtual strain gauge on the narrow part of the tensile test specimen. (B) The testing setup showing the video-extensometer camera positioned parallel to the tensile test piece.....	71
Figure 3-6 Compression test specimen along with the testing images. (A) The test piece dimensions, (B) At the start of the compression test, (C) At the end of the compression test. ....	72
Figure 3-7 Planar shear testing using flat bracket as gripping. (A) The planar shear test piece dimensions, (B) The flat metal brackets positioning along with the strain gauges along the test piece, (C) Planar shear testing rig using video-extensometer setup .....	73
Figure 3-8 Planar shear modified rig. (A) L-shaped planar shear brackets, (B) Planar shear rig.....	75
Figure 3-9 Planar shear testing rig using DIC setup. On the left is the positioning of the two DIC cameras while the left image show the clamping of the test piece using the modified bracket design ensuring no slipping from the tension machine clamps.....	76
Figure 3-10 (A) Biaxial stretching apparatus with the test specimen in the middle attached to the gripping clamps, (B) The different gripping clamps, the clamp on the left was used instead of the one on the left to accommodate the grooving of the middle lower clamp to avoid stretching the test piece. ....	77
Figure 3-11 Biaxial stretching configuration and specimen geometry A) The test setting with the specimen placed and the video-extensometer camera angled vertical on the test specimen, B) Test sample with the forces marked to represent the direction of pulling cords on the bottom the biaxial test specimen outline and geometry dimensions.....	78
Figure 3-12 Strain gauges. (A) The 8 strain gauges on the test sample placed by a white matte corrector, (B) The strain gauges in the extensometer software .....	79

- Figure 3-13 Preliminary model project schematic for two stages 2-way FSI ANSYS 17.2. 1<sup>st</sup> Stage FSI components include transient structural component connected to Fluent sharing the geometry. The two components setup is shared through the system coupling and the results of both component post-FSI is shared in a combined results component. The 2<sup>nd</sup> stage geometry is controlled by the pre-stressed structural geometry and the fluid geometry is controlled by the pre-stressed Fluent modified solution..... 84
- Figure 3-14 Block diagram of the computational model validation rig setup. The 3D printed geometry is connected to two one-way check valves. The flow sensor is connected to the outlet check valve and controlled by an Arduino coded program with the result display on a PLX-DAQ excel macro on a connected PC..... 88
- Figure 3-15 Experimental setting of the computational model validation. (A) The experimental setting. (B) The alignment of the preliminary model and the tubing along with the flow sensor. (C) Secured manual pump with the compression machine and the flow sensor. .... 89
- Figure 3-16 Physical model design for 3D printing. The inlet and outlet were 3D printed as 73-77 shore hardness while the sphere was printed in a 27 shore hardness. The geometry was printed in 1 mm thickness. .... 90
- Figure 3-17 Subject-specific simulation workflow of the left ventricle implemented in this work starting from scanning the porcine heart to the final simulation results ..... 92
- Figure 3-18 Porcine heart preparation process. (A) The fluids used for fixating and staining. (B) Porcine heart fixating container. (C) Porcine heart size comparison showing good tissue structure and low shrinkage..... 94
- Figure 3-19 3D representation of the DICOM images in MIMICS20 with thresholding mask to extract the surrounding parts. The images in the top right view represent the axial images (XY-view or Top-view) and are surrounded by a red border. The upper left view (surrounded by an orange border) shows the coronal images that are the images resliced in the XZ-direction (Front-view). The lower left view (surrounded by a green border) shows the sagittal images that are the images resliced in the YZ-direction (Side-view). The lower right view (surrounded by a light-green border) shows the 3D view. .... 95
- Figure 3-20 3D model generation and pre-processing steps using Mimics and 3-Matics software. Each image represent a step in the segmentation process. (A), (B) and (C) have been segmented in MIMICS while image (D) is segmented in 3-Matics. (A) The 3D representation after applying the threshold mask, (B) 3D representation after smoothing and wrapping, (C) 3D representation of the left ventricle segmentation from the whole heart. (D) The left ventricle segmentation and applying the inlet and outlet boundary conditions in 3-Matics. .... 96
- Figure 3-21 Left ventricle meshing in 3-Matics representing the fluid volume and the solid shell surface (A) volume mesh, (B) volume mesh in Y section, (C) solid wall surface mesh, (D) solid wall surface mesh in Y section..... 97
- Figure 3-22 Subject-Specific Geometry. (A) rpresenting the 3 dimensional view of the LV and the compression plates, (B) rresents the -XY orientation of the geometry..... 99
- Figure 3-23 Left Ventricle virtual topology surfaces. (A) +Z view, (B) +X view, (C) -Z view, (D) -X view ..... 101

- Figure 3-24 Model mesh skewness in ANSYS, (A) Structural mesh with shell solid of 1mm thickness, (B) Structural mesh with parts colour showing 2 perpendicular sections with 0.3 mm element size, (C) Fluid mesh with 0.3 mm element size, (D) Fluid region mesh with a section plane normal to the inlet and outlet..... 103
- Figure 3-25 Subject- specific ANSYS project schematic diagram. Additional parts are added to accommodate the imported geometry process illustrated in Finite element modeller and mesh. 1<sup>st</sup> Stage FSI components include transient structural component connected to the imported and meshed geometry from the finite element modeller component. The fluid geometry is directly connected to the meshed geometry from the finite element modeller component The two components setup is shared through the system coupling and the results of both component post-FSI is shared in a combined results component. The 2<sup>nd</sup> stage geometry is controlled by the pre-stressed structural geometry and the fluid geometry is controlled by the pre-stressed Fluent modified solution. The additional results components are added to import the mapping summary of each stage along with the exported post-CFD compatible data from the solved fluid iterations. .... 105
- Figure 4-1 Tensile test measured results Stress-strain curve: (A) 10 mm/min speed with standard deviation error bars, (B) 10 and 500 mm/min stress-strain curve; showed different stiffness in different strain rate measurements recording higher stiffness (20% higher at 80% strain) and tensile strength at break during higher strain rate..... 108
- Figure 4-2 Planar shear measured results represented by the stress-strain relation curve..... 109
- Figure 4-3 Comparison between the different measuring techniques in planar shear test showing higher strain data than the DIC measurements.(A) The experimental strain rate for the planar shear test, (B) an enlarged area of interest for lower strain rate to show the difference between the different measuring techniques. .... 110
- Figure 4-4 Failure of the original clamp design due to slipping of the metal plates and the machine clamps. Instead of tearing of the test piece in the horizontal central line, the material failed from the adhering attachment to the brackets showing no alteration to the painted strain gauges..... 111
- Figure 4-5 Strain rate curve for different strain gauges in the biaxial test. Different strains were recorded at different inner diameter values of the testing specimen and are colour coded in the graph. .... 112
- Figure 4-6 True stress-strain comparison between experimental and predicted material testing data in MCalibration curve fitting: (A) Combined testing data for true stresses, (B) Tensile test data, (C) Biaxial test data, (D) Planar shear test data, (E) Compression test data ..... 114
- Figure 4-7 Biaxial data comparison between the Tango+Black and porcine left ventricle tissue: (A) Biaxial true stress-strain curve of Tango+Black, (B) Left ventricle biaxial true stress-stretch curve (Ahmad et al., Unpublished). It should be noted that the stresses in the material testing is in MPa while in the tissue it is kPa..... 115
- Figure 4-8 Computational validation data for the biaxial material testing curve fitting. The preliminary model biaxial behaviour lies on the biaxial material model profile while showing that the model compression strain lies in the low strain rate part of the calibrated material model..... 116

- Figure 4-9 Tensile test computational validation. This represents the equivalent elastic strain distribution in transient structural ANSYS17.2. The test piece with pattern end design showing consistent equivalent elastic strain on the narrow part of the test piece. .... 118
- Figure 4-10 Material shear behaviour as viewed by the two DIC cameras: (A) The strain consistency during the test with the speckled pattern area of the test piece strain map distribution, and (B) Failure images of the planar test sample at the end of the test showing the area of the tear near horizontal central line and the attached test piece after the sample breaking point. .... 119
- Figure 4-11 Computational validation for the planar shear test using one or two directional tensions. On the left is the computational model for tension from two sides, and on the right is the planar shear computational model of the tension from one side. Both results show similar material behaviour and strain map distribution, which validates the use of either method for the test. .... 120
- Figure 4-12 Planar shear test strain gauge comparison: A) Strain measurement data from the video-extensometer - each series represents a virtual strain gauge placed on the test sample as seen on B ( B) Strain map from the video-extensometer showing the placement of the virtual strain gauges. .... 121
- Figure 4-13 Equibiaxial test computational validation for  $1/8^{\text{th}}$  of the equi-biaxial specimen: (A) Boundary conditions and degree of freedom of the computational model. The letters present the areas of the model constrains (B) Equivalent elastic strain for computational validation of the biaxial test representing area of consistent strain in the middle of the specimen(near the centre)..... 123
- Figure 4-14 Comparison between computational validation equibiaxial and compression tests data ..... 124
- Figure 4-15 On the left are the velocity plane vectors map distributions, and on the right are the velocity streamline swirling strength map distributions in post CFD of the compression stage FSI simulation for  $0 < t < 0.2$ . The velocity is represented by vectors' increasing magnitude in the outlet indicated by the colour-coded map legend and the flow. The vortex formation is shown during different time steps in different locations 126
- Figure 4-16 On the left are the velocity plane vectors map distributions, and on the right are the velocity streamline swirling strength map distributions in post CFD of the compression stage FSI simulation for  $0.2 < t < 0.4$ . The velocity is represented by vectors' increasing magnitude in the outlet indicated by the colour-coded map legend and the flow. The vortex formation is shown during different time steps in different locations 127
- Figure 4-17 On the left are the velocity plane vectors map distributions, and on the right are the velocity streamline swirling strength map distributions in post CFD of the compression stage FSI simulation at  $t=0.5$ . The velocity is represented by vectors' increasing magnitude in the outlet indicated by the colour-coded map legend and the flow. The vortex formation is shown during different time steps in different locations..... 128
- Figure 4-18 Velocity profile of the preliminary model during different time steps of the compression FSI stage. The graph on the top represents the velocity profile in accordance with the outlet position in the Y axis. The image below represents the outlet velocity in accordance with the time steps.

- The time steps data are colour coded for each time step showing increasing magnitude with each time step. .... 130
- Figure 4-19 Velocity plane vectors and their streamline swirling strength map distribution in post CFD of the release stage of the FSI simulation. On the top are the velocity plane vectors map distribution and on below are the velocity streamline swirling strength map distribution in post CFD of the compression stage of the FSI simulation. The velocity is represented by vectors' increasing magnitude in the inlet indicated by the colour-coded map legend and the flow. The vortex formation is shown during different time steps. .... 131
- Figure 4-20 Velocity profile of the preliminary model during different time steps of the release FSI stage. .... 132
- Figure 4-21 Pressure contour plane map distribution in post CFD of the compression stage FSI simulation for  $0 < t < 0.2$  sec. The pressure contour map distribution represented by increasing magnitude along the axis indicated by the colour-coded map legend and the flow. The vortex formation is shown during different time steps in different locations. 134
- Figure 4-22 Pressure contour plane map distribution in post CFD of the compression stage FSI simulation for  $0.15 < t \leq 0.5$  sec. The pressure contour map distribution represented by increasing magnitude along the axis indicated by the colour-coded map legend and the flow. The vortex formation is shown during different time steps in different locations. 135
- Figure 4-23 Pressure contour plane map distribution in post CFD of the release stage FSI simulation. The pressure contour map distribution represented by increasing magnitude along the axis indicated by the colour-coded map legend and the flow. The vortex formation is shown during different time steps in different locations. .... 136
- Figure 4-24 Wall shear map distribution in post CFD of the compression stage FSI simulation. The WSS contour map distribution is represented by increasing magnitude on the fluid surface indicated by the colour-coded map legend and the flow. The gradient formation is shown during different time steps in different locations. .... 138
- Figure 4-25 Wall shear map distribution in post CFD of the release stage FSI simulation. The WSS contour map distribution represented by increasing magnitude on the fluid surface indicated by the colour coded map legend and the flow. The gradient formation is shown during different time steps in different locations. .... 140
- Figure 4-26 Equivalent Von-mises stress distribution map of the 1st stage FSI. On the left is the front view, and on the right is the top view for  $0 \leq t \leq 0.2$  sec. .... 142
- Figure 4-27 Equivalent Von-mises stress distribution map of the 1st stage FSI. On the left is the ZY vie (front view), and on the right is the XZ (top view) for  $0.3 \leq t \leq 0.5$  sec. .... 143
- Figure 4-28 Equivalent elastic strain distribution map of the 1st stage FSI. On the left is the ZY vie (front view), and on the right is the XZ (top view) for  $0 \leq t \leq 0.2$  sec. .... 144
- Figure 4-29 Equivalent elastic strain distribution map of the 1st stage FSI. On the left is ZY view (front view), and on the right is the XZ (top view) for  $0.3 \leq t \leq 0.5$  sec. .... 145

- Figure 4-30 Strain energy distribution map of the 1st stage FSI. On the left is the front view ZY vie (front view), and on the right is the XZ (top view) for  $0 \leq t \leq 0.2$  sec ..... 146
- Figure 4-31 Strain energy distribution map of the 1st stage FSI. On the left is the front view ZY vie (front view), and on the right is the XZ (top view) for  $0.3 \leq t \leq 0.5$  sec..... 147
- Figure 4-32 The inlet and outlet velocity profile obtained from the flow sensor in the validation rig design. The profile showing the velocity through the compression and release as the velocity is a function of flow rate... 149
- Figure 4-33 Velocity vs time of the validated computational model with the experimental data. The impulse results represents the data extracted from post-CFD in reference to the time of the computational simulation, while the velocity profile results are the data obtained from the flow sensor during the validation rig..... 150
- Figure 4-34 Total mesh deformation during the compression phase of the FSI simulation in transient structural in the YZ coordinate. The compression and support plates are shown as rigid shell surfaces during the compression and the colour coded distribution map represent the areas of element deformation characteristic during the compression. .... 151
- Figure 4-35 Total mesh deformation during the compression phase of the FSI simulation in transient structural in the ZX coordinate. The compression and support plates are shown as rigid shell surfaces during the compression and the colour coded distribution map represent the areas of element deformation characteristic during the compression. .... 152
- Figure 4-36 Pressure contour of the subject-specific fluid in the CFD post during the compression stage of FSI. On the right are the streamlines for those pressure gradients during different time steps throughout the simulation. The collected data are for  $0 \leq t \leq 0.1$  sec and the orientation is changed between the images for better representation of the data, the coordinate is indicated in the lower left corner for each image... 155
- Figure 4-37 Pressure contour of the subject-specific fluid in the CFD post during the compression stage of FSI. On the right are the streamlines for those pressure gradients during different time steps throughout the simulation. The collected data are for  $0.2 \leq t \leq 0.4$  sec and the orientation is changed between the images for better representation of the data, the coordinate is indicated in the lower left corner for each image... 156
- Figure 4-38 Pressure contour of the subject-specific fluid in the CFD post during the compression stage of FSI. On the right are the streamlines for those pressure gradients during different time steps throughout the simulation. The collected data are for  $t = 0.5$  sec and the orientation is changed between the images for better representation of the data, the coordinate is indicated in the lower left corner for each image..... 157
- Figure 4-39 Pressure contour of the subject-specific fluid in the CFD post during the release stage of FSI. On the right are the streamlines for those pressure gradients during different time steps throughout the simulation. The collected data are for  $0 \leq t \leq 0.1$  sec and the orientation is changed between the images for better representation of the data, the coordinate is indicated in the lower left corner for each image. .... 158
- Figure 4-40 Pressure contour of the subject-specific fluid in the CFD post during the release stage of FSI. On the right are the streamlines for those pressure gradients during different time steps throughout the simulation. The collected data are for  $0.2 \leq t \leq 0.4$  sec and the orientation is changed

	<i>between the images for better representation of the data, the coordinate is indicated in the lower left corner for each image. ....</i>	159
Figure 4-41	<i>Pressure contour of the subject-specific fluid in the CFD post during the release stage of FSI. On the right are the streamlines for those pressure gradients during different time steps throughout the simulation. The collected data are for <math>t=0.5</math> sec and the orientation is changed between the images for better representation of the data, the coordinate is indicated in the lower left corner for each image.....</i>	160
Figure 4-42	<i>Velocity vectors for the fluid across the X+ three-point plane (inlet, outlet and apex plane) of the LV fluid in post CFD during 1st stage of FSI for <math>0 \leq t \leq 0.2</math> sec. ....</i>	162
Figure 4-43	<i>Velocity vectors for the fluid across the X+ three-point plane (inlet, outlet and apex plane) of the LV fluid in post CFD during 1st stage of FSI for <math>0.3 \leq t \leq 0.5</math> sec.....</i>	163
Figure 4-44	<i>On the left, velocity vectors for the LV fluid across the outlet Y plane, and on the right, velocity vectors for the LV fluid across the inlet Y plane in CFD post during 1st stage of FSI for <math>0 \leq t \leq 0.1</math> sec. ....</i>	165
Figure 4-45	<i>On the left, velocity vectors for the LV fluid across the outlet Y plane, and on the right, velocity vectors for the LV fluid across the inlet Y plane in CFD post during 1st stage of FSI for <math>0.2 \leq t \leq 0.3</math> sec. ....</i>	166
Figure 4-46	<i>On the left, velocity vectors for the LV fluid across the outlet Y plane, and on the right, velocity vectors for the LV fluid across the inlet Y plane in CFD post during 1st stage of FSI for <math>t=0.5</math> sec.....</i>	167
Figure 4-47	<i>Velocity profile streamlines of the LV fluid in the CFD post during 1<sup>st</sup> stage of FSI for <math>0 \leq t \leq 0.2</math> sec. ....</i>	169
Figure 4-48	<i>Velocity profile streamlines of the LV fluid in the CFD post during 1<sup>st</sup> stage of FSI for <math>0.3 \leq t \leq 0.5</math> sec. ....</i>	170
Figure 4-49	<i>Velocity vectors for the fluid across the inlet and outlet plane of the LV fluid in CFD post during 2nd stage of FSI for <math>0 \leq t \leq 0.2</math> sec.....</i>	171
Figure 4-50	<i>Velocity vectors for the fluid across the inlet and outlet plane of the LV fluid in CFD post during 2nd stage of FSI for <math>0.3 \leq t \leq 0.5</math> sec.....</i>	172
Figure 4-51	<i>On the left are velocity vectors for the LV fluid across the outlet Y plane, and on the right, the velocity vectors for the LV fluid across the inlet Y plane in CFD post during the 2nd stage of FSI for <math>0 \leq t \leq 0.1</math> sec.....</i>	174
Figure 4-52	<i>On the left are velocity vectors for the LV fluid across the outlet Y plane, and on the right, the velocity vectors for the LV fluid across the inlet Y plane in CFD post during the 2nd stage of FSI for <math>0.2 \leq t \leq 0.3</math> sec.....</i>	175
Figure 4-53	<i>On the left are velocity vectors for the LV fluid across the outlet Y plane, and on the right, the velocity vectors for the LV fluid across the inlet Y plane in CFD post during the 2nd stage of FSI for <math>t=0.5</math> sec. ....</i>	176
Figure 4-54	<i>Velocity profile measured across the centre of the outlet of the LV at different times during the compression phase of FSI simulation.....</i>	177
Figure 4-55	<i>Velocity profile measured across the centre of the LV at different times during the release phase of the FSI simulation.....</i>	178
Figure 4-56	<i>Dynamic viscosity vs shear rate for the Carreau fluid model (A) during the compression phase of the subject-specific FSI simulation, (B) during the release phase of the subject-specific FSI simulation .....</i>	179
Figure 4-57	<i>LV Total deformation distribution map of the 1<sup>st</sup> stage of FSI (isometric view) for <math>0 \leq t \leq 0.2</math> sec .....</i>	181



Figure 4-58 LV Total deformation distribution map of the 1 <sup>st</sup> stage of FSI (isometric view) for $0.3 \leq t \leq 0.5$ sec .....	182
Figure 4-59 Subject-specific equivalent elastic stress distribution map in CFD post of the compression stage of FSI during multiple time steps. On the left are the XY (front view) and on the right are the ZX view for $0 \leq t \leq 0.2$ sec. ....	184
Figure 4-60 Subject-specific equivalent elastic stress distribution map in CFD post of the compression stage of FSI during multiple time steps. On the left are the XY (front view) and on the right are the ZX view for $0.3 \leq t \leq 0.4$ sec. ....	185
Figure 4-61 Subject-specific equivalent elastic stress distribution map in CFD post of the compression stage of FSI during multiple time steps. On the left are the XY (front view) and on the right are the ZX view for $t=0.5$ sec. .	186
Figure 4-62 Subject-specific model equivalent elastic stress distribution map in CFD post of the release stage of FSI for different simulation times for $0 \leq t \leq 0.2$ sec. The images on the right represent the isometric view and the opposite view is shown on the left. ....	188
Figure 4-63 Subject-specific model equivalent elastic stress distribution map in CFD post of the release stage of FSI for different simulation times for $0.3 \leq t \leq 0.4$ sec. The images on the right represent the isometric view and the opposite view is shown on the left. ....	189
Figure 4-64 Subject-specific model equivalent elastic stress distribution map in CFD post of the release stage of FSI for different simulation times for $t=0.5$ sec. The images on the right represent the isometric view and the opposite view is shown on the left. ....	190
Figure 4-65 Subject-specific equivalent elastic strain distribution map in CFD post of the compression stage of FSI during multiple time steps for $0 \leq t \leq 0.2$ sec. On the left are the XY (front view), and on the right, are the ZX view .....	191
Figure 4-66 Subject-specific equivalent elastic strain distribution map in CFD post of the compression stage of FSI during multiple time steps for $0.3 \leq t \leq 0.4$ sec. On the left are the XY (front view), and on the right, are the ZX view.....	192
Figure 4-67 Subject-specific equivalent elastic strain distribution map in CFD post of the compression stage of FSI during multiple time steps for $t=0.5$ sec. On the left are the XY (front view), and on the right, are the ZX view .....	193
Figure 4-68 Subject-base model: Equivalent elastic strain distribution map in CFD post of the release stage of FSI different to the simulation time for $0 \leq t \leq 0.2$ sec. The images on the right are for the isometric view, and those of the opposite view are shown on the left.....	195
Figure 4-69 Subject-base model: Equivalent elastic strain distribution map in CFD post of the release stage of FSI different to the simulation time for $0.3 \leq t \leq 0.4$ sec. The images on the right are for the isometric view, and those of the opposite view are shown on the left.....	196
Figure 4-70 Subject-base model: Equivalent elastic strain distribution map in CFD post of the release stage of FSI different to the simulation time for $t=0.5$ sec. The images on the right are for the isometric view, and those of the opposite view are shown on the left.....	197
Figure 5-1 Mesh sensitivity for the preliminary model. The skewness, orthogonal quality, and element quality show steady values for mesh size between	

- 0.8-0.09 mm. The aspect ratio will continue to increase with element size decrease. ....201
- Figure 5-2 Velocity vector verification between different elements mesh and step size ANSYS16 Fluent. The images on the top represent velocity vectors of two-step size simulation results. The image on the bottom represents the difference between the two vectors. ....202
- Figure 5-3 Pressure contour verification between different mesh elements and step size ANSYS16 Fluent: The images on the top represent pressure contours of two step-size simulation results. The image on the bottom represents the difference between the two contours. ....203
- Figure 5-4 Contact status for the shell elements during the FSI simulation: During different time steps, the areas of contact are colour coded representing the elements close, far, penetration, and gap formation, which shows the lack of penetration elements during the simulation and the decrease of the gap between the compressing plates and the sphere surface. ....205
- Figure 5-5 Mapping summary in the solution information of the preliminary model along with the source and target mapping compatibility: The similar colour surfaces show 100% compatibility as the unmapped surfaces would be indicated with blue coloured areas. The mapping summary is presented at the beginning of the simulation run showing 100% mapping between the source and target of the data transfer representing the structure and fluid in the FSI simulation. ....206
- Figure 5-6 CT scans of piglet heart using a lab-based Zeiss Xradia 520 (Carl Zeiss XRM, Pleasanton, CA, USA) X-ray. The images represent screenshots of the scanning video starting from (a) to (i). ....208
- Figure 5-7 Coupling solution monitoring mapping summary and the mapping compatibility of the source and target of the structure and fluid contacting surfaces. The similarly coloured surfaces show 100% compatibility as the unmapped surfaces would be indicated with blue-coloured areas. The mapping summary is presented at the beginning of the simulation run, showing 100% mapping between the source and target of the data transfer representing the structure and fluid in the FSI simulation. ....209

## List of Acronyms

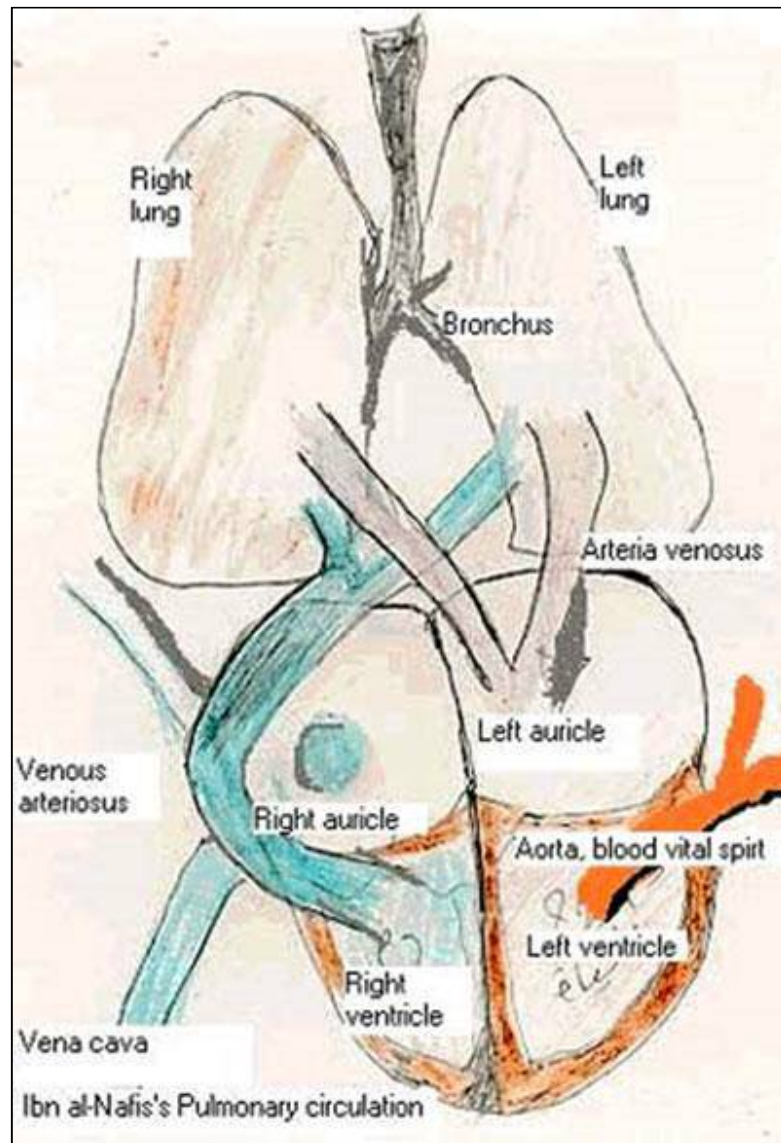
FSI	Fluid-Structure Interaction
CPR	Cardiopulmonary Resuscitation
LV	Left Ventricle
CFD	Computational Fluid Dynamics
FEA	Finite Element Analysis
MRI	Magnetic Resonance Imaging
CT	Computed Tomography
WSS	Wall Shear Stress
SA	Sino-Atrial
AV	Atrio-Ventricular
CA	Cardiac Arrest
CPP	Coronary Perfusion Pressure
ROSC	Return Of Spontaneous Circulation
ALS	Advanced Life Support
SCV	Synchronized Compression / Ventilation
CO	Cardiac Output
RA	Right Atrium
MBF	Myocardial Blood Flow
CI	Cardiac Index
TT	Two Thumbs
TF	Two Fingers
ILCOR	International Liaison Committee On Resuscitation
ECG	Echocardiography
PPE	Pressure Poisson Equation
ALE	Arbitrary Lagrange-Euler
AO	Aortic Orifice
MO	Mitral Orifice
TV	Tricuspid Valve
MV	Mitral Valve
IVS	Interventricular Septum
PMHS	Post Mortem Human Subject
FE	Finite Element
GP	Generalised-Power Law
CAD	Computer-Aided Design
BS	British Standards

DIC	Digital Image Correlation
VFM	Virtual Field Method
PEBT	Planar Equi-Biaxial Testing
UV	Ultraviolet
AM	Additive Manufacturing
TS	Transient Structural
LPM	Liter Per Minute
LED	Light Emitting Diode
PBFS	Phosphate Buffered Formal Saline
DICOM	Digital Imaging and Communications in Medicine
STL	Stereo lithography
CPU	Central Processing Unit
BLS	Basic Life Support
RMS	Root Mean Square
PJD-3DP	Polyjet Direct 3D Printing
GUI	Graphical user interface

## List of Nomenclature

$\rho$	density
$t$	time
$S_m$	mass
$\bar{\tau}$	Stress tensor
$\rho \vec{g}$	The gravitational body force
$\vec{F}$	External body forces
$\mu$	viscosity
$l$	The unit tensor
$v$	velocity
$v_x, v_y, \text{ and } v_z$	The components of the velocity vectors in the cartesian coordinates of X, Y and Z respectively
$P$	pressure
$R_x, R_y, \text{ and } R_z$	the distributed resistances
$f$	Body force
$E$	Young's modulus
$\nu$	Poisson's ratio
$T$	Temperature
$T_0$	The reference temperature
$\mu_0$	The asymptotic viscosities for the lowest shear rate
$\mu_\infty$	The asymptotic viscosities for the highest shear rate
$\lambda$	the relaxation time constant
$n$	power law index
$Sh_A$	Shore A hardness
$R$	Radius of indenter
$C_1, C_2, \text{ and } C_3$	Constitutive model coefficients
$\lambda_1, \lambda_2, \text{ and } \lambda_3$	the principal stretch ratios
$I_1, I_2 \text{ and } I_3$	three strain invariants
$L$	the original length and
$u$	the deformation
$W$	the strain energy per unit volume
$C_{ij}$	material constants
$J$	determinant of the elastic deformation gradient
$\bar{\lambda}_p \text{ (} p=1,2,3 \text{)}$	Deviatoric principle stretches, defined as $\bar{\lambda}_p = j^{-\frac{1}{3}} \lambda_p$
$N, \mu_p, \alpha_p \text{ and } d_p$	material constants
$\sigma$	Stress

$F$	The biaxial load
$b$	Width of the biaxial specimen
$c$	Thickness of the biaxial specimen
$D_i$	Diameter as measured between punch holes
$th$	The original thickness
$\sigma_{true}$	True stress
$\sigma_{nom}$	Nominal (engineering) stress
$\varepsilon_{nom}$	Nominal (engineering) strain
$\varepsilon_{true}$	True strain



The heart and pulmonary circulations as described by Ibn Al-Nafis (1213-1288)

*“When hearing something unusual, do not pre-emptively reject it, for that would be folly. Indeed, unconventional things may be true, and familiar and praised things may prove to be lies. Truth is truth unto itself, not because many people say it is.”*

*Ibn Al-Nafis, “Commentary on Anatomy in Avicenna’s Canon”*

# Chapter 1. Introduction

## 1.1. Motivation for the Study

Understanding of the human cardiovascular system has recently been accelerated through the use of blood flow simulations. It is now recognized that cardiac pathologies, such as atherosclerosis or aneurysms, are closely related with blood flow characteristics, such as areas of flow reversal or low and oscillatory shear stress. Therefore, a detailed understanding of the local haemodynamics can have valuable clinical application. The developments in the acquisition of medical data and the recent evolution on the performance of computers now make it possible to deliver subject-specific information on blood flow behaviour.

Modelling the human circulatory system remains, however, a very difficult and challenging task because of its complexity and heterogeneity, both geometrically and functionally. Moreover, blood flow is characterised by three dimensional (3D) pulse waves due to the fluid-structure interaction (FSI) between blood and the cardiovascular wall.

To provide data to enhance clinical management strategies, we need to be able to predict the flow in the human heart, which requires modelling the time-dependent geometry of the ventricles, atriums and the cardiac valves during the cardiac cycle and this is highly complex. This thesis is adopting these principles to provide an initial insight into blood flow during the compression-phase of cardiopulmonary resuscitation (CPR). Improved knowledge of blood flow during CPR will provide a platform to understand how to optimise chest compression strategies, to maximise the success of this life-critical intervention. Current guidelines, especially for infants, are predominantly derived for animal-based experiments and so scope remains for a more accurate and precise understanding of blood flow.

The will to resuscitate emerged during the Enlightenment as demonstrated by rescue societies. It took approximately 200 years for the way of resuscitation to be found. The elements of ventilation, chest compression, and defibrillation had to be discovered separately and integrated for reversal of sudden death to become a reality. The discipline of resuscitation was founded on the scientific method of experimentation. Many incorrect starts, particularly in ventilation and defibrillation, happened before new identifications led to effective techniques. (Halperin et al., 2004)



Fluid-structure interaction (FSI) and Left Ventricle (LV) fluid flow are important characteristics in CPR and must be taken into account in the analysis and development of heart modelling and updating the CPR guidelines. FSI enables investigation of the effect on fluid flow as a consequence of its interaction with the deforming cardiac wall. This is called the haemodynamic effect and is concerned with how the mechanical and physiological properties of blood influence the pressure and flow through the body. Advances in numerical methods and three-dimensional imaging techniques have enabled the quantification of cardiovascular mechanics in subject-specific anatomic and physiologic models. Subject-specific models are being used to guide cell culture and animal experiments and test hypotheses related to the role of biomechanical factors in vascular diseases. The subject-specific modelling has enabled an entirely new application of cardiovascular mechanics, namely predicting outcomes of alternate therapeutic interventions for individual patients. (Mihalef et al., 2010, Ionasec et al., 2009, Baretta et al., 2012, Tang et al., 2008)

CPR describes an instance where the natural rhythm of the heart has ceased, with manual chest compressions instead serving to expel blood. It is already understood that the extent of chest compression and the displacement-time relationship influence the effectiveness of CPR outcomes, predominantly as a consequence of the rate of supplying oxygenated blood to the vital organs. Hence, the capability of FSI to more accurately simulate blood flow provides a new and novel opportunity to identify the most effective chest compression strategy to oxygenate the life-critical tissues. The effects of displacement and duration of the compression have been investigated by (Rottenberg, 2014, Anne L Solevåg<sup>1</sup> et al., 2012, Iglesias et al., 2010, Halperin et al., 2004). However to the author's best knowledge, few studies have focussed on investigating the most effective chest compression strategies to achieve the optimal fluid flow from the left and right ventricle during infant CPR. This study presents a 3D (FSI) model of an infant porcine left ventricle using the commercial software ANSYS finite element analysis (FEA) system, coupled with the computational fluid dynamic (CFD) software Fluent, to investigate blood haemodynamics during a single CPR compression.

This study has developed a subject-specific model for the simulation of the human cardiovascular system when exposed to representative loading conditions of CPR. The model has been designed in an abstract setting to ease the development of preliminary model for the fluid-structure coupling of cardiovascular compartment representation.

## 1.2. The Goal of the Present Study

This research presents an investigation of the haemodynamic behaviour of the left ventricle during a CPR compression. Establishing a novel platform to investigate the chest compression efficacy in infant CPR has been the aim of this work. Measurement of blood flow in humans during CPR has led to an emphasis on the importance of sustained compression during clinical CPR. Variables such as the blood volume and its distribution, vascular resistance, chest compression force, or drugs may all change the optimum compression rate and duration during CPR. (Peters and Ihle, 1990a, Peters and Ihle, 1990b, Udriște and Neagu, 2010, Gerrit J. Noordergraaf et al., 2005).

Despite numerous experimental and computational studies considering the parameters affecting the CPR mechanism, very few have considered how best to achieve the optimal systemic blood flow during infant CPR. Scope exists, therefore, to develop a platform that enables investigation of chest compression strategies that will achieve the optimal blood output, via an FSI model. This study adds to the existing research by investigating the coupled effects of blood flow and a simplified left ventricle, using a two-way FSI model. This approach will enable prediction of the velocity and pressure distribution produced by the blood flowing during compression and release of the left ventricle wall which gives a computational evidence to the required blood flow behaviour for CPR compression development.

The preliminary geometry of the left ventricle was designed to verify the FSI approach, followed by an investigation using subject-specific geometry. Commercial software (Transient Structural and FLUENT) were used for the solid and fluid solvers, separately but connected in a system coupler within ANSYS.

The following objectives are set to achieve the aim of establishing a novel platform to investigate the chest compression efficacy in infant CPR. Since the focus of the current study is to investigate the compression method and its effect on the blood flow during CPR:

- Creating structural and CFD models and simulating the fluid-structural interface between the two in order to get the preliminary computational fluid flow model during compression.
- Validating the preliminary computational model by designing a 3D printed physical model of a material properties with approximate simulation to the heart tissue material.
- Testing the model with the CPR compression parameters to validate the computational model dynamics of the fluid flow.

- Processing the scans of infant cardiovascular MRI and/or CT images using image processing software to create an initial simplified model for the left ventricle of the heart.
- Applying the numerical and geometrical assumptions to the primary CFD model to develop a dynamic flow model.
- Analysing and post processing the model through the study of the factors that affect the blood flow during CPR to shed the light on these parameters for better CPR technique performance.

### **1.3. Thesis Layout**

The present work consists of six chapters. The individual chapters have the following content:

#### **1.3.1. Chapter Two- Literature Review**

Chapter Two presents a review of the fundamental theory of cardiovascular biomechanics, in particular the cardiopulmonary resuscitation process mechanism. Description of the medical background behind the modelling including the anatomy and physiology of the cardiovascular system as well as an overview of the CPR procedure and its effect on circulation. This chapter also includes the principles of FEA, CFD and FSI, simulation software used in this thesis.

The extensive review considers the following topics:

- Adult and infant anatomical and physiological differences through the normal cardiac cycle and during the CPR process.
- The use of animal cardiovascular surrogates to represent the human physiology and the differences between the models
- Existing methods for geometrical representation of the cardiovascular system, specifically mathematical formulation of the left ventricle modelling.
- Application and selection of various tissue-like behaviour materials in cardiovascular model design and the existing mechanical properties evaluation techniques for both natural tissue and modelling materials.
- Theory and mathematical formulation of constitutive material models, and experimental performance evaluation techniques including their achievements, accuracy, applicability, and limitations.

### 1.3.2. Chapter Three – Materials and Methods

This chapter illustrates the simulation workflow for FEA, CFD and FSI simulations in a preliminary model design. The experimental validation procedure is explained along with the material testing. The final part of this chapter is to illustrate the anatomical-specific model, various meshing and processing approaches for the applications are presented.

The following steps of the method are implemented in the models:

- The methodology and applied boundary conditions are stated for the preliminary model.
- Presentation of the parameters regarding the model boundary conditions for FEA, CFD and FSI are described alongside the structural and fluid material models.
- Computational model validation process including design and materials used and material testing procedure for every test.
- Subject-specific model geometry design procedure including CT scanning preparation process of the piglet heart. Also system coupling setting's modification compared to the preliminary model system coupling settings in ANSYS.

### 1.3.3. Chapter Four – Results and Discussion

In this Chapter, fluid and structural performances of the models are evaluated based on FSI analysis results. The main measure in the fluid domain is specified as blood flow velocity distribution on various 2D planar locations through the geometry. The characteristics of pressure and wall shear stress (WSS) on the interacting surfaces are analysed, as is the structural domain, based on the link of pressure from fluid domain and its effects as metrics of total deformation and equivalent Von-Mises Stress.

The following topics are explored:

- Preliminary model results and discussion regarding the simulation monitoring and convergence.
- Fluid flow distribution is presented by velocity vectors, streams lines on reference planes and supplementary planes as well as the pressure distributions.
- Computational model validation process results and the corresponding discussion for each test data as well as their computational validation
- Subject-specific model results and their discussion regarding the simulation monitoring and the running simulation convergence

- Characteristics of the blood flow is studied by recording the variation of measurements of maximum velocity and the velocity profile. Observation of flow regime in terms of pressure and viscosity profile and tracing of recirculation zone near the boundaries.
- Similarly to preliminary model structural results are presented as the contours of total deformation, Von-Mises Stress and equivalent strains.

#### **1.3.4. Chapter Five \_ Technical Achievements and Limitations**

Computational model quality including convergence, boundary condition meshing and their related mapping as well as model stability. This step was performed to eliminate any causes of data shift or inconsistency due to software computational artefacts.

This chapter included the following monitoring techniques:

- Simulation quality assurance study to evaluate the system coupling process in terms of monitoring charts of the applied software consisting components.
- Computational challenges and computational limitations of the proposed models.
- The data transfer mapping quality assurance and the mesh study outcome, thus verifying the model's sensitivity quality.
- Computational and experimental limitations

#### **1.3.5. Chapter Six – Conclusions and Future Work**

In this Chapter, the outcome of the research in previous chapters is discussed where the proposed model is justified as an optimum design. Further on in this Chapter, conclusions are drawn with emphasis on the validity of results and achievements of the objectives outlined in Chapter 1. In addition, future direction to this research is discussed and outlined below:

- Computational research needs are highlighted as the improvements on anatomical geometry components based on more realistic data acquisition from natural human heart.
- Further enhancements on the algorithms of multi domain coupling to be more robust where updated CPR process can be improved.

## Chapter 2. Literature Review

### 2.1. Chapter Overview

This literature review was conducted up until the 1<sup>st</sup> June 2018 and encompasses books, scholarly articles, and any other sources relevant to cardiovascular system modelling and theory. This literature review provides a description, summary, and critical evaluation of these works and is intended to demonstrate how this research fits within the larger field of study.

The extensive review considers the following topics:

#### **Heart and Blood Circulation:**

- The theories of the blood flow mechanism during the cardiac cycle in a normal heart are examined and compared to the optimal output from the CPR process.
- The CPR guidelines are updated on a 5-yearly basis, drawing upon the latest research; the current guidelines and latest research are explained in this chapter.
- Comparison between adult and infant anatomy, the biomechanics of the heart, and the comparison between the human and animal research studying the biomechanics of the heart is also reviewed.

#### **Computational modelling:**

- Modelling of the anatomical system including the cardiovascular system is reviewed in this chapter, identifying the mathematical equations defining tissue behaviour and how these are integrated into the modelling software used in this work.
- As a validation step for a computational model requires material representation, the literature studying hyperelastic material properties is reviewed in this chapter along with the methods used by researchers to accommodate the material behaviour.

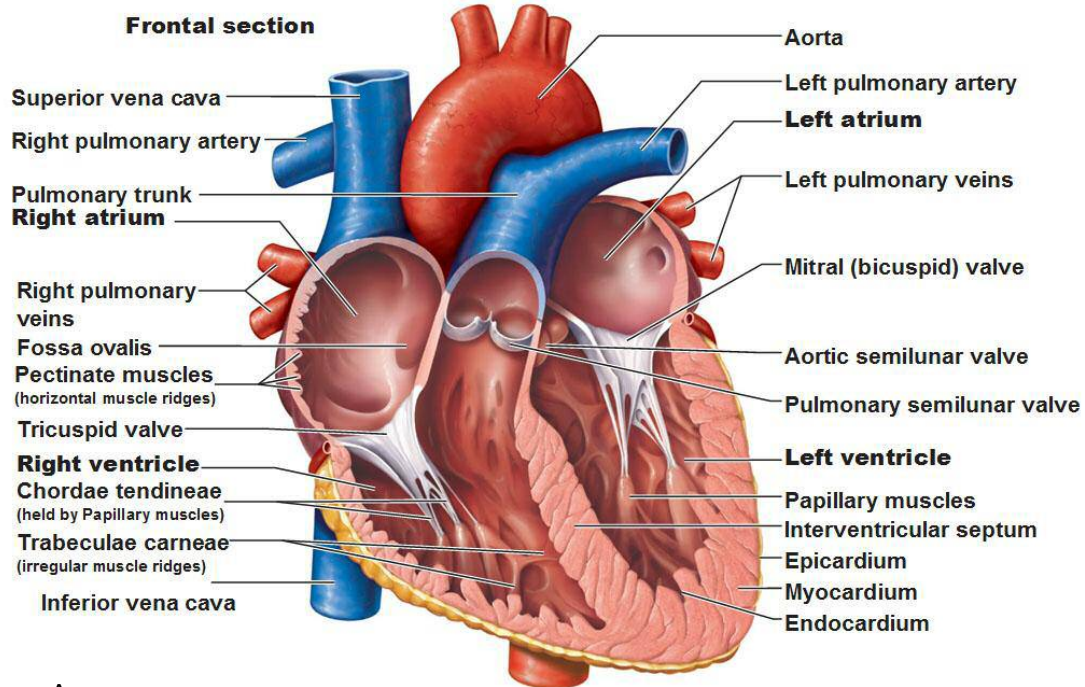
## 2.2. Heart and Blood Circulation

The heart is a hollow muscular organ of four chambers: two ventricles and two atria. It is the functional pump of the blood circulation. The aorta and pulmonary artery are connected to the left and right ventricles respectively by semilunar valves. Furthermore, the left and the right atria support the filling of the ventricles. The atria are connected to the ventricles through the mitral and the tricuspid valves respectively, which are also known as the atrioventricular valves; these allow the blood to pass only in one direction (Hazer, 2009).

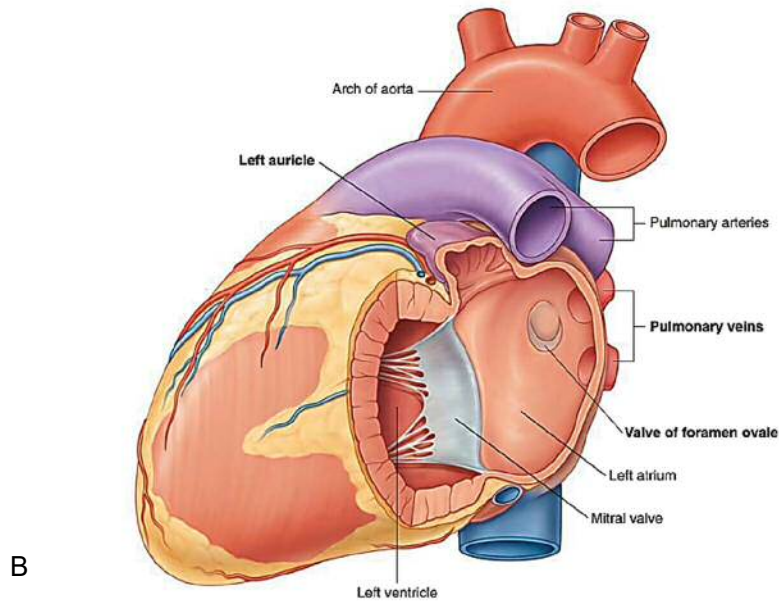
The circulation of the blood begins in the right atrium targeted by the sinoatrial node (SA). The SA node, which works as the primary pacemaker, sends cyclical electrical depolarization and polarization into the right ventricle through the tricuspid valve, as shown in Figure 2-1. These signals extend at a velocity of 1 m/s into the surrounding muscles of the atria causing it to contract. A delay occurs in the atrio-ventricular node (AV) permitting the filling of the ventricles. The right ventricle pumps the blood through the pulmonary valve into the pulmonary artery, which transfers it to the lungs. In the lungs, the blood gets oxygenated before it flows back through the pulmonary vein to the left atrium. The blood then passes to the left ventricle through the mitral valve where, under high pressure during muscular contraction, it gets expelled into the aorta. After the exchange with the cells throughout the body, the deoxygenated blood returns through the two vena cavae and back to the right atrium (Silbernagl and Lang, 2000, Oertel and Krittian, 2012).

The cardiac cycle may be divided into four phases (Silbernagl and Lang, 2000), as illustrated in Figure 2-2. The mitral valve is open during the filling owing to the slightly higher pressure in the left atrium than in the left ventricle. The pressure in the left ventricle then increases as it expands while the aortic pressure decreases continuously, corresponding to the blood flow in the arterial vascular system, but it still remains sufficiently high that the aortic valve remains closed. With the start of the contraction phase, the ventricle pressure exceeds the atrium pressure, and as a consequence, the mitral valve closes. During the isovolumetric contraction, the ventricular pressure reaches 166 mbar, thus exceeding the aortic pressure, and forces the aortic valve open. At this stage, in an adult, a constant volume of approximately 80 ml blood flows out into the aorta while the pressure increases from its minimum value of 107 mbar to its maximum of 160 mbar. The aortic valve then closes during relaxation causing the ventricle pressure to drop again below the pressure in the aorta. Isovolumetric relaxation follows until the ventricle pressure is below the pressure in the atrium. The mitral valve opens, and the cardiac cycle starts again.

## Heart Interior



A



B

Figure 2-1 Human heart and cardiac circulation diagram (Pearson Education, 2010). (A) Representing the major cardiac structure of the heart compartments, valves, and connecting vessels. (B) represent the external view of the left ventricle (Drake et al., 2010).



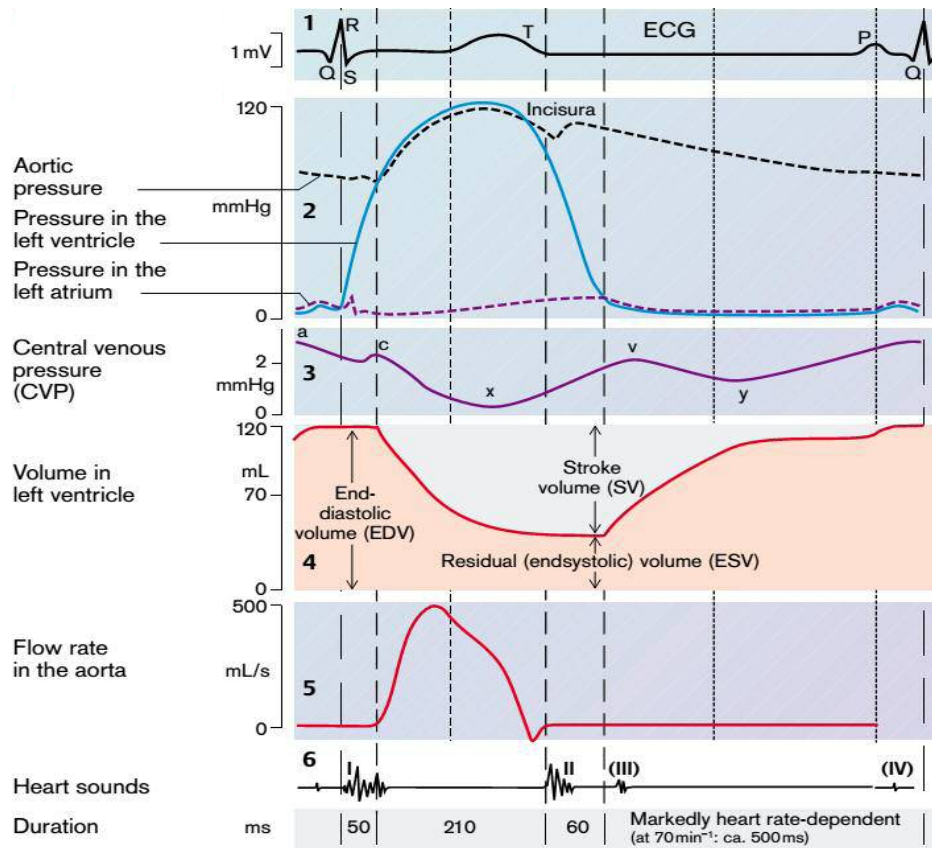


Figure 2-2 Cardiac Cycle: Systole with isovolumetric contraction (I) and ejection (IIa and IIb) phases; Diastole with isovolumetric relaxation (III) and filling (IVa and IVb) phases (Silbernagl and Lang, 2000)

Intake jets initially form during the filling process, when the mitral and tricuspid valves open, accompanied by a ring vortex after one quarter of a cardiac cycle (see Figure 2-3). As the vortex moves into the ventricle, its velocity decreases. There is no flow through the apex of the ventricle at this time. As the intake process continues further, because of the significant deformation in the left ventricle, the ring vortex inclines towards the apex of the ventricle. As this happens, the velocity of the 3D flow decreases until eventually, the intake process is completed and the mitral valve shuts. Further deformation of the vortex structure is determined by the inertia of the flow. In parallel, the upper part of the ring vortex induces a secondary vortex in the aortic channel (Oertel and Krittian, 2012).

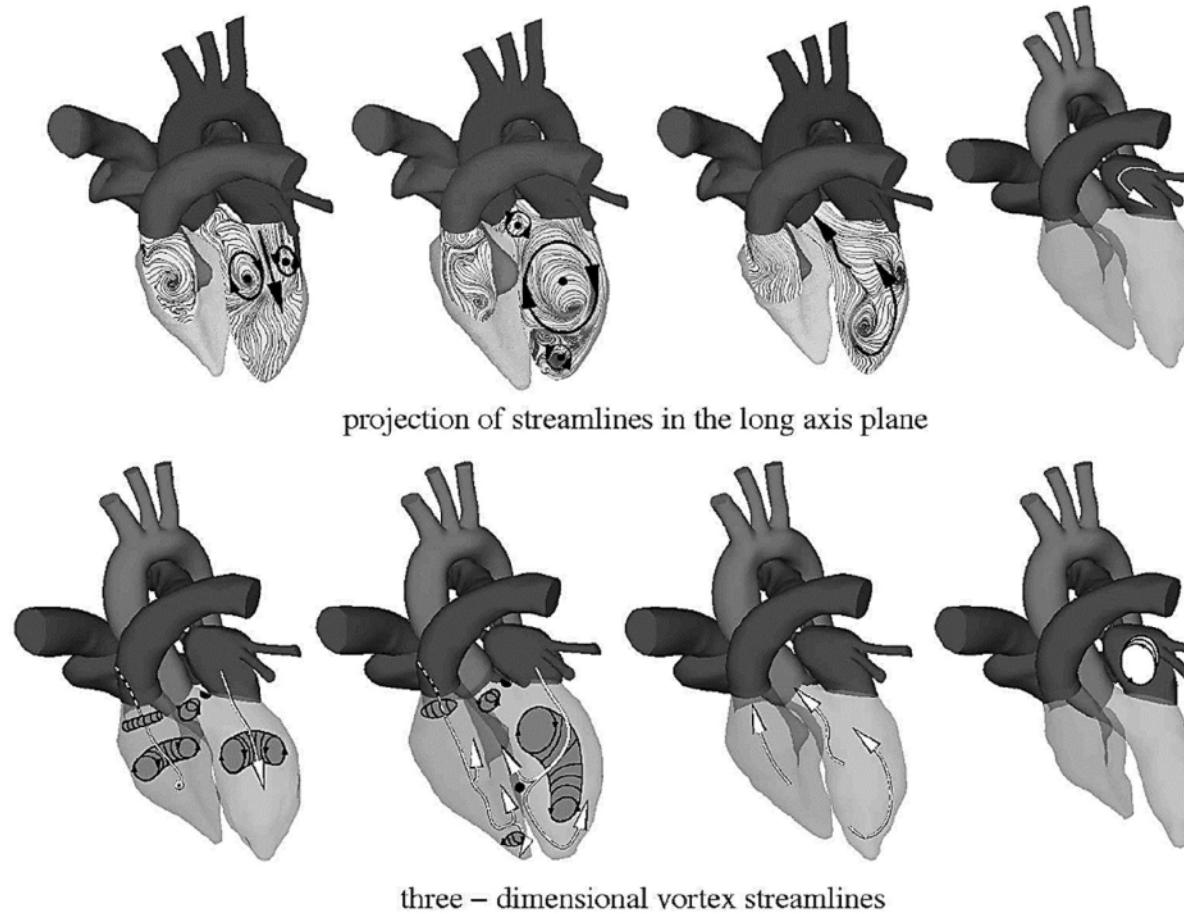


Figure 2-3 Three-dimensional flow in the ventricles and projections of the streamlines in the long-axis plane. As the mitral and tricuspid valves close during the filling process accompanied by a ring vortex after one quarter of a cardiac cycle. These occur to balance out the deceleration of the inflow. In the diastole continues, because of the motion of the cardiac myocardium, the ring vortex increases in size. (Oertel and Krittitan, 2012)

## 2.3. Paediatric Cardiopulmonary Resuscitation (CPR) Overview

Establishing a secure airway is one of the primary tasks of the emergency care provider during resuscitation. Sufficient ventilation can reduce hypoxia and hypercapnia. Decisions regarding timing and which type of ventilation method to use are influenced by the patient's oxygenation status, duration of arrest, expected difficulties with airway control, and operator experience and training in accordance with the ILCOR guidelines.

Guidelines on paediatric life support must incorporate the best, most simple, and most feasible scientific evidence available (Maconochie et al., 2015). International guidelines are based on three main principles:

1. The incidence of critical illness, particularly cardiopulmonary arrest, and injury in children is much lower than in adults.
2. The illnesses and pathophysiological responses of paediatric patients often differ from those seen in adults.
3. Many paediatric emergencies are managed primarily by providers who are not paediatric specialists and who have limited paediatric emergency medical experience.

One can identify four distinct phases of cardiac arrest (CA) and CPR interventions: pre-arrest, no flow (untreated CA), low flow (CPR), and post-resuscitation. Interventions (Table 2-1) to improve the outcome from paediatric CA should optimise the time and phase of CPR as suggested in Table 2-1 (Ornato and Peberdy, 2005). Effective CPR attempts to optimise coronary perfusion pressure (CPP) and cardiac output to critical organs to support the viability of vital organs during the low-flow phase. Important tenets of basic life support (BLS) are PUSH HARD, PUSH FAST, and minimise interruptions. Optimal CPP, exhaled carbon dioxide, and cardiac output during the low-flow phase of CPR are consistently associated with improved chance of the return of spontaneous circulation (ROSC) and improved short- and long-term outcomes (Ornato and Peberdy, 2005).

Table 2-1 Paediatric phases of CA and resuscitation interventions CA, cardiac arrest; BLS, basic life support; ALS, advanced life support; CPR, cardiopulmonary resuscitation (Ornato and Peberdy, 2005)

<b>Phase</b>	<b>Interventions</b>
Pre-arrest phase (protect)	<ul style="list-style-type: none"> <li>•Optimise community education regarding child safety</li> <li>•Optimise patient monitoring</li> <li>•Prioritise interventions to avoid progression of respiratory failure and/or shock to CA</li> </ul>
Arrest (no-flow) phase (preserve)	<ul style="list-style-type: none"> <li>•Minimise interval to BLS and ALS</li> <li>•Organise 911 /Code Blue Response system</li> <li>•Preserve cardiac and cerebral substrate</li> <li>•Minimise interval to fibrillation, when indicated</li> </ul>
Low-flow (CPR)phase (resuscitate)	<ul style="list-style-type: none"> <li>•Effective CPR to optimise myocardial blood flow and cardiac output (coronary and cerebral perfusion pressures and end-tidal CO<sub>2</sub>)</li> <li>•Consider adjuncts to improve vital organ perfusion during CPR</li> <li>•Match oxygen delivery to oxygen demand</li> <li>•Consider extracorporeal CPR if standard CPR/ ALS not promptly successful</li> </ul>
Postresuscitation phase (immediate) (hours to day)	<ul style="list-style-type: none"> <li>•Optimise cardiac output and cerebral perfusion</li> <li>•Treat arrhythmias, if indicated</li> <li>•Avoid hyperglycaemia, hyperthermia</li> <li>•Consider mild resuscitative systemic hypothermia (for 24-48 hours following resuscitation)</li> <li>•Possible future role for antioxidants, anti-inflammatory agents, thrombolytics, mediators of hibernation, and modulation of excitatory neurotransmitters</li> </ul>
Postresuscitation phase longer term rehabilitation (regenerate)	<ul style="list-style-type: none"> <li>•Early intervention with occupational and physical therapy</li> <li>•Bioengineering and technology interface</li> <li>•Possible future role for stem cell transplantation</li> </ul>

There are several theories and observations that explain the mechanics of the circulation during CPR in adults:

1. Conduit Observation: During chest compression with lung inflation, the left ventricle represents a passive conduit rather than a pump.
2. Cardiac Pump Mechanism: Pressure on the sternum compresses the heart between the ribcage and the spine forcing the blood to flow from the ventricles while the relaxation of that pressure from the sternum will allow the heart to fill.
3. Thoracic Pump Hypothesis: Flow generation by intrathoracic pressure gradient produces an arteriovenous pressure gradient at the thoracic inlet.

4. Thoracic Pump Mechanism: This is a combination of the conduit observation and the thoracic pump hypothesis.

To restore the flow function of the heart, there must be optimum flow depending on the rate, compression duration, and flow, and this condition is crucial irrespective of the explaining mechanism. Flow velocity is estimated from unidirectional Doppler measurements to represent carotid blood flow. Variables such as the blood volume and its distribution, vascular resistance, chest compression force, or drugs may all change the optimum compression rate and duration during CPR. (Peters and Ihle, 1990a, Peters and Ihle, 1990b, Udriște and Neagu, 2010, Gerrit J. Noordergraaf et al., 2005)

During sternal compression, the mitral and aortic valves are open, and they are closed during compression release. This was recorded by a 2D-echocardiography in adults (Ornato and Peberdy, 2005, Yannopoulos et al., 2005).

### **2.3.1. Theories of Blood Flow Mechanism during CPR**

Theories of blood flow during CPR are based on the observation of the pressure changes during the procedure. As the intrathoracic pressure changes during CPR, it may result in either mitral valve opening or closure, depending on whether the lung volume is increased or decreased. An increase in intrathoracic pressure could inflate the lung, close the mitral valve, and empty the left ventricle into the aorta, and yet not selectively squeeze the heart. Although synchronized compression / ventilation (SCV) is the more commonly used term (than passive airway pressure and compression), it is considered a misnomer since it implies, perhaps permanently, that lung inflation rather than the pressure change constitutes the important principle (Ornato and Peberdy, 2005). During chest compression, the rapid increase in arterial pressure is primarily the consequence of an (intrathoracic) pressure pulse rather than due to ejection of blood from the heart (Peters and Ihle, 1990a, Peters and Ihle, 1990b).

Blood is circulated during CPR by at least three different mechanisms:

- a) The cardiac pump: direct compression of the heart between the sternum and the spine. This mechanism is predominant in young children because of the relatively compliant thoracic wall.
- b) The thoracic pump: increase in intrathoracic pressure generating a gradient for blood to flow from the pulmonary vasculature, through the heart, and into the peripheral circulation.

- c) The abdominal pump: abdominal compression forces arterial blood from the abdomen to the periphery against a closed aortic valve and forces venous blood from the inferior vena cava back to the heart.

Theoretic proposals regarding the effects of rate and duration are closely entwined with these theories. Proponents of the cardiac pump model of blood flow during CPR argue that blood flow during CPR is dependent on the closure of the mitral valve during compression. As long as the compression duration allows the heart to be compressed to its full extent, the stroke volume will be constant regardless of rate, and CO will increase with the increasing rate. Conversely, the thoracic pump theorists say that forward flow during CPR is related to intrathoracic pressure fluxes, with the heart acting as a conduit for the flow.

Work in adult animal models suggests that cardiac compression need not occur for there to be aortic blood flow during CPR. The rise of intrathoracic pressure generates an extrathoracic arteriovenous pressure gradient, and enhancing this gradient increases cerebral perfusion. When conventional external chest compression is used in adult animal models, cerebral and myocardial blood flow and intrathoracic pressure generation are extremely low. In adult and animal models of CA, circumferential (Vest) CPR improves CPR haemodynamics dramatically. In smaller infants, it is often possible to encircle the chest with both hands and depress the sternum with the thumbs while compressing the thorax circumferentially. In an infant model of CPR, the two-thumb method of compression results in higher systolic and diastolic blood pressures and a higher pulse pressure than traditional two-finger compression of the sternum (Ornato and Peberdy, 2005).

In Dean et al. (1987) study, pressures were recorded from the intrathoracic aorta, left ventricle, and right atrium with Statham P23 Db transducers levelled at the right atrium. Left ventricular, right atrial, and thoracic aortic pressures during compression (systole) and relaxation (diastole) phases were read visually from the recordings, as were mean pressures. High-frequency overshoot during compression was excluded when it occurred. Systolic and mean pressures were considered to reflect the potential generation of intrathoracic vascular pressure during chest compression and were used for analysis. Diastolic pressure was not analysed further, as it reflects the efficacy of flow generation, venous return, and peripheral resistance more than intrathoracic vascular pressure generation during chest compression.

The major findings of Dean et al. (1987) study are that during CPR, there are alterations in the chest geometry which are dependent on the age of the animal; the effective production of intrathoracic vascular pressures can be related to changes in chest geometry by a simple model of the thorax as an elliptical cylinder. In humans, pressures generated during CPR are higher than those observed in animal studies, and they speculated that this is because the

human chest has a thoracic index much less than unity. The clinical results of CPR are better than would be expected from the very low cerebral and myocardial flows measured in the laboratory.

### **2.3.2. Effective Method of Chest Compression**

Measurement of blood flow in humans during CPR has led to an emphasis on the importance of sustained compression during clinical CPR. However, there is a lack of clear understanding relating to the most effective method of chest compression during CPR. In Dean et al. (1990) study, the thoracic index of animals used was close to unity, which is much closer to the human infant (thoracic index 0.6) than to dogs (thoracic index 1.6). Furthermore, human infants have a very compliant chest wall and are easily compressed during clinical CPR. Piglets used in these studies have exhibited a similar compliance. This is why this model was considered to be more applicable to human infants and children than results obtained in other species. Cerebral perfusion depends largely on the ability to generate forward blood flow by either a direct cardiac compression pump or an intrathoracic pump mechanism. In both age groups, the duty cycle affected cerebral perfusion pressure primarily by altering aortic blood pressure.

These two studies (Dean et al., 1987, Dean et al., 1990) studied age-related effects of compression rate and duration and age-related changes in chest geometry during cardiopulmonary resuscitation. They concluded that the duty cycle significantly affects cerebral perfusion pressure during conventional CPR in 2- and 8-week-old piglets. When the duty cycle is prolonged beyond an optimal point, the relaxation time becomes inadequate and chest recoil is impaired. This limits venous return and subsequent pressure generation. The relaxation time required for chest recoil is longer in 8- than in 2-week-old piglets, and higher compression rates can be used in 2-week-old piglets at a comparable duty cycle. They also found that changes in chest geometry which occur during conventional CPR in piglets differ by the age group of the animals.

The production of intrathoracic vascular pressure during CPR is largely dependent on the initial thoracic index and the change in the thoracic index as a result of deformity produced during compressions. This deformity may provide leverage for pulsatile displacement to generate pulsatile intrathoracic pressure as long as the deformation is not so extreme as to limit pulsatile displacement. The model results (Dean et al., 1990, Dean et al., 1987) suggested that the failure of conventional CPR in animals cannot be extrapolated to humans; on the contrary, the efficacy of conventional CPR in humans would be predicted by the model.

They could not identify the optimal compression rate in either age group, or state which animal group produces better cerebral perfusion during conventional CPR at any given setting. Also, they did not address whether prolonged compressions will result in better perfusion over a prolonged period of CPR, and nor did they measure arterial blood gases or actual regional blood flow in this study.

Those favouring the cardiac pump model suggest that the increased rate itself is beneficial to increase CO, while those favouring the thoracic pump model suggest that the increased rate allows for greater relative compression duration to be maintained more easily during CPR. In the model by Swart et al. (1994), total blood flow is thought to be increased by increasing compression duration rather than rate, and any beneficial effect of an increased rate may be due to the relative increase in the percentage of compression duration with an increasing rate. Cardiac output and mean arterial pressure have been shown to increase with increasing depths of compression between 2.5 cm and 6 cm in a mechanical model of CPR. In a trial of human resuscitation using mechanical CPR, increased compression force resulted in increases in systolic aortic pressure and end tidal CO. Also, the results have shown that short compressions are ineffective and that chest compressions are optimized by rhythmic 50% down stroke and 50%-release patterns.

Swart et al. (1994) study had methodological limitations related to the use of fluid-filled catheters in the measurement of RA pressures. The same measurement technique was used for all CPR techniques on all animals; thus, systematic bias may have resulted in false CPP measurements, but the magnitude of difference in CPPs would not be affected. A theoretical limitation was encountered because the study was not designed to aid in the differentiation of cardiac pump vs thoracic pump CPR mechanisms. While the mechanism of blood flow in CPR is of considerable interest, and its understanding could aid in the development of new CPR techniques, the purpose of the study was to better define the performance parameters of the HI-CPR technique, regardless of its mechanism.

### **2.3.3. CPR Procedure, Regulations, and Improvements**

Since the Standards for Cardiopulmonary Resuscitation and Emergency Cardiac Care were introduced in 1974, several updates to these guidelines have been issued. Over this time, the guidelines have come full circle, moving from simple to complicated and then to simple again. Many studies have been performed to investigate the effect of different parameters affecting the quality of CPR with an emphasis on what is effective in improving survival. Since the focus of the current study is to investigate the compression method and its effect on the blood flow during CPR, this section will review and discuss some of the literature investigating that



parameter during CPR regarding procedure, existing regulations, and methods of improvement.

Zuercher et al. (2010), for example, discussed whether residual leaning adversely affects cardiac index (CI) and left ventricular myocardial blood flow (MBF) in a piglet model of paediatric CPR. They hypothesized that residual leaning at 20% of the force required to maintain aortic systolic pressure of 85 mmHg would have substantial negative effects on CI and left ventricular MBF, but that 10% residual leaning would have minimal or no effect. Furthermore, complete chest recoil can generate negative intrathoracic pressure during CPR, thereby improving venous return and cardiac output.

Zuercher et al. (2010) measured aortic and right atrial pressures, electrocardiogram, and end-tidal partial pressure of carbon dioxide by using hardware from Gould Instrument Systems (LDS, Middleton, WI), continuously displayed on a P3 Plus Ponemah Physiology Platform (DSI, St Paul, MN) and recorded on a laptop computer (Gateway, Sioux City, SD) for data analysis. All haemodynamic and mechanical data were recorded at a frequency of 200 Hz. Coronary perfusion pressure was calculated as the difference between aortic pressure and right atrial pressure in the mid-relaxation phase of compression. These parameters changed over time, consistent with previous documented vascular pressures and blood flows with prolonged CPR. Zuercher et al. (2010) study, while using healthy young piglets with excellent CPR performance quality, might have yielded different results had the CPR been performed on sick children using poor quality CPR. Hence, studies in humans are needed to evaluate the effects of the residual leaning force on intrathoracic pressure, vascular pressures, venous return to the heart, and coronary and cerebral perfusion.

Tsai et al. (2012) used CPR compression regulations as a baseline and selected a wide range of displacements for the parametric analysis for their study as a reference for the applied force while gripping a child. As expected, changing compression displacement did not alter the distribution of stress, but linearly affected the maximum stress in the rib. It was unknown what stress causes fracture in the infant rib (Figure 2-4). This shows the importance of the CPR regulations to support other infant medical associated studies. Tsai et al. (2012) study, while focusing on the rib fracture caused by abuse, drew attention to the compression technique used in paediatric CPR. The poor quality of the compression, as discussed in this section, leads to poor blood flow in the circulation; however, the poor quality of the compression may lead to extensive injuries to other anatomical structures in an infant. Thus, it is important to develop novel methods and technology that allow the quantification of the thoracic response to chest compressions when monitoring CPR quality. A study integrated a load cell and accelerometer sensor package into a clinical monitor/ defibrillator to track chest compression

and applied force during CPR. The sensor is interposed between the palms of the hands of the person performing CPR and the sternum of the patient. The accelerometer signal is processed with a double-integration algorithm, yielding deflection. Those devices can provide feedback on the rate, depth, force, and sternal pressure release during CPR, which in turn, can improve the quality of CPR delivered during training and during actual CPR delivery.

Martin et al. (2013b) considered four parameters affecting the quality of CPR in infants and other factors influencing those parameters. Comparison of the compliance with international recommendations of the two-thumb (TT) and two-finger (TF) infant chest compression techniques was examined. This study was the first to fully evaluate the compliance of simulated infant CPR chest compressions against 2010 internationally recommended targets (Biarent et al., 2010). With excessive chest compression rates and prolonged compression duty cycles prevalent, both techniques rarely complied with all four targets. Thus, whilst the guidelines may be regularly updated to reflect the latest scientific understanding, there remains a delay regarding practitioners precisely carrying out these instructions. Improved arterial pressures in both infant and adult human subjects during increased chest compression depth supports infant CPR blood flow theories.

Martin et al. (2013b) study showed that increased chest compression depths result in favourable haemodynamic outcomes, such as increased superior coronary flow and cardiac output in animal surrogates. Prolonged compression duty cycles, combined with increased compression rates, result in inadequate chest wall relaxation, thus impeding the venous return of blood to the heart and adversely affecting cardiac output, cerebral perfusion pressures, and cerebral blood flow. The other study compared the chest compression performance to recommended targets and compression depths to a proposed thoracic over-compression threshold. Compressions reached greater depths across both techniques using the maximum compression depth, thereby achieving the recommended targets. In the modified manikin improved duty cycle compliance, however, the chest compression rate was consistently too high. Overall, the quality of chest compressions remained poor in comparison with internationally recommended guidelines (Martin et al., 2013c, Biarent et al., 2010). That study was the first to develop a more “physiological” manikin design that enabled resuscitators to perform chest compressions to greater depths.

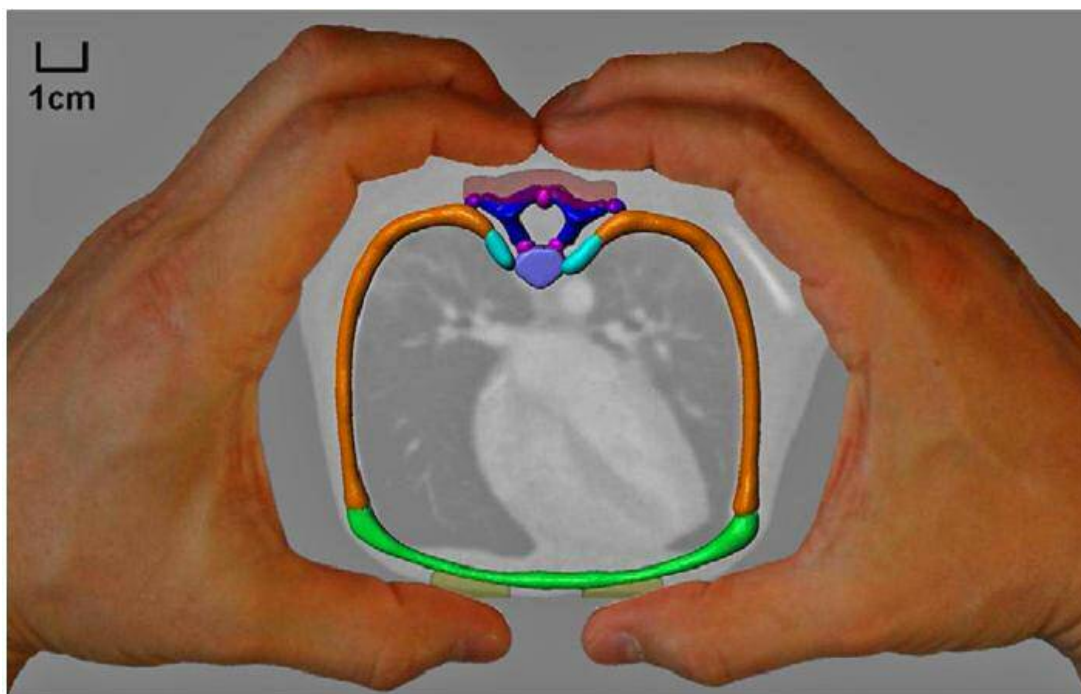


*Figure 2-4 Hand-positioning during lateral grabbing of an infant, depicted to scale. Positions of the anterior displacement points are depicted by the two faint yellow bars. Positions of the posterior displacement points are depicted by the faint red bar. (The anatomic structures include paired sixth rib (orange), sixth vertebral body (dark blue), inter-vertebral disks (light purple), rib head cartilage apophyses (cyan), transverse process cartilage apophyses (dark purple), vertebral synchondroses cartilage (magenta), and anterior costal cartilage (green). (Tsai et al., 2012)*

Another study by Martin et al. (2013a) demonstrated how 'real-time' feedback during simulated infant CPR leads to a dramatic improvement in quality, resulting in compliance with internationally recommended targets. Improved quality was also demonstrated by deeper compressions, which were recognised to achieve improved haemodynamics. The International Liaison Committee for Resuscitation (ILCOR) has investigated the importance of the depth of chest compression during CPR and how it may affect the cardiac output and mean arterial pressure (Babbs et al., 1983). Thus, the reduction in rate, if transferable to clinical CPR scenarios, could allow for optimal venous return into the heart prior to recirculation. A successful duty cycle is also important in ensuring sufficient opportunity for cardiac refill prior to the next compression (Martin et al., 2013a).

In those studies, chest compression depths may have been restricted by the manikin to unrepresentative depths. In addition, the instructors' awareness that they are being observed might affect their performance. All these factors may be limitations to Martin's work. Also, in the second study, the use of the TT technique increased the compression depths, release forces, and compression duty cycles provided by the participant during simulated infant CPR,

regardless of the manikin design. However, use of the original manikin design resulted in an improved compliance with chest compression depth targets and a reduced compliance with compression duty cycle targets. When using the more “physiological” manikin design, however, the use of the TT technique reduced compliance with the compression duty cycle targets and increased the likelihood of thoracic over-compression, whilst use of the TF technique increased the under-compression of the thorax (Martin et al., 2013c).

Related to Martin’s work was (Maher et al., 2009) study of the depth of compressions on the sternum and its effect on the intra-arterial pressure during CPR. The depth was increased to approximately half the anteroposterior chest diameter if the systolic blood pressure response was inadequate. Blood pressure tracings were reviewed, and close recordings were evaluated as compressions were attempted at a third and half the anteroposterior chest diameter. The age range of six infants was from 2 weeks to 7.3 months, and the median age was 1.0 month. The infant cases in this study had pulseless cardiac arrest in the postoperative period following cardiac surgery. Attempting to compress the chest at half the chest diameter increased systolic blood pressure by 62% compared to attempting to compress third that diameter. Arterial blood pressure was continuously monitored and recorded on a central monitoring system. The optimal depth varies depending on patient characteristics, intravascular and intracardiac volume, and other factors. The study represented a very limited number of patients, and may not be applicable to all infants and children. Those cardiac arrests occurred after cardiac surgery among children suffering from cardiac compromise; therefore, hemodynamic observations in infants whose cardiac arrests were precipitated by a primary respiratory event may be different. The most important limitation is that the attempted depths of compressions at 1/2 and 1/3 the anteroposterior diameter of the chest during CPR were only qualitatively estimated, but were not quantitatively measured. Nevertheless, the higher blood pressures were associated with the attempts at deeper compressions. Also, they demonstrated a greater blood pressure response, but did not determine changes in blood flow or oxygen delivery.

Those studies used human infants and/or manikins to demonstrate the factors affecting the quality of the infant CPR. In Rudikoff et al. (1980), the mechanism of forward flow produced by precordial compression during CPR was investigated with the aid of echocardiographic and hemodynamic measurements in anesthetized, mechanically ventilated domestic pigs. In the study, both mitral and tricuspid valves opened during compression diastole and closed during compression systole. Valve motion persisted throughout the resuscitation procedure in 17 of 22 animals which were hemodynamically resuscitated. There was a 25 percent reduction in the left ventricular area during the compression systole. In the successfully resuscitated animals, maximum pressure generated during compression systole in the aorta was observed

to exceed that of the right atrium throughout the 12-mm interval of precordial compression. Those observations provided evidence of direct cardiac compression as the mechanism accounted for effective forward blood flow during CPR.

In those studies, the generation of higher blood pressures during CPR may be necessary to overcome increased pulmonary resistance in order to increase pulmonary blood flow, gas exchange, and delivery of blood to the left side of the heart. Monitoring intra-arterial blood pressure during those experiments may be preferable to adjust the depth of compression to blood pressures that are within acceptable ranges for an infant rather than using a specific compression depth or pre-set ratio of chest wall depth. The persistence of valve function, chamber compression, and pressure gradients during precordial compression was predictive of successful resuscitation. The absence of these factors prognosticates the failure of resuscitation and explains, in part, the inconsistency of prior reports. All of these observations and experimental improvement suggestions are indications that more research is required into techniques to improve infant CPR to identify the most efficient procedure and hence update the international guidelines accordingly.

## **2.4. Cardiovascular (Fluid and/or Structure) modelling**

To predict the flow in the human heart, time-dependent geometry of the ventricle, the atrium, and the cardiac valves during one cardiac cycle should be modelled. In the literature, many approaches to modelling the electro-mechanical pump behaviour of the heart are found. Studies that evaluate cardiovascular velocities, their changes through the cardiac cycle, and the consequent pressure gradients improve the understanding of subject-specific blood flow in relation to adjacent soft tissue movements. Oertel and Krittian (2012) described the orthotropic properties of the passive tissue by implementing a constitutive law whose parameters are derived from a model of collagen fibres and in vitro stress measurements on animal hearts. They also introduced a model of the active tissue properties, based on isolated animal muscle experiments, to predict distributions of the principal strain at the end of the contraction phase of the cardiac cycle. Advances in medical imaging techniques, such as echocardiography (ECG), magnetic resonance imaging (MRI), and computed tomography (CT) as well as segmentation software allow accurate measurements to be taken of cardiac geometry, wall motion, and inflow conditions and provide high resolution datasets for characterising individual patients. This development supports a paradigm shift away from the predefined clinical indices determining treatment options and introduces a move towards the true personalisation of care based on imaging and modelling of an individual's specific physiology.

Krittian et al. (2012) ran four subject-specific test cases and the computational engine presented by Krittian's work contributed to non-invasive access to relative pressure fields, incorporated the effects of both blood flow acceleration and viscous dissipation, and enables enhanced evaluation of cardiovascular blood flow. However, while those results illustrated the potential of the FEM system to solve the PPE problem, further work is required to understand the behaviour of pressure estimation in vivo. The influence of MR image acquisition factors on physical correctness is of particular interest in terms of the interpretation of cardiovascular Reynolds numbers. Changes in the pressure reference value through discontinuities, such as during the valve opening and closing process, require a more sophisticated measurement input (Krittian et al., 2012).

For the flow calculation, as shown in Figure 2-5, three regions can be distinguished when modelling the cardiovascular flow-structure interaction in the left ventricle. In the first region, the motion of the coupling interface leads to a substantial Lagrange description of the flow quantities. A combined Lagrange-Euler approach is required in the second transition region, and at a sufficiently large distance from the interface in the third region, the Euler formulation is used. Figure 2-5 shows the division of regions with a characteristic computational grid for the flow calculation of the human heart.

Espa et al. (2012) used a laboratory model reproducing the main characteristics of the heart pump to investigate the flow in a ventricle model during a cardiac cycle. The flow pattern inside a model of the left ventricle was experimentally analysed (Figure 2-5). The model simulating the left ventricle consisted of a flexible, transparent sack made of silicone rubber. The sack was secured on a circular plate and connected by means of two Plexiglas conduits to a constant head reservoir. Two check valves were mounted along the outlet and the inlet conduits respectively so as not to affect the inflow and outflow. The inflow enters the ventricle during the diastole with a top-hat shaped velocity profile that quite accurately resembles the main features of the physiological conditions during a continuous cardiac cycle, except for the absence of the leaflets. The circulatory system was modelled by inserting two adjustable head losses and a compliance chamber in the circuit. The leaflets at the mitral orifice do not play a fundamental role in the phenomenon.

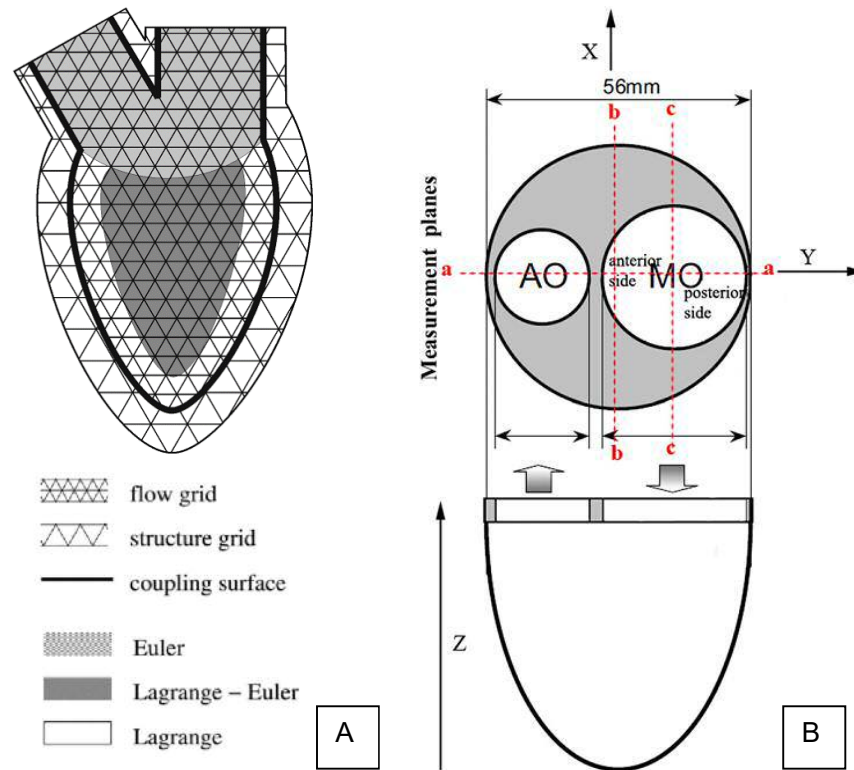


Figure 2-5 A) Division of regions for the ALE Lagrange-Euler formulation of the flow-structure coupling for the human ventricle (Oertel and Krittan, 2012), B) Position of the measurement planes. Aortic orifice (AO) as the outlet and Mitral orifice (MO) as inlet. (Espa et al., 2012)

This caused the redirection of the diastolic jet toward the posterior ventricular wall. The redirection is prone to the formation of a single vortical structure, which directs the fluid directly to the aortic valve during the systolic ejection and, in this case, due to the absence of the leaflets. Measuring the velocity fields on planes with different orientations considered in the fluid domain highlighted the three-dimensional nature of the intraventricular flow. In addition, the application of Lagrangian methodologies provided information on the dispersion properties of the flow at different length-scales giving a further confirmation of the two-dimensional nature of the flow structure before the systolic ejection.

### 2.4.1. Animal Studies in Cardiac Modelling

Cardiac tissue, as a soft biological tissue, is regarded as an incompressible material for modelling purposes. The numerical modelling assumptions are developed from isotropic to transversely isotropic models based on invariants and on the Green-Lagrangian strain tensor. Later, orthotropic models have been proposed because the myocardium shows distinct

mechanical responses along the six simple shear modes associated with its three mutually orthogonal planes. Recently, Holzapfel and Ogden (2009) suggested an incompressible, thick-walled, orthotropic, convex and micro-structurally motivated constitutive model. The myocardial tissue has hitherto generally been treated as a hyperelastic material due to the lack of experimental evidence for a viscoelastic behaviour. However, a hysteresis response was observed in Dokos et al. (2002) tests and a more affirmative investigation was conducted by Sommer et al. (2015) in which the viscoelastic mechanical response was recovered in both biaxial and shear experiments with various stretch amplitudes.

However, the orthotropic viscoelastic model was used for experimental data, which does not involve capturing the time-dependent behaviour of the human myocardium, such as the stress relaxation which occurs during biaxial extension and triaxial shear tests (Gultekin et al., 2016).

The variation in the mechanical properties of biological heart tissue under test is rather large and since such variability in animal mechanical properties would also be present in human tissue, then an isotropic averaged model may be an acceptable approach. Lally et al. (2004b) characterised the nonlinear anisotropic elastic behaviour of healthy porcine coronary arteries under uniaxial and equi-biaxial tension. Porcine coronary tissue was chosen for its availability and its similarity to human arterial tissue. A biaxial test device previously used to test human femoral arterial tissue samples was further developed to test porcine coronary tissue specimens in their study. Even though anisotropy is demonstrated, it was proposed that an isotropic hyperelastic model may adequately represent the properties of an artery, provided that an axial stretch is applied to the vessel to simulate the *in vivo* longitudinal tethering on the vessel (Lally et al., 2004b).

Crick et al. (1998) examined the porcine and human cardiac anatomy by dissecting 14 hearts from neonates and 13 hearts from young adult animals. All hearts were normal (no congenital heart defects), and were obtained from healthy animals that had no recognisable cardiovascular disease. In the study, both ventricles were well described in terms of inlet, apical trabecular and outlet components.

The relative proportion of ventricular dimensions to the overall size of the heart was observed to be much smaller in neonatal porcine hearts compared with the adult hearts. Morphologically, the left ventricle of the pig Figure 2-6 had features in common with human hearts, but also possessed some notable differences. The left ventricular wall of the adult pig was much thicker than that of a size-matched human heart (Figure 2-6); however, this difference was more subtle in the neonatal pig hearts examined.



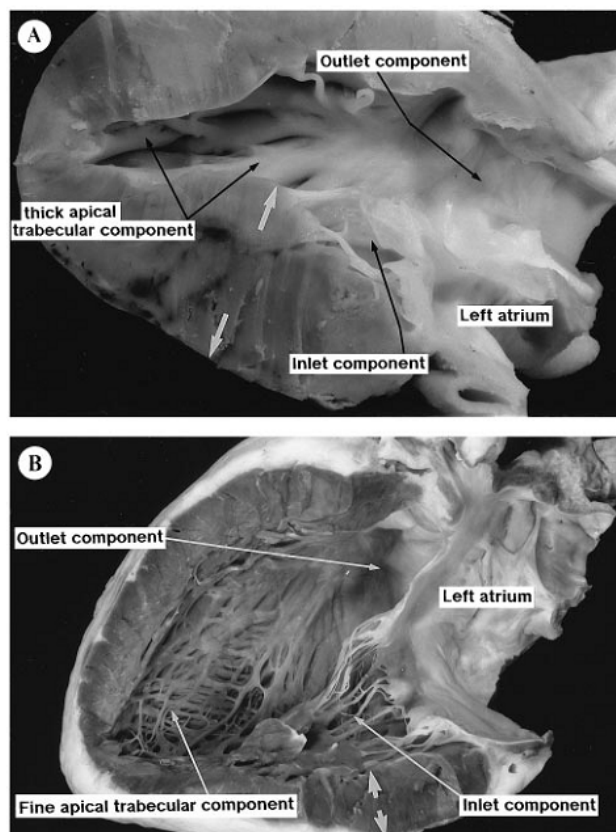


Figure 2-6 Internal view of the porcine (A) and human (B) left ventricle, showing its inlet, outlet and apical trabecular component parts. The fine criss-crossing left ventricular trabeculations of the human heart are replaced by much coarser muscles in the pig. The greater thickness of the porcine left ventricular free wall compared with that of man is indicated (between closed arrows). The mitral valve and its paired papillary muscle attachments are structurally very similar in man and pig. (Crick et al., 1998)

An overall view of comparative morphology of both left and right chambers was achieved by the examination of a 4-chamber section (Figure 2-7). This section in the porcine heart demonstrated that the left chambers represented approximately two-thirds of the section, with the interventricular septum displaced towards the right. As mentioned previously, this dominance was also reflected in the fact that the apex was composed entirely of left ventricular musculature. This observation is also found in Matshes and Trevenen (2011) study when dissecting infant hearts and comparing them to adult hearts; Figure 2-8 is good example of that. Figure 2-7 showed that both left and right chambers represented approximately equal proportions of the section, with the interventricular septum occupying an almost central position. The left ventricle of the pig also possesses some notable structural differences compared with that of the human heart. The most striking of these is the much thicker porcine left ventricular wall of the pig. The anterior displacement of the porcine aortic trunk compared

with that of man is significant, although its general orientation appears to be compatible with that of man (Crick et al., 1998).

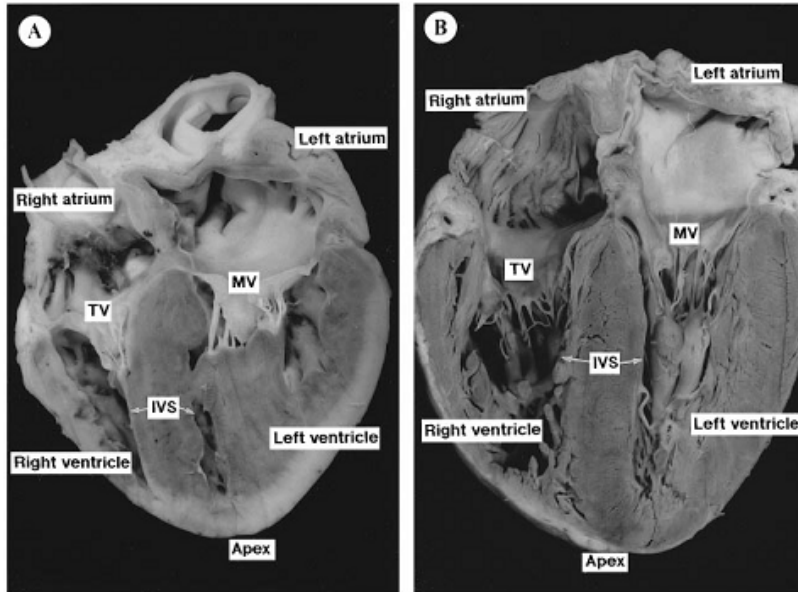
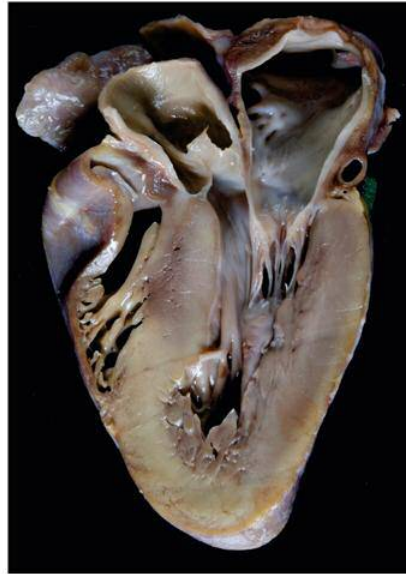


Figure 2-7 Four chamber sections of the porcine (A) and human (B) heart illustrating the differences in the morphological proportions of atrial and ventricular chambers. In the porcine heart the greater proportion of the section is taken up by the left chambers, especially the left ventricle, which means that the interventricular septum is situated more to the right of the heart. This also means the apex is composed entirely of left ventricular musculature, unlike the apex of the human heart. In the human heart, the left chambers are less dominant, and as a result, the interventricular septum occupies a more central position within the section. TV, leaflets of tricuspid valve; MV, leaflets of mitral valve; IVS, interventricular septum (Crick et al., 1998).

Crick et al. (1998) study showed some differences between the porcine heart and the human adult heart while mentioning similarities with the anatomy of the heart, especially for the left ventricle. This is evident in many cardiovascular studies that based their experimentation on the porcine heart (Neurauter et al., 2009, Lelovas et al., 2014, LALLY et al., 2004a, Yannopoulos et al., 2005, Zuercher et al., 2010, Bassols et al., 2014). Some similarities can be seen between the piglet heart and the infant human heart (Figure 2-8).



*Figure 2-8 Infant heart with a slightly 'bulky' left ventricle was subsequently perfusion-fixed with formalin. The heart was then cut in a left ventricular outflow tract view which did not demonstrate any outflow tract pathology. (Matshes and Trevenen, 2011)*

These autopsy images (Figure 2-8 and Figure 2-9) show that the left ventricle size and position have some similarities to the piglet heart, which shows that for a computational study, the modelling of the left ventricle of the porcine heart would give approximate and promising similarities to the infant heart with further investigation in future research (Matshes and Trevenen, 2011).

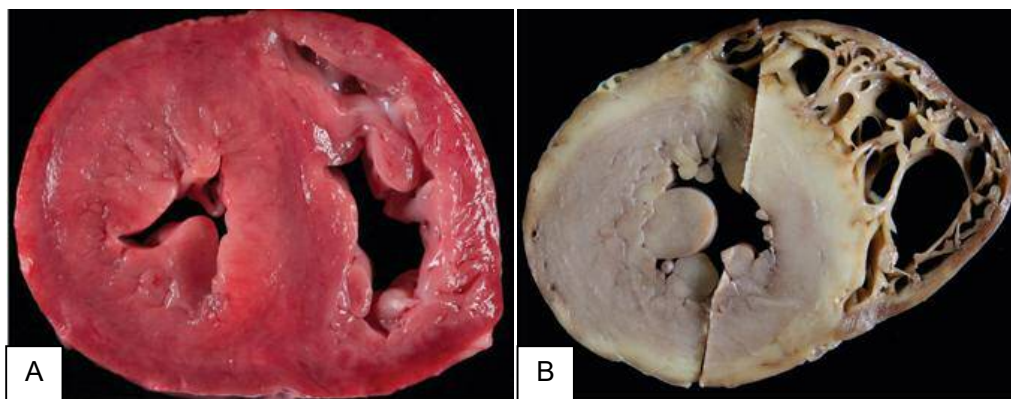


*Figure 2-9 A) Infant heart had an unremarkable external morphology. The apical half of the heart was removed, and the remainder of the heart was dissected along the pathway of blood flow in continuity with the lungs and great vessels. The apical half of the heart was then serially sectioned. B) These contiguous sections of the heart represent serial sections from the heart demonstrated in Figure 2-8. Regardless of the plane of the section selected for evaluation, the myocardium should be thoroughly assessed for pathology (Matshes and Trevenen, 2011).*

### 2.4.2. Infant vs Adult

Although cardiac arrest (CA) has some common features in children and adults, paediatric CPR differs from that in adults for the following reasons (Ornato and Peberdy, 2005):

- Children are anatomically and physiologically different from adults, as the infant heart is immediately posterior to the lower third of the sternum, which suggest that focusing compressions in this area may optimise the cardiac pump in paediatric CPR (Matshes and Trevenen, 2011).
- The pathogenesis of the cardiac arrests (CAs) and the most common rhythm disturbances are different in children.
- Children of various ages exhibit developmental changes that affect cardiac and respiratory physiology before, during, and after CA, such as transition from amniotic fluid to gaseous environment and having a much smaller cardiac and respiratory reserve.
- Many children who experience in-hospital CA have pre-existing developmental challenges and other organ dysfunction.

Muscles and tendons are bio-tissues with large differences in mechanical properties at different ages; therefore, the mechanical properties of muscle and tendon tissue were measured in various studies and in different conditions. Many studies were also published comparing human bio-tissue to that of animals (mostly porcine). Some studies hypothesised that the main differences between children and adult properties are based on different levels of muscle tone. Because the muscles are fully developed only in a very later state / age (Meyer et al., 2011), not many body regions can be mechanically affected by an increase in muscle tone (e.g., the neck musculature of a young child cannot support the head/neck in the same way as in an adult body because of different geometrical proportions between the head and the whole body). According to Yang et al. (2006), looking at the thorax and the abdomen region of children, the muscle tone variations can be neglected (muscles in passive state); therefore, it is not possible to define standard values / mechanical properties. However, it can be assumed that the densities and the Young moduli of this tissue in a relaxed state do not change with increased age. Since no detailed information / PMHS (Post Mortem Human Subject) test data for children's bio-tissue has been published so far, other soft tissues, the solid and hollow inner organs, and the skin and fat tissue differ in geometrical dimensions between the child and the adult age, but it can be assumed that the mechanical properties do not differ to any significant degree. Although this assumption is used in many studies, further mechanical properties testing is needed for infant biological tissue.

Considering the validation of a human child FE-Model, with the mechanical properties of the bio tissues taken from adult models / test results, one way to create a validated model seems to be to use "adult" validation tests and scale down the response corridors to the child's level, based on different dimensions (Yang et al., 2006).

Adult hearts, in contrast to infant hearts, are routinely and efficiently evaluated by medical examiners because of the large anatomic structure compared to those of infants and because of the ethical approval for dissections along with the imaging use contradictions with infants. Medical researchers who investigate infant cardiovascular diseases as well as infant deaths are required to consider a large number of natural and non-natural causes due to broad anatomical and physiological differences. For example, the routine dissection of an infant heart as if it were an adult heart may lead to malformations and diseases being overlooked that may have been the underlying cause of death (Matshes and Trevenen, 2011). Given the findings in Tsai et al. (2012) study, the primary importance was obtaining age-appropriate material properties of cortical and trabecular rib bone and cartilage, and examining the level and effect of perichondrium in infants of this age. The use of high resolution CT images provided better bone resolution, thus enabling more accurate modelling of the rib. Openshaw et al. (1984) studied the age-related changes in rib cage geometry which were found from measurements made on chest radiographs and on CT scans while finite element modelling shows promise as a tool to elucidate the mechanisms of rib fractures in abused infants (Tsai et al., 2012). One of the strengths in this study was the detailed anatomical geometry extracted from the CT scans of infants.

More studies showed the difference between material properties in infants and those of adults (Li et al., 2010, Takahashi and Frost, 1966, Agnew et al., 2013). Sandoz et al. (2011) study aimed to help the understanding of the in vivo behaviour of the child trunk subjected to repetitive non-injurious mechanical loading. The study has investigated the mechanics of the in vivo infant and toddler trunk during respiratory physiotherapy. The recorded load and displacement were analysed, and the child trunk had revealed the capacity to resist non-injurious repetitive dynamic loadings. The results provided additional mechanical information and will help to improve the bio fidelity of both numerical and mechanical child models at a non-injurious level.

## 2.5. System Coupling

The simulation of multi-physics applications where different physical phenomena are involved, such as fluid-structure interactions, is a challenge in engineering computational technology. Many challenging FSI applications, such as airfoil flutter, flow-induced vibration, membrane valve simulation, fuel injection, elastic artery modelling, and fuel-tank sloshing need an easier coupling method (Chitrakar et al., 2014, Kuntz and Menter, 2004, Liaghat, 2014, Wang et al., 2016). A simulation strategy aims to solve each part with an existing software package and to couple both processes by a data interface between the software codes. ANSYS 14.0 introduced system coupling, which is a new ANSYS Workbench component system for two-way fluid–structure interaction (FSI) offering an extensible architecture for coupled analysis (Scampoli, 2012). This suite of analysis software facilitated the creation of single- and multidisciplinary simulations (ANSYS, 2018). Multidisciplinary simulations are offered both within the context of a single piece of software (for example, within one solver) and through various mechanisms to couple a single piece of software with others, such as importing external data from static sources. These coupling mechanisms provide optimal solutions for the analyses that follow the single, specific workflow that they were built to solve. Coupling participants are systems that will send and/or receive data in a coupled analysis. Supported systems in Workbench include the analysis system, which in this work, represents Transient Structural and Fluid Flow (Fluent), and the component system as Fluent, CFX, or external data.

The execution of analyses involving couplings between any of these participants is managed by the runtime component of the System Coupling system. The five primary synchronization points used to manage advancement through the coupled analysis are shown in Figure 2-10 featuring notes regarding the processing that occurs between these points, as well as the coupling step and iteration loop structure. Each of these synchronization points represents a gateway beyond which a given process may not advance until all other processes are ready.

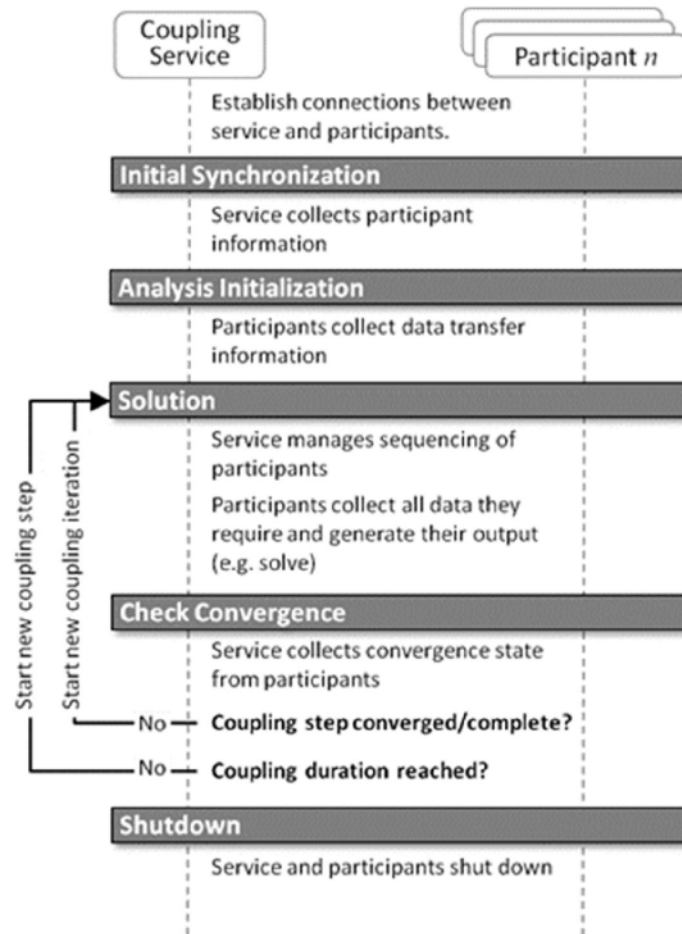


Figure 2-10 Execution Sequence Diagram for the System Coupling Service and Co-Simulation Participant, synchronization points are shown in dark grey. (ANSYS, 2018)

Details regarding processing between the Solution and Check Convergence synchronization points are shown in Figure 2-11. During this stage of the analysis, the coupling service controls the advancement of co-simulation participants through two secondary synchronization points. The sequencing of solvers is controlled by manipulating the relative order in which the solvers advance beyond these secondary synchronization points. All participants traverse the duration of the entire coupling step during each coupling iteration, however, to traverse the coupling step duration in one or more steps, each of which may include one or more solver iterations. If multiple steps are used within one coupling step, then this is referred to as sub-stepping (or sub-cycling). The advantage of using existing software packages is that one can benefit from their advanced features, as demonstrated in (Kuntz and Menter, 2004) work using the commercial software packages ANSYS for the structural analysis and CFX of ANSYS® for the flow simulation.

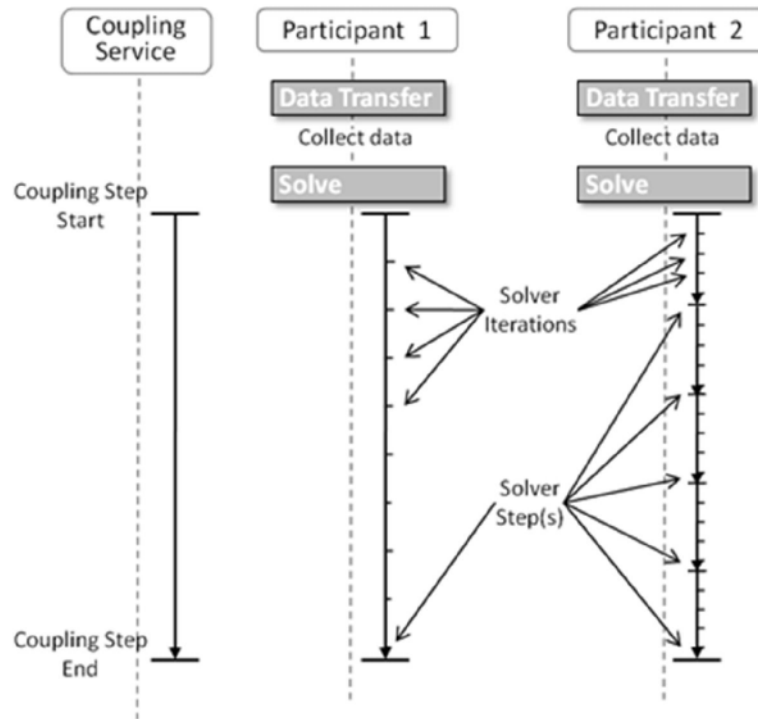


Figure 2-11 Processing Details for the System Coupling Service and Co-Simulation Participants. Secondary synchronization points: Data Transfer and Solve, both shown in light grey. (ANSYS, 2018)

The setup of the individual participant solvers for a system coupling simulation is very similar to the normal workflow for either a fluid or structural simulation alone. In ANSYS Fluent, defining a system coupling dynamic mesh zone helps identify surfaces in the CFD model that will accept the motion from the calculated structural deformations (Scampoli, 2012). Kuntz and Menter (2004) used CFX and structural for their simulation comparison of the flutter frequency in a wide range of Mach numbers which needed coupling code of ANSYS and CFX different from Fluent.

Numerical simulation for intraventricular flow are limited despite their importance in understanding left ventricular function and are more complicated computationally when heart valve function is taken into account. Zhong et al. (2013) modelled the left ventricle with both mitral and aortic valves integrated in 2D. The FSI approach was applied to the leaflets of valves to simulate the interaction between blood and the leaflet; in addition, a subject-specific ventricular wall was prescribed according to the MRI data. The 2D approach was able to qualitatively predict the intraventricular flow by demonstrating vortex formation and development in the left ventricle, and this was beneficial to develop 3D numerical studies. The arbitrary Lagrangian–Eulerian (ALE) approach was employed to handle the large mesh



deformation induced by the beating ventricular wall and moving leaflets. Leaflet dynamics were predicted numerically by FSI. The study advanced the methodology for further numerical studies of the left ventricular flow regarding the flow characteristics and numerical methods. Another 2D study on the dynamics of the leaflets and their influence on the transmitral and intraventricular flow was introduced by (Hellevik et al.), who aimed to assess the impact of left ventricular initial pressures and vortices on the mitral leaflet dynamics. Their simulations showed that the initial pressure configuration in the left heart is significant for the mitral valve dynamics, and also indicated that the mitral valve flutter has important bearings on the vortex formation in the vicinity of the mitral valves. An explicitly coupled fluid structure interaction scheme was utilized for the numerical simulations using a 2D transient representation of the left ventricular wall movement imposed as boundary conditions for the simulations. The structural calculations were simplified, and involved only the mitral valves. Whether the mitral valve flutter reduces the total energy dissipation by the possible reduction in power of the vortices or whether it simply redistributes energy from fluid to leaflets remains to be investigated.

### **2.5.1. Cardiovascular System Coupling Models**

As mentioned before, simulating the flow in the heart needs time dependant coupling, and that was employed in Arefin and Morsi (2014) 3D model using incompressible viscous fluid. Nonlinear viscous fluid and the stress tensor equations were coupled with the full Navier–Stoke’s equations together with the Arbitrary Lagrangian–Eulerian and elasticity in the solid domain. The hemodynamic characteristics inside a physiologically correct three-dimensional LV model using a fluid structure interaction scheme were examined under various heartbeat conditions during early filling wave (E-wave), diastasis, and atrial contraction wave (A-wave). These conditions provided the velocity profile for the boundary conditions to drive the model simulation. The results were discussed in terms of the variation in the intraventricular pressure, wall shear stress (WSS), and the fluid flow patterns inside the LV model. For the FSI model, ANSYS 15.0 was used to compute the entire simulation by the steps displayed in Figure 2-12. The material density and the isotropic characteristics were inserted into the geometry; subsequently, the meshing was computed by using the ALE equations, and then the coupling procedure was selected. The total time throughout the filling phase was used as recommended by (Cheng et al., 2005).

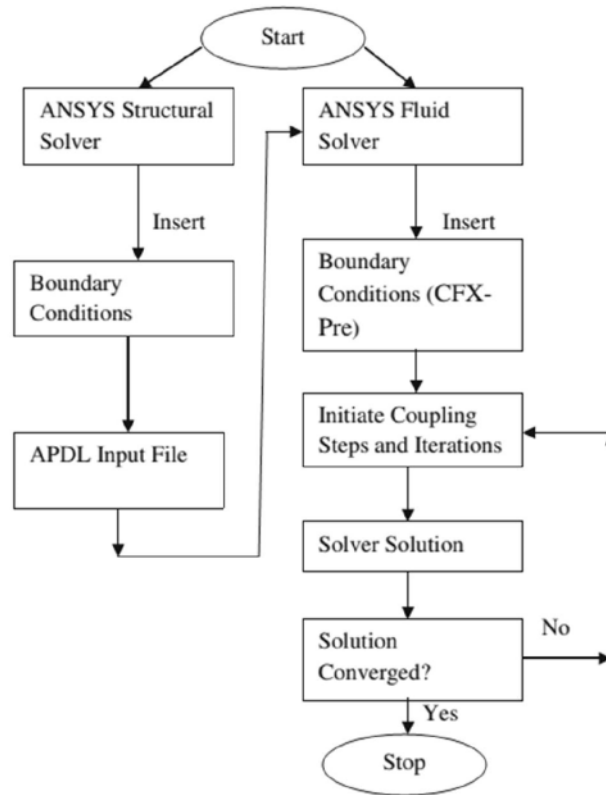


Figure 2-12 Flow chart for the LV simulation procedure illustrating the conditions for the simulation convergence during the entire simulation. (Arefin and Morsi, 2014).

If the structure model requires boundary conditions, the stability result could be obtained only by choosing homogeneous boundary conditions for the structure. Formaggia et al. (2007) considered the coupling between 3D (Navier-Stokes equations for incompressible Newtonian fluids) and 1D (hyperbolic system of partial differential equations) FSI models describing blood flow inside compliant vessels. A non-standard formulation for the Navier-Stokes equations was adopted to provide suitable boundary conditions for the coupling of the models. Several comparative numerical tests illustrating the coupling were presented showing that if the structure wall model does not require boundary conditions, the stability result is readily obtained. In both cases, the stability of the 3D-1D FSI coupling was obtained without imposing the continuity of the area at the coupling interface.

Suitable boundary conditions were derived from a 1-D wave propagation model, but also the initial axial pressure distribution in Beulen et al. (2009) study, where a time-periodic method for weakly coupled FSI models was presented. The analysis of periodic unsteady incompressible flow inside compliant vessels was of considerable interest for the simulation

of blood flow in arteries. The time-periodic method was successfully applied to straight, curved, and bifurcating geometries. The new approach proved to have a far better computational stability than weakly coupled methods based on time step-wise coupling, especially in vessels with a length that is an order of magnitude larger than the radius. The simulations showed that the time-periodic method can be a valuable tool in the simulation of blood flow in arteries, however, convergence may not be achieved for compliant vessels with an axial length scale that is large compared to the characteristic radius.

To relate the subcellular molecular events to organ-level physiology in the heart, Watanabe et al. (2004) developed a 3D finite-element-based simulation program incorporating the cellular mechanisms of excitation-contraction coupling and its propagation, and simulated the FSI involved in the contraction and relaxation of the human left ventricle. The FitzHugh-Nagumo model (Fitzhugh, 1961, Nagumo et al., 1962) and four-state model representing the cross-bridge kinetics were adopted for the cellular model. Both ventricular wall and blood in the cavity were modelled by finite element mesh, and an arbitrary Lagrangian Eulerian finite element method with automatic mesh updating has been formulated for large domain changes. The boundaries of the fluid were assumed to consist of open boundaries and the interface with a deformable structure. Using an electrical analog of pulmonary circulation and the left atrium as a preload and the Windkessel model as an afterload, the dynamics of ventricular filling as well as ejection were simulated. The study successfully reproduced the biphasic filling flow consisting of early rapid filling and atrial contraction similar to that reported in clinical observation. Furthermore, fluid-structure analysis was useful to analyse the wave propagation velocity of the filling flow. This simulator when produced was a possible powerful tool for establishing a link between molecular abnormality and the clinical disorder at the macroscopic level.

The effect of myocardial contraction and relaxation on overall heart function is closely coupled to the dynamic behaviour of blood flow through the heart chambers. Mechanical energy is transferred to pump blood and supply the body through the physical coupling of the kinematics and the transfer of momentum between the ventricular chambers and the myocardium. Translating this energy exchange to cardiac output is much more difficult to determine although the underlying coupling mechanisms are straightforward. This energy transfer is a source of major physiological and clinical interest. Answering questions on the functional behaviour of the heart requires a detailed knowledge of cardiac mechanics.

Usually, coupling requires the conservation of both kinematic and force transduction across the common interface of the fluid and the solid. The fundamental aim in coupling a fluid problem, such as ventricular blood flow, to a solid problem, such as cardiac mechanics, is to

relate the force and kinematic behaviour of each subsystem (Nordsletten et al., 2011a, Nordsletten et al., 2011b, Nordsletten).

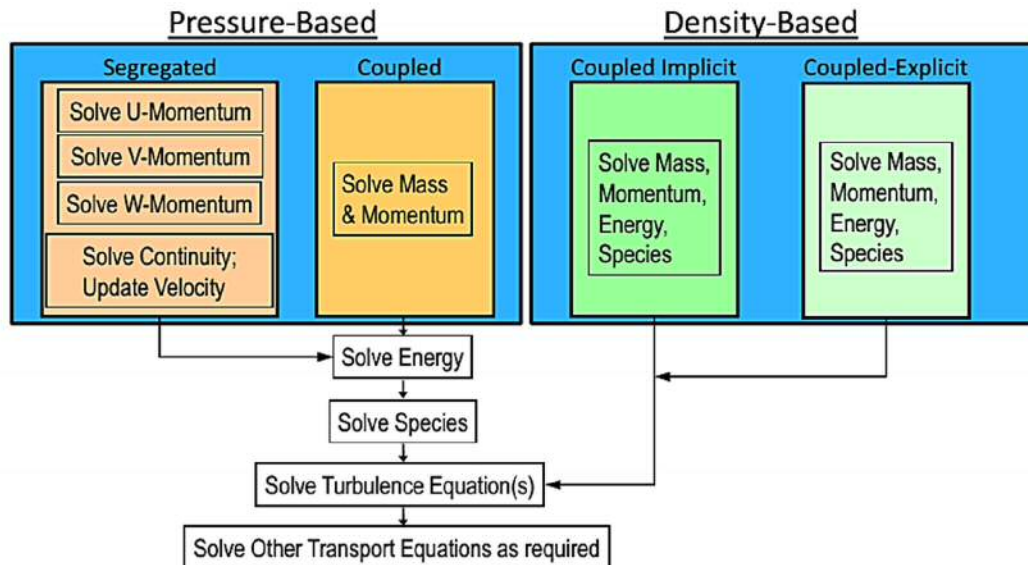


Figure 2-13 ANSYS FLUENT available solvers (2016)

Pressure-velocity coupling algorithms in ANSYS Fluent are derived by reformatting the continuity equation. The pressure equation is derived in such a way that the velocity field, corrected by the pressure, satisfies continuity. The energy equation (where appropriate) is solved sequentially, and additional scalar equations are also solved in a segregated (sequential) fashion. Pressure-based is the default option, and it is recommended to be used for most problems because it handles the range of Mach numbers from 0 to ~2-3 while density-based option is normally only used for higher Mach numbers, or for specialized cases, such as capturing interacting shock waves (Liaghat, 2014).

In general, Hazer et al. (2006b) explained the process of “patient-specific” or subject-specific computational modelling consisting of the stages represented in Figure 2-14. The simulation workflow is a chain that begins with the segmentation of the subject-specific tomographic images after 3D reconstruction. From the segmented data using segmentation software, an initial geometrical model is created and has to be pre-processed to remove geometrical imperfections and prepare the geometry for initial meshing when needed for export. Then, the high-quality meshes required for running and converging the simulations are generated in the simulation software when using separate software for segmentation and simulation. Reliable physical models must be defined in order to determine the system of equations to be solved. Realistic initial and boundary conditions, based on individual and physiological measured data, are required for the solution of the system of partial differential equations. Mathematical

models based on appropriate numerical methods need to be defined in order to discretize the system of equations and perform the simulations. Finally, proper representation and evaluation of the results is necessary to visualize, analyse, and quantify the parameters of interest.

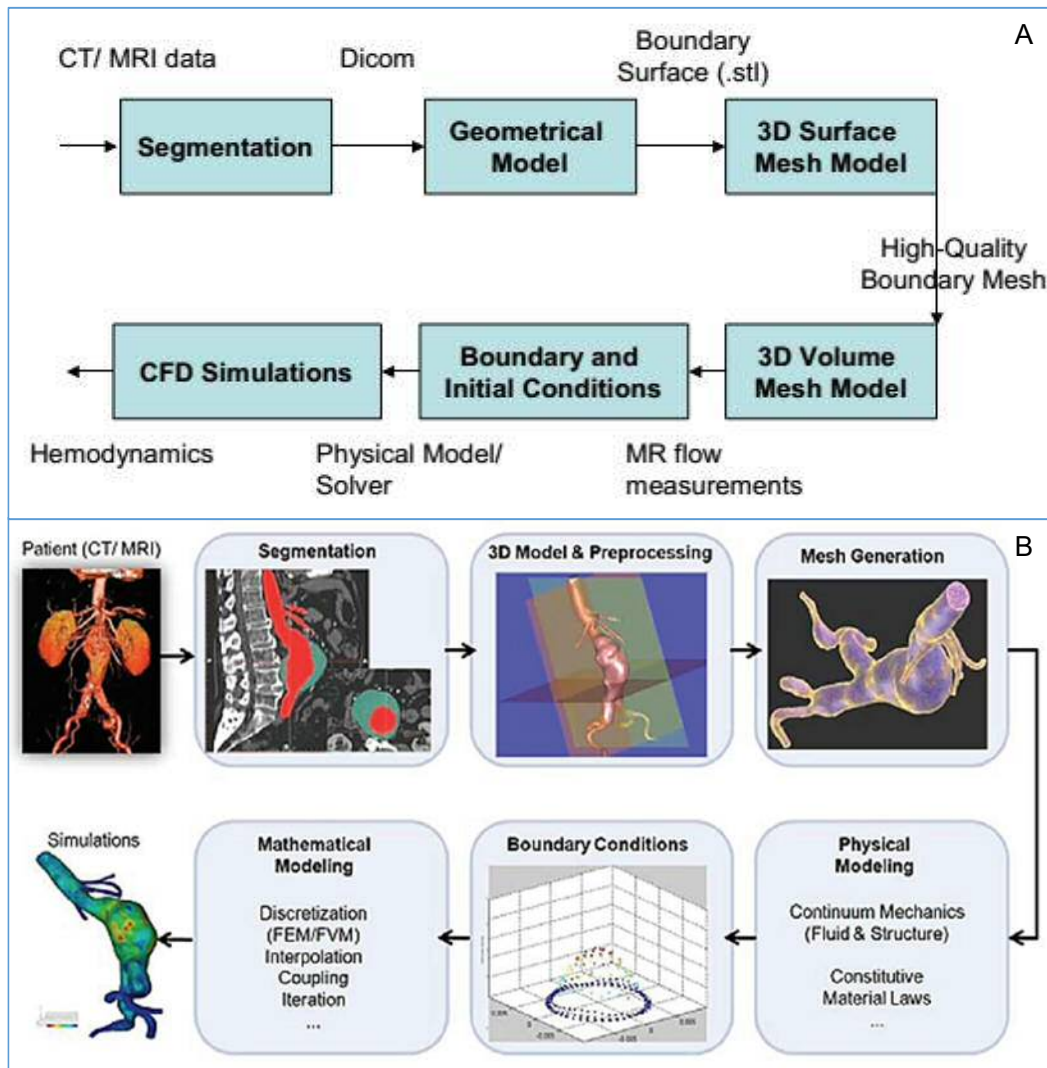


Figure 2-14 Subject-specific simulation workflow (Hazer et al., 2006b, Hazer et al., 2006a). (A) The workflow representing the resulting file types in each step, (B) image-based abdominal aortic model workflow

## 2.5.2. Governing Equations and Material Models

Modelling the fluid flow in a multi-physical system requires boundary conditions for the flow in a containing/contacting solid structure. Laminar fluid-flow is computed by using the principles of conservation of mass, momentum, and energy equations. The governing equations are mathematically discretized by means of finite element-based methods, and subsequently, the Navier–Stokes equations for the time-dependent incompressible viscous fluid coupled with the continuity equation are used in the simulation (ANSYS, 2016, Arefin and Morsi, 2014):

$$\frac{\partial \rho}{\partial t} + \nabla \cdot (\rho \vec{v}) = S_m \quad \text{Equation 2-1}$$

The above equation (Equation 2-1) is the general form of the mass conservation or continuity equation and is valid for incompressible flows. The source  $S_m$  is the mass added to the continuous phase from the dispersed second phase and any user defined sources.

The momentum equations are given as (Batchelor, 2000, Kundu and Cohen, 2008, Panton, 2005) :

$$\frac{\partial}{\partial t} (\rho \vec{v}) + \rho \vec{v} \cdot \nabla \vec{v} = -\nabla p + \nabla \cdot (\bar{\bar{\tau}}) + \rho \vec{F} \quad \text{Equation 2-2}$$

Where  $p$  is the static pressure,  $\bar{\bar{\tau}}$  is the stress tensor,  $\vec{F}$  external body forces, respectively.  $\bar{\bar{\tau}}$  also contains other model-dependant source terms, such as porous-media and user-defined sources,  $v$  is the velocity.

The  $\bar{\bar{\tau}}$  is the stress tensor and is given by:

$$\bar{\bar{\tau}} = \mu \left[ (\nabla \vec{v} + \nabla \vec{v}^T) - \frac{2}{3} \nabla \cdot \vec{v} l \right] \quad \text{Equation 2-3}$$

where  $\mu$  is the viscosity,  $l$  is the unit tensor, and the second term on the right hand side is the effect of volume dilation.

For 3D axisymmetric geometries, the axial momentum conservation equations are given by:

$$\begin{aligned} \frac{\partial \rho v_x}{\partial t} + \frac{\partial(\rho v_x v_x)}{\partial x} + \frac{\partial(\rho v_y v_x)}{\partial y} + \frac{\partial(\rho v_z v_x)}{\partial z} \\ = \rho g_x - \frac{\partial P}{\partial x} + R_x + \frac{\partial}{\partial x} \left( \mu \frac{\partial v_x}{\partial x} \right) + \frac{\partial}{\partial y} \left( \mu \frac{\partial v_x}{\partial y} \right) + \frac{\partial}{\partial z} \left( \mu \frac{\partial v_x}{\partial z} \right) \end{aligned} \quad \text{Equation 2-4}$$

$$\begin{aligned} \frac{\partial \rho v_y}{\partial t} + \frac{\partial(\rho v_x v_y)}{\partial x} + \frac{\partial(\rho v_y v_y)}{\partial y} + \frac{\partial(\rho v_z v_y)}{\partial z} \\ = \rho g_y - \frac{\partial P}{\partial y} + R_y + \frac{\partial}{\partial x} \left( \mu \frac{\partial v_y}{\partial x} \right) + \frac{\partial}{\partial y} \left( \mu \frac{\partial v_y}{\partial y} \right) + \frac{\partial}{\partial z} \left( \mu \frac{\partial v_y}{\partial z} \right) \end{aligned} \quad \text{Equation 2-5}$$

$$\begin{aligned} \frac{\partial \rho v_z}{\partial t} + \frac{\partial(\rho v_x v_z)}{\partial x} + \frac{\partial(\rho v_y v_z)}{\partial y} + \frac{\partial(\rho v_z v_z)}{\partial z} \\ = \rho g_z - \frac{\partial P}{\partial z} + R_z + \frac{\partial}{\partial x} \left( \mu \frac{\partial v_z}{\partial x} \right) + \frac{\partial}{\partial y} \left( \mu \frac{\partial v_z}{\partial y} \right) + \frac{\partial}{\partial z} \left( \mu \frac{\partial v_z}{\partial z} \right) \end{aligned} \quad \text{Equation 2-6}$$

$v_x, v_y$  and  $v_z$  are considered as the components of the velocity vectors in the cartesian coordinates of X, Y and Z respectively;  $\rho$  and  $\mu$  represent the density and viscosity respectively. For the elasticity in the solid domain, the motion equation for displacement is used and presented as:

$$\nabla \cdot \bar{\tau} + f = 0 \quad \text{Equation 2-7}$$

Where  $f$  is the body force.

In this case of a small deformation, the stress tensor is given by the following thermoelastic constitutive equation:

$$\bar{\tau} = \frac{E}{1+\nu} \left( \frac{\nu}{1-2\nu} \text{tr}(\epsilon) I + \epsilon \right) - \frac{E}{1-2\nu} \alpha (T - T_0) I \quad \text{Equation 2-8}$$

where  $E$  is the Young's modulus,  $\nu$  is the Poisson's ratio,  $T$  is the temperature,  $T_0$  is the reference temperature, and  $I$  is unit tensor.

For an incompressible fluid of laminar flow, the Carreau–Yasuda generalized Newtonian model is given by (Janela et al., 2010):

$$\mu(\dot{\gamma}) = \mu_\infty + (\mu_0 + \mu_\infty) \cdot (1 + (\lambda \dot{\gamma})^a)^{\frac{n-1}{a}} \quad \text{Equation 2-9}$$

Here  $\lambda > 0$ , and  $n, a = 2$ , corresponding to the so-called Carreau model. The coefficients  $\mu_0$  and  $\mu_\infty$  are the asymptotic viscosities for the lowest and highest shear rates respectively which corresponds, in a pipe flow, to the lowest pressure drop.

In most published studies, the blood is modelled as Newtonian. (Doost et al., 2016) study proved that this is not entirely accurate, as the blood viscosity varies with the shear rate in a non-linear manner. The study investigated the effect of Newtonian assumption on the degree of accuracy of intraventricular haemodynamics. Various non-Newtonian models and the Newtonian model were used in the analysis of the intraventricular flow and the viscosity of the blood Table 2-2. The non-Newtonian models had a significant influence on the intraventricular flow dynamics.

Table 2-2 Various non-Newtonian constitutive equations have been used to mimic the blood rheology (Doost et al., 2016)

Model name	The constitutive equation	Coefficients
Carreau	$\mu(\dot{\gamma}) = \mu_{\infty} + (\mu_0 - \mu_{\infty})(1 + (\lambda\dot{\gamma})^2)^{\frac{n-1}{2}}$	$\mu_{\infty}=0.0035 \text{ Pa s}$ , $\mu_0= 0.056 \text{ Pa s}$ , $\lambda = 3.313005$ , $n=0.3568$
Casson	$\mu(\dot{\gamma}) = \left( \sqrt{\mu_c} + \sqrt{\frac{\tau_c}{\dot{\gamma}}} \right)^2$ $\mu(\dot{\gamma}) = k(\dot{\gamma})(\dot{\gamma})^{n(\dot{\gamma})-1}$	$\mu_c=0.00414$ , $\tau_c=0.0038$
Generalised power-law (GP)	$k(\dot{\gamma}) = \mu_{\infty} + \Delta\mu \exp\left(-\left(1 + \frac{\dot{\gamma}}{a}\right) \exp\left(-\frac{b}{\dot{\gamma}}\right)\right)$ $n(\dot{\gamma}) = n_{\infty} - \Delta n \exp\left(-\left(1 + \frac{\dot{\gamma}}{c}\right) \exp\left(-\frac{d}{\dot{\gamma}}\right)\right)$	$\mu_{\infty} = 0.0035 \text{ Pa s}$ , $\mu_0 = 0.25$ , $a = 50$ , $b=3$ , $n_{\infty} = 1.0$ , $\Delta n = 0.45$ , $c = 50$ , $d = 4$
K-L	$\mu(\dot{\gamma}) = \left(\frac{1}{\dot{\gamma}}\right) (\tau_c + \mu_c(\alpha_2\sqrt{\dot{\gamma}} + \alpha_1\dot{\gamma}))$	$\tau_c = 0.0035$ , $\mu_c = 0.005$ , $\alpha_1 = 1$ , $\alpha_2 = 1.19523$
Cross	$\mu(\dot{\gamma}) = \mu_{\infty} + \frac{\mu_0 - \mu_{\infty}}{1 + (\lambda\dot{\gamma})^a}$	$\mu_{\infty}=0.0035 \text{ Pa s}$ , $\mu_0= 0.0364 \text{ Pa s}$ , $\lambda=0.38$ , $a = 1.45$

Doost et al. (2016) compared the intraventricular flow pattern of different models and observed that the number and magnitude of small vortices for different models were different. The findings indicated that the Newtonian assumption could not adequately simulate the flow dynamic within the LV over the cardiac cycle, which can be attributed to the pulsatile and recirculation nature of the flow and the low blood shear rate. Viscosity in different non-Newtonian models had a high value in the apex and the middle of the LV, which was attributed to the low shear rate in these regions. Wall shear stress maximum value in some non-Newtonian models, such as the KL and Cross models, was less than the Newtonian model,



but for other models, the maximum WSS of the non-Newtonian models was significantly higher than for the Newtonian model.

The Carreau model is characterized by the zero  $\mu_0$  and the infinite  $\mu_\infty$  shear rate viscosities (Figure 2-15), by the relaxation time constant  $\lambda$ , by the power law index  $n$ , and by the reference temperature  $T_\alpha$ .  $\mu_0$  and  $\mu_\infty$  represent the upper and lower limiting values of the blood viscosities, respectively.  $\lambda$  and  $n$  describe the transition and deviation of the blood from the Newtonian fluid, respectively.  $T_\alpha$  is the reference temperature at which the viscosity is temperature-independent, that is, for which  $F(T) = 1$ . These non-Newtonian input parameters depend on the constituents of the blood, and they are chosen for the viscous constitutive equations with:

$$\mu_0 = 0.056 \text{ Nsm}^{-2}; \mu_\infty = 0.0035 \text{ Nsm}^{-2}; \lambda = 3.313\text{s}; n = 0.357; T_\alpha = 310 \text{ K}$$

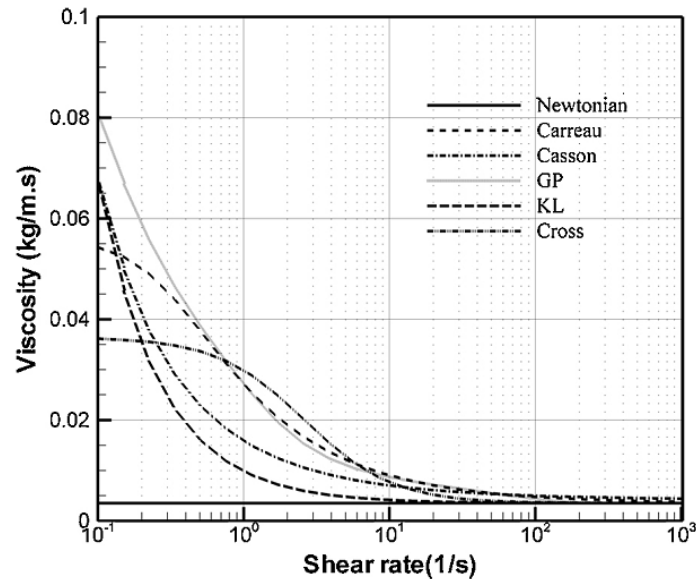


Figure 2-15 The apparent viscosity of different non-Newtonian models versus the shear rate. the viscosity is higher than the Newtonian viscosity in the range of shear rate less than  $10^2 \text{ s}^{-1}$  and it reaches the Newtonian viscosity for the shear rate higher than  $10^3 \text{ s}^{-1}$  (Doost et al., 2016)

### 2.5.3. Meshing

Experimental testing on human participants and cadaveric specimens provides researchers in biomechanics with valuable insights into how anatomical parts of the human body respond to loading and why they might become injured as a result of different loading scenarios. However, in many instances, experimental testing on humans and cadavers is not always feasible. For example, to ensure the safety of participants, in vivo testing must be limited to sub-maximal loads and non-invasive testing techniques. Furthermore, failure tests on cadaveric specimens are inherently destructive and can become costly. Also, it is very complicated to obtain authorisation for ethical approval for paediatric testing. In comparison, finite element models provide a feasible alternative for predicting the response under a variety of loading conditions, and so they have become a popular and powerful tool among biomechanics and orthopaedics researchers over the last 20 to 30 years. As reported by Erdemir et al. (2012), there was a 6,000% increase in the number of finite element modelling papers published between the years 1980 and 2009. However, the attention to mesh quality, model validation, and appropriate energy balance methods during this period has not adequately kept pace – although attention has been increased - with the general use of finite element modelling approaches. The mesh would be generated from CAD (Computer Aided Design) geometry efficiently and accurately, which affects the calculation accuracy and speed. However, a successfully transferred CAD model does not mean that the model is ready for meshing in its current state. The usual reason is that the original model is often not the correct representation of the model which is required.

Improvements to auto-meshers mean that, increasingly, they are flawless; however, manual changes in the mesh cannot be avoided even on the geometry-reduced model. The goal of meshing in ANSYS Workbench and 3-Matics is to provide robust, easy to use meshing tools that will simplify the mesh generation process. These tools have the benefit of being highly automated along with having a moderate to high degree of user control. Good quality mesh correctly and adequately describes the real geometrical representation of the model (in terms of the sufficient resolution required for the simulation). Figure 2-16 shows the effect of reducing the number of mesh elements of the sphere by roughing. In some cases, the difference between these representations may be important, but mostly, it depends on the frequency and the importance of the reference locations (Krutilek and Raida, 2015, Cifuentes and Kalbag, 1992, Burkhart et al., 2013, Oliveira and Sundnes, 2016, Ramos and Simoes, 2006).

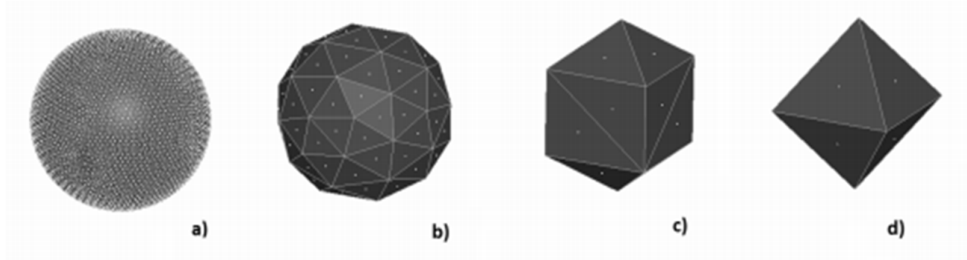


Figure 2-16 Mesh of the sphere with different number of elements: a) 3034, b) 88, c) 16, d) 8.(Krutilek and Raida, 2015)

Oliveira and Sundnes (2016) compared different element types for simulations of cardiac electrophysiology and mechanics, with the aim of testing the common conception that hexahedral elements are superior to tetrahedral for solid mechanics applications, and to compare the elements' performance for coupled simulations (Figure 2-17). There were no firm conclusions regarding the suitability of different element types, as all element types produced unacceptable errors for the coarsest mesh, and also for one level of refinement. The errors were normally considered too large for practical applications. Although the elements considered in the study were widely used in the cardiac modelling community, and are among the most widely available element types in automatic meshing software, that study had a number of limitations, as it focused on a limited selection of element types, and considered two relatively simple model problems. Cubic Hermite interpolation is common for cardiac modelling; however, Hermite elements were not available in the FE frameworks available for this study. Other limitations include the simplicity of the two test cases. A fully coupled simulation with a propagating signal may give additional results, but will also considerably complicate the analysis, since the meshes considered were too coarse for conduction of the electrical signal.

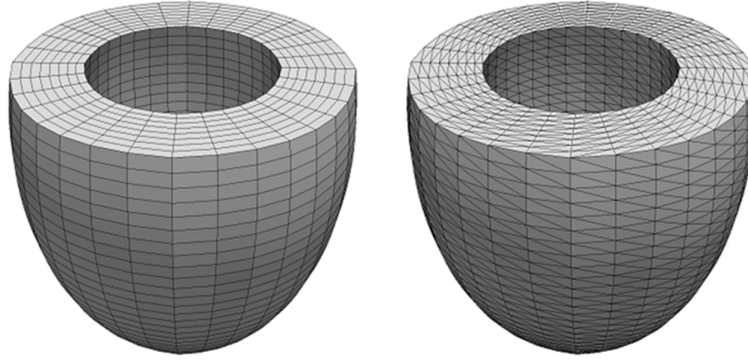


Figure 2-17 An ellipsoidal geometry was used for the mechanical test cases with hexahedra and tetrahedral (Oliveira and Sundnes, 2016)

Previous CFD studies have employed the structured mesh generation method to create the total cardiopulmonary connection simulation model. In Liu et al. (2004) study, a realistic total cardiopulmonary connection model with complete anatomical features was numerically simulated using both structured and unstructured mesh generation methods. It has value in that it took a real-world case and studied it at grid resolutions that are larger than normal but practical and found distinct differences in the predicted flows and energy losses. Their study showed that the flow fields in the structured and unstructured mesh were qualitatively similar under most left pulmonary artery flow split conditions. However, the large gap between the control volume and viscous dissipation methods needed to be studied further, and at the Reynolds number range considered in that study, these simulations would still have high computational costs and would not be practical in the clinical pace. The parameters describing grid quality including skewness and aspect ratio were checked in using CFD-GEOM and were well within the good quality range.

Orthogonal quality is derived directly from Fluent solver discretization. For a cell, it is the minimum of:

$$\frac{A_i \cdot f_i}{|\vec{A}_i \parallel \vec{f}_i|} \quad \frac{A_i \cdot c_i}{|\vec{A}_i \parallel \vec{c}_i|}$$

Computed for each  $i$ . For the faces, it is computed as the minimum of

$$\frac{A_i \cdot e_i}{|\vec{A}_i \parallel \vec{e}_i|}$$

Computed for each edge  $l$  where  $A_i$  is the face normal vector,  $f_i$  is a vector from the centroid of the cell to the centroid of that face,  $c_i$  is a vector from the centroid of the cell to the centroid of the adjacent cell, and  $e_i$  is the vector from the centroid of the face to the centroid of the edge. At boundaries and internal walls,  $c_i$  is ignored in the computations of orthogonal quality (Figure 2-18).

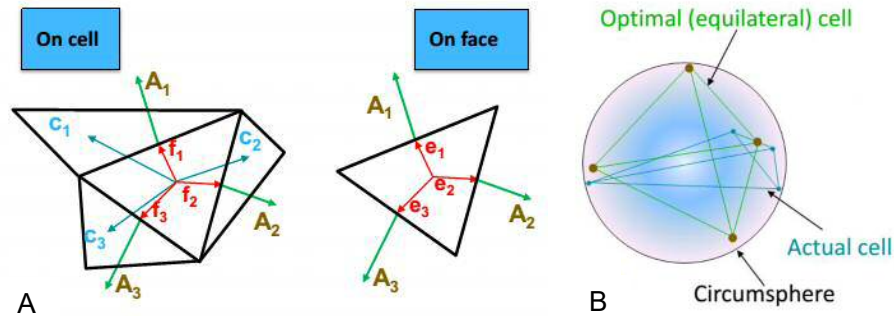


Figure 2-18 Mesh parameters. On the left are the orthogonal quality vectors and on the right is skewness cell description (ANSYS, 2018)

There are two methods for determining the skewness equilateral, namely, volume deviation, which is applied only for triangles and tetrahedrons, and normalised angle deviation, which applies to all cell and face shapes, and is used for hexa, prisms and pyramids:

$$\text{skewness} = \frac{\text{optimal cell size} - \text{cell size}}{\text{optimal cell size}} \quad \text{skewness} = \max \left[ \frac{\theta_{\max} - \theta_e}{18 \theta - \theta_e}, \frac{\theta_e - \theta_{\min}}{\theta_e} \right]$$

Where  $\theta_e$  is the equiangular face/cell (60 for tets and tris, and 90 for quads and hexas). To achieve a good mesh quality, low orthogonal quality or high skewness values are not recommended where the minimum recommended orthogonal quality  $> 0.1$ , or maximum skewness  $< 0.95$ . However, these values may differ depending on the physics and the location of the cell. The time step size is an important parameter in transient simulations (Figure 2-19).  $\Delta t$  must be small enough to resolve time-dependant features. If the time step is too large to resolve transient changes, the solution points generally will not lie on the true solution because the true behaviour has not been resolved, while a smaller time step can resolve solution at least 10-20  $\Delta t$  per period.

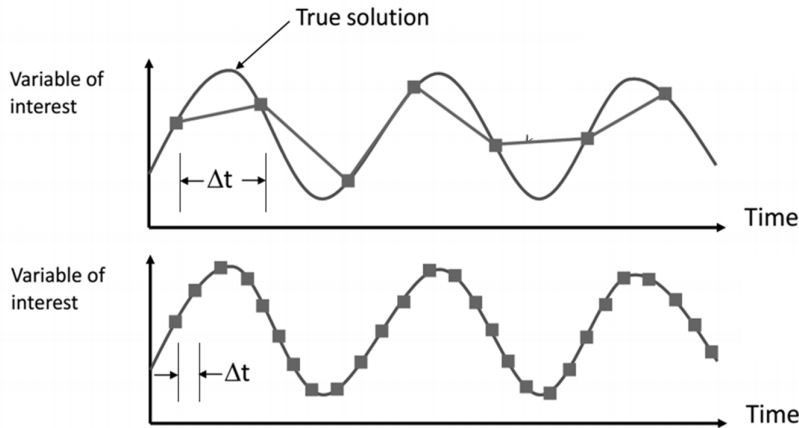


Figure 2-19 Time step effect on ANSYS transient simulation. Decreasing the  $\Delta t$  increase the iteration step behaviour of the variable of interest. (ANSYS, 2018)

### 2.5.4. 3D Printed Material Properties

For rubberlike material 3D printing models with smooth surfaces, PolyJet is an ideal method. This technology can produce multi-material and multi-colour parts, and can match specific Shore A values. Using photopolymers inkjetted in extremely thin layers, PolyJet can build accurate and detailed parts with fast lead times and no need for post-production finishing. It works by jetting photopolymer materials in ultra-thin layers onto a build platform. Each layer is cured by UV light immediately afterwards, producing fully cured models that can be handled and used immediately, without post-curing. The gel-like support material, designed to support complicated geometries, can be removed by water jetting. (Barclift and Williams, 2012) examined the sensitivity of part material properties to variations in the process parameters. A protocol of experiments was conducted using a full-factorial design to analyse the effects of three parameters on the specimens' tensile strength and tensile modulus: the in-build plane part orientation (X-Y), the out-of-build plane part orientation (Z), and the distance between specimens (Figure 2-20). The experimental data suggested that Z-orientation can affect the accuracy of a part's thicknesses and widths. This is because the Z-resolution of the PJD-3DP process (32-60 mm layer thickness) is better than the X-Y printing resolution (600 dpi). This is unique to the PJD-3DP process, as most AM processes have poor dimensional accuracy for features aligned along the Z-axis due to the discretized nature of the layer-by-layer approach. Also, XY and YX parts did not show any statistically significant effects on material performance. Barclift and Williams (2012) hypothesised that YX-oriented parts would be weaker due to jetting from discretized nozzles being found to be incorrect. The Z-plane oriented parts did not show any statistically significant improvements in material performance. The hypothesis behind that was that parts with XZ and YZ orientation would lead to increased

curing due to “print-through”, so they would be stronger due to an increase in the number of layers. XY and XZ parts and specimens with widths along the Z-axis were, on average, stronger; however, the results were not statistically significant. The part spacing in the X-Y plane showed statistically significant effects on material performance. As hypothesized by Barclift and Williams (2012), parts printed closer together in the X-Y plane were stronger than parts printed further apart. This increase in material properties is hypothesized to be related to the manner in which the PJD-3DP indiscriminately patterns UV light during processing. This leads to the conclusion that when printing multiple parts that span multiple print paths, UV irradiation from the printing-block can over-cure parts in paths adjacent to the current printing path.

Those results showed that orienting specimens in an XZ orientation with minimal part spacing resulted in the highest tensile strength and modulus, whereas orienting specimens in the YZ orientation at the farthest part spacing led to the lowest mechanical properties. According to the literature, this is because part spacing has the largest effect on the tensile strength while the three parameters produced no statistically significant effects on the tensile modulus (Barclift and Williams, 2012, Keszy and Kotlinksi, 2010).

The PolyJet 3D printing process provides the ability to print graded materials featuring both stiff and elastomeric polymers. It allows for a variety of new design possibilities for additive manufacturing, such as living hinges, shock absorbing casings, and integrated gaskets. Such design features typically rely upon the ability of traditional elastomers to experience large and repeated strains without permanent deformation or damage. However, voids and other flaws inherent to many additive manufacturing (AM) processes can have a significant negative impact on the fatigue life of elastomeric AM materials. Moore and Williams (2012) tested fatigue life in multiple elastomeric specimens fabricated using the Objet Polyjet process (TangoBlackPlus) material. They characterised the fatigue properties of a 3D printed elastomer (specifically, Objet’s TangoBlackPlus), and they found that, on average, the multi-material interface between elastomer and non-elastomer did not appear to have a shorter fatigue life than the material itself, and they noticed that reductions in the cross sectional area, such as the neck of the fatigue specimens, may cause a serious reduction in fatigue life, even if the reductions are gradual. Shear forces on the multi-material interface have a negative impact on the fatigue life of the multi-material interface. Also, a relationship between strain and fatigue life was found, and despite voids that are inherent to the 3DP process, the material specimens exhibited a long life at a low extension ratio (up to 106 cycles at 20% elongation). These studies, and many more (Baeck et al., 2017, Bruyas, 2015) currently undergone to give an insight into the behaviour of 3D printed material show the role of 3D printed materials’

involvement in industry and technology. Although they show that there are still areas that need to be studied; the printed materials may vary in behaviour and each material should be mechanically tested to get the corresponding material model required in a computational model.

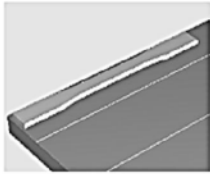
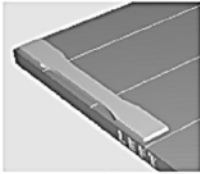
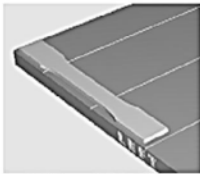
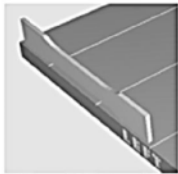
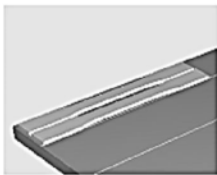
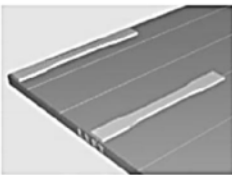
<b><u>Parameter: X-Y Orientation</u></b>	
	
XY	YX
<b><u>Description:</u></b> The in-plane build orientation of the part such that its length is parallel or perpendicular with respect to the front of the build tray.	<b><u>Hypothesis:</u></b> Orienting parts across print-head paths, may lead to lower mechanical properties due to banding from discretized jetting nozzles.
<b><u>Parameter: Z-Orientation</u></b>	
	
YX or XY (flat)	YZ or XZ (angled)
<b><u>Description:</u></b> The build direction orientation of the part such that the width, not the length, lays flat or angled with respect to the X-Y plane.	<b><u>Hypothesis:</u></b> An increase in the number of layers causes curing “print-through” and thus increased mechanical properties for parts with widths aligned in the Z plane (as noted for SL in [17]).
<b><u>Parameter: Part Spacing</u></b>	
	
Tight Spacing	Far Spacing
<b><u>Description:</u></b> The overall spacing between parts in X-Y plane of the build-tray.	<b><u>Hypothesis:</u></b> Smaller spacing may lead to increased mechanical properties due to potential UV over-cure effect.

Figure 2-20 Experimental Parameters describing the selected parameters (X-Y Orientation, Z Orientation, and Part Spacing), and the rationale for their selection (i.e., hypothesized effect) (Barclift and Williams, 2012)



### **Material Characterisation**

Use of the finite element (FE) method is now widespread throughout industry for the purpose of aiding design, and standard FE techniques are used very electively for common engineering materials, such as steel and other metals. Although the use of highly elastic, rubber-like materials is also widespread with different applications, especially medical instruments and implants, frequently, the rubber components are not considered in any FE analysis. The lack of available data relating stress and strain in these materials is generally cited as the rationale for this omission.

Rubber materials exhibit a non-linear elastic relationship between stress and strain and thus cannot be modelled as the most common engineering case of isotropic materials using Young's modulus and Poisson's ratio alone. Further data are not generated by generally used testing techniques, including the British Standard (BS) 903, which does not generate a general stress/strain relationship but provides values of stress at a given elongation. Unlike the well-known approach for common engineering materials, this information is of limited use in FE analysis using Young's modulus. Representation of the stress/strain relationship for rubber materials is considerably more complex. This has led to the generation of several formulae for describing rubber material properties, such as Mooney-Rivlin, Ogden, Blatz-Ko and Ko and Razgunas etc., and each formula requires specific mathematical constants in order to represent a particular rubber. For rubber manufacturers, this leads to the specific problem of which formulation they should provide constants for, while for FE users, it causes problems in terms of formulation they should use to model the material and the loading conditions of the component in order to provide the most useful information.

The deformation behaviour of elastomers is often characterised by specifying the Shore A hardness, and less often via the modulus of elasticity. The reason for this is probably because measuring the modulus of elasticity of elastomers by means of the usual methods is not very simple. This fact must be viewed in light of the practical interest in knowing the modulus of elasticity at least in terms of a useful order of magnitude. After all, the modulus of elasticity is needed above all when calculating a component's design, whether by means of analytical equations or the finite-element method (FEM). In elastomers, in contrast to other polymeric and metallic materials, the stiffness is linked to the hardness and, as a consequence thereof, the proposal by (Kunz and Studer, 2006) to determine the modulus of elasticity as a measure of the hardness by means of a modified Shore A test procedure. Comparison of the modulus of elasticity in compression with the Shore A hardness shows first of all that the theory of Boussinesq, as the link between both quantities, is adequate. Secondly, the effects not accounted for with this theory can be incorporated via a correction function. By applying the

method of least squares, the following relationship is obtained for calculating the modulus of elasticity in compression from the Shore A hardness:

$$E = \frac{1 - \mu^2}{2 \cdot R \cdot C_3} \cdot \frac{C_1 + C_2 \cdot Sh_A}{100 - Sh_A} \cdot (2.6 - 0.02 \cdot Sh_A) \text{ [N/mm}^2\text{]} \quad \text{Equation 2-10}$$

The slight effect of test specimen thickness can, if necessary, be taken into account via functions that depend on test specimen thickness in place of the constants in the correction function. As a consequence, it is possible to convert Shore A hardness values in databases with satisfying accuracy directly into the values of the modulus of elasticity and then employ them for calculations involving tensile and/or compressive loads (Kunz and Studer, 2006, Meththananda et al., 2009).

### **Mathematical models of material behaviour**

An evaluation of the microscopic differences between common engineering materials (such as steel) and elastomers is beyond the scope of this work. Conventional materials can be characterised as having an initial almost constant Hookean elastic region. This elastic region will typically cover only very small strains. Loading beyond the yield stress ( $\sigma_{\text{yield}}$  in Figure 2-21) causes irreversible plastic deformation. For most engineering applications, the material is designed to remain elastic since the distortion of the material is not severe or permanent when unloaded. This is shown in Figure 2-21, where it can be seen that only a fraction of the strain to failure is used.

Elastomers are characterised as being capable of large elastic deformations, being almost incompressible, and having a non-linear stress/strain relationship, as shown in Figure 2-21. The material will remain elastic until failure.

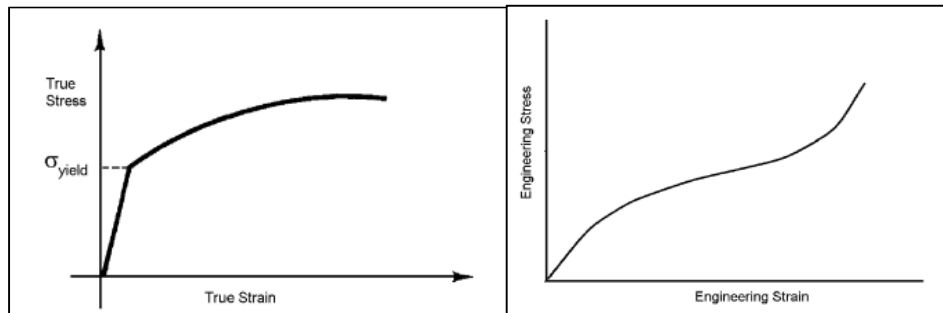


Figure 2-21 a) Elasto-plastic stiffness curve (not to scale). b) Elastomeric stiffness curve (not to scale) (Pearson and Pickering, 2001)

For finite element analysis, a mathematical representation of the material stress/strain relationship is required. For common isotropic, homogeneous materials which obey Hooke's Law (and so can be completely defined using Young's modulus and Poisson's ratio), a model approximating the stress/strain relationship shown in Figure 2-21, when loaded below the yield stress will work well. The common material models for elastomers are not based on Hooke's Law, but on a consideration of stored strain energy, and instead of directly relating to the strain of the material, these models relate to three strain invariants  $I_1$ ,  $I_2$  and  $I_3$

$$I_1 = \lambda_1^2 + \lambda_2^2 + \lambda_3^2 \quad \text{Equation 2-11}$$

$$I_2 = \lambda_2^2 \lambda_3^2 + \lambda_3^2 \lambda_1^2 + \lambda_1^2 \lambda_2^2 \quad \text{Equation 2-12}$$

$$I_3 = \lambda_1^2 \lambda_2^2 \lambda_3^2 \quad \text{Equation 2-13}$$

where  $\lambda_1$ ,  $\lambda_2$ , and  $\lambda_3$  are the principal stretch ratios, which are defined as

$$\lambda_i = \frac{L_i + u_i}{L_i} \quad \text{Equation 2-14}$$

where  $L$  is the original length and  $u$  is the deformation.

All these models assume that the strain energy per unit volume ( $W$ ) is a function of these strain invariants. Assuming that the material is incompressible, it is inferred that  $I_3$  becomes 1. At zero strain  $I_1=I_2=3$ , to ensure that  $W$  is 0 at 0 strain, it can be expressed as a function of  $(I_1-3)$  and  $(I_2-3)$ . The general Mooney-Rivlin equation is a polynomial series expansion of the form

$$W = \sum_{i=1, j=1}^{\infty} C_{ij} (I_1 - 3)^i (I_2 - 3)^j \quad \text{Equation 2-15}$$

Where  $C_{ij}$  are material constants. Using the first coefficient of  $I_1$  gives the neo-Hookean relationship

$$W = C_{10} (I_1 - 3)^i \quad \text{Equation 2-16}$$

Where  $C_{10}$  is a material constant. This formulation can also be derived from a statistical theory based on the entropy of deformation of molecular chains.

According to (Rivlin, 1948), despite the known limitations of this model to describe particular stress states, these models can be used for various structural components with local values of the strains up to about 200%. To date, the Mooney-Rivlin model has been widely used for

rubber-like materials, as it allows a simple definition of the quasi-static temperature dependency and suffices to define the shear modulus  $G$  as a function of the temperature.

The Ogden model, proposed by Ogden (1972a), is a phenomenological model that is based on principal stretches instead of invariants. It captures stiffening of the stress-strain curve and models rubber accurately for large ranges of deformation. This model should not be used with limited testing but only in uniaxial tests. A good agreement has been observed between the Ogden model and Treloar's experimental data for unfilled rubber for extensions up to 700% (Ogden, 1972b).

$$W = \sum_{i=1}^N \frac{2\mu_i}{\alpha_i^2} (\lambda_1^{\alpha_i} + \lambda_2^{\alpha_i} + \lambda_3^{\alpha_i} - 3) + \sum_{i=1}^N \frac{1}{D_i} (J_{el} - 1)^{2i} \quad \text{Equation 2-17}$$

### **3D printed material characteristics for FE analysis**

Given the general lack of availability of material property data for elastomeric materials, the only option is to determine the material coefficients experimentally. The types of tests commonly performed to determine different material characteristics are shown in Figure 2-22. Assuming that hyperelastic materials are incompressible reduces the number of tests required to determine the material characteristics, since hydrostatic stresses can be superimposed on other stresses without altering the material deformation. This shows that there are only three different types of stress/strain data from six different tests, as shown in Figure 2-22.

Theoretically, uniaxial tension testing and uniaxial compression testing may provide data suitable for determining both uniaxial and equi-biaxial material behaviour, while shear behaviour of the material cannot be determined accurately from these tests alone. The accuracy of the determined material constants cannot be relied upon when applied to components subjected to significant shear stress. Therefore, only loading conditions which match the known test data (both in terms of modes of deformation, uniaxial, biaxial and shear stresses and extent of deformation) can be predicted with confidence.

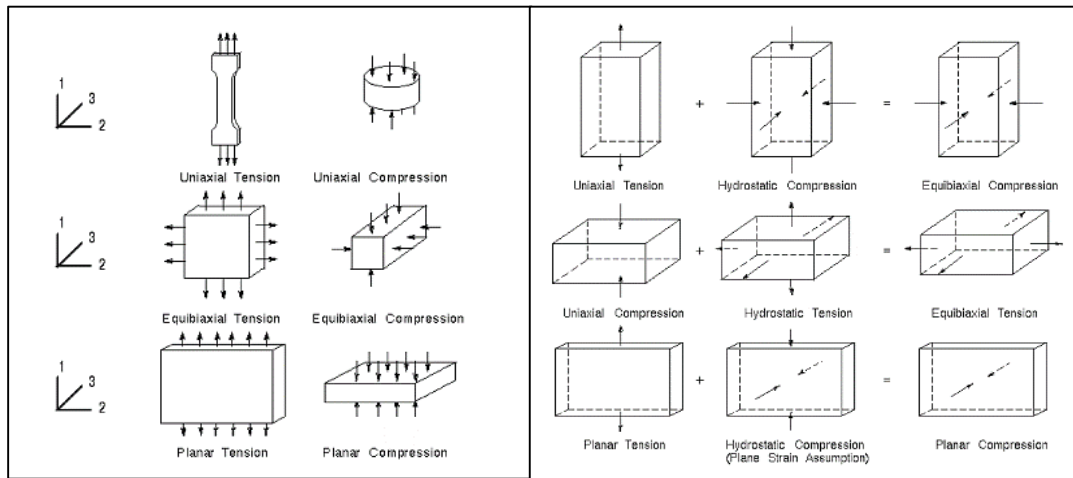


Figure 2-22 Material testing techniques. (A) Test Methods for determining material properties, (B) Superposition of hydrostatic stresses (Pearson and Pickering, 2001)

If the model is insensitive to changes in the material constants, these constants do not need to be accurately determined. However, in order to provide the most robust solution to the problem being analysed, the choice of material model has to be validated. To make sure that the material undergoes the modes of deformation accounted for in the tests, it is advisable to determine the model's sensitivity to variations in the material constants (parametric analysis). The obvious approach is to perform a simple tensile test, such as that described in BS 37 (Standardization, 2005), but instead of recording the stress at specified elongations, a complete stress/strain curve of the form shown in Figure 2-21 should be generated. To determine the material coefficients, curve fitting should be solved for a chosen material model. Fortunately, some FE packages, like ANSYS, contain 'built in' routines, whereby the experimental stress/strain data is fitted to a chosen elastomeric model. The only problem remaining is which material model to choose. In this work, the Mooney-Rivlin model was chosen as it fitted the material's testing data behaviour.

The use of a single test type may not produce a representative material definition for the expected loading conditions. If the assembly is primarily subjected to shear loading, then the FE analysis provided only with tensile data may provide incorrect answers due to a lack of detailed knowledge about the material's shear response. The other consideration to be taken into account during the experimental test is the degree of loading. If the component is expected to be subjected to a 400% strain, then data curve-fitted to the 100% strain may not be reliable since the extrapolation of material data outside the tested range may fail to model the true response.

For the general case, where the loading conditions and magnitudes are unknown, the most reliable solution is to carry out as wide a range of tests as possible and fit the material models to all the data. This avoids any problems where the strain invariants  $I_1$  and  $I_2$  are related, which may fail to describe the stored energy for any general strain. (Pearson and Pickering, 2001) noted that for a single strain type, experiments usually conform to a two term Mooney-Rivlin equation, but that using this equation for general strain, i.e., a loading type which does not conform to the test, is an extrapolation which cannot be definitively said to be correct.

Successful FE analysis of elastomeric components can be achieved using simple material determination methods, so determining which model best suits the analysis case can only be done with confidence by verifying the different elastomeric models with experimental tests and applying a set of criteria to determine the required model. This choice would include most accurate overall tests, most accurate for the dominant loading type, best convergence, etc. (Pearson and Pickering, 2001). Among these, the Mooney–Rivlin and Ogden models are the most used. Both of them give a good description of the material with concordance of the ground state shear modulus and with low root mean square (RMS) error. Furthermore, their implementation into Abaqus® FEA code showed good agreement between simulations and experimentation, even when they are applied to additional tensional states (e.g., planar) (Sasso et al., 2008). In both cases, at least uniaxial and biaxial stretching tests are required to fit the model and extract material parameters. In (Sasso et al., 2008) research, an experimental rig was set up to carry out equi-biaxial tests: the classic bulge test method has been coupled with optical devices allowing measurement in real time of the stress and elongation levels of the specimen. Uniaxial stretching tests were performed by means of a standard tensile machine and a video extensometer. Quasi-static experimental results were used to calibrate hyperelastic models. Finally, a planar tension test was carried out to validate the material models fitted from uniaxial and equi-biaxial data. FEA simulations of the test procedures gave a useful comparison between numerical and experimental data.

### **Planar Tension Test for Hyperelastic Material**

The concepts of simple and pure shear differ only by a rotation for small deformations. However, correlations between them are not well defined in the case of large deformations. Moreira and Nunes (2013) compared these two states of deformation by means of experimental and theoretical approaches. An incompressible isotropic hyperelastic material was used. The experimental procedures were performed using digital image correlation (DIC). The simple shear deformation was obtained by single lap joint testing, while the pure shear was achieved by means of planar tension testing. Classical hyperelastic constitutive equations available in the literature were used. As a consequence, the results indicated that simple shear

cannot be considered as pure shear combined with a rotation when large deformation is assumed, as is widely considered in the literature. Different to simple shear, the pure shear state is obtained in a thin sheet under uniaxial extension. The pure shear occurs only in the central part of the sheet. Figure 2-23 illustrates a small region at the central part of a rectangular sheet of material stretched along a parallel pair of clamped edges. Assuming that the material is incompressible, i.e.,  $\lambda_1\lambda_2\lambda_3 = 1$ , the principal stretches can be expressed as  $\lambda_1=1$ ,  $\lambda_2=1$  and  $\lambda_3=\lambda^{-1}$ . Thus, the deformed configuration is given by

$$x_1 = \lambda X_1, x_2 = X_2 \text{ and } x_3 = \frac{1}{\lambda} X_3 \quad \text{Equation 2-18}$$

The associated principal stretches are defined as a function of initial and final lengths ( $L_0$  and  $L$ ) in the stretched direction. In the case of tangential stress, the divergence between simple and pure shear occurs for deformation larger than 30%. Furthermore, the relationship between the principal stresses and principal stretches was also investigated, showing a divergence between simple and pure shear, mainly for large stretch values. In order to support the results, the shear modulus was evaluated by means of the Ogden model, showing the same value for both cases. The results indicated that, overall, simple shear cannot be considered as pure shear combined with a rotation when large deformation is assumed, as is widely considered in the literature (Moreira and Nunes, 2013).

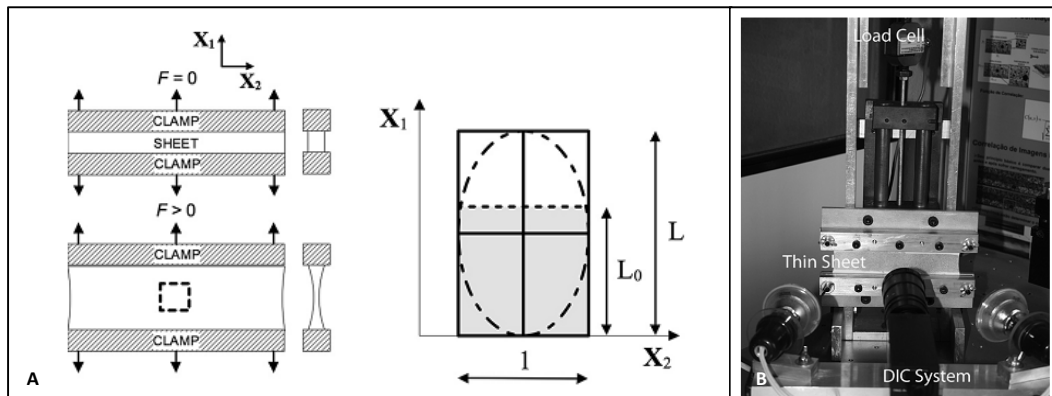


Figure 2-23 Pure shear testing rig. (A) illustrates a small region at the central part of a rectangular sheet of material stretched along a parallel pair of clamped edges, (B) Experimental arrangement for pure shear (Moreira and Nunes, 2013)

An ideal planar tension test generates a plane stress–plane strain condition in the specimen. This occurs when the width of the specimen is much greater than the height, the transversal deformation is near to zero only in the middle of the specimen, and the stress–strain distributions are quite heterogeneous. Even if no information is available on the local deformations and stresses, global entities, such as load and total displacement, can be

compared with those resulting from an FEA analysis, where the material has been defined with the previously fitted constitutive models obtained from uniaxial and/or equi-biaxial data. (Sasso et al., 2008) designed a test rig where a strain measurement system is not required. A flat rubber specimen was glued to metal brackets in such a way that the effective undeformed length was 15 mm, and the width of 60 mm was fixed on the boundaries throughout the test with 1.7 mm thickness. The brackets had an “L” shape in order to match the clamping of the tensile machine. Displacement was applied at 2 mm/ min, and crosshead position and load are recorded during the test.

The digital image correlation technique was applied in Palmieri et al. (2009) paper to acquire strain fields on flat rubber specimens with different aspect ratios (Figure 2-24). Those samples generate heterogeneous tensions distributions (from uniaxial up to increasingly biaxial) when loaded with a standard traction machine (Figure 2-24). A recursive numerical procedure was proposed in order to find the best fit material-dependent parameters of a particular hyperelastic model. Global load data, deformation data of the surface of the specimen, and stress distribution data obtained starting from a guess set of constitutive law parameters were used to calculate the terms and coefficients of the VFM equations. Two independent virtual fields were involved in the procedure to use as many as possible of the available data. After a recursive process, where the global error defined from VFM equations was minimized, and data from all specimen geometries were combined together, it was possible to obtain a set of material parameters able to reproduce a heterogeneous planar tensional state (Shahzad et al., 2015).

Lally et al. (2004b) chose the Mooney-Rivlin constitutive models of arterial tissue on the basis of uniaxial and average longitudinal and circumferential equi-biaxial test data. Three different hyperelastic models were established to represent the test specimens that exhibited a high stiffness, an average stiffness, and a low stiffness response; these three models allow the analyst to account for the variability in the arterial tissue mechanical properties. The testing equibiaxial device applies an equal force to the four sides of a square specimen creating a biaxial stretch that demonstrates the anisotropy of arterial tissue. The nonlinear elastic behaviour was marked in both uniaxial and biaxial tests. The tissue demonstrated higher stiffness in the circumferential direction in four out of eight cases subjected to biaxial tension.



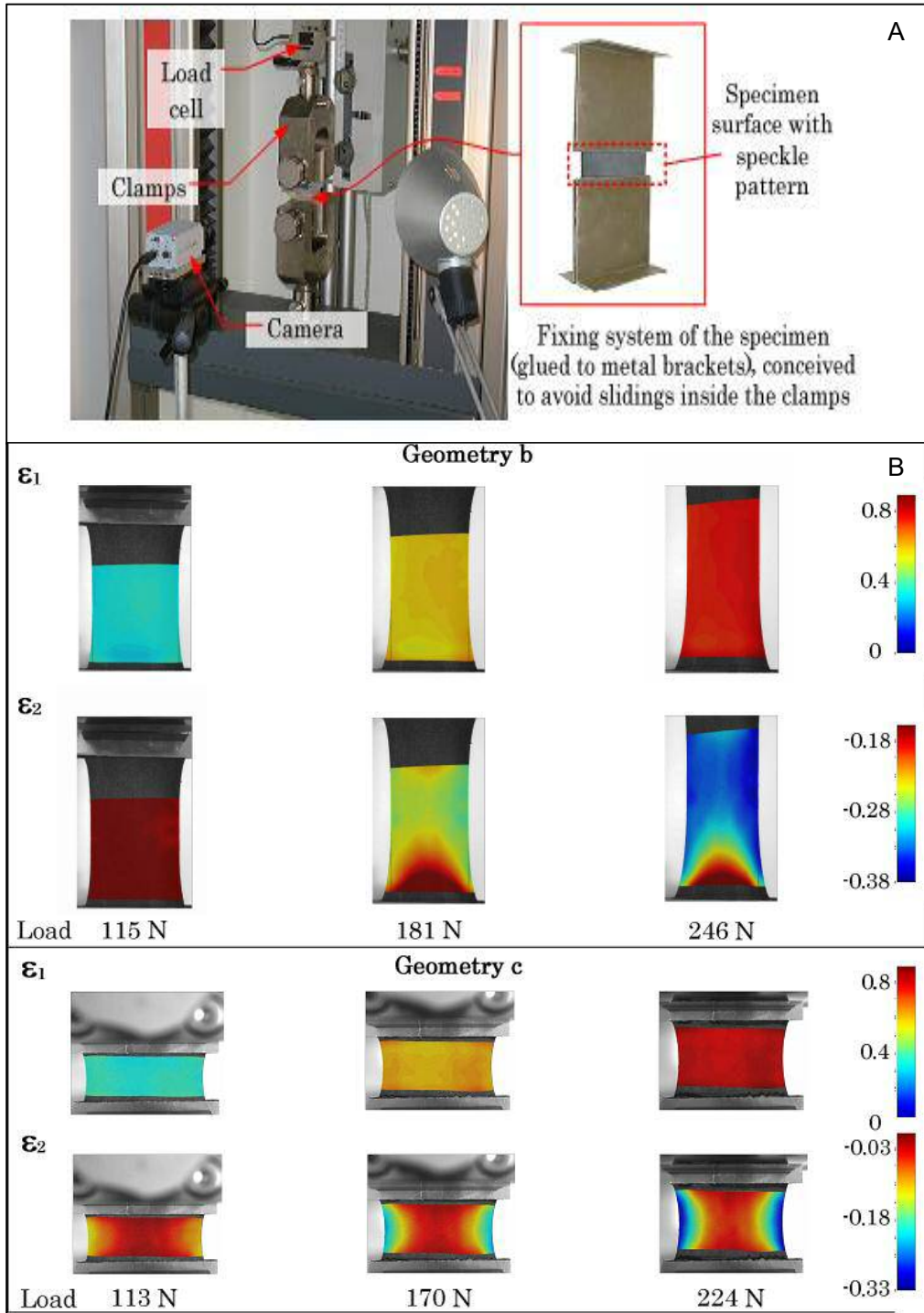


Figure 2-24 Planar shear testing. (A) Test rig for planar tension tests: specimen, tensile and vision system (Palmieri et al., 2009), (B) Strain maps of the three different specimen. Principal strains on plane are plotted for three different values of load (Palmieri et al., 2009)

These constitutive models are suitable for use in widely available finite element codes to test medical devices—the constitutive models include the key feature of nonlinear stiffening associated with both uniaxial and biaxial stretching. An anisotropic model would be more accurate, but because of the variability in the tissue elasticity, it is necessary for a host-specific anisotropic model to accurately represent the arterial tissue. Those proposed models present an appropriate compromise between the complexity of a host-specific anisotropic model and the simpler approach of using a hyperelastic model, or a number of hyperelastic models, which are based on uniaxial data alone (Lally et al., 2004b).

### **Biaxial Testing for Hyperelastic Material**

It is desirable to represent the three major strain states, which are uniaxial tension, uniaxial compression, and pure shear, to configure the material model. However, it is difficult to perform the uniaxial compression test without introducing other strain states, caused by friction between the specimen and the plates, which will affect the accuracy. The analysis of the standard button indicates that for small levels of friction, the deviation from the pure uniaxial compressive strain state causes significant errors (Axel Products, 2000). Jim Day (Jim Day et al., 2000) designed an equibiaxial testing apparatus to determine if a pure compressive strain could be obtained accurately and whether an equibiaxial tension state of strain is equivalent to a uniaxial compressive strain. The apparatus has advantages, like achieving a strain condition equivalent to simple compression while avoiding the inherent experimental errors associated with compression mainly as friction. Being able to perform strain and load control experiments as well as to examine equilibrium behaviour is another advantage. Moreover, the test can be performed at loading rates equivalent to the rates used in tension and shear for the same material.

Several other experimental approaches to the biaxial straining of elastomers have been developed with different sample geometry and thickness, for instance, expanding a thin elastomer membrane using air pressure (Sasso et al., 2008, Sasso et al., 2007, Sasso and Amodio, 2006). However, strain control as well as sheet thickness is difficult to obtain with this procedure making it difficult to create conditions that complement the other strain states required to get a full set of data for fitting hyperelastic constitutive equations. The second approach involves the gripping of a rectangular specimen around the perimeter and stretching the specimen with multiple arms or cable bearing. This approach has been used with great success by several investigator systems (Shahzad et al., 2015, Avanzini and Battini, 2016, Crocker et al., 1999). The advantage of this approach is that it allows the investigator to examine elastomer deformation in unequal biaxial deformation states. However, disadvantages arise with the measurement of strain and the calculation of stress, and the test seems relatively complex.

For small-sized specimens, (Avanzini and Battini, 2016) tested a rubber specimen (caotchouc) that underwent large elastic deformations with homogeneous isotropic properties. Specimens' shapes were derived from a selection of configurations and were cut from a sheet of material with a thickness of 0.5 mm, considering different configurations, as summarized in Figure 2-25. Four configurations had cruciform shapes that differed regarding the presence of a fillet between intersecting arms, tapering, or the inclusion of longitudinal slits to improve the efficiency of load transfer. A square specimen was tested using four hooks for each side, and a uniaxial tensile test was also carried out on a rectangular strip.

The inverse method involves creating an FE model of the material property test, and by varying the values of material parameters, the solution of the model is iterated until some constraints imposed in terms of force or prescribed displacement are satisfied. (Seibert et al., 2014) applied this technique in the presence of uniaxial and biaxial loads for an estimation of parameters of Neo-Hookean and Mooney-Rivlin laws for silicon rubbers. Overall, it can be concluded that a comparison of the results obtained with different test rigs and different specimen shapes is not always straightforward due to the variety of test configurations that were adopted and the difficulties present when interpreting results. Nonetheless, the inverse method proved to be a useful approach to compare different biaxial testing methodologies, overcoming the problem of determining real stress states by correction factors to improve fitting accuracy. Similar values of materials' parameters were, in fact, obtained in the presence of completely different specimen geometries.

In Avanzini and Battini (2016), when a cruciform specimen was used, arms with slits substantially improved the efficiency of load transfer to the central region and the degree of biaxial uniformity. With tapered arms specimens, the central region could be subjected to high stress and strain levels, but a possibility of significant decay of uniformity presented, and this may impair strain measurements. A square specimen tested with hooks provided a viable method for biaxial testing, but required special care regarding sample manipulation and hooks application due to high sensitivity to even small mounting errors. With this test, which uses complex shapes of specimen, different materials may impose different constraints in terms of machinability. When dealing with highly nonlinear materials, stress correction factors should be determined with some understanding of the constitutive law to be used and of the strain range of interest.

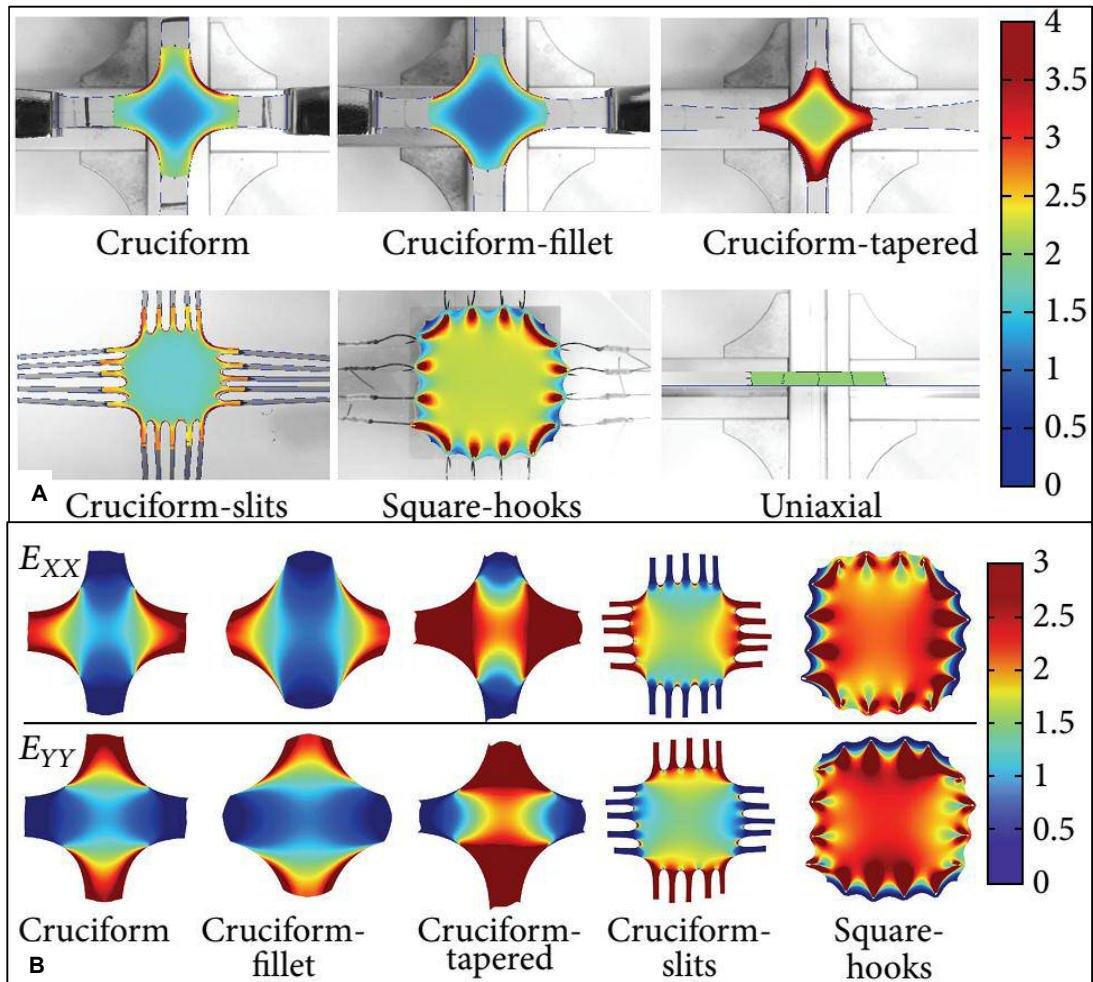


Figure 2-25 Contour maps of (A) von-Mises stress (MPa) superimposed on real deformed shapes of the specimens, (B) Green-Lagrange strains  $E_{XX}$ ,  $E_{YY}$ . (Avanzini and Battini, 2016)

Avanzini and Battini (2016) proved that integrating the use of the inverse method with markers' measurements can actually lead to the determination of very similar sets of material parameters (and a corresponding stress strain curve), even if very different experimental configurations are adopted. Such evidence is important, as it overcomes the problem of introducing correction factors for stress determination, allowing comparison of different degrees of efficiency of specimens' shapes and loading modes.

Experimental campaigns based on planar equibiaxial testing (PEBT) have been conducted in different studies on the investigated specimens in order to determine independently their material properties. The PEBT experimental apparatus shown in Figure 2-26 is shaped as a frame onto which are mounted 12 linear slide guides and 12 loose pulleys used by Cosola et al. (2008) to determine the material model. At the extremities of the mobile parts of each linear

slide, there are two screw holes of 2.6 mm diameter: one stabilises the membrane while the other carries the flexible thread where calibrated weights are applied. Linear guides force the boundary of the membrane to expand in the radial direction generating the equibiaxial state in the centre of the specimen. Seven different calibrated weights ranging from 50 to 500 g for the rubber membrane and from 50 to 600 g for the pericardium patch were applied to the specimens to cause the progressive deformation of the membrane.

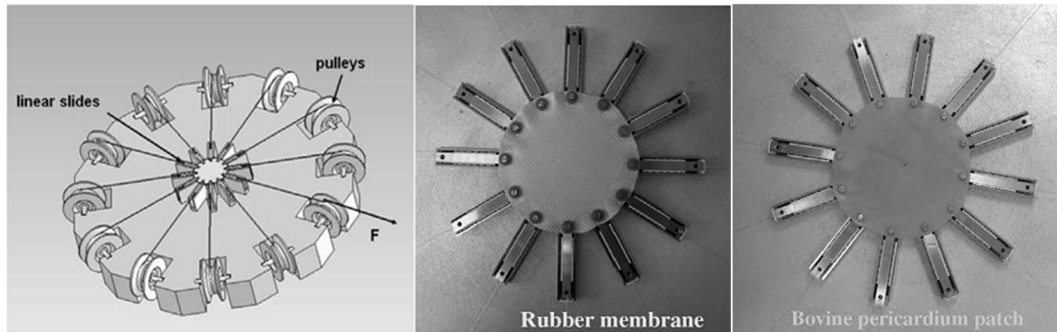


Figure 2-26 Schematic and detailed view of the planar equibiaxial testing apparatus for determining target value of material properties. (Cosola et al., 2008)

The existence of analytical solutions for identification problems in anisotropic hyperelasticity is a highly debated question because of the huge mathematical complexity, which does not allow the researcher to employ the straightforward material property fitting procedures available for isotropic hyperelastic materials. The constitutive behaviour of anisotropic materials identified via hybrid procedures should always be validated by carrying out other independent tests or validated by the inverse method (Cosola et al., 2008).

## Chapter 3. Materials and Methods

### 3.1. Chapter Overview

This chapter describes the novel and innovative approach used to investigate neonatal CPR, developing a FSI computational simulation validated using an additively manufactured physical model.

The following experimental work steps are stated in this chapter:

- **Establishing a prototype FSI model:** An FSI model simulating compressing a hyper-elastic sphere at third of its diameter is described, with the appropriate boundary conditions and degree of freedom for the structural and computational fluid dynamics setting. This preliminary FSI model will be the foundation of a more geometrical and material complicated model that will detailed later in the chapter.
- **Material Characteristics:** Experimental data from four deformation tests were obtained to input into ANSYS in order to calibrate hyperelastic model coefficients for given rubber behaviour. Material testing methods are illustrating the conducted method, rig designs, and the obtained data optimisation method.
- **Physical validation of the FSI model:** The FSI model required hyper-elastic material data, which was produced via a series of experiments. Physical testing was also performed to validate the FSI simulation.
- **Subject-specific model to investigate infant CPR:** Micro-computer tomography images of a porcine surrogate enabled production of a subject-specific model. Mesh development and loading conditions are described, which enabled generation of output data representative of blood flow from the left ventricle during CPR.

## 3.2. Preliminary Computational Model

### 3.2.1. Two-Way FSI

In two-way FSI modelling, the results of the CFD analysis are transferred to the FE model, then the subsequently calculated displacements at the interface are transferred back to the CFD analysis. The coupling capability that is currently available enables Fluent to work with the ANSYS Mechanical solver within an ANSYS Multi-field simulation. During coupled simulations, the ANSYS Fluent and Mechanical solvers execute the simulation through a sequence of multi-field time steps, each of which consist of one or more coupling iterations (Figure 3-1). Coupled simulations begin with the execution of the ANSYS Mechanical and Fluent solvers. The Mechanical solver acts as a coupling master process to which the Fluent-Solver connects. Initial analysis is performed for the structural part with the specified fundamental properties (density, Young's modulus and Poisson's ratio) for the structure. The connection is established through a third solver called the "System Coupling" Figure 3-1. Once the connection is established, the solvers advance through a sequence of pre-defined synchronisation points. At each of these synchronisation points, each field solver gathers the required data from the other solver in order to advance to the next point. The iterations are repeated until a maximum number of iterations are reached or until the data transferred between solvers and all field equations have converged. The FSI simulation with the loads described later is run for different numbers of iterations depending on the time step. The number of iterations must be selected in such a way to reach a steady-state condition.

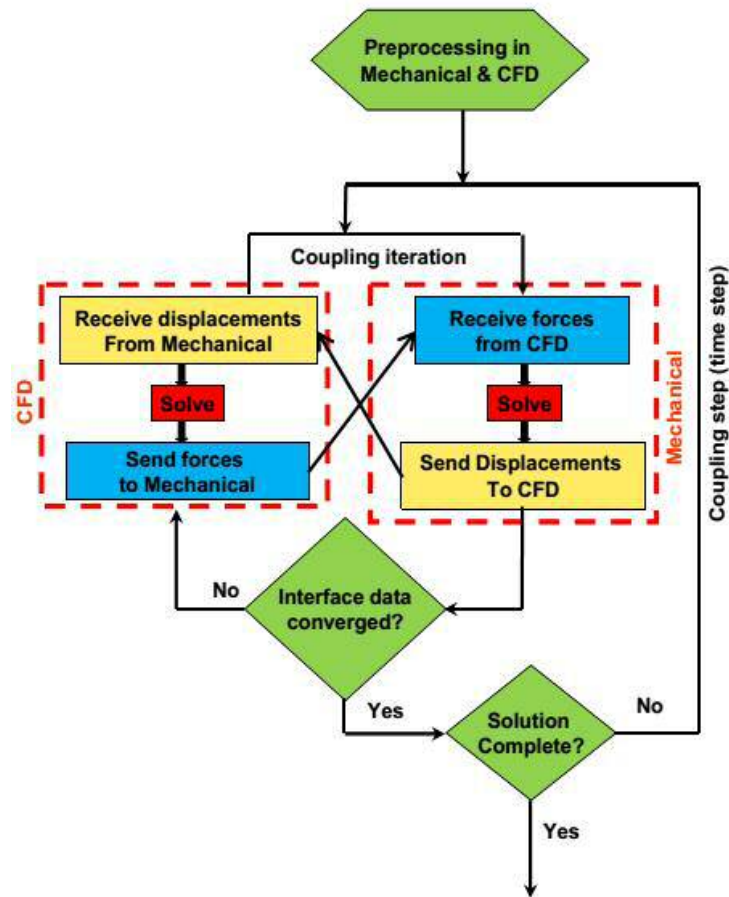


Figure 3-1 FSI workflow flowchart representing the forces and displacements transferred between the two operating solvers (CFD and Mechanical)

### Geometry and Material

In order to investigate the compression parameter of the CPR technique on the blood flow, a proposed model of the left ventricle under compression was required to be designed in ANSYS software. As the left ventricle of a subject-specific computational model is a complicated geometry obtained by MRI or CT images and since the validation process of such model requires a geometrical and material complicated physical representation, a preliminary model was designed representing the left ventricle as a sphere and boundary conditions dimensions measured from infant MRI images using MIMICS software. MIMICS software provides measuring tools in different planes of the scanned images. The model geometry was designed in ANSYS 17.2 Design Modeler with shell elements for the surface and of 4.33, 8.62mm radius



for the outlet and inlet respectively. The inlet and outlet were bonded to the sphere with 8.17, 6 mm length respectively for the solid parts with 1mm thickness Table 3-1. The fluid part represents the cavity created by the solid shell and was designed by projecting the cavity created by the shell surfaces. Compression rigid plate was designed to apply the required compression on the sphere surface and another plate was designed to serve as a fixed support to the sphere during the simulation. The material was assigned for the compression plates as the default structural steel with rigid stiffness behaviour (Figure 3-2). The shell sphere was assigned a hyperelastic flexible nonlinear material as Tango+ Black with Mooney-Rivlin material model (Bruyas, 2015). The model was assumed to have the hyperelastic material properties (Veress et al., 2002, Veress et al., 2005, Augenstein et al., 2006, Mao et al., 2017, Haddad and Samani, 2017). The material shore hardness was calculated from the Young Modulus of the materials used in (Yang et al., 2006). The conversion between material shore hardness and Young modulus was calculated according to (Kunz and Studer, 2006). This was calculated by imposing the Shore A hardness values in databases with satisfying accuracy directly into values of the modulus of elasticity and employ them for calculations involving tensile and/or compressive loads. This conversion was needed as the tissue properties of the left ventricle is not available as a constitutive model in ANSYS and requires user defined coding expertise that could not be acquired during the study timetable.

Table 3-1 Geometry information of the preliminary model computational design

Object Name	Sphere-lower	Sphere-upper	Sphere-middle	Inlet	Outlet	support	force surface
<b>Bounding Box</b>							
Length X	21.448 mm		25.736 mm	8.1729 mm	6.0322 mm	25. mm	26. mm
Length Y	5. mm		18. mm	14.17 mm	6.1247 mm	15. mm	20. mm
Length Z	21.448 mm		28. mm	14.17 mm	6.1247 mm	36. mm	37. mm
<b>Properties</b>							
Volume	436.96 mm <sup>3</sup>	437.31 mm <sup>3</sup>	1380.5 mm <sup>3</sup>	363.82 mm <sup>3</sup>	116.07 mm <sup>3</sup>	1650. mm <sup>3</sup>	2002. mm <sup>3</sup>
Mass	4.8078e-004 kg	4.8117e-004 kg	1.519e-003 kg	2.856e-003 kg	9.1113e-004 kg	1.2953e-002 kg	1.5716e-002 kg
Centroid X	1.3251e-017 mm	6.0292e-017 mm	-1.2852 mm	16.161 mm	-16.677 mm	-1. mm	
Centroid Y	-11.479 mm	11.478 mm	-1.6988e-003 mm	-1.0927e-016 mm	4.2814e-017 mm	-13.091 mm	10.805 mm
Centroid Z	-4.8462e-016 mm	0. mm	-1.2368e-005 mm	2.9139e-016 mm	2.2834e-016 mm	5.1335e-016 mm	8.4619e-016 mm
Moment of Inertia Ip1	1.5701e-002 kg·mm <sup>2</sup>	1.5729e-002 kg·mm <sup>2</sup>	0.18755 kg·mm <sup>2</sup>	0.14246 kg·mm <sup>2</sup>	8.4906e-003 kg·mm <sup>2</sup>	2.9616 kg·mm <sup>2</sup>	4.3201 kg·mm <sup>2</sup>
Moment of Inertia Ip2	2.9405e-002 kg·mm <sup>2</sup>	2.9461e-002 kg·mm <sup>2</sup>	0.24905 kg·mm <sup>2</sup>	8.7105e-002 kg·mm <sup>2</sup>	7.0046e-003 kg·mm <sup>2</sup>	3.3452 kg·mm <sup>2</sup>	4.541 kg·mm <sup>2</sup>
Moment of Inertia Ip3	1.5701e-002 kg·mm <sup>2</sup>	1.5729e-002 kg·mm <sup>2</sup>	0.1501 kg·mm <sup>2</sup>	8.7105e-002 kg·mm <sup>2</sup>	7.0046e-003 kg·mm <sup>2</sup>	0.96564 kg·mm <sup>2</sup>	1.5497 kg·mm <sup>2</sup>
Surface Area(approx.)	436.96 mm <sup>2</sup>	437.31 mm <sup>2</sup>	1380.5 mm <sup>2</sup>	363.82 mm <sup>2</sup>	116.07 mm <sup>2</sup>	1650. mm <sup>2</sup>	2002. mm <sup>2</sup>

### **Meshing and Elements Configurations**

Both regions were meshed together using computational ANSYS FE/TS and CFD/Fluent packages. In each package the structural and fluid part are meshed using the same meshing methods and sizing criteria using 100% relevance standard mechanical physics preference in FE/TS while using the same percentage but CFD physics preference in the meshing preceding the Fluent setup. This will allow the meshing methods to comply with the corresponding part before suppressing the irrelevant other part. After meshing the two regions in FE/TS the fluid geometry is suppressed and the solid geometry is suppressed in the CFD mesh. In the CFD mesh each surface was defined for the corresponding boundary conditions along with identifying the fluid volume. Meshing the two regions in each package together is important to get a 100% compatibility between the contacting coupling source and target surfaces

minimising the meshing issues later on during the FSI simulation. The element size was set at 0.8mm for both regions with fine relevance centre and span angle centre (Figure 3-2).

Both regions were discretised with a minimum edge length of 0.2 mm and maximum edge length size of 0.9 mm. The fluid elements are surrounded by 4 layer inflated layers near the structure boundary. MultiZone meshing method was used for the fluid region with prism mapped mesh type. The total number of 27520 nodes and 36414 tetrahedral volume elements are mapped into the fluid region.

The mesh checking capability in ANSYS Fluent examines various aspects of the mesh, including the mesh topology, periodic boundaries, simplex counters, and (for axisymmetric cases) node position with respect to the axis, and provides a mesh check report with details about domain extents, statistics related to cell volume and face area, and information about any problems associated with the mesh. This check was examined before each simulation and a mesh quality report was generated to report the skewness, orthogonal quality and aspect ratio of the fluid zone prior to interface.

The meshing system is adopted after performing the mesh independency analysis starting from 27520 nodes and 36414 volume elements for fluid domain. The element size was reduced according to a mesh study and until reached to its final value. The mesh study results are in the chapter five. The mesh was updated with every size element and the simulation was run to record the mesh quality and velocity, pressure and flow data from the first and second stage FSI.

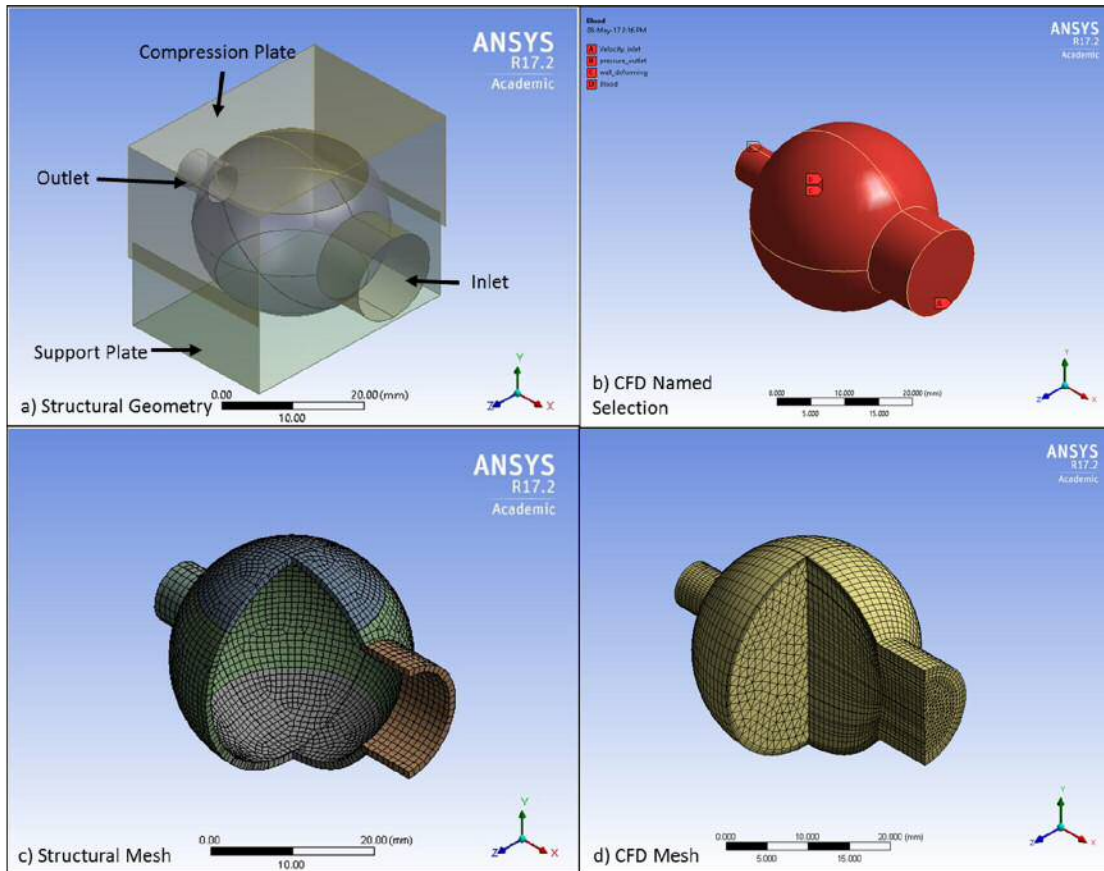


Figure 3-2 Model geometry with boundary zones (A) Structural geometry with shell solid of 1mm thickness (B) Fluid region with surfaces name selection. Mesh with parts colour showing 2 perpendicular sections with 0.8 mm element size. (C) Structural Shell mesh (D) Fluid region mesh

### 3.2.2. Material Characterisation

Constitutive models for hyperelastic materials are developed from strain energy functions and require nominal stress vs. nominal strain data to fit most models available. In general, it is desirable to represent the three major strain states which are; uniaxial tension, uniaxial compression, and pure shear. If compressibility is a concern then bulk compressibility information is also recommended. The uniaxial tension strain state is easily obtained and the pure shear test can be performed using a planar tension test with excellent, repeatable accuracy.

In this work, experimental data from four deformation tests were obtained to input into ANSYS in order to calibrate hyperelastic model coefficients for given rubber behaviour. In this section testing methods are illustrated for those test which were conducted and designed depending

on the literature testing techniques for hyperelastic material as discussed in section 2.5.4. DIC technique along with the video-extensometer employed for strain measurements in tensile, planar and biaxial specimen.

As the tests were designed according to the hyperelastic material, some of the conventional testing techniques and/or testing specimens' designs were modified. Therefore computational validation were used to validate the behaviour of the designed tests following the steps shown in Figure 3-3

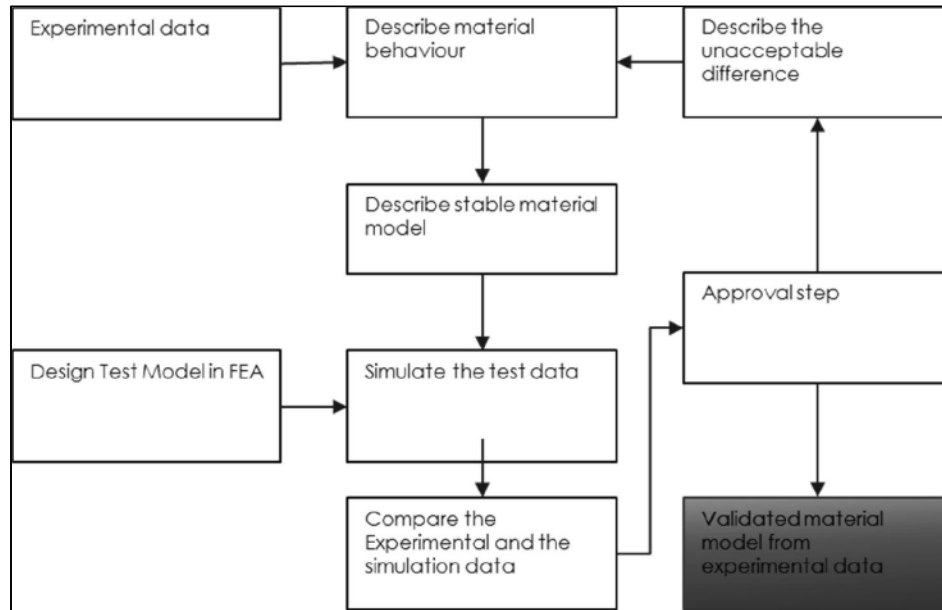


Figure 3-3 Material model computational validation process from experimental data

### **Characterising Uniaxial Tension and Compression**

To obtain the constitutive material model in ANSYS computational model, material testing was conducted to test the material behaviour under different types of loading. Uniaxial tensile tests were performed following the standard method BS ISO 37:2011 (Institution, 2012) using a type 1 specimen. To avoid the possible slipping of the specimens from the grip, two types of specimens were designed as shown in Figure 3-4 with different end patterns. Both designs were tested with two speeds 10 and 500 mm/min. Four samples were used for each test. The two different loading speed were used to evaluate the strain rate effect on the material. Preloading cycles were used for each test as 5, 10, 15 cycles per speed with an additional loading cycle till failure. Zwick 050 tensile machine was used with 50KN load cell and an IMT-CAMO28 video-extensometer to measure the strain at the narrow part of the specimen, with an 8mm focal length lens (Figure 3-5). The strain was measured applying two marker points on the narrow portion of the specimen and considered as a strain gauge.

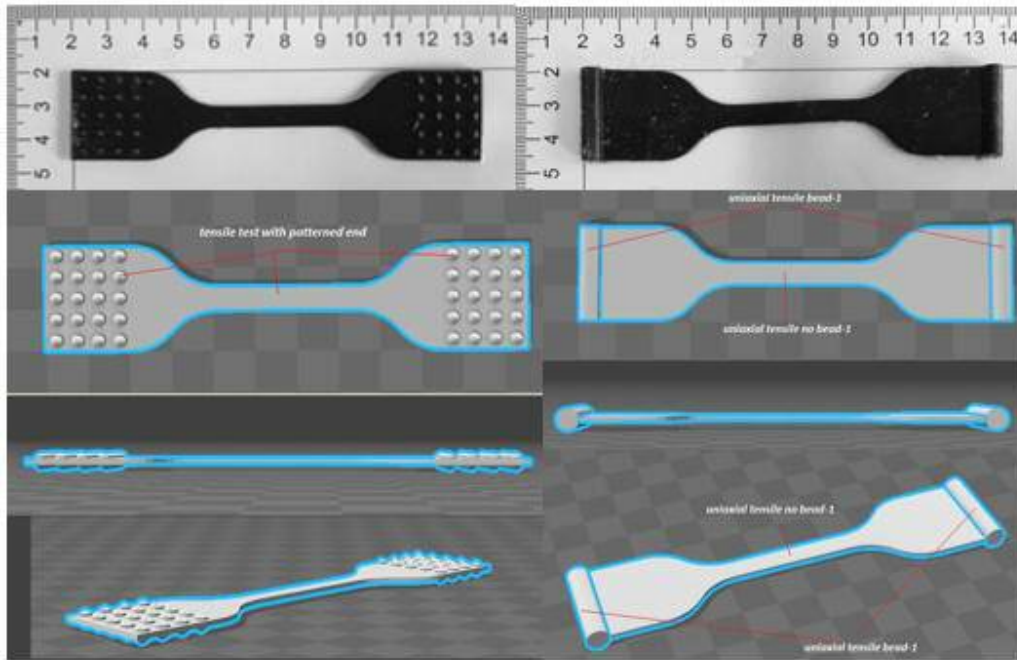


Figure 3-4 Tensile test specimens with modified geometry to avoid slipping. Left images represents the patterned end geometrical modifications with different aspect views. The right images represent the beaded end geometrical modification to the standard tensile test specimen.

Compression test specimens were tested according to the BS ISO 7743 (Standards, 2011) using method C as the reference for the test piece geometry and procedure Figure 3-6.

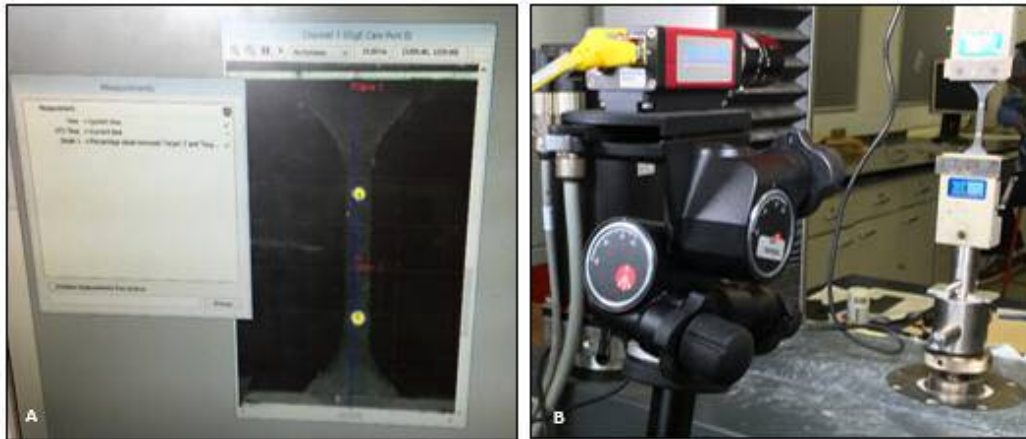


Figure 3-5 Tensile test measurement using video-extensometer. (A) The virtual strain gauge on the narrow part of the tensile test specimen. (B) The testing setup showing the video-extensometer camera positioned parallel to the tensile test piece.

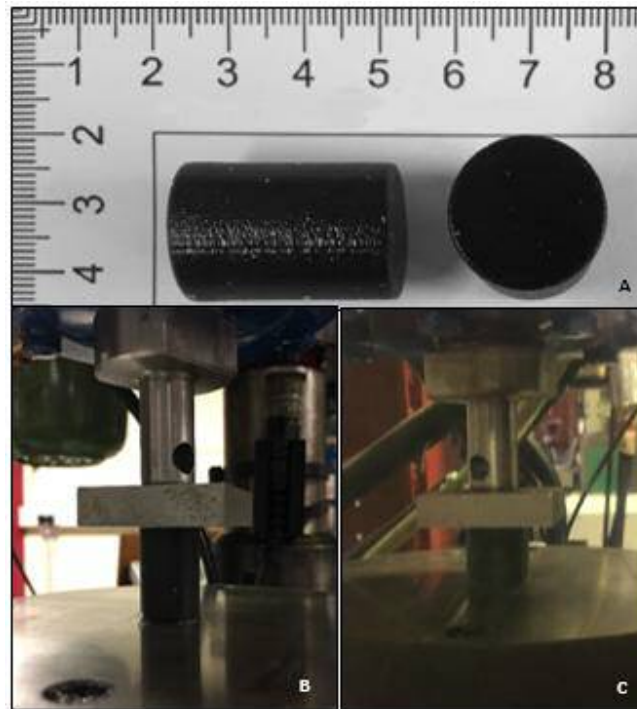
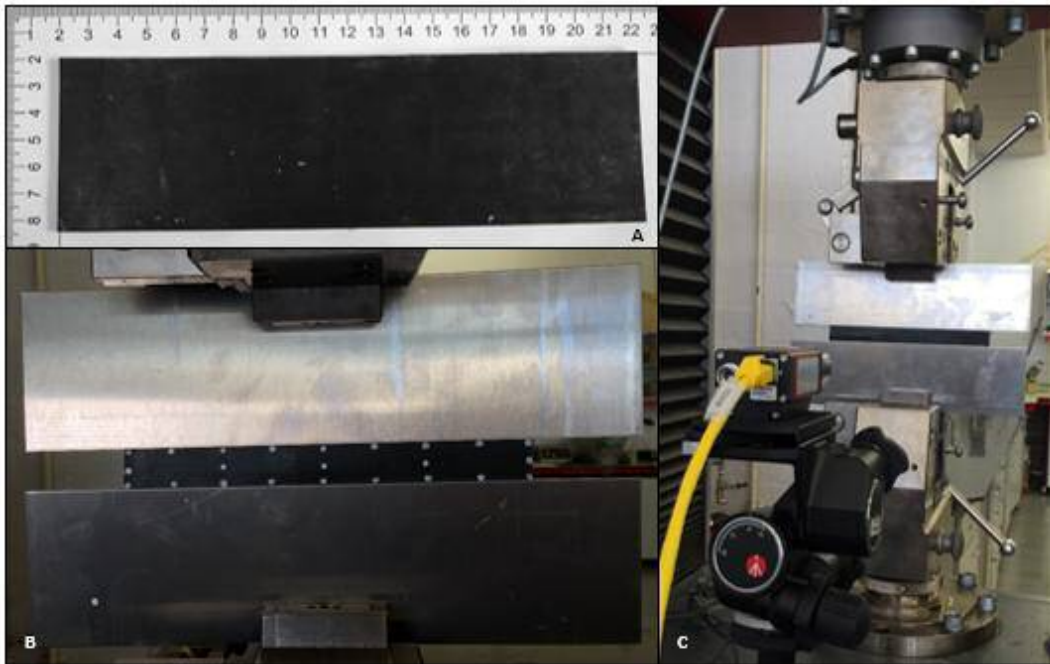


Figure 3-6 Compression test specimen along with the testing images. (A) The test piece dimensions, (B) At the start of the compression test, (C) At the end of the compression test.

### **Characterising Planar Tension Behaviour**

Hyperelastic materials constitutive model requires the data of at least three material tests to calibrate a model consisting of the material behaviour under range of tested type of loading. To calculate that model planar tension behaviour of the 3D printed material was tested to better the material model constitutive model used in the preliminary FSI simulation. The key feature of the planar test is that, unlike conventional uniaxial tensile tests, there are no lateral strains. Experimentally this was achieved by using specimens with an extremely high aspect ratio (Figure 3-7). Planar tension test specimens are tested in tension with a large aspect ratio (ratio of width to gauge length). The grips prevent contraction in the width direction. Thus, the specimen is tested in a condition of plane strain rather than the plane stress condition that characterises the uniaxial tension test. Tango+ Black specimens were prepared as 60 mm by 200 mm wide rectangles. A grip separation of 20 mm was used. The widened grips clamp the specimen along its wide axis. This constrains the lateral contraction of the specimens provided that the clamping force is maintained. One problem was that, since the specimen was supposed to contract in the through-thickness direction, the clamping would not be uniformly maintained at large strains. Some lateral contraction may occur in the width direction and, eventually, the specimen will start to slip from the grips. This may limit the valid ranges of

strain for the subsequent analyses. To resolve this problem a strong scotch-weld contact adhesive 10 was used between the material and the clamps and it was left to dry overnight for better results. The large size of the test specimen increases the chances of inclusion of a critical flaw within the active area of the specimen leading to premature failure. The grips of the loading machine was not suitable for the wide edge of the sample so an aluminium clamps were designed with 80mm by 300 mm wide rectangles.



*Figure 3-7 Planar shear testing using flat bracket as gripping. (A) The planar shear test piece dimensions, (B) The flat metal brackets positioning along with the strain gauges along the test piece, (C) Planar shear testing rig using video-extensometer setup*

Tests were performed at 10 mm/min which was the same strain rate as the uniaxial test. Strain was determined from specimen displacement measurements using a non-contacting Video-extensometer (IMT\_CAMO28). Images in the field of view of the camera were analysed to locate the positions of contrasting gauge marks on the specimen surface. The changes of gauge mark positions relative to their starting positions were used to determine strains. This device had the capability of measuring extensions simultaneously in two orthogonal directions. For example, the axial extension and transverse contraction of a uniaxial test specimen may be measured to determine Poisson's ratio. A further advantage of this device was that measurements may be made over several gauge sections. A more specialised module of the



extensometer software allows measurement of the location (in 2-dimensions) of contrasting dots on the specimen. This can allow a limited degree of strain mapping. For this test Video-extensometer (IMT\_CAMO28) was used to measure 9 strain gauges along the specimen with 2 transversal gauges.

Five preloading cycles were performed to 5 mm extension and the 6<sup>th</sup> cycle was to failure. Two tests were performed and both had the same issue of slipping between the machine grip and the clamps. This led to the design of the L shape clamps with the same width of 300 mm Figure 3-8. The same adhesive was used to attach the material to the brackets. For this test a DIC system was used to measure the strain along the middle area of the sample. White face paint was used to apply the speckle pattern on the middle area of the exposed sample. The test machine used consisted of a Zwick 0100 of 100 kN load cell and was controlled using Zwick/Roel's software which records the load cell and the crosshead displacement outputs. Stress was calculated from the load values obtained from the load cell using the following equation:

$$\sigma = \frac{F}{b \times c} \quad \text{Equation 3-1}$$

where,  $\sigma$  is the stress,  $F$  is the load;  $b$  and  $c$  are the width and thickness of the specimen. For uniaxial and planar test specimens the load used was that directly measured. Removing the material after testing from the brackets causes the bracket area to scratch and thus repeated testing using the same brackets may give error due to adhering inconsistency. The large number and size of samples that have to be printed for the planar tests along with brackets discourages large numbers of repeats. According to Crocker et al. (1999) difference in strain rates may have an effect on the accuracy of the FE hyperelastic coefficients obtained from the uniaxial, planar and biaxial tension data. For this reason two loading speeds were used in this test 10 and 2.5mm/min.

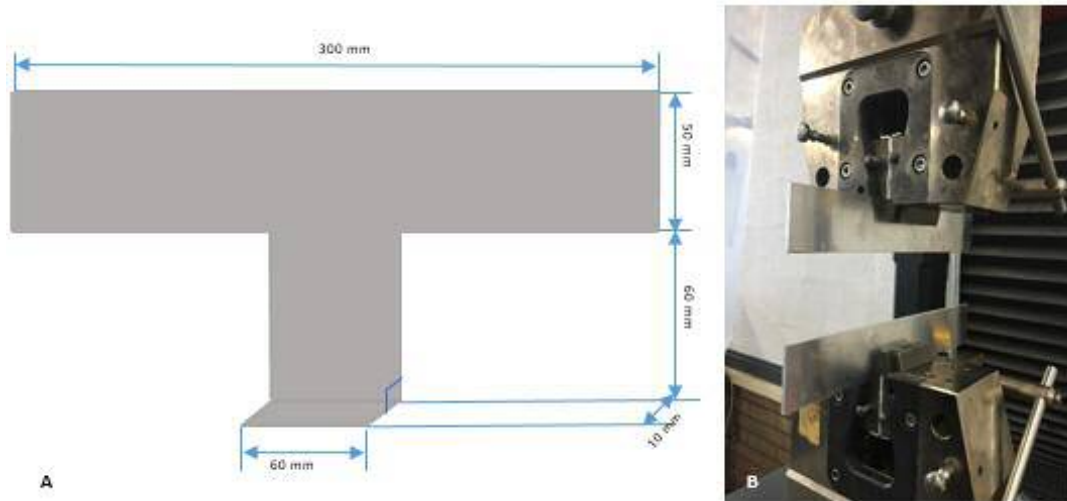
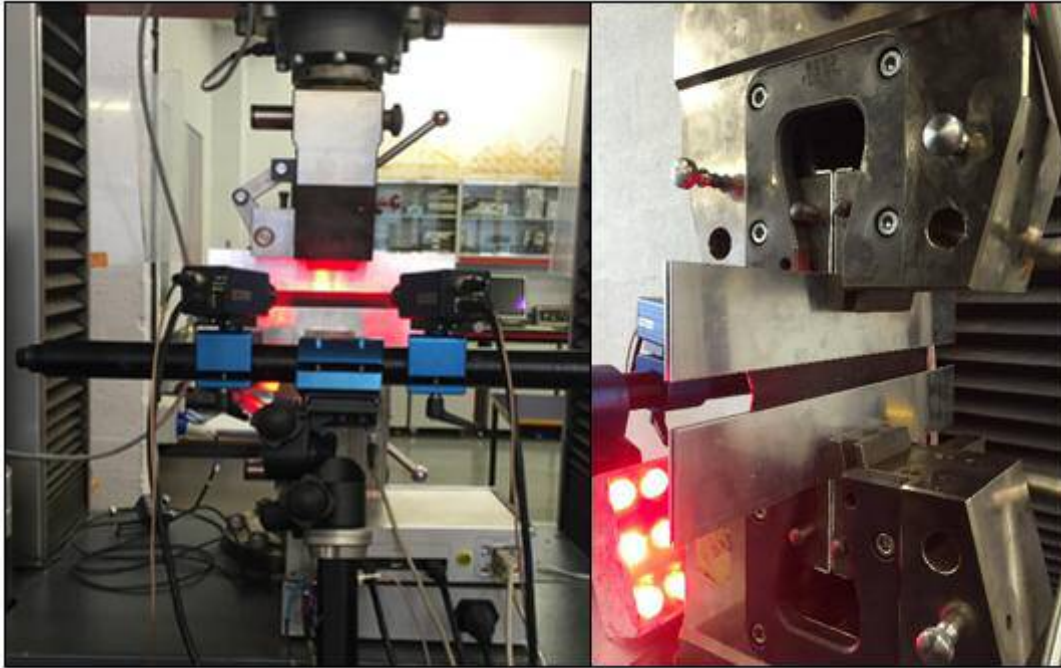


Figure 3-8 Planar shear modified rig. (A) L-shaped planar shear brackets, (B) Planar shear rig

Two tests were performed with five preloading cycles in the first test. The DIC machine accuracy was set for image every 10 seconds.

The DIC system used was the Q-400 (Dantec Dynamics), consisting of the necessary software, a HiLis light source and a data logging system to connect the cameras to the laptop. The HiLis light source is a high intensity LED illumination system which provides cool and homogeneous illumination. Two Limes digital cameras (1600x1200 2/Megapixels resolution) were used with the system, along with Schneider Kreuznach XNP 2.0/28 compact lenses with >5.9 modification range, >174 mm working distance and >232mm object to image distance (Figure 3-9).

The collected data was compared with the predicted results from the computational planar shear model. The test was then repeated without the preloading cycles to obtain more images during the test hence more of the collected data (image every 2 seconds). Also for the second test material strips were added at the angled side of the bracket to maintain gap separation and load distribution uniformity throughout the rig. As the load was low compared to the machine load cell so there was small noise during the strain measurement test. The strain was measured using two regions of interest during DIC data processing. Those two points were placed in the middle part of the specimen.



*Figure 3-9 Planar shear testing rig using DIC setup. On the left is the positioning of the two DIC cameras while the left image show the clamping of the test piece using the modified bracket design ensuring no slipping from the tension machine clamps*

### **Characterising Biaxial Behaviour**

For hyperelastic materials tensile, compression and planar shear tests should be conducted to measure the material behaviour, but the studies have shown that compression test is not enough to provide the material behaviour due to friction issue and other factors explained in section 2.5.4. Therefore, biaxial testing was conducted to measure the material behaviour as the material under equi-biaxial tension produce areas of compression at the centre of the test specimens. This test was run using an equi-biaxial rig designed by Robinson et al. (Unpublished). To apply radial forces in the apparatus, 16 small grips were mechanically attached to the top and bottom surfaces of the perimeter of the specimen using spring force attachment. The grips were pulled radially outward by thin flexible cables which are redirected around pulleys to a common loading plate (Figure 3-10). When the loading cell is moved upwards, all of the attachment points move equally in a radial direction and a state of equal biaxial strain is developed in the centre of the specimen (Figure 3-11).



Figure 3-10 (A) Biaxial stretching apparatus with the test specimen in the middle attached to the gripping clamps, (B) The different gripping clamps, the clamp on the left was used instead of the one on the left to accommodate the grooving of the middle lower clamp to avoid stretching the test piece.

The actual shape of the specimen is not a simple disk as shown in Figure 3-11. There are 16 radial cuts introduced into the disc specimen so that there were no tangential forces between the grips this prevents material to flow within the grip. Small holes are introduced at the ends of the radial cuts so that the specimen is less likely to tear.

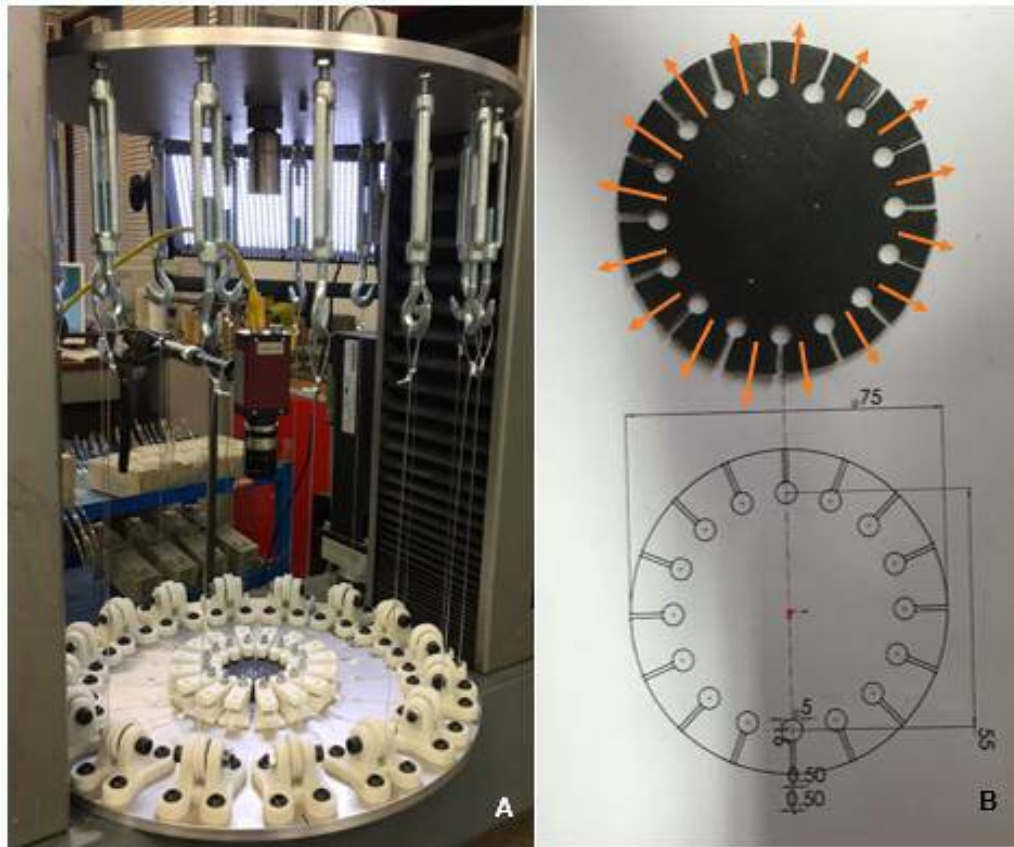


Figure 3-11 Biaxial stretching configuration and specimen geometry A) The test setting with the specimen placed and the video-extensometer camera angled vertical on the test specimen, B) Test sample with the forces marked to represent the direction of pulling cords on the bottom the biaxial test specimen outline and geometry dimensions.

The test samples were 3D printed with the desired geometry with 3mm thickness. As the test samples were thicker material the gripping clamps were changed to accommodate the new thickness. Also the gap between the cuts was increased to be 1mm to be compatible with the new clamps and prevent generating forces between the grips. To ensure that the cords were in an equal initial loading forces, 16 equal length plates were placed between the pulleys and the gripping clamps before starting the test and the cords were tightened accordingly then the plates were removed when the test starts (Figure 3-10).

To determine the strain, a non-contacting Video-extensometer (IMT\_CAMO28) was used to measure the strain on the surface of the specimen away from the grips. For this test 8 DIC strain gauges across the specimen diameter with different length were created to measure the strain across different distances from the centre of the sample (Figure 3-12). Four test samples were used and the total force transmitted by the 16 grips to the common loading plate was

measured using a strain gauge load cell. The nominal equi-biaxial stress contained inside the specimen inner diameter ( $D_i$ ) was calculated as follows:

$$\sigma = F / (\pi * D_i * th) \quad \text{Equation 3-2}$$

Where  $D_i$  = Diameter as measured between punch holes  $F$  is the sum of radial forces,  $th$  is the original thickness and  $\sigma$  is the engineering stress.

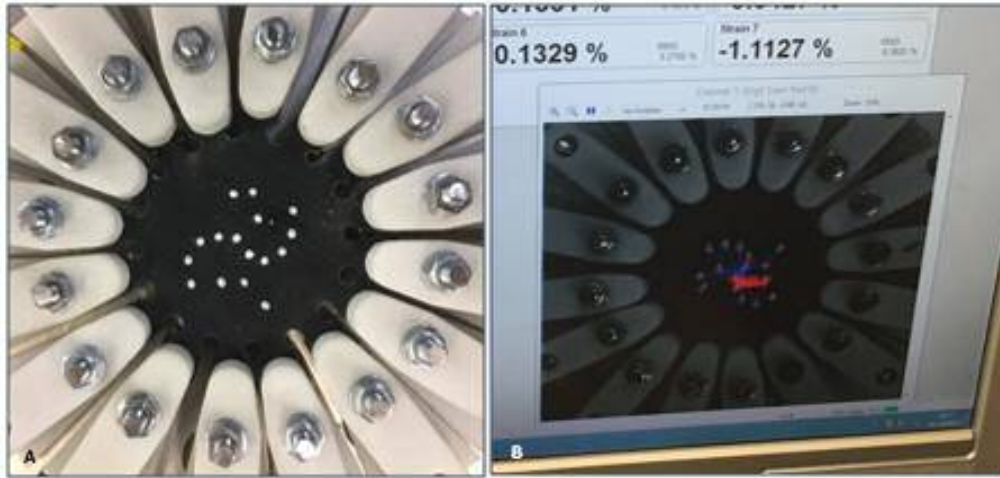


Figure 3-12 Strain gauges. (A) The 8 strain gauges on the test sample placed by a white matte corrector, (B) The strain gauges in the extensometer software

### **Material Model Calibration**

Curve fitting is a way to describe the mechanical property available in ANSYS. The hyperelastic model can define orthotropic or anisotropic material behaviour and is valid for small elastic strains. It is characterised by a linear relationship between stress and strain (Hooke's Law). To validate the hyperelastic model coefficients, curve-fitting using ANSYS17.2 software was used. The hyperelastic model proposed in this project was Mooney-Rivlin. In order to check the accuracy of curve-fitting, an FEA model for the mechanical tests was designed to simulate the material behaviour under loading. The geometry for each test was based on the specimens dimensions and was designed using Solidworks2015. Predicted stress-strain curve were compared with the measured results for planar shear test. The stress-strain data input for the planar test model was for the tensile and compression tests using nominal values for both.

The material model coefficients were measured using uniaxial tensile, biaxial and planar shear tests. For this work, these parameters were obtained by applying these test data as an input

for the Mooney-Rivlin material model. While the stress and strain entered in ANSYS was of nominal form, the results of the computational models were in true stress/true strain values. This can be easily converted for verification purposes using the equations:

$$\sigma_{true} = \sigma_{nom}(1 + \varepsilon_{nom}) \quad \text{Equation 3-3}$$

$$\varepsilon_{true} = \ln(1 + \varepsilon_{nom}) \quad \text{Equation 3-4}$$

Among the number of models available in literature and implemented into commercial FE codes, Mooney-Rivlin material model was found to be the most suitable choice and after curve fitting it was tested to be the best compatible material behaviour. For the two analysed deformational states in ANSYS i.e. equi-biaxial and simple shear, the Mooney-Rivlin model gives a stable analytical description of the material stress–strain response and a good agreement between numerical and experimental data, even at large values of strains. All the tests were validated using ANSYS software and to get the predicted test data for the next test. The predicted data were compared to the measured data to check the importance of the next test to get the correct material model. These steps were taken into consideration according to the validation process illustrated in Figure 3-3.

To obtain the material model, curve fitting is needed to be applied on the measured testing data. ANSYS workbench has a built-in curve fitting toolbox in the engineering data. The material curve fitting calculates coefficients of material models that approximate the provided experimental data. The three experimental data along with the material density were entered from a spreadsheet into the table pane as engineering stress and strain columns. Multiple material models are built in the ANSYS workbench and for hyperelastic material different models were solved for the same experimental data to compare the curve fitting material behaviour to the measured data curves with both norm and absolute error. After solving the curve fitting the material coefficients were copied and the material has been tested in computational model to validate the module. Although ANSYS has built in material curve-fitting functionality, the specialised MCalibration software was used to generate a material model that achieved greater correlation with the experimental data. MCalibration is a GUI application for Windows and Linux computers that can be used to calibrate all material models in the PolyUMod library, and native material models in Abaqus, ANSYS, LS-DYNA, MSC.Marc, and COMSOL. It takes existing experimental data and then finds the best material parameters for the selected material model. The calibrated material model can then be exported to the FE software (e.g. Abaqus/CAE, ANSYS WB, MSC.Marc).

Four material testing data were loaded in the MCalibration software and multiple models were tested to find the best fit to the material measured data. A parametric study was then run within the software and the chosen material model was run in the computational model to test the material behaviour with a tensile test computational model.

### **3.2.3. Computational Model Parametric Adjustments**

This section will list the parameters for processing the solid and fluid parts of the FSI computational model and the system coupling components in ANSYS software. The same procedure will take place in the subject-specific model except some parameters that needed to be changed according to the related geometry and material used in the model. Those parameters and settings were chosen according to mechanical behaviour of the model as well as factors influencing the stability of the model and reducing the computational cost of the simulation.

#### ***Transient Structural (FE)***

For the structural region the contact between the two compressing plates was considered asymmetrical frictionless behaviour while bonded type was used to define the connection between the inlet and outlet edges with the sphere edges. This contact type prevented the inlet and outlet parts from disconnecting during the compressing simulation. Frictional connection was used for the compressing plates with the sphere surface. The surfaces was used for minimal area for the upper and lower sphere with adjusting to touch interface treatment to minimise the penetration and gap between the contacting surfaces. The moving compressing plates were setup with remote displacement degree of freedom with the lower plate to be static and the upper plate moving in a third of the diameter of the sphere displacement in the Y direction and the fluid solid interface load was set to the entire inner surface of the solid region consisting of 12 surfaces. As the material is hyperelastic and considered rubber-like, the 'large deflection' was turned on with one step, as recommended by the ANSYS FSI settings. The inclusion of large deflection means that ANSYS accounts for changes in stiffness due to changes in shape of the parts in the simulation as a result of nonlinearity in the material model. Although it is recommended not to add sub-steps, ten sub-steps were used with the auto time stepping switched off. To accommodate this change the time stepping in the system coupling was adjusted accordingly and will be explained later. Before setting up the CFD/Fluent solving, a crucial step was to check if the mechanical aspect of the FSI was running with no computational errors or warnings. This was to identify the



connection setting and degree of freedom of the FE region before interfacing with the fluid volume and send forces to the interfacing surfaces.

### **Fluent (CFD)**

For the CFD part of the simulation, settings are characterised and examined in the ANSYS Fluent package separately from the mechanical setting (Figure 3-13). After updating the fluid mesh, Fluent setup is launched with parallel processing using 6 cores of 8 for CFD transient simulation, and 2 for mechanical and pressure based solver. Laminar flow was assumed.(Dahl, 2012)

The material was considered of non-Newtonian fluid (section 2.5.2) with Carreau viscosity model. The viscosity model parameters were (3.313s time constant, 0.3568 power-law index, 0.056 kg/m<sup>-1</sup> zero shear viscosity and 0.0035 kg/m<sup>-1</sup> ∞ shear viscosity) with 1060 kg/m<sup>3</sup> density (Zhong et al., 2013, Doost et al., 2016). For the first stage of the FSI the inlet was considered as a no slip moving wall while the outlet was considered as an outflow opening. This condition by default indicates that the fluid sticks to the wall and moves with the same velocity at the wall. For the dynamic mesh, smoothing and re-meshing was used. For smoothing, 0.45 Poisson's ratio with linear elastic solid method was applied as the FSI interface is adjacent to an unconstrained outlet and the outlet is a moving boundary. Smoothing and re-meshing was used together to produce better quality mesh and allow larger time step hence reducing simulation time. Local cell and face re-meshing was a crucial dynamic mesh to be used in case the skewness becomes larger than 0.98 during the simulation and as the fluid was meshed with multi-zone prism voxels. Blood, inlet and outlet boundary conditions were considered as deforming zones and to define the coupling interface surface the wall surface dynamic mesh was controlled by the system coupling zone. The model is already considered unstable for using incompressible fluid, so stabilizing the interfacing surface was important using a volume-based method with 6 scale stabilizing factor. This factor was used based on trial-and-error, to stabilise the area-weighted average of velocity and pressure in the surface monitoring during the simulation. To get the best convergence required for the simulation the convergence behaviour was monitored (Figure A-2) and the curve trend was observed once the curve showed good quality convergence behaviour the stabilisation factor was set according to that. This monitoring results will be discussed in Appendix A and monitoring data will be explained then. As ANSYS suggests there's no standard number of stabilisation factors and the only way to get the desired amount is parameter optimisation starting from 1 to 1000 which introduces damping to the pressure gradient and virtual pressure damping near the wall. This damping does not affect the physical behaviour of the model, instead just stabilising the

behaviour of the convergence. The stabilisation factor neither effects nor increases convergence, as the model may still diverge with better stabilisation and vice versa.

Hybrid initialization was use in the model, to improve the convergence robustness for multiphase flow and accelerate CFD solution. This process is more complex than standard initialization, using boundary conditions and then solves an Euler problem and uses the solution to this Euler problem as the initial guess. Hybrid initialisation is like a programmed environment based on the solving of Laplace's equation to determine the pressure and velocity parameters. All other subsequent parameters, such as the temperature, turbulence, frictions etc., have been taken as per the standard program or pre-defined augmented reality. The standard initialisation asks user to enter each and every value to define an appropriate environment and to augment the reality inside the ANSYS at a greater degree. Standard initialization allows the specification of all the variables directly as initial estimates. To specify non-constant fields requires further investigation, but an arbitrary spatial distribution of all variables could be specified everywhere as an initial approximation. Standard initialization requires an initial estimate.

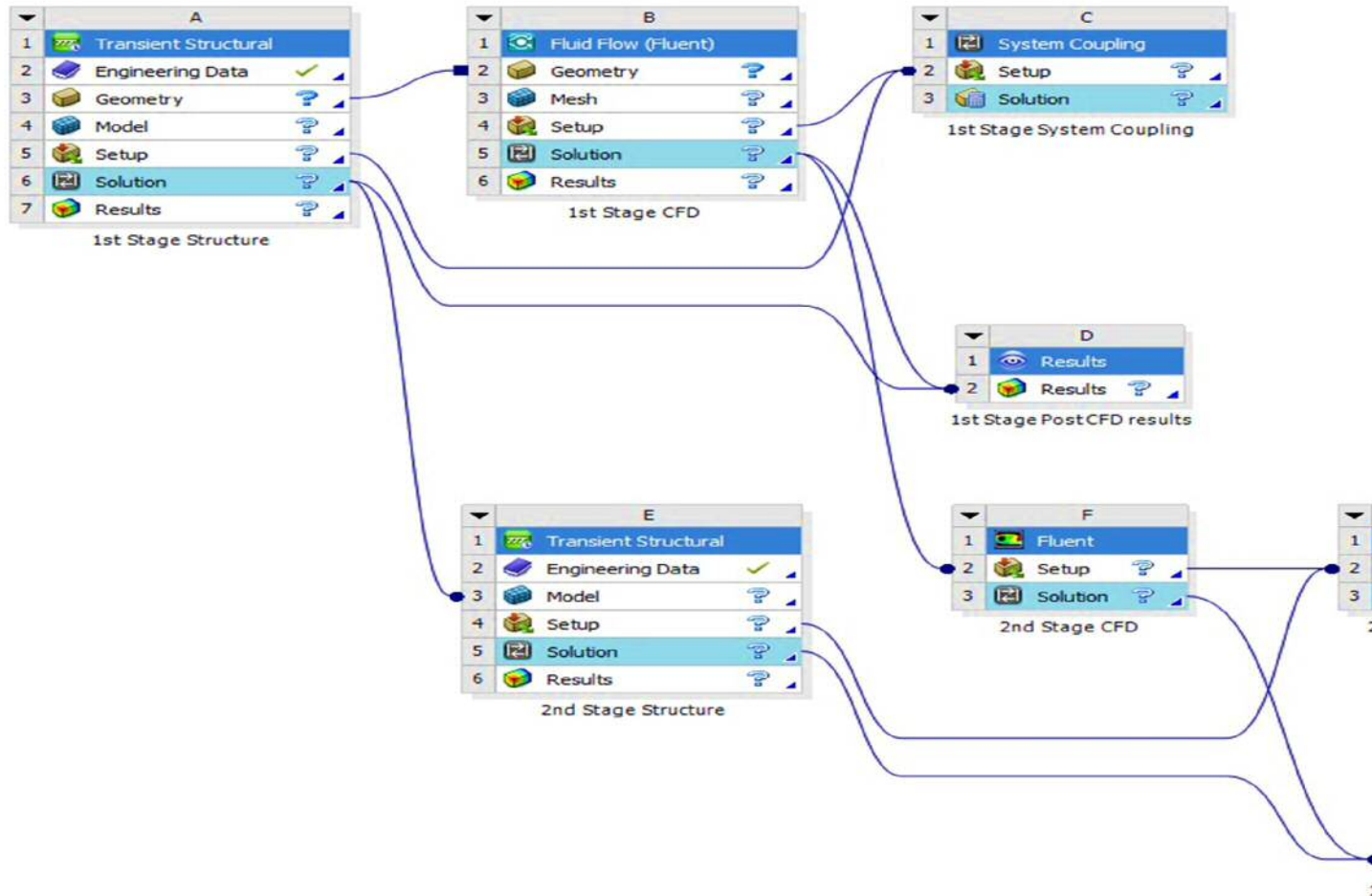


Figure 3-13 Preliminary model project schematic for two stages 2-way FSI ANSYS 17.2. 1<sup>st</sup> Stage FSI components include transient structural component and fluid flow component sharing the geometry. The two components setup is shared through the system coupling and the results of both component post-FSI is shared in a common results component. The 2<sup>nd</sup> stage geometry is controlled by the pre-stressed structural geometry and the fluid geometry is controlled by the pre-stressed Fluent model.

The pressure-velocity solution method for hybrid mesh type used the coupled scheme with second order spatial discretisation. Whilst it is computationally expensive, for complex flow alignment with the mesh it is better to use this method to get convergence at later iteration steps. Maximum Fluent iterations was set to four after experimenting with higher number as this reduces the simulation time with enough steps for convergence.

To monitor the progress of the FSI simulation a CFD compatible file was exported for the fluid zone with the required monitoring quantities with two time steps frequency to match the transient structural time steps. To monitor the pressure and velocity convergence in post CFD processing, three surface monitors were created with area weighted average and it was monitored throughout the running time to check the convergence for the boundaries and diagnose simulation issues in each time step. To finalise the checking routine prior to system coupling setting a case check is performed to report any mesh and boundary condition issues.

### ***System Coupling (FSI)***

For the system coupling the end time was set to 0.5 as it is the simulation end time controlled by the mechanical load (Figure 3-13). The step size was set to 0.025 and it controls the Fluent time stepping with 1 minimum iteration and 5 maximum iterations. Two data transfer were generated to control the exchange of forces and displacements between the structural and fluid regions. The transferring surfaces were already set in mechanical and Fluent packages and are selected accordingly to represent the interfacing surfaces with 1 under relaxation factor and 0.01 convergence target. To monitor the mapping of the interfacing surfaces in post CFD an export file was generated and to get results in each 2 time steps intermediate restart data output was selected with 2 step interval. This frequency was selected to match the results step number between the mechanical and CFD and synchronise the data in post-processing.

#### **3.2.4. Release (Filling) Stage FSI**

In this stage the model will undergo relaxation after being compressed in the previous stage to study the flow entering the model instead of out. In this stage there are number of limitations regarding the meshing and boundary conditions as it is a pre-stressed model which will be explained in details. The geometry is imported from the pre-stressed model solutions in the mechanical and the CFD separately and this differ from the first stage where the geometry was shared between the two parts. This will cause some incompatibility of mesh between the two contacting interface surfaces. The connection between the two stages are illustrated in

Figure 3-13 and this will show the limitation of re-meshing the fluid part as the meshing part of Fluent is already eliminated in the schematic connection. Although it appears as if the model can be meshed in mechanical according to Figure 3-13, this is not the case when working to set the second stage in mechanical where the mesh option in the outline tree is suppressed limiting the modification of the pre-stressed geometry. The analysis setting though can be modified according to the required setting for this stage regarding time stepping which was set to 1 second end time and five sub steps. As in the first stage the auto time stepping is deactivated with large deflection switched on as the model is working with the same material. As per the first stage edge bonded connection between the sphere and the inlet and outlet was set to prevent disconnecting during the simulation later. The fluid solid interfacing surfaces were selected and two remote displacement in the Y direction were created for the upper and lower surfaces of the sphere of 0.5 and 0 mm respectively reducing the loading area to minimise the computational cost. To reduce the amount of nodes involved in the loading the pinball region was reduced to 7mm for both displacements. To check the accuracy of the setting the mechanical model was solved separately then the generated data were cleared before the coupling simulation for creating the restart point.

For the CFD part the simulation is controlled by serial computational core where the flow model, material and cell zones are imported from the first stage while the boundary conditions are changed according to the loading setting. In this stage the outlet was considered a no slip moving wall relative to adjacent cell zone. The inlet was considered as an absolute pressure-inlet with the wall deforming as the coupling interface surface. Dynamic mesh settings were set similar to the first stage changing the zone scale to each boundary accordingly. The solution method and control were similar to the first stage with hybrid initialization. The time stepping was set to 0.05 although it will be controlled by the system coupling later with 5 maximum iterations. To monitor the resulted data along with the simulation progress throughout the running model three surface monitors were created with area weighted average for the required variables convergence and a CFD compatible data export file for the fluid zone was created for the required quantity data to be ready after the simulation ends for post-CFD processing. Checking the mesh quality and the boundary conditions is as crucial as the first part to identify the incompatible surfaces and the quality of the selected dynamic mesh parameters. After saving the project the system coupling is automatically updated with the mechanical and CFD settings.

The system coupling end time was set to 1 s with 0.05 time stepping limiting the iteration between 1 and 5. Just like the first stage two data transfer was generated with the fluid solid interface surfaces in mechanical and the wall deforming in Fluent as the loading transferring

regions sending forces and displacement through these surfaces under 1 relaxation factor and 0.01 RMS convergence target. Other settings were the same as the first stage and the simulation starts with updating the solution cell in the system coupling.

### **3.3. Computational model validation**

In order to validate the FSI simulation, a physical model was designed and investigated. The geometry and mechanical behaviour of the computational model was replicated using the Polyjet additive manufacturing process, enabling the fluid flow of the experimental and analytical models to be compared. This section will illustrate the validation rig design and setting (Figure 3-14). All the material testing along with the validation rig were designed and conducted in Cardiff University School of Engineering laboratories.

#### **3.3.1. Validation Rig Design**

The Arduino software provide a tool to monitor the flow and the associated data required for the validation including the velocity. The data was harvested using a Microsoft Excel macro (PLX-DAQ), which allows the transfer of data from the Arduino software to an MS Excel sheet with added code to the original Arduino code to be compatible to the macro. The PLX-DAQ macro allowed the flow rate and velocity to be displayed during the experiment and as the computational compression was set in 0.5 s the Arduino code was modified accordingly to give results at each 0.1 s. The code included the conversion between the flow rate and the velocity in both boundary conditions according to the continuity equation as seen in Appendix (C).

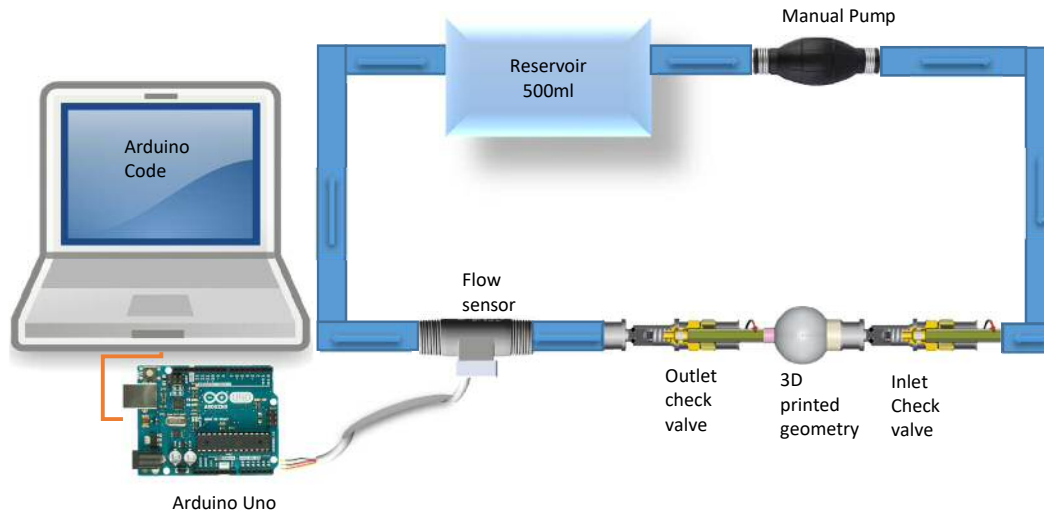


*Figure 3-14 Block diagram of the computational model validation rig setup. The 3D printed geometry is connected to two one-way check valves. The flow sensor is connected to the outlet check valve and controlled by an Arduino coded program with the result display on a PLX-DAQ excel macro on a connected PC*

Although the computational model was designed to simulate one compression, the experimental work was set to 15 compressions to predict the complete simulation and provide future work data. The experimental setup required a greater period of time to produce stabilised results, unlike the computational model (Figure 3-15). The flow sensor was connected to a reservoir which is then connected to a manual pump to initiate the flow between compressions and to initiate the flow in the sphere filling it up before the first compression. All the connections were made by a flexible rubber tubes and a series of plastic pipe adaptors with different diameters' sizes to be compatible with the different rubber pipes. The inlet and outlet were sealed using Teflon sealing tape to avoid leakage through the experiment. The compression was applied to the sphere with a compression machine to make sure it uses the same displacement and speed as the computational model.

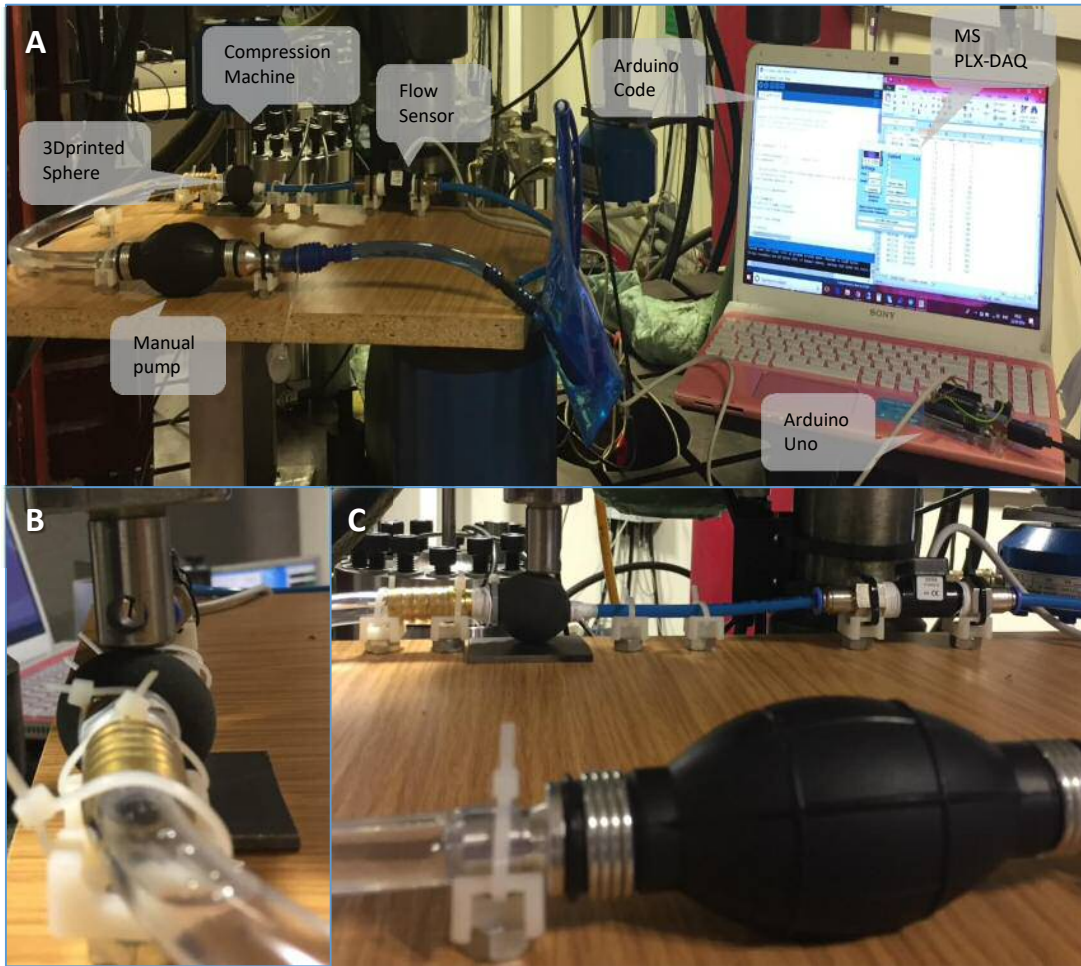


Figure 3-15 Experimental setting of the computational model validation. (A) The experimental setting. (B) The alignment of the preliminary model and the tubing along with the flow sensor. (C) Secured manual pump with the compression machine and the flow sensor.

### 3.3.2. 3D Printed Geometry Design

The sphere was printed in Tango+Black of 30 Shore A hardness and 1mm thickness (Appendix F). As described in section (3.2.1), the materials were chosen as hyperelastic material with calculated shore hardness according to the heart tissue material representation by (Yang et al., 2006) and conversion technique by (Kunz and Studer, 2006). The shore hardness was approximated to the available 3D printed materials listed in Appendix E. The inlet and outlet were printed as a 70 shore A hardness material to be attached to the 1-way check valves. The check valves were set to a 0.01 and 0.016 MPa for the inlet and outlet respectively. A flow sensor was attached after the outlet check valve to measure the fluid flow



generated by manually compressing the sphere Figure 3-16. The geometry was designed using Solidworks software and the files were saved as .stl file type to be sent for 3D printing.

The sphere was attached to two Nickel-Plated brass adjustable non-return valves. The two valves were adjusted to a certain pressure to allow the valve to open to a certain amount of pressure preventing the valves to open at the same time. The outlet valve was then connected to a FT110 turbine flow sensor with 2-30 LPM flow range and 1000PPL frequency Figure 3-14. The flow sensor was controlled by an Aduino-Uno micro controller board with 14 digital input/output pins. The Arduino is connected to a laptop computer with Arduino software to monitor the flow during the experiment and record the data using an Arduino code.

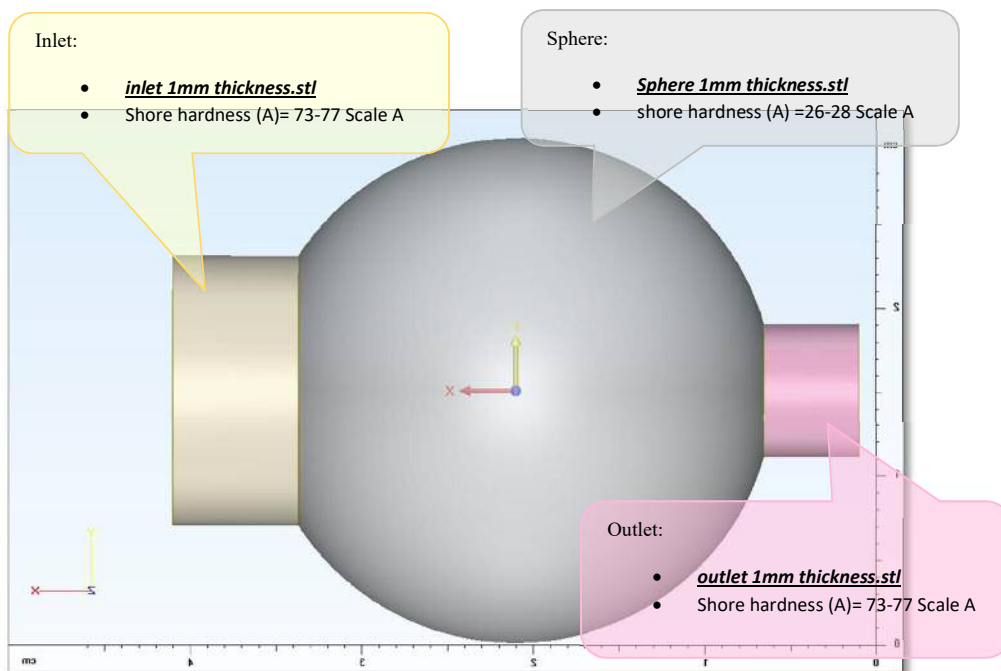


Figure 3-16 Physical model design for 3D printing. The inlet and outlet were 3D printed as 73-77 shore hardness while the sphere was printed in a 27 shore hardness. The geometry was printed in 1 mm thickness.

## 3.4. Subject-Specific Computational Model

### 3.4.1. Model Geometry

To design the subject-specific model a geometry of the left ventricle was required to be imported in ANSYS structural and fluid component. MRI images are widely used for soft tissue

representation in patient specific studies, however, the available MRI infant images were of insufficient quality to successfully segment the heart. The segmentation was performed using MIMICs and 3-Matics software using series of threshold masks to give an approximation to the actual living organs with no significant segmentation for the four chambers nor the main vessels of the heart. Although the MRIs shows greater resolution for the soft tissue but for ethical reasons it was not possible to obtain CT images of human infants without exposing them to a long time CT radiation.

This limitation required CT imaging infant porcine heart to obtain the required geometry of an infant left ventricle to be imported in ANSYS structural and fluid component. The next section will explain the imaging technique, segmentation process, geometry, and meshing procedure used for the heart.

### **3.4.2. Porcine Left Ventricle Computational Workflow**

Processing subject-specific computational modelling consists of the stages represented in Figure 3-17. The simulation workflow is a chain that begins with the segmentation of the anatomical tomographic images after 3D reconstruction. From the segmented data, an initial geometrical model is created and has to be pre-processed. High-quality meshes were then generated for running and in this case two stages of mesh were used in different software for better converging in the simulations. Reliable physical models must be defined in order to determine the system of equations to be solved. Initial and boundary conditions, based on individual and physiological measured data, are required for the solution of the system of partial differential equations. Mathematical models based on appropriate numerical methods need to be defined in order to discretize the system of equations and perform the simulations. Finally, proper representation and evaluation of the results is necessary to visualize, analyse and quantify the parameters of interest.

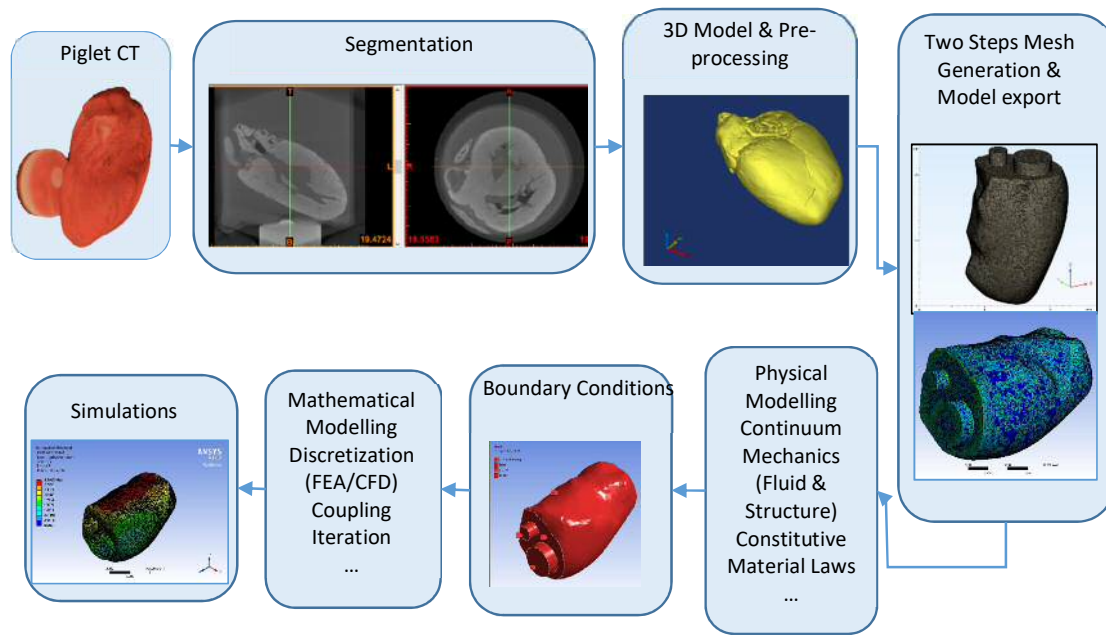


Figure 3-17 Subject-specific simulation workflow of the left ventricle implemented in this work starting from scanning the porcine heart to the final simulation results

### 3.4.3. Porcine Heart CT Scanning

A 3D model of the left ventricle geometry was built using Materialise software Mimics 20 and micro-CT images of one-day-old neonatal porcine hearts. The porcine heart was obtained from a farm in Wales, from a fully developed piglet most likely to have died from hypoxia either during or immediately after birth. The piglet's heart was collected within hours of its death and transported to Swansea University College of Engineering stored in ice-cooled boxes at 4°C. Micro-CT contrast enhancement is dependent on the use of contrast agents, optimised for concentration, incubation time and specimen size. The heart was immersed in a PBFS for fixation with limited tissue shrinkage and the phosphate buffered formal saline (PBFS) solution was changed as necessary to avoid acidic conditions. The recommended fixation period is for at least 48 hours (Stephenson et al., 2012) and for this specimen the heart was in the fixative solution for a month for the fixative solution penetrating the whole tissue layers. After that, the heart was rinsed to remove excess fixation solution and prepare it for dehydration process. The heart was then immersed into different concentrations of the dehydration solution Table 3-2.

Table 3-2 Dehydration solution concentration

Ethanol concentration (%)	Ethanol solution (ml)	Saline (ml)	Time (pm)
50	40	40	12
75	60	20	1
87.5	70	10	2
93.75	75	5	3
100	80	0	4

The heart was then placed in 100% ethanol solution three weeks (Figure 3-18). The long period of fixation and dehydration prevents shrinkage of the tissue and preserves it during the staining process. For the staining of the tissue the heart was immersed in the 10% iodine stain. The recommended iodine concentration is  $\geq 7.5\%$ . The heart size requires leaving the tissue in the stain for more than four days to allow penetration into the deep tissue layers. Before scanning the heart, it was rinsed with ethanol to remove excess stain. The heart was then placed in a plastic container filled with ethanol fluid for resolution purposes and to avoid dehydration during the scanning procedure. The first scanning showed that the iodine stain did not penetrate the whole thickness of the tissue so the specimen was left in the stain for an additional 3 weeks.

The whole heart was imaged using a lab-based Zeiss Xradia 520 (Carl Zeiss XRM, Pleasanton, CA, USA)(AG, 2018) X-ray Microscope, using a CCD detector system with scintillator-coupled visible light optics, and tungsten transmission target.



Figure 3-18 Porcine heart preparation process. (A) The fluids used for fixating and staining. (B) Porcine heart fixating container. (C) Porcine heart size comparison showing good tissue structure and low shrinkage.

An X-ray tube voltage of 100 kV, power of 9 W, and a tube current of 90  $\mu$ A were used, with an exposure of 1000 ms, and a total of 3201 projections. An objective lens giving an optical magnification of 0.4X was selected with binning set to 2, producing an isotropic voxel (3-D pixel) size of 30.346  $\mu$ m. The tomograms were reconstructed from 2-D projections using a Zeiss commercial software package (XMReconstructor, Carl Zeiss), a cone-beam reconstruction algorithm based on filtered back-projection.

### 3.4.4. Image Reconstruction and Initial Meshing

XMReconstructor was also used to produce 2D grey scale slices and DICOM files for subsequent analysis. The major components of the piglet heart were observed in such a way that the normal anatomical relationships are preserved in the micro-CT images. The images represent as nearly as possible the geometry that pertains for a still heart.

Image analysis enables segmentation of the left ventricle and its major openings, as a single dataset. MIMICS (Materialise, Leuven, Belgium) is a software tool for visualizing and segmenting medical images (such as CT and MRI) and rendering 3D objects using a combination of manual demarcation, image thresholding, and level-set segmentation. To perform the segmentation a set of thresholds were used to create a 3D heart tissue image that can be processed later (Figure 3-19). To extract the left ventricle, threshold masks were edited in each slide of the imported DICOM images for three planes. The part was then smoothed with 0.7 smoothing factor and wrapped with 0.5mm closing distance. The left ventricle was then exported to 3-Matics 12 (Materialise, Leuven, Belgium) for meshing and preparing the model to be exported to ANSYS.

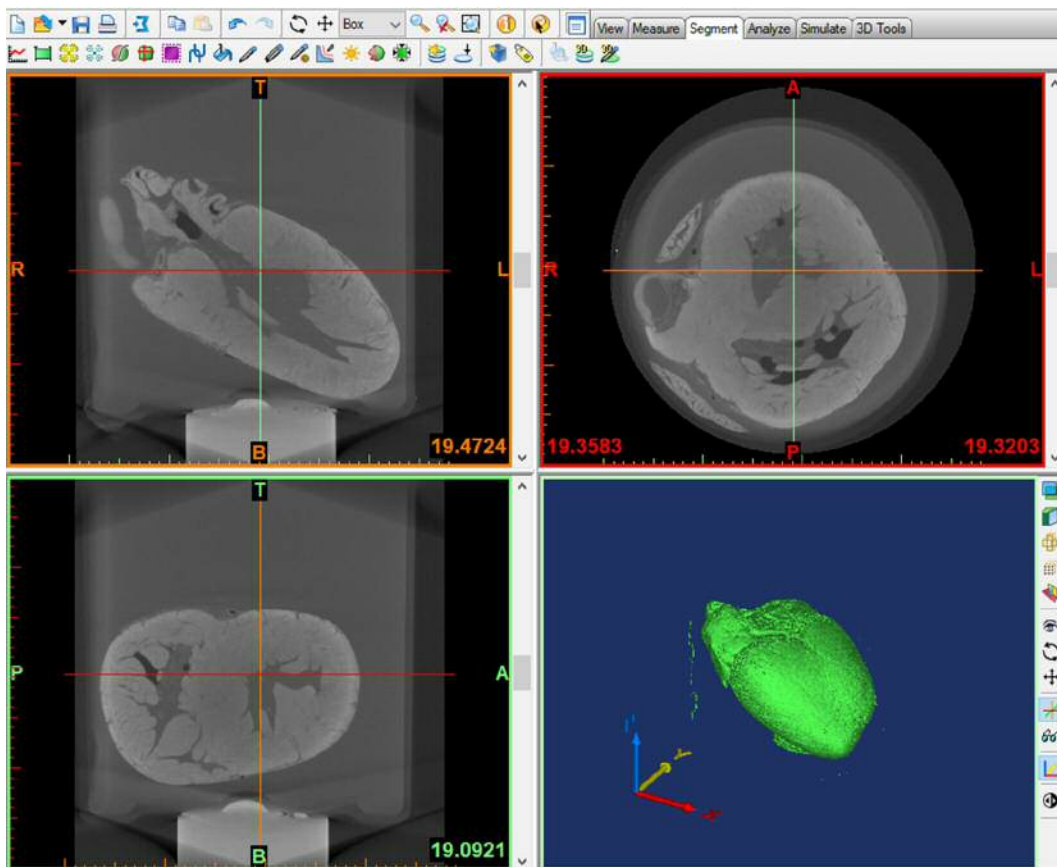
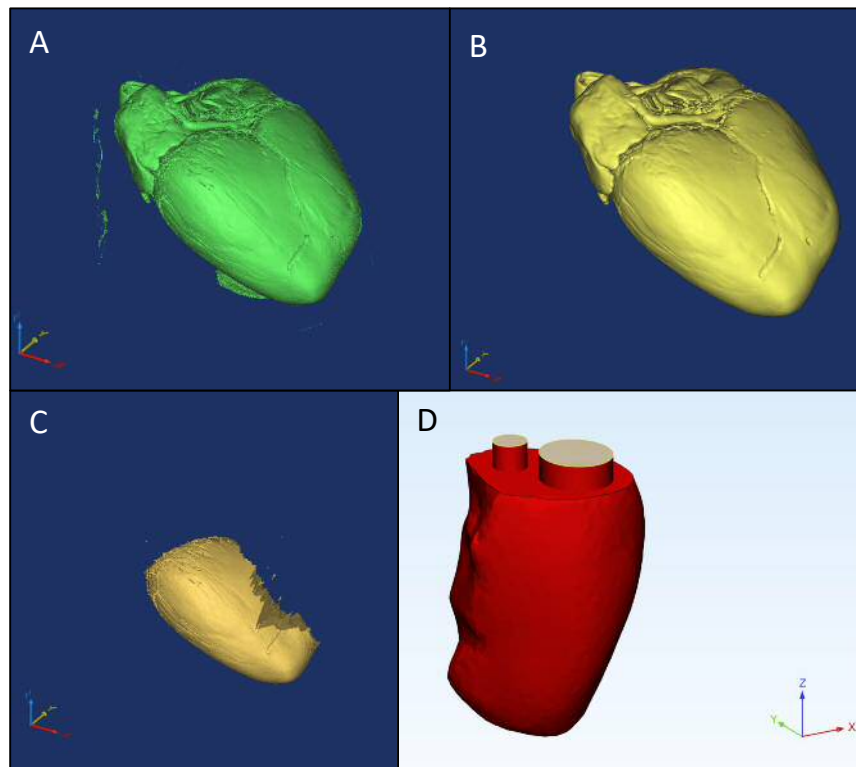


Figure 3-19 3D representation of the DICOM images in MIMICS20 with thresholding mask to extract the surrounding parts. The images in the top right view represent the axial images (XY-view or Top-view) and are surrounded by a red border. The upper left view (surrounded by an orange border) shows the coronal images that are the images resliced in the XZ-direction (Front-view). The lower left view (surrounded by a green border) shows the sagittal images that are the images resliced in the YZ-direction (Side-view). The lower right view (surrounded by a light-green border) shows the 3D view.

This software combines CAD tools with pre-processing capabilities working on triangulated (STL) files which makes it suitable for freeform 3D data. To represent the inlet and outlet to the left ventricle, two openings were designed in 3-Matics (Espa et al., 2012). The model was then smoothed and wrapped again for better surface representation and to achieve enhanced mesh quality.

Figure 3-20 shows the generation and pre-processing of the segmented geometrical model. The concatenation of all 2D slices into one dataset and the triangulation of the set of points representing the image file as well as thresholding is shown in (A). The smoothing and wrapping filter effects are illustrated in (B) and show a clear improvement of the surface quality. The clipped surface and volume of the left ventricle is shown in (C) and the smoothed, wrapped and added boundary conditions, which allows the blood to flow in normal direction to the inlet and out of the outlet faces, is shown in (D).



*Figure 3-20 3D model generation and pre-processing steps using Mimics and 3-Matics software. Each image represent a step in the segmentation process. (A), (B) and (C) have been segmented in MIMICS while image (D) is segmented in 3-Matics. (A) The 3D representation after applying the threshold mask, (B) 3D representation after smoothing and wrapping, (C) 3D representation of the left ventricle segmentation from the whole heart. (D) The left ventricle segmentation and applying the inlet and outlet boundary conditions in 3-Matics.*

The surface of the part was separated to be copied to a new part representing the solid wall of the model with shell elements while the volume was set as the fluid part of the model. A surface and volume mesh was performed with 0.5 and tet 4 .5 maximum edge length respectively Figure 3-21. The surface wall triangles was then flipped to invert the shell surface active connection side. This step is crucial as to represent the contacting faces in ANSYS when setting the FSI surface load. The fluid volume was exported to ANSYS as a mesh file while the solid shell was exported as an Iges file. Those parts will be meshed again in ANSYS to be compatible with the simulation loads so those meshing criteria and settings are for exporting reasons.

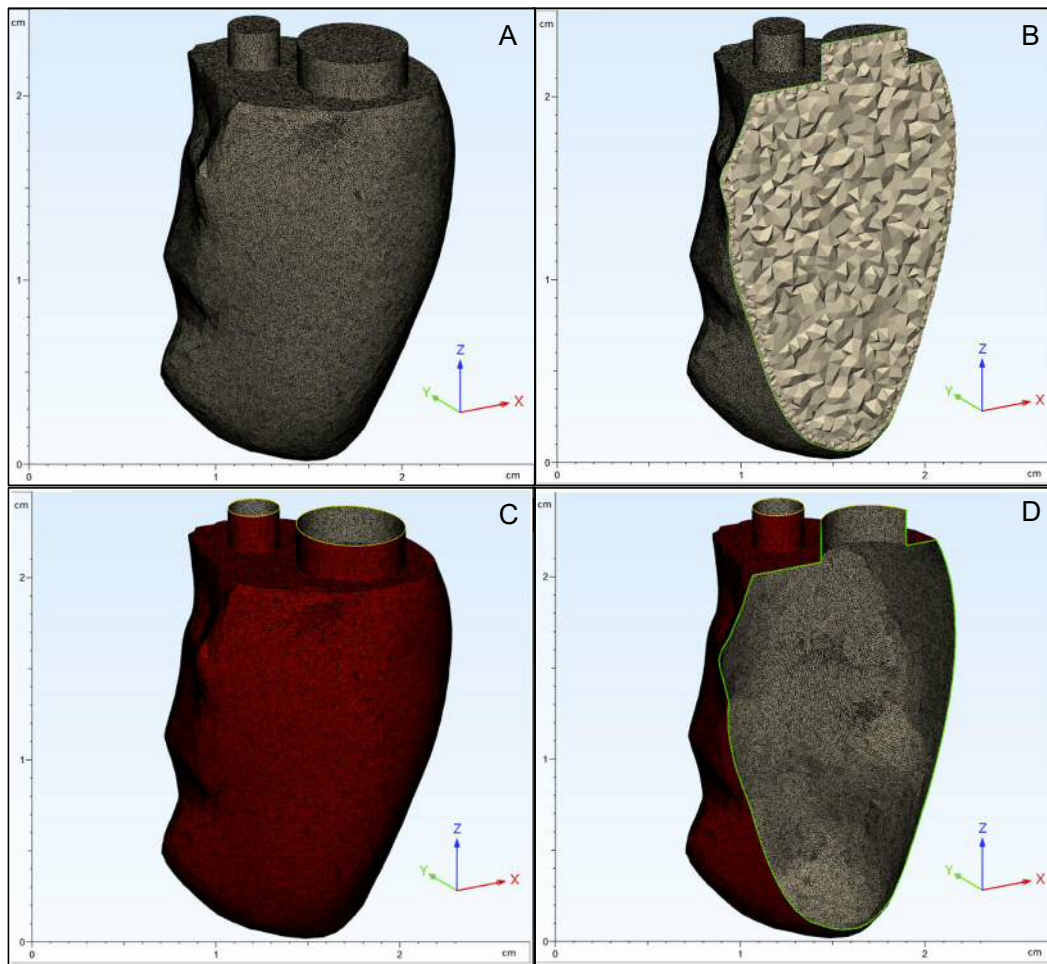


Figure 3-21 Left ventricle meshing in 3-Matics representing the fluid volume and the solid shell surface (A) volume mesh, (B) volume mesh in Y section, (C) solid wall surface mesh, (D) solid wall surface mesh in Y section



### 3.4.5. Mechanical Simulation Process

This section will list the parameters for processing the solid and fluid parts of the FSI computational model and the system coupling components in ANSYS software. The same procedure took place in the preliminary model except some parameters that needed to be changed according to the related left ventricle geometry and tissue representation material used in the model. Those parameters and settings were chosen according to mechanical behaviour of the model as well as factors influencing the stability of the model and reducing the computational cost of the simulation.

In ANSYS the fluid file is imported in FE element modeller as a mesh file and then it is linked with an external mesh component to be meshed with high quality that is compatible with ANSYS simulation criteria. The LV was meshed using 100% relevance CFD physics preference with medium span angle centre. Total thickness inflation was used with 0.3 mm element size. Boundary conditions named selection was generated according to the Fluent processing requirements. This was then linked to Fluent setup while the surface solid shell was imported directly in the Transient structural geometry as an Iges file. This means that instead of sharing geometry as in the preliminary model, the geometry was separated but share the same coordinates and spatial position to ensure compatible contact between the coupling surfaces (Table 3-3).

Second stage of the FSI was following the same procedure as the preliminary method and the modifications made was according to the modification made in the following sections (Figure 3-25). The placement of the compression plates are illustrated in Figure 3-22 where the upper plate represents the moving comprssion and the lower plate represents the fixed supporting plate. The orientation of the geometry was chosen to simulate the anatomical orientation of the left ventricle.

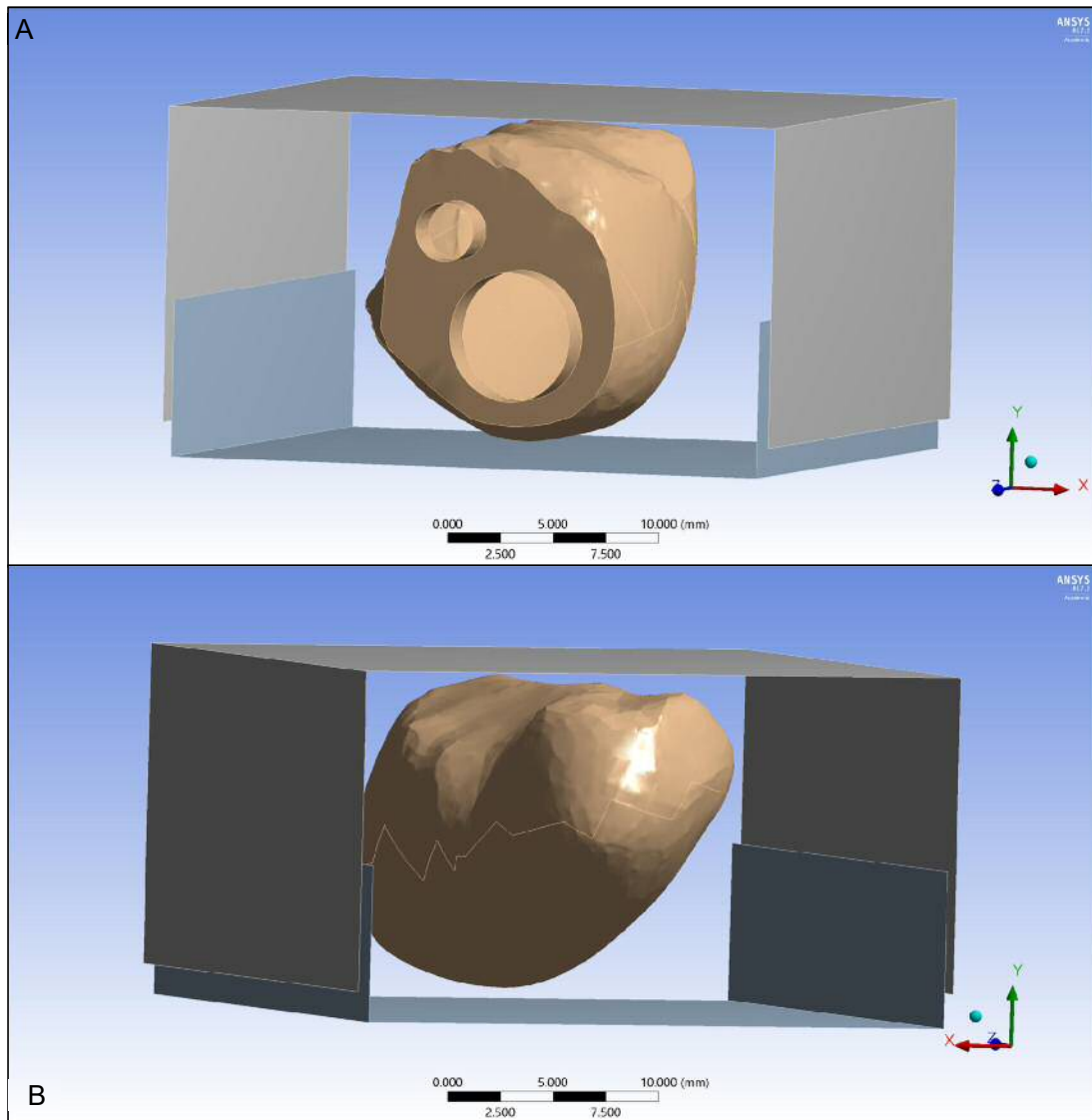


Figure 3-22 Subject-Specific Geometry. (A) representing the 3 dimensional view of the LV and the compression plates, (B) represents the -XY orientation of the geometry

Table 3-3 Left ventricle subject-specific model geometry information

Object Name	Compression	Support	Shell	Fluid 1
<b>Bounding Box</b>				
Length X	30. mm	29. mm	14.873 mm	14.888 mm
Length Y	15.146 mm	7.4348 mm	14.68 mm	14.696 mm
Length Z	30. mm		25.043 mm	25.08 mm
<b>Properties</b>				
Volume	1803.4 mm <sup>3</sup>	1315.3 mm <sup>3</sup>	760.64 mm <sup>3</sup>	2796.2 mm <sup>3</sup>
Mass	1.4157e-002 kg	1.0325e-002 kg	8.3694e-004 kg	
Centroid X	21.097 mm	20.983 mm	21.024 mm	21.098 mm
Centroid Y	21.298 mm	9.7354 mm	17.341 mm	17.179 mm
Centroid Z	15. mm		16.54 mm	16.591 mm
Moment of Inertia Ip1	1.3964 kg·mm <sup>2</sup>	0.82225 kg·mm <sup>2</sup>	5.9768e-002 kg·mm <sup>2</sup>	
Moment of Inertia Ip2	3.1874 kg·mm <sup>2</sup>	1.9879 kg·mm <sup>2</sup>	5.7063e-002 kg·mm <sup>2</sup>	
Moment of Inertia Ip3	2.4602 kg·mm <sup>2</sup>	1.2614 kg·mm <sup>2</sup>	3.0796e-002 kg·mm <sup>2</sup>	
Surface Area(approx.)	1803.4 mm <sup>2</sup>	1315.3 mm <sup>2</sup>	1086.6 mm <sup>2</sup>	
<b>Statistics</b>				
Nodes	1892	1365	13588	1115541
Elements	1801	1291	27081	709582

### **Transient Structural Settings**

For the structural region the contact between the two compressing plate was considered as an asymmetrical frictionless behaviour. The contacting surfaces were chosen according to the virtual topology added to the shell surface (Figure 3-23). This is due to the importing process used for the shell and fluid parts from 3-Matics. Frictional connection was used for the compressing plates with the LV surface. The surfaces was used for minimal area for the upper and lower sphere with adjusting to touch interface treatment to minimise the penetration and gap between the contacting surfaces. The moving compressing plates were setup with remote displacement degree of freedom with the lower plate to be static. The upper plate was designed to move down to a third of the diameter of the geometry displacement in the Y direction and the fluid solid interface load was set to the entire inner surface of the solid region consisting of one topological surface. As the material is hyperelastic and considered rubber-like material, the large deflection was turned on with one step recommended by the ANSYS FSI settings. The sub-stepping used in the preliminary model was removed and 1 sub-step

was used following the ANSYS FSI recommendation setting. Before setting up the CFD/Fluent solving the structural part the mechanical aspect of the FSI was running with no computational errors or warnings.

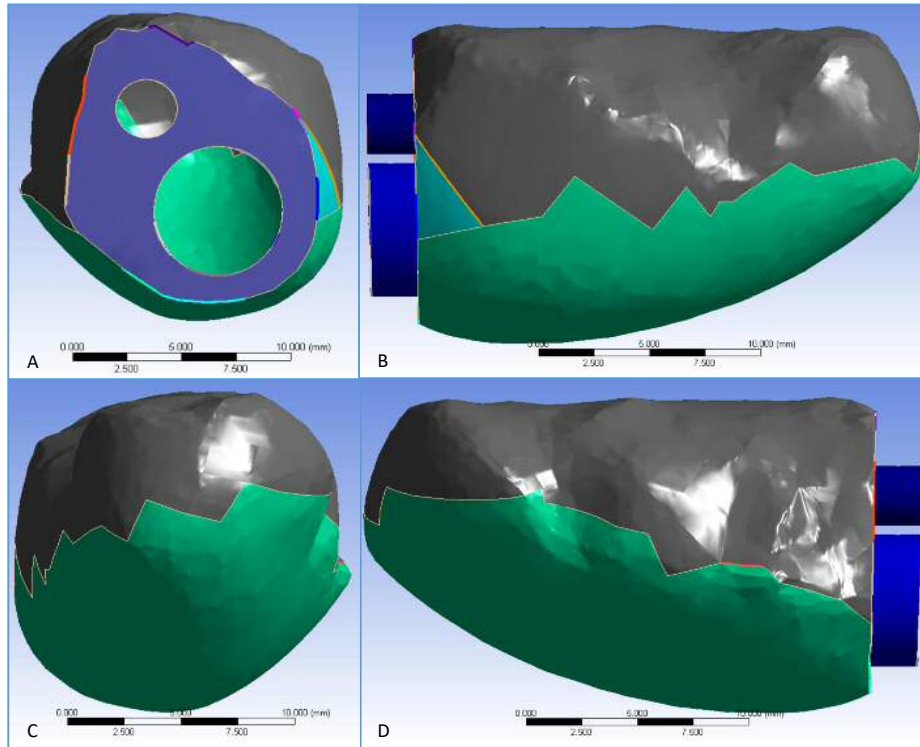


Figure 3-23 Left Ventricle virtual topology surfaces. (A) +Z view, (B) +X view, (C) -Z view, (D) -X view

### Fluent CFD Setting

For the CFD part of the simulation the setting is characterised and examined in the ANSYS Fluent package completely separated from the mechanical setting. After updating the fluid mesh, Fluent setup is launched with parallel processing using 6 cores of 8 for CFD transient simulation and 2 for mechanical and pressure based solver. Laminar flow was assumed (Dahl, 2012). Meshing the fluid zone was done separately from the Fluent analysis system and this is due to the imported file type compatibility with finite element modeller and it cannot be imported directly to Fluent (Figure 3-24) with tetrahedrons meshing elements (Lassilaa et al., 2012).

The same fluid material model was used as the preliminary model. For the first stage of the FSI the inlet was considered as a no slip moving wall while the outlet was considered as an outflow opening. For the dynamic mesh, smoothing along with re-meshing was used. For

smoothing 0.45 Poisson's ratio with linear elastic solid method was applied as the FSI interface is adjacent to an unconstrained outlet and the outlet is a moving boundary. Blood, inlet and outlet boundary conditions were considered as deforming zones and to define the coupling interface surface, the wall surface dynamic mesh was controlled by the system coupling zone. The model is already considered unstable for using incompressible fluid so stabilizing the interfacing surface was important using volume-based method with 800 scale stabilizing factor. This factors was used based on parameter optimisation method to stabilise the area weighted average of velocity and pressure in the surface monitoring during the simulation. To get the best convergence required for the simulation, the convergence behaviour was monitored and the curve shape was observed. Once the curve showed good quality convergence behaviour the stabilisation factor was set according to that.

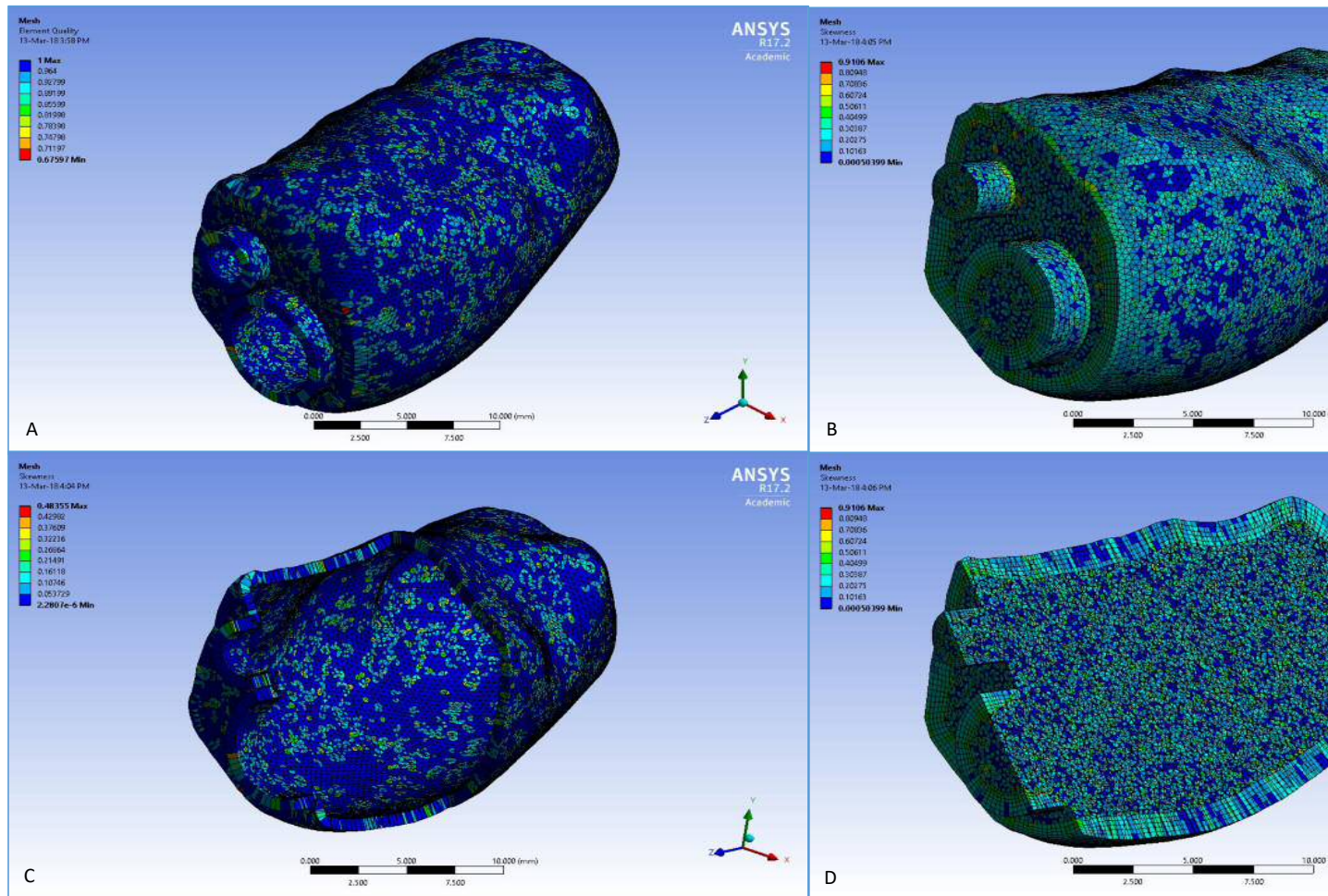


Figure 3-24 Model mesh skewness in ANSYS, (A) Structural mesh with shell solid of 1mm thickness, (B) Structural mesh with parts colour showing 0.3 mm element size, (C) Fluid mesh with 0.3 mm element size, (D) Fluid region mesh with a section plane normal to the inlet and outlet

### ***System Coupling Setting***

For the system coupling the end time was set to 0.5 as it is the simulation end time controlled by the mechanical load (Figure 3-25). The step size was set to 0.005 and it controls the fluent time stepping with 1 minimum iteration and 5 maximum iterations. Two data transfer were generated to control the exchange of forces and displacements between the structural and fluid regions. The transferring surfaces were already set in mechanical and fluent packages and are selected accordingly to represent the interfacing surfaces with 1 under relaxation factor and 0.01 convergence target. To monitor the mapping of the interfacing surfaces in post-CFD, an export file was generated and to get results in each 2 time steps intermediate restart data output was selected with 2 step interval. This frequency was selected to match the results step number between the mechanical and CFD, and synchronise the data in post-processing. This process was the same process used in the preliminary model although results component system was added after the simulation to import the CFD post compatible file. This file shows the additional selected monitors and variables chosen in Fluent prior to the simulation. Also, scene animation was chosen as a sequence with contours and vectors for the pressure, wall shear, viscosity and velocity to be analysed in Fluent after the simulation finish. This step should be made before the simulation starts as the file will be generated during the running simulation and it will not be possible to display the animation after. Figure 3-25 illustrate the project schematic diagram for the subject-specific model and shows the component system added to the model differently from the preliminary model.

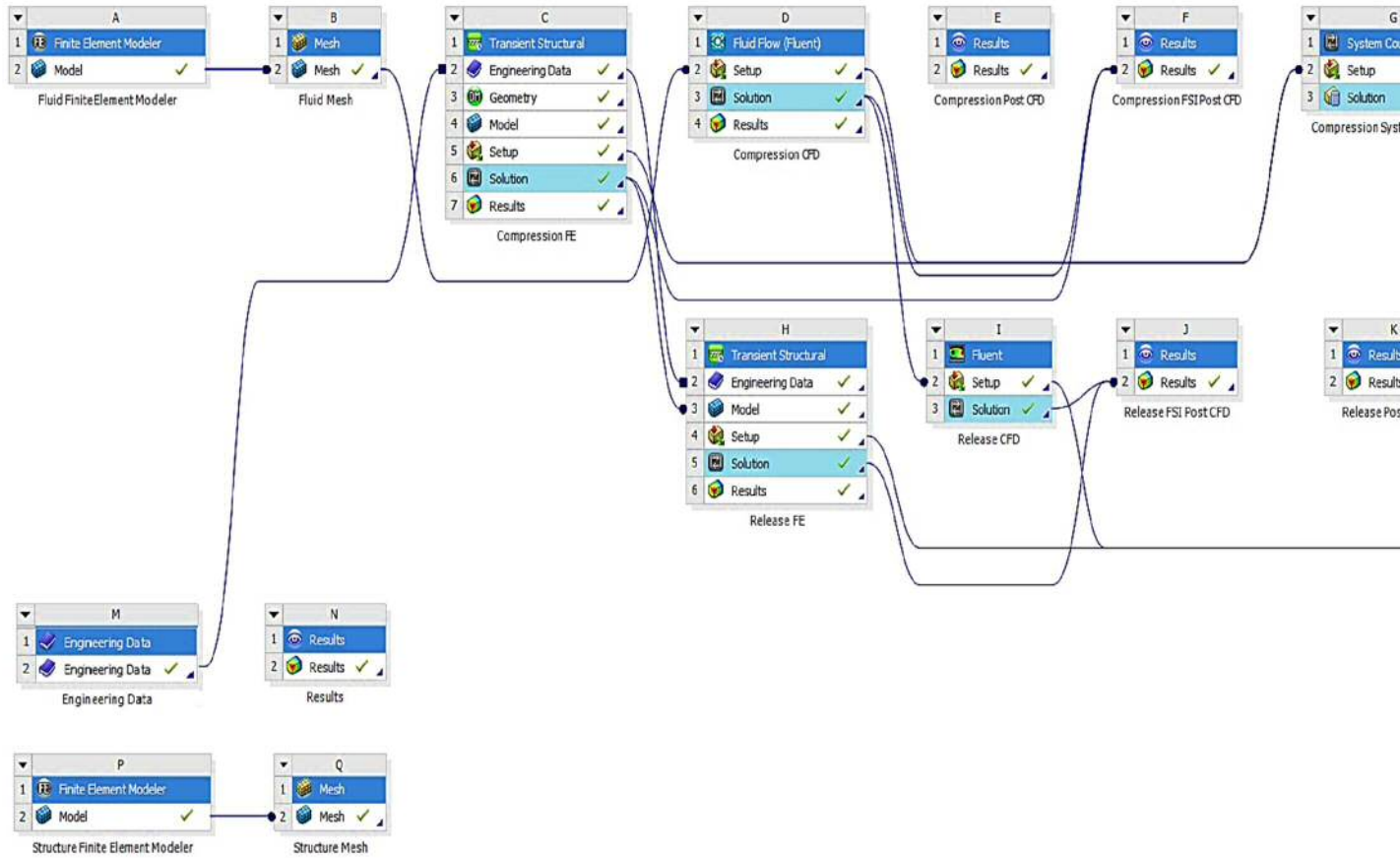


Figure 3-25 Subject- specific ANSYS project schematic diagram. Additional parts are added to accommodate the imported geometry process modeller and mesh. 1<sup>st</sup> Stage FSI components include transient structural component connected to the imported and meshed geometry from the fluid modeller component. The fluid geometry is directly connected to the meshed geometry from the finite element modeller component. The two components are connected to the system coupling and the results of both component post-FSI is shared in a combined results component. The 2<sup>nd</sup> stage geometry is controlled by the transient structural component and the fluid geometry is controlled by the pre-stressed Fluent modified solution. The additional results components are added to import the results of each stage along with the exported post-CFD compatible data from the solved fluid iterations.



## Chapter 4. Results and Discussion

### 4.1. Chapter Overview

This chapter describes the results and provides a discussion of these data. fluid and structural performances of the models are evaluated based on FSI analysis results. The main measure in the fluid domain is specified as blood flow velocity distribution on various 2D planar locations through the geometry. The characteristics of pressure and wall shear stress (WSS) on the interacting surfaces are analysed, as is the structural domain, based on the link of pressure from fluid domain and its effects as metrics of total deformation and equivalent Von-Mises Stress. The following results are included and discussed in this chapter:

#### **Preliminary Model:**

- Material characterisation studies to provide material data to input into the FSI model including computational validation of their corresponding methods
- Preliminary FSI model to evaluate the parameters critical for successful simulation in terms of structural and CFD data with the successful model
- Studies evaluating the mesh sensitivity, time-step, and mapping compatibility

#### **Subject-Specific Model:**

- Porcine CT subject-specific model 2-way FSI during compression and pre-stressed release phase
- Structural data in terms of the stress, strain, and total deformation and their relative discussion
- Blood flow behaviour in terms of velocity, pressure, and viscosity data compared to literature and preliminary computational model

## 4.2. Preliminary Model

### 4.2.1. Material Characterisation Results

A Tango+ Black co-polymer was selected from across a series of material datasheets, based on exhibition of a hyper-elastic response that is broadly comparable to cardiac tissue. Establishing a suitable material early in the study was important, as it provided an opportunity for it to be fully understood and integrated into the more complex FSI modelling that was to follow. This co-polymer was selected both for its behaviour and because it could also be manufactured via Polyjet additive manufacturing, enabling the fabrication of an identical geometry to the FSI simulation, meaning it represented an ideal test route for validation. The mechanical parameters of this co-polymer need first to be characterised via experimental investigation, and then digitised for input into the FSI/ANSYS software. The four mechanical tests are detailed in this section with the corresponding computational model for validation purposes.

#### ***Tensile test***

Uniaxial and planar test cycles were controlled by a short program written in the test machine's scripting language. The mean uniaxial behaviour in the extension data described a non-linear response. Five preconditioning cycles were performed, with both types of testing samples demonstrating consistent behaviour in all conditioning cycles showing linear behaviour in that region. In general, the slopes of the graphs are mostly linear beyond the 40% strain. The maximum elastic modulus – this is the modulus derived from the steep linearised part of the curve – under uniaxial testing was recorded at 0.36 MPa. Cycles conducted at 10 mm/s have stress vs. strain behaviour that loops back on themselves. Slippage did not occur during the test due to the test specimen modification mentioned in section 3.2.2. Tensile data demonstrated the difference between the test samples at the higher strain as can be seen in the recorded standard deviation shown in Figure 4-1 due to the different failing location of the test specimens. However, each of the specimens' failing location was not near the neck of the test sample following the British standards testing process requirements.

British standards for tensile testing recommend a 500 mm/min tension speed; however, the material was tested in a 10 mm/min speed to accommodate the strain rate range of the preliminary computational model. The material showed different stiffness in different strain-rate measurements recording higher stiffness (20% higher at the 80% strain) and tensile

strength at break during a higher strain rate. The test computational validation is discussed in the next section.

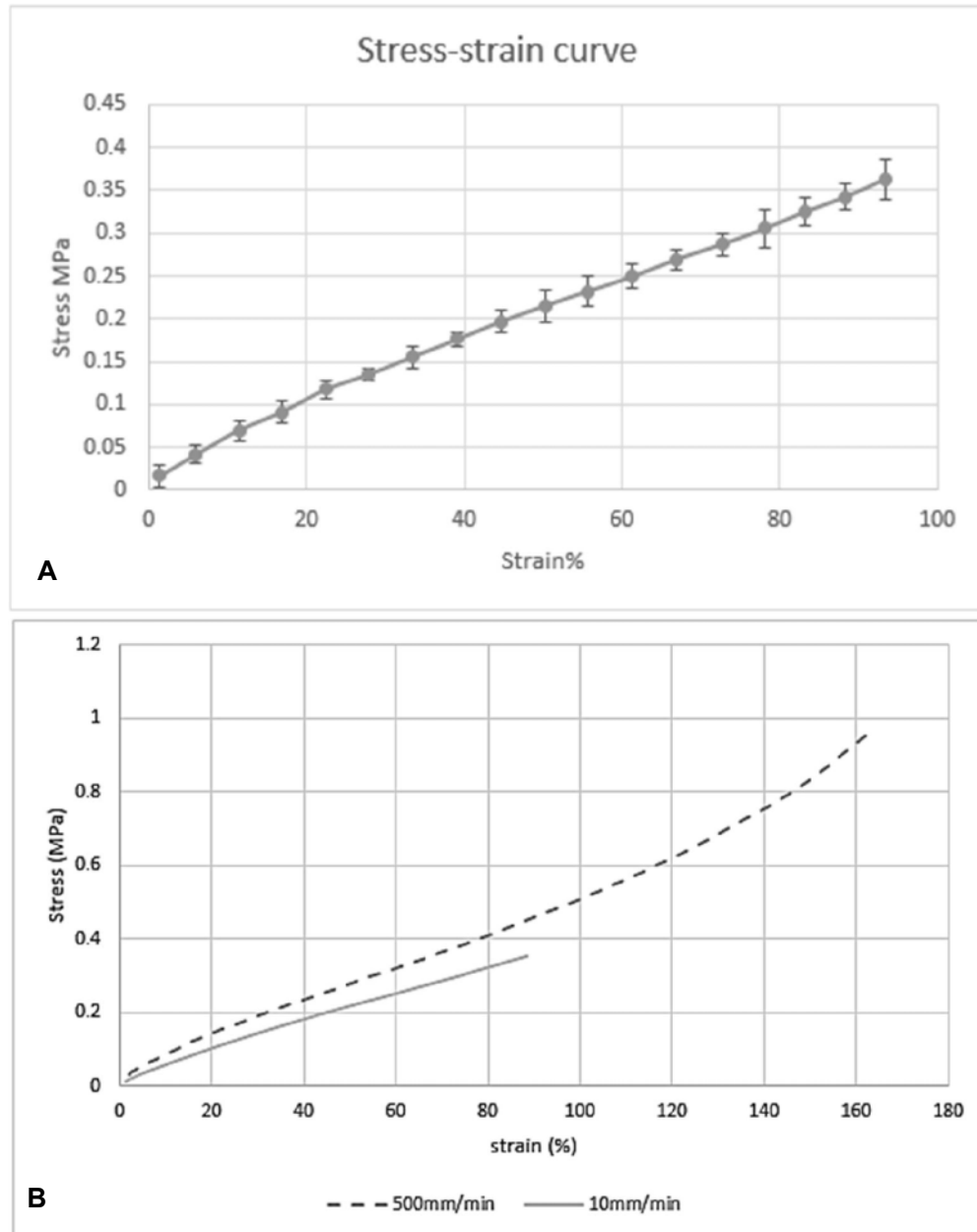


Figure 4-1 Tensile test measured results Stress-strain curve: (A) 10 mm/min speed with standard deviation error bars, (B) 10 and 500 mm/min stress-strain curve; showed different stiffness in different strain rate measurements recording higher stiffness (20% higher at 80% strain) and tensile strength at break during higher strain rate

## Planar Test

Planar shear data was presented for two sets of strain measuring techniques as explained in section 3.2.2. Consistency between the two methods was observed regarding stress and strain behaviour while video-extensometer-measured strains had a higher strain measurement over the test time and showed inconsistency of the recorded strain near failure; hence, data from the DIC measuring technique was used in the model parametric optimisation in MCalibration, as will be explained in Section 4.2.2. The planar shear material behaviour showed non-linear stress-strain behaviour and higher stiffness than the tensile characteristics due to hyperelastic material behaviour with different applied stresses. Through the planar test, different strain gauges along the length of the specimen revealed good consistency of data (Figure 4-2 and Figure 4-3). The different measuring techniques is highlighted in Figure 4-3B.

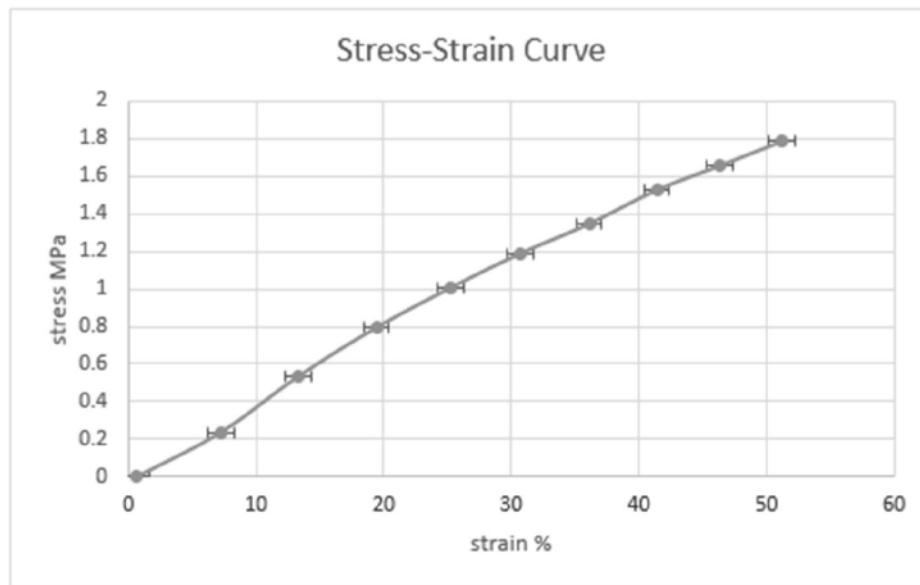


Figure 4-2 Planar shear measured results represented by the stress-strain relation curve

The metal clamps were continuously slipping from the machine grips, and uneven test results were obtained causing stresses on the edge of the test piece (Figure 4-4). This led the test pieces to dislocate from the clamps instead of experiencing strain along the tension axis. To eliminate this issue, the shape of the metal brackets was changed after the first experimental testing. The modified metal brackets were designed to fit the clamps in the Zwick machine.

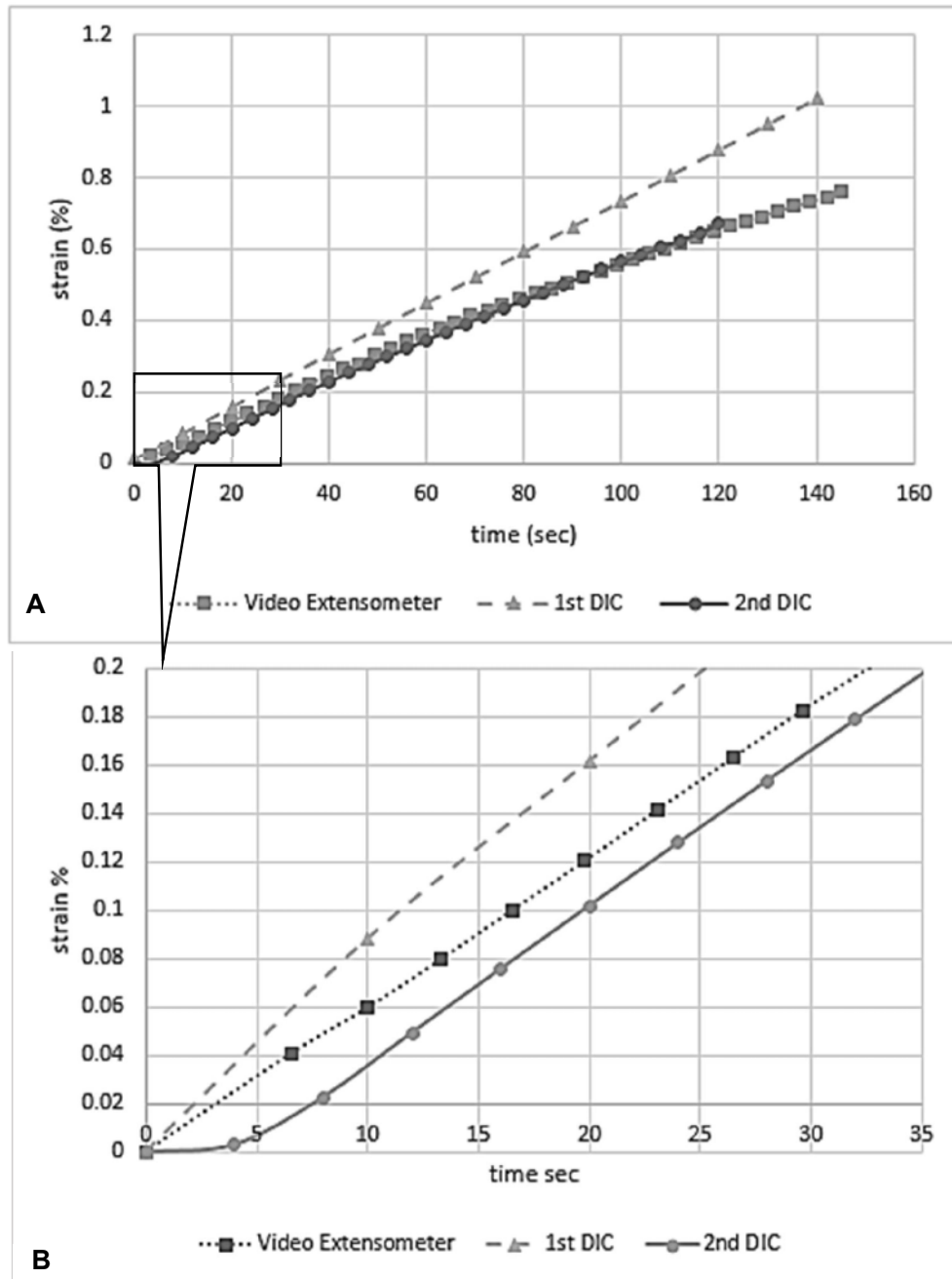


Figure 4-3 Comparison between the different measuring techniques in planar shear test showing higher strain data than the DIC measurements. (A) The experimental strain rate for the planar shear test, (B) an enlarged area of interest for lower strain rate to show the difference between the different measuring techniques.

The new design introduced a hinge shape, which fits the geometry of the machine clamps. Also, a 10x10 mm piece of material was glued on the inner corners of the brackets to ensure

equivalent thickness distribution of the brackets separation during the test. The modified test protocol overcame this problem of clamp slippage.



*Figure 4-4 Failure of the original clamp design due to slipping of the metal plates and the machine clamps. Instead of tearing of the test piece in the horizontal central line, the material failed from the adhering attachment to the brackets showing no alteration to the painted strain gauges.*

### **Equibiaxial Test**

Tango+Black possesses non-linear, anisotropic mechanical responses. The measurement curve is approximately linear for strains larger than 20%. This kind of behaviour can be described by a rubber-like material mode. The four sample biaxial tests showed good repetition data, and the strain from different strains around the centre of the specimen shows that the choice of the strain gauge length has little to no effect on the stress-strain curve. Although there were eight strain gauges of different lengths, they gave very close results (Figure 4-5). The engineering strain and stress data exported to ANSYS was the average of the four tests.

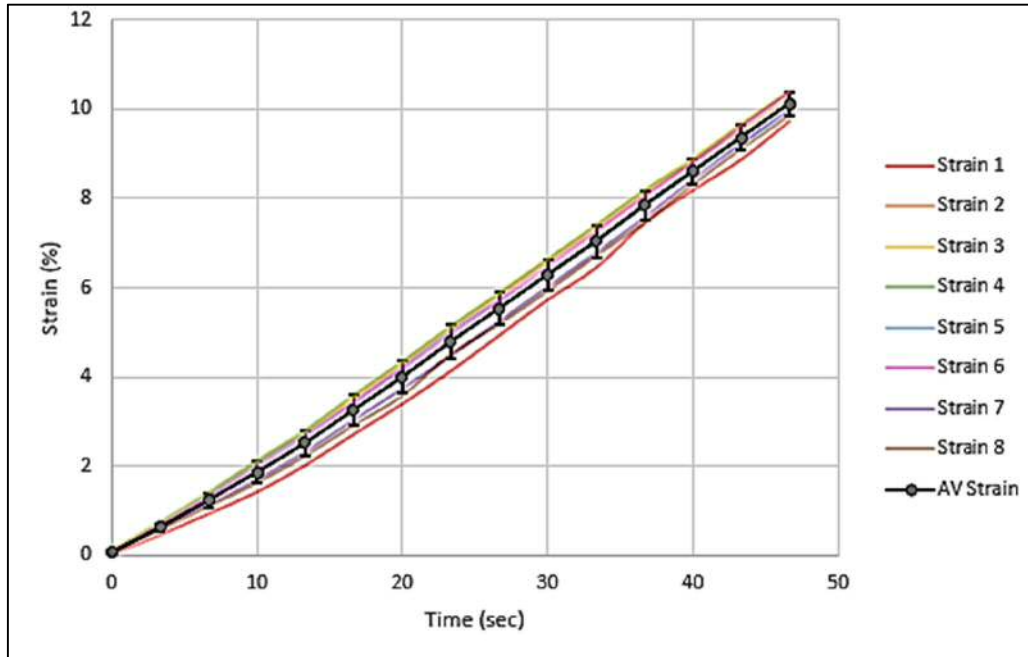


Figure 4-5 Strain rate curve for different strain gauges in the biaxial test. Different strains were recorded at different inner diameter values of the testing specimen and are colour coded in the graph.

Following the sample preparations for the previous tests, the samples were first designed as a 1 mm thickness from a 1 mm Tango+ Black 3D printed sheet, and the test piece was torn at the start of the test from the gripping area. This happened as the samples were cut from a sheet that was not printed in accordance with the designed geometry, which caused areas of stress from the gripping areas. This was also due to the shape of the plastic clamps, as they were designed with a circular protrusion to accommodate stiffer hyperelastic materials (Figure 3-10B). To avoid this happening, matching grooved clamps were used, and thicker test samples were designed and 3D printed with a matte surface finish to avoid slipping. This enhanced the testing technique, as there was no minimum variation between the test samples' data.

#### 4.2.2. Material Model Parametric Optimisation

True stress and strain behaviour of the tensile and planar shear predicted data showed consistent behaviour in strains below 2.5. After this, the experimental data had higher stiffness for a higher strain rate. As per the biaxial and compression data, the stiffness was relatively similar at a strain lower than 1.25. Higher strains showed deviation from the predicted data recording higher stiffness at 2% strain in the biaxial predicted data.

Keeping in mind that there is no universally favourable hyperelastic model, it is desirable to be able to apply the modification with a varying stiffness to any hyperelastic potential model to improve the model for relating strains. This was observed in the different model curve fitting in MCalibration.

For material model calibration, two different pieces of software were used. MCalibration software was used to calibrate the material data providing the option for multiple material models with the option of a parametric study after curve fitting for the resultant material constants. To differentiate between different possible material models, five hyperelastic material models were tested for calibration. Neo-Hookean and 5-term polynomial material models failed in the FSI model while Mooney-Rivlin, Ogden, and Yeoh material models produced closely converged simulation data in the model. The Mooney-Rivlin material model was chosen, as it showed better approximation to the biaxial measured data, as shown in Figure 4-6 and Figure 4-8.



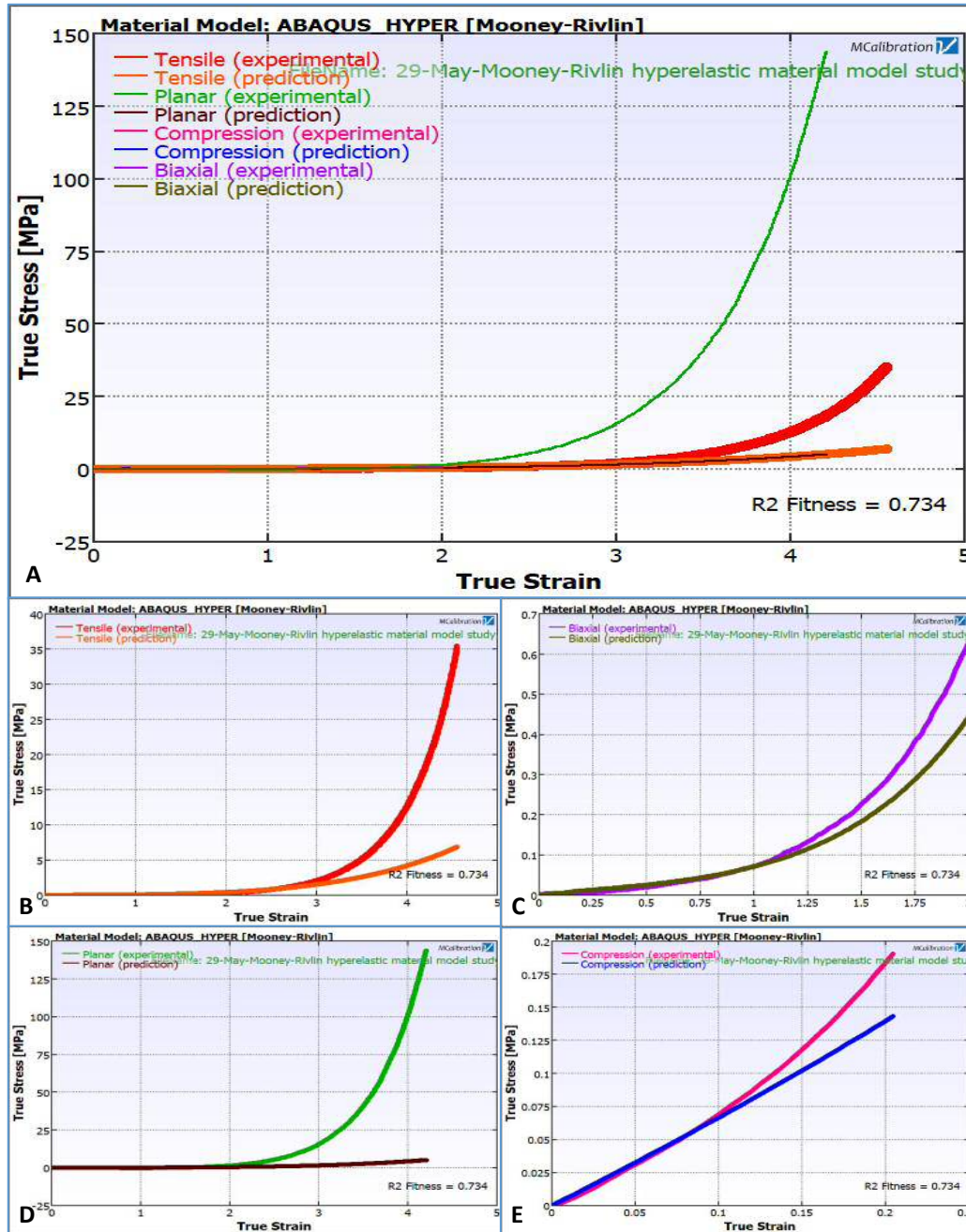


Figure 4-6 True stress-strain comparison between experimental and predicted material testing data in MCalibration curve fitting: (A) Combined testing data for true stresses, (B) Tensile test data, (C) Biaxial test data, (D) Planar shear test data, (E) Compression test data

To examine the stiffness of the material compared to the cardiac tissue, testing of the biaxial data of the experimental and fitted model was performed. The biaxial data showed that the stiffness of the material is lower than the tissue in the very low strain rate. As the strain rate

increases, the material shows higher stiffness; the material will tolerate a high strain rate while the tissue will fail above a 0.1 strain rate. It is important to mention that the material testing strain rate was 10 mm/min while the tissue testing was under 0.5 mm/min (Ahmad et al., Unpublished). This may cause the difference in the behaviour, as it can be noted that the material behaves differently in different strain rates, as explained in the previous section. Moreover, the preliminary model compression strain rate lies within the low strain range of the material profile - hence the use of a low strain rate in the testing methods. The material and tissue comparison graphs are shown in Figure 4-7.

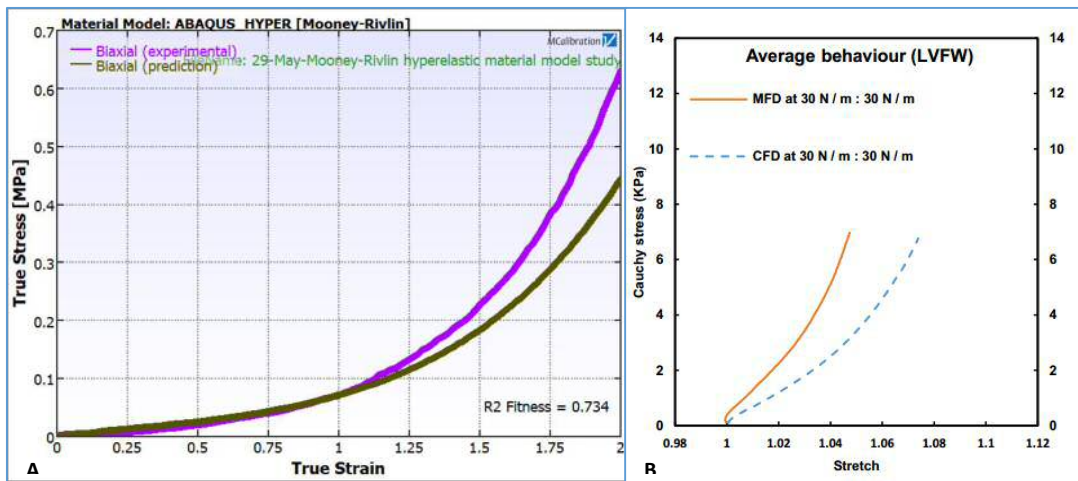


Figure 4-7 Biaxial data comparison between the Tango+Black and porcine left ventricle tissue: (A) Biaxial true stress-strain curve of Tango+Black, (B) Left ventricle biaxial true stress-stretch curve (Ahmad et al., Unpublished). It should be noted that the stresses in the material testing is in MPa while in the tissue it is kPa.

The preliminary FSI model material experienced compression during the simulation; hence, the biaxial predicted data for the material is more significant for the choice of the hyperelastic material model. This is obvious from Figure 4-8, where the biaxial material testing data have been compared with the behaviour of the solid material after the converged simulation. This shows that the compression used in the FSI model lies in the early stage of the material model strain behaviour and thus validates the choice of the engineering data entered in the preliminary model FE. The data imported in ANSYS have been used as engineering stress and strain in accordance with the software requirement for curve fitting and material identification while the resultant data from the ANSYS simulation are presented in a true form according to the ANSYS solution characteristics. This is an important issue in ANSYS, which has to be considered in material testing validation.

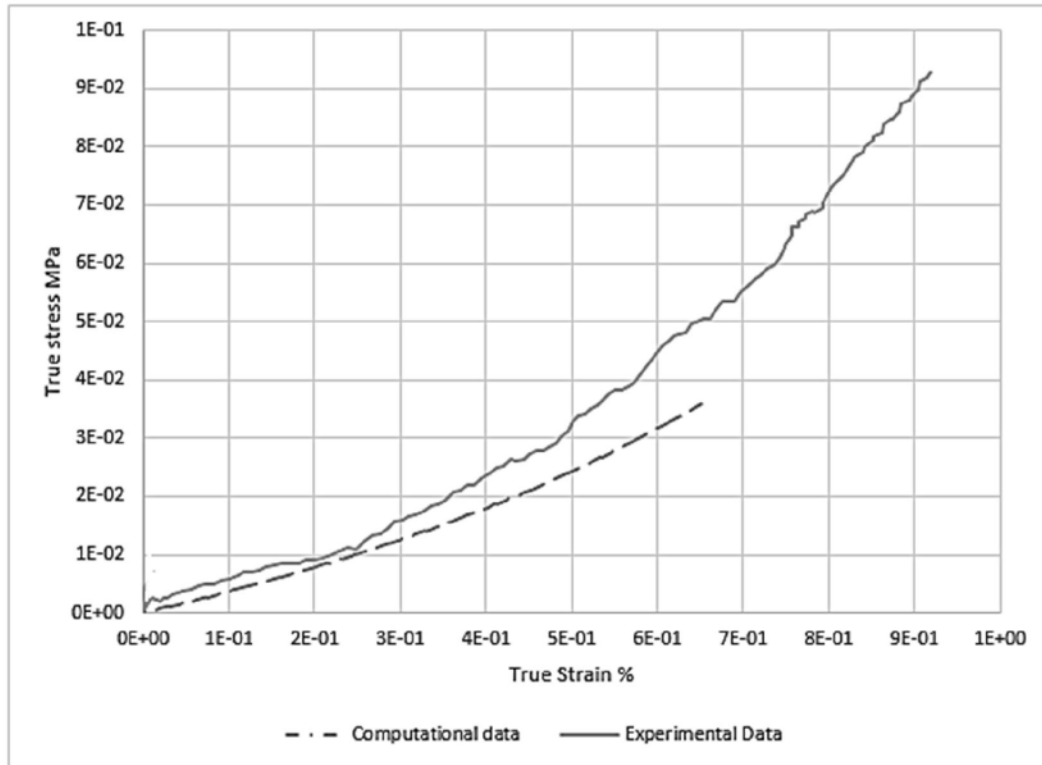


Figure 4-8 Computational validation data for the biaxial material testing curve fitting. The preliminary model biaxial behaviour lies on the biaxial material model profile while showing that the model compression strain lies in the low strain rate part of the calibrated material model.

At first, the measured data were calibrated in ANSYS; however, the material models showed unreliable data, as most tests did not fit the measured curves, and the material models used in the preliminary model failed to simulate the FSI model. Indeed, the development of the hyperelastic wall model enabled the study of the impact of different nonlinear material models on the subject-specific model, and the FSI allows us to assess the load more accurately. Importantly, our results show that for small strain problems, all three hyperelastic models yield very similar results. However, in two of the material models, starting with the finite element simulation, the characteristics of individual nonlinearity of each model differed in a way that terminated the FSI model simulation and caused extreme compression to the loaded surfaces, which caused extreme changes in the fluid element dynamic geometry.

### 4.2.3. Material Testing Computational Validation

In the literature for hyperelastic materials, biaxial and planar shear tests usually need some rig design and test piece modifications (Sasso et al., 2008, Moreira and Nunes, 2013, Shahzad et al., 2015, Palmieri et al., 2009). The uniaxial tension in the procedure is usually assumed

to be straightforward, and the British standards should be followed, but this is not true in most cases. Many hyperelastic materials need modification of the uniaxial tensile testing procedure, and thus, modification of the test specimen pieces is required too. In order to validate the methods used in these tests, computational models were used to examine the consistency of the measured strain along the testing piece for each test.

### **Tensile test**

The resulting equivalent strain distribution across the tensile test piece showed consistent data. This consistency validated the strain gauge placement of the experimental tests. British standards recommend avoiding the placement of the strain gauges on the neck of the piece, and this was obvious in the computational model where the strains varied in that area. Moreover, samples that failed from the neck of the test piece were neglected as recommended by British standards, and that was validated in the computational model, as test pieces failed in areas away from the neck. Different labels were added along the narrow portion to show the strain consistency validating the measured strain gauge in the video-extensometer (Figure 4-9). The test piece for the computational model was designed to have symmetry along the axis, and  $\frac{1}{4}$  of the test piece was used in the simulation to reduce the computational cost. The material used for the computational model was the Mooney-Rivlin model. True stress and strain was used in the validation process, as ANSYS stress results are in true form.

For this material, the test piece dimensions were following the British standards (Institution, 2012) and as required by them, any modification to the design should be mentioned in the results. The two design modifications for the uniaxial tension were tested using the same procedure and the same imaging technique.

For the validation of the testing procedure, a computational model was used to simulate the procedure with the test speed, and the dumb-bell modified ending was designed in Solidworks Education Edition software. The pattern end test piece was chosen for the measured data, and the computational model design and the geometry was then imported into ANSYS software for analysis and simulation settings. The Solidworks software was chosen for the design to get the exact geometry used for the .stl file used for the 3D printed test pieces (Figure 4-9).

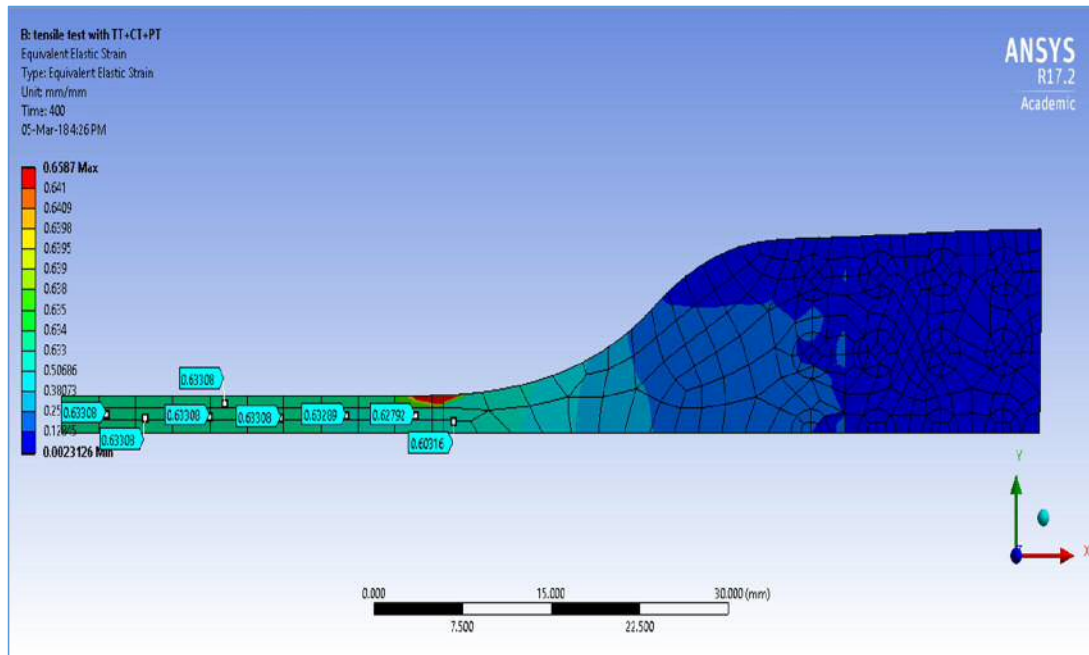


Figure 4-9 Tensile test computational validation. This represents the equivalent elastic strain distribution in transient structural ANSYS17.2. The test piece with pattern end design showing consistent equivalent elastic strain on the narrow part of the test piece.

### Planar Shear

A planar shear experimental testing rig design was validated using the computational model of the planar shear test with the 2D ANSYS workbench model. The computational equivalent of strain distribution demonstrated that the strain along the middle of the specimen is equal, and the necking occurs at the transverse edges, creating areas of total compression in the middle of the test piece. This can also be seen in the strain distribution consistency of the strain distribution during the planar test, as can be seen in Figure 4-10.

In order to create the planar shear tension forces on the material sample, two directional forces should be applied, but according to the literature, this can be done using a one-directional force with modified displacement (Palmieri et al., 2009, Moreira and Nunes, 2013, Sasso et al., 2008, Shahzad et al., 2015). However, the planar shear computational validation model results show that applying tension using one side of a tension machine with a fixed other side gives the same strain measurement, thus validating the procedure used in measuring the planar shear strain and stress by the designed rig.

The geometry of the tested sample was designed applying different loadings. One model considered one quarter of the testing sample applying frictionless support on the symmetrical areas while applying displacement loading on the length of the geometry; this will simulate the

two-directional loading. The second model was considered as one half of the geometry applying frictionless support on one side of the rectangular geometry while applying displacement loading to one side and fixed support to the other, ensuring that only one side is pulled during the simulation, with double the amount of displacement used in the first model. The simulation was carried out for the same time, and hence at same speed, and with a multistep analysis setting for a hyperelastic material of the Mooney-Rivlin material model. The simulation result is shown in Figure 4-11 where the elastic strain is measured for both models at the end of the simulation.

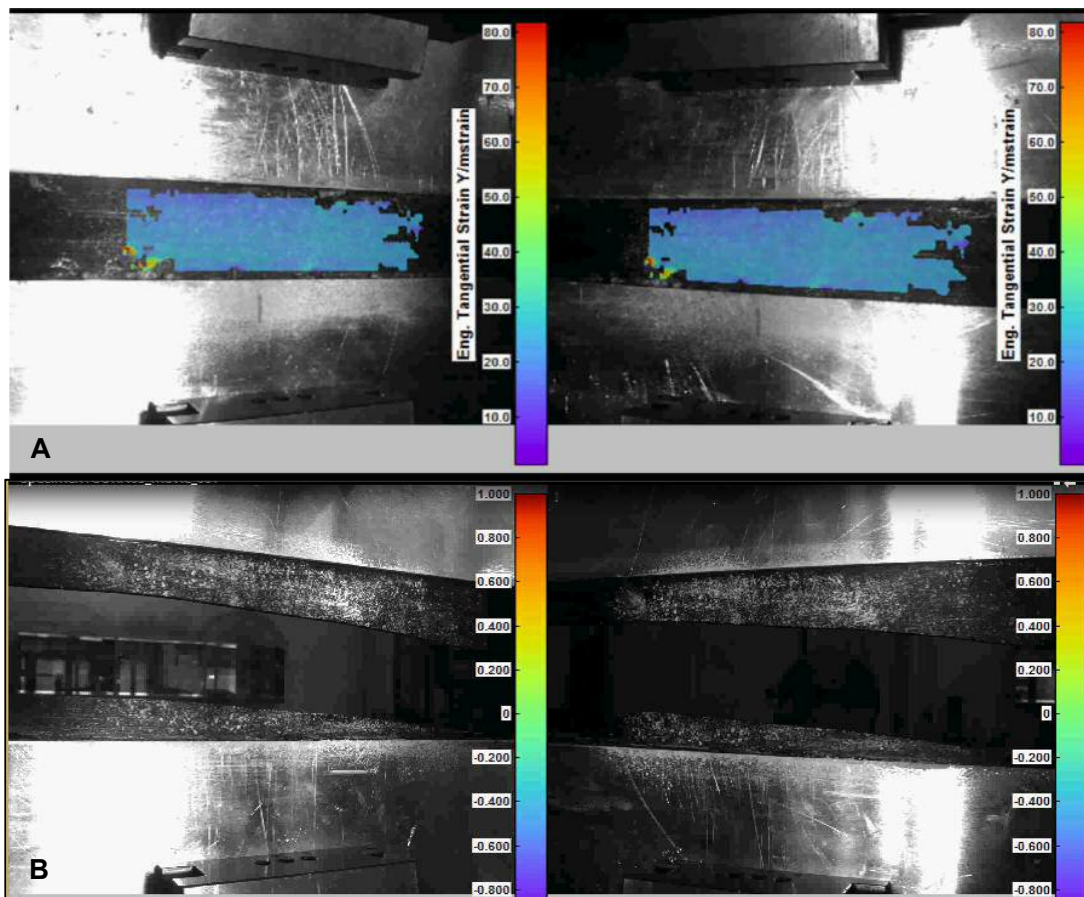


Figure 4-10 Material shear behaviour as viewed by the two DIC cameras: (A) The strain consistency during the test with the speckled pattern area of the test piece strain map distribution, and (B) Failure images of the planar test sample at the end of the test showing the area of the tear near horizontal central line and the attached test piece after the sample breaking point.

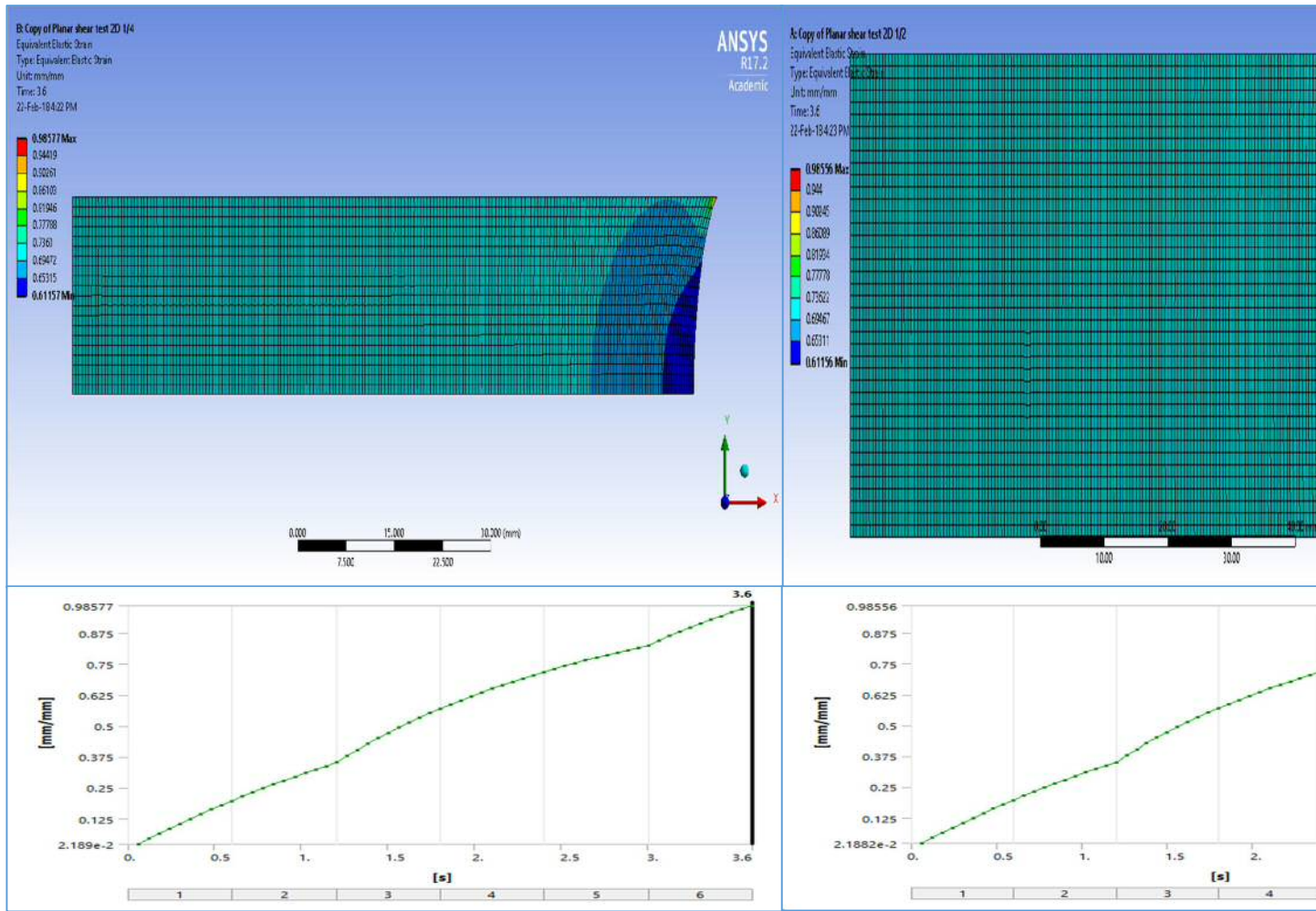


Figure 4-11 Computational validation for the planar shear test using one or two directional tensions. On the left is the computational model for tension from two sides, on the right is the planar shear computational model of the tension from one side. Both results show similar material behaviour and strain map distribution. The use of either method for the test.

Although any strain gauge along the X axis of the specimen measurement was acceptable (Figure 4-12), the average of the central strain gauges replicated the computational technique for test validation. This also validates the use of two different methods of imaging with this rig, as both the video-extensometer and the DIC gave consistent measurements during the test (Figure 4-3).

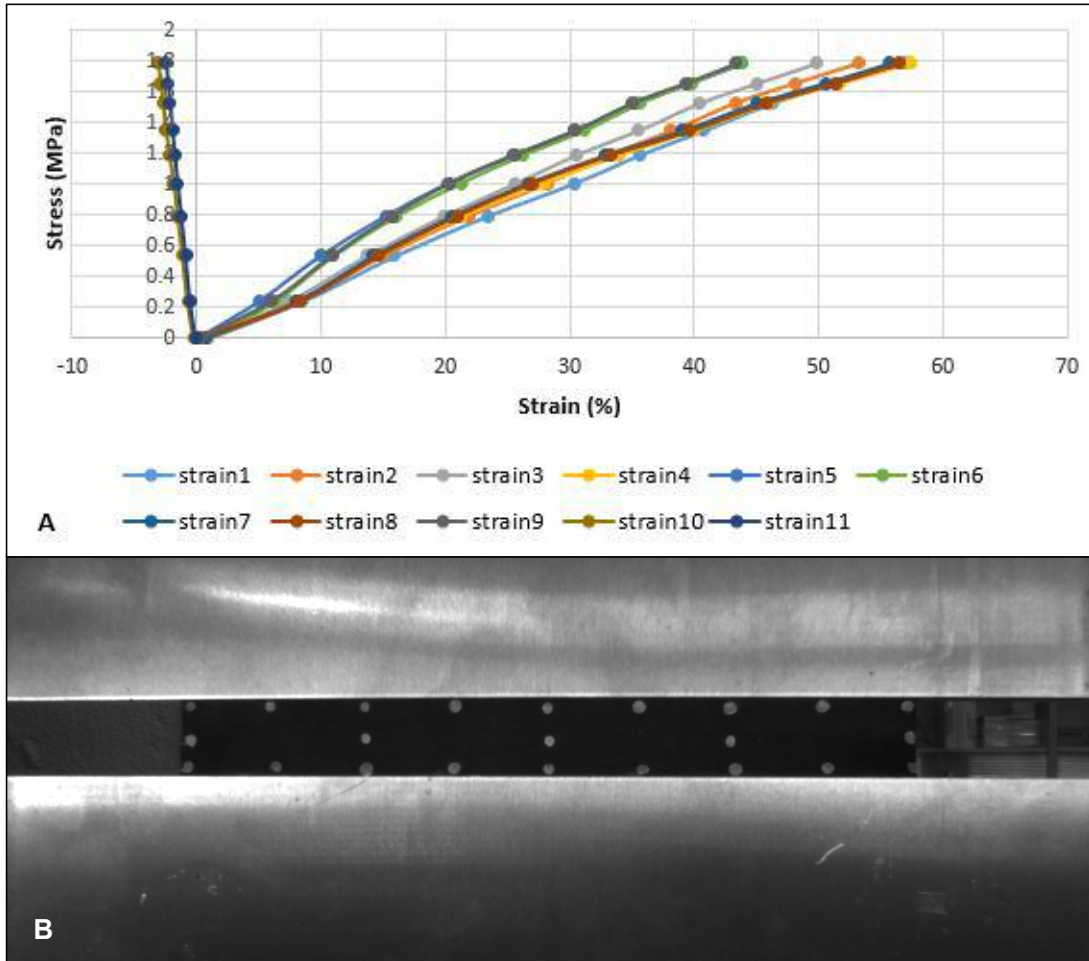


Figure 4-12 Planar shear test strain gauge comparison: A) Strain measurement data from the video-extensometer - each series represents a virtual strain gauge placed on the test sample as seen on B ( B) Strain map from the video-extensometer showing the placement of the virtual strain gauges.

### **Equibiaxial test**

Computational validation for the biaxial test rig was conducted using the FE model in ANSYS workbench. The elastic strain distribution map demonstrated that all the inner diameter areas have the same material behaviour, ensuring that all the strain gauges taken from this area will



give the same result, and this computationally validates the biaxial rig, which gives confidence in using the rig for the proposed hyperelastic material. The computational model validation shows the possibility of considering any strain gauge used in the zone passing through the centre of the specimen. However, the average strain gauge result was used in the experimental test measurement for better consistency through the multiple specimens testing to eliminate any tension inconsistency in the pulling cords. This model was designed with one quarter of the complete geometry to reduce the computational cost. The symmetry surfaces were considered as a frictionless support degree of freedom with an additional frictionless support degree of freedom for the circular area making the geometry one eighth (Figure 4-13).

The tension was applied to all four gripping areas that were normal on the surface; this involved using the displacement components rather than the vector to apply the exact angle. The analysis was run during 96 seconds with a tension and releasing motion of the remote displacement, and to accommodate the hyperelastic behaviour, sub stepping was used with 25 initial, 10 minimum, and 100 maximum sub steps. For the material properties, the data from the tensile and planar shear were used to predict the biaxial data implying the Mooney-Rivlin material model.

The areas around the clamps' "necking" of the tensed sample gave different results from the inner diameter area, so the recommendation is to place the strain gauges inside that diameter. While during the test, eight strain gauges were taken, only one was sufficient to give the strain data. The stress data were taken directly from the tensile machine.

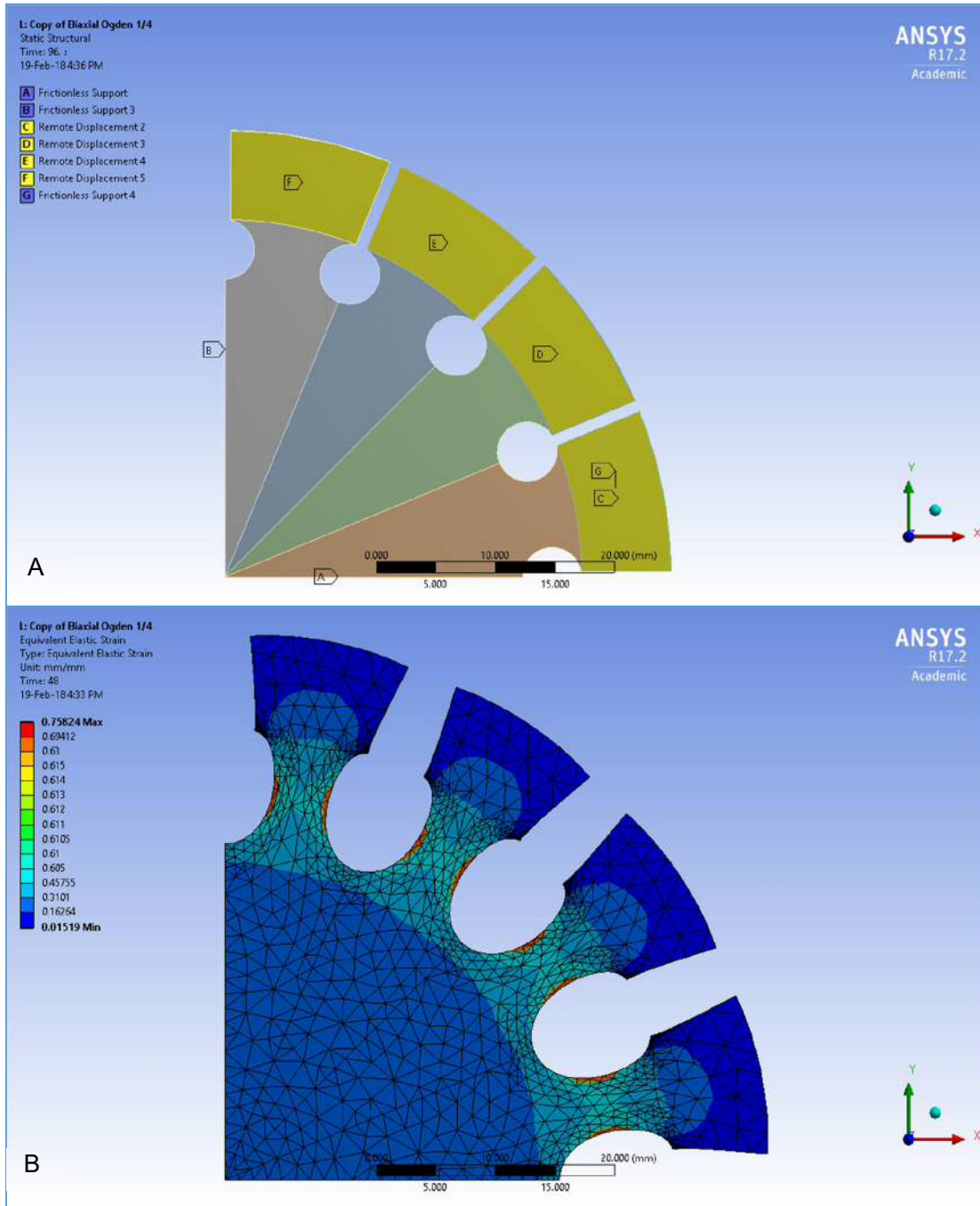


Figure 4-13 Equibiaxial test computational validation for 1/8<sup>th</sup> of the equi-biaxial specimen: (A) Boundary conditions and degree of freedom of the computational model. The letters present the areas of the model constrains (B) Equivalent elastic strain for computational validation of the biaxial test representing area of consistent strain in the middle of the specimen (near the centre)

From (Axel Products, 2000) compression material test analysis, even very small levels of friction can significantly affect the measured stiffness. Furthermore, this effect is apparent at both low and high strains. Although during the compression test used in this study, lubrication

was used between the testing material and the machine, there was no indication whether there was any friction or slipping. The testing material suffered slipping during the tensile test, which required modification to the standard specimen geometry. This indicates the possibility of slipping during the compression test causing incorrect compression data. This is particularly troubling because friction values for elastomers are typically a function of normal force and are not well characterized. Using adhesive with the specimen, as was used in the planar test, will introduce a layer of a material, causing deviation to the compression data. For those reasons, the experimental compression data cannot be corrected with a significant degree of certainty. Figure 4-14 presents the obtained compression data according to British Standards (2011) and the measured data compared to the equibiaxial data obtained according to the computationally validated equi-biaxial test rig.

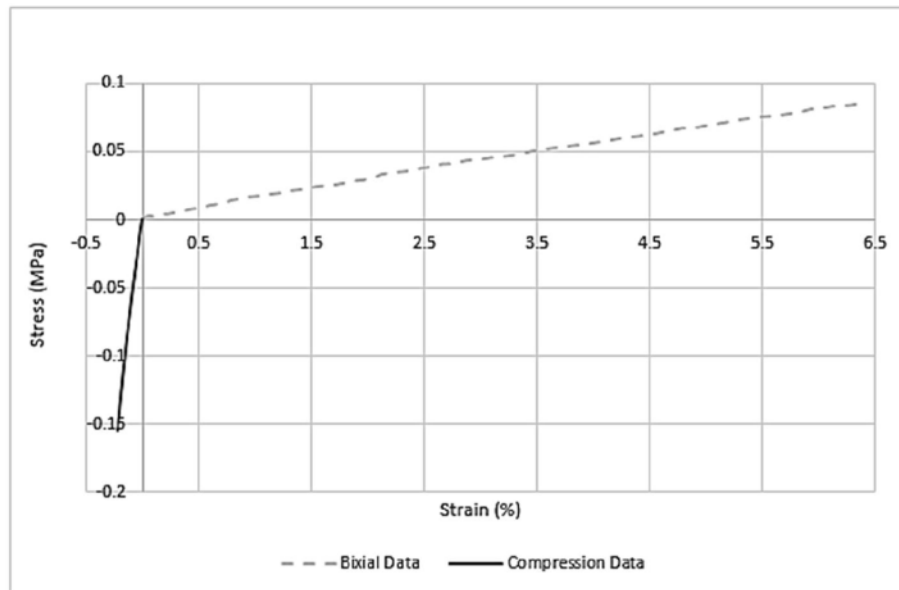


Figure 4-14 Comparison between computational validation equibiaxial and compression tests data

An additional complication to the compression test data was the curve fitting possibility in ANSYS, as it appears ANSYS material curve fitting relies on tensile, biaxial and planar shear material testing data, so a modification to the entered tensile data would be introduced including the compression test data, and that caused inconsistency with the strain rate range of the imported data.

#### 4.2.4. Post-CFD results and Discussion

All the solutions identified in these sections are computationally stable, as recorded and presented later in Appendix A. Dynamic simulations are required to study the stability of the

solutions; hence, the chosen stabilisation factor was 8. This number was considered low compared to the complicated geometry design. Also, the use of water as the material implemented for this model made it more stable than using the Carreau model of blood.

### **Velocity Profile and Distribution**

Velocity profile, magnitude, and vortex formation were monitored in the CFD-post. The fluid motion behaviour was examined during different iteration steps during the simulation. The fluid output from the sphere begins with the initiation of compression, reaching a maximum flow rate at  $t=0.3$  s. After this point, the maximum outflow jet progresses through the outlet, and the fluid continues to flow causing swirling vectors to disappear from the middle sphere and to move to the top and bottom with a velocity magnitude of 0.0365 m/s. Moreover, it was observed that the higher velocity was found near the top and outlet at the start, but it decreased with time, reaching its highest magnitude near the end of compression at 0.0699 m/s.

The characteristics of the flow pattern during the compression exhibited increasing magnitude throughout the simulation. The XY cross sectional plane in the post CFD is taken using velocity vectors along the compression with the associated velocity swirling vectors (Figure 4-15 to Figure 4-17).

Two vortices start at the bottom of the sphere with apposite rotating rings. At the beginning of the release, the fluid starts to enter the model and when it reaches its peak, maximum inflow jets are progressed through the inlet, and the fluid continues to flow causing those previously mentioned rings. The swirling vectors starting at the inlet wall seem to increase with time, but with a lower velocity magnitude. During release, the velocity distribution at the beginning and at the end of this phase is associated with swirling vectors. This is associated with the vortex formation mentioned above and confirms the fluid flow behaviour during the compression cross-sectional plane through the fluid flow model in post CFD (Figure 4-20). The velocity increases during the release recording its highest speed at the inlet. The maximum swirling vectors were found near the inlet. The velocity profile curves show that the highest velocity magnitude is reached at  $t=0.5$  s, which is at the end of the simulation. Although the vortex formation starts at  $t=0.1$  s, the noticeable increase in the outlet flow is seen at  $t=0.3$  s in the velocity profile.

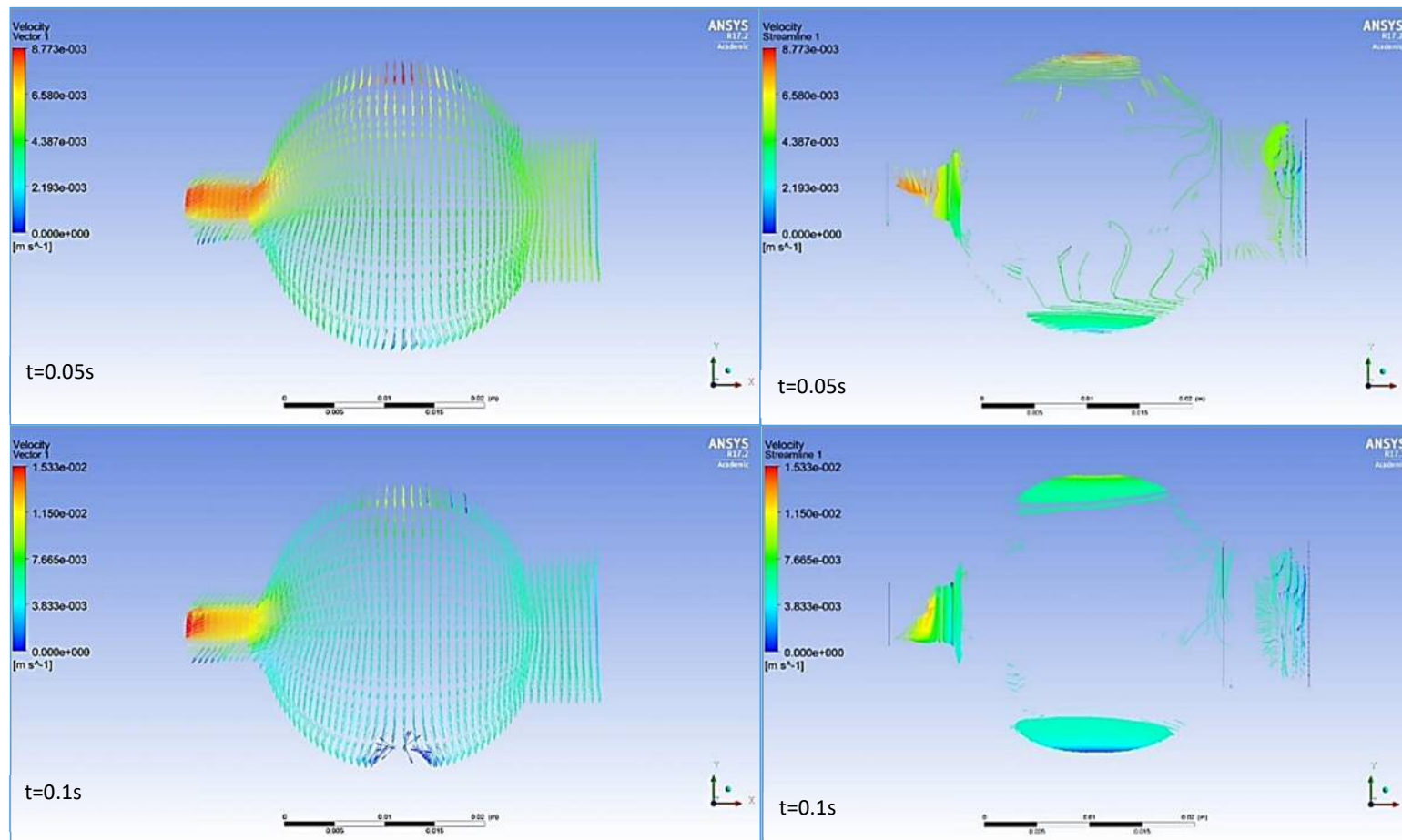


Figure 4-15 On the left are the velocity plane vectors map distributions, and on the right are the velocity streamline swirling strength map distributions in post CFD of the compression stage FSI simulation for  $0 < t < 0.2$ . The velocity is represented by vectors' increasing magnitude in the outlet indicated by the colour-coded map legend and the flow. The vortex formation is shown during different time steps in different locations

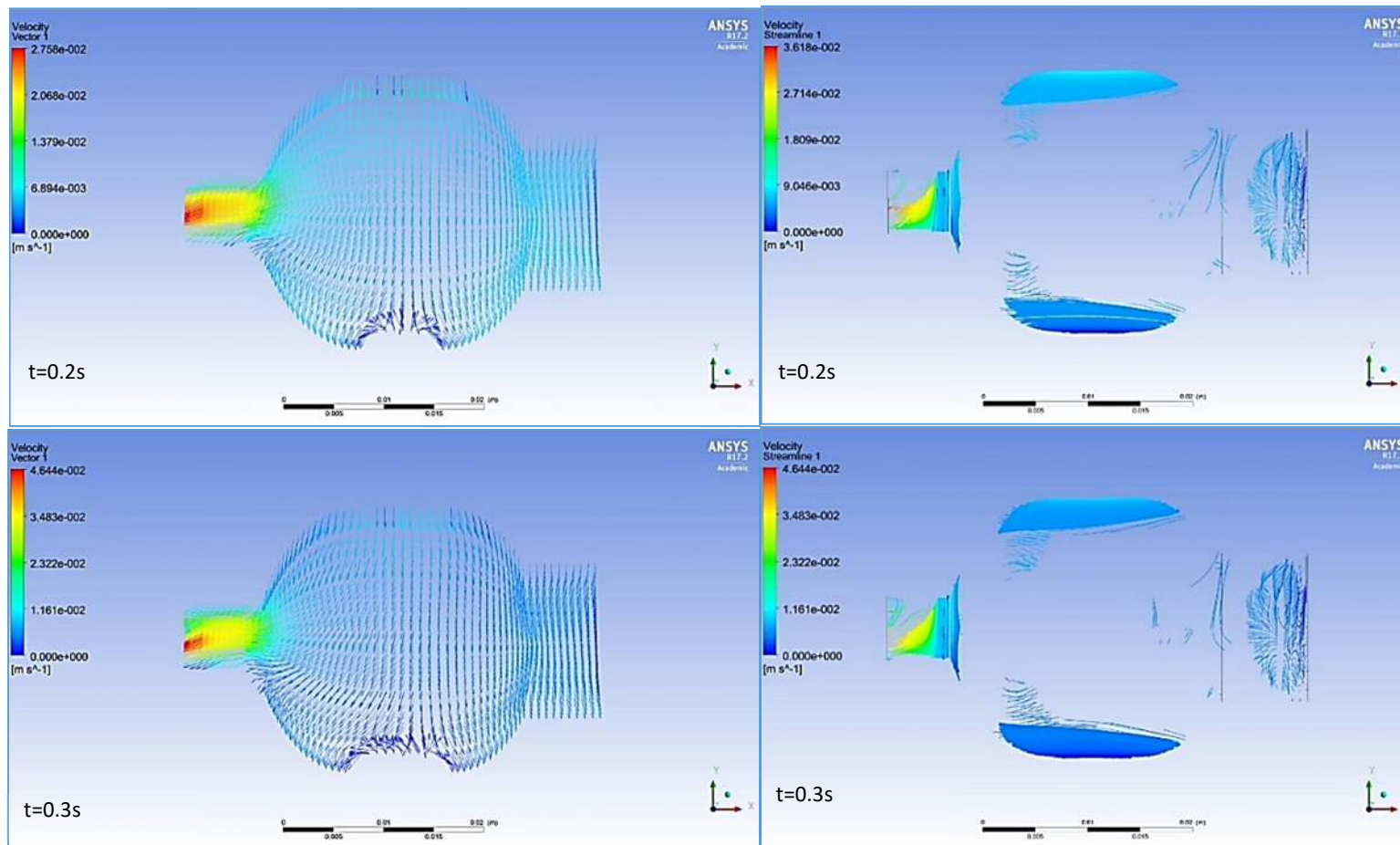


Figure 4-16 On the left are the velocity plane vectors map distributions, and on the right are the velocity streamline swirling strength map distributions in post CFD of the compression stage FSI simulation for  $0.2 < t < 0.4$ . The velocity is represented by vectors' increasing magnitude in the outlet indicated by the colour-coded map legend and the flow. The vortex formation is shown during different time steps in different locations

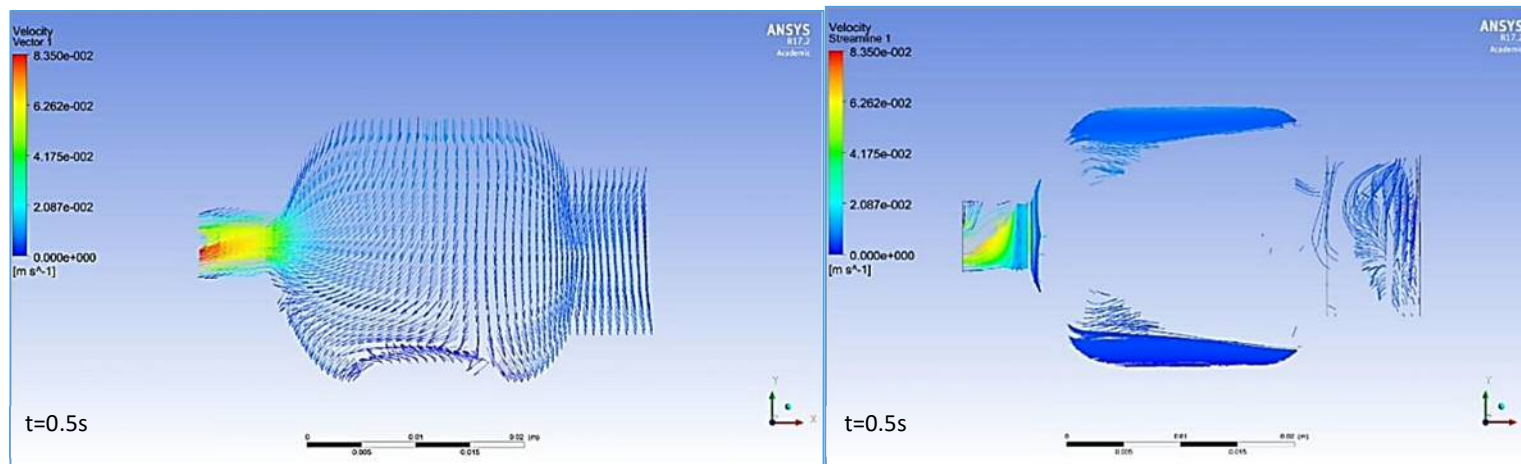


Figure 4-17 On the left are the velocity plane vectors map distributions, and on the right are the velocity streamline swirling strength map distributions in post CFD of the compression stage FSI simulation at  $t=0.5$ . The velocity is represented by vectors' increasing magnitude in the outlet indicated by the colour-coded map legend and the flow. The vortex formation is shown during different time steps in different locations.

The velocity profile was also obtained from ANSYS CFD-post at different time steps representing the velocity magnitude in relation to the dimensionless Y position of the outlet boundary conditions. The velocity profile exhibited increasing magnitude, reaching its highest value at the end of the simulation. This indicates the effect of the compression displacement of the geometry during the FSI. The position of the outlet shifted during the simulation as the boundary condition degree of freedom permitted the Y dimension deformation restricting the X and Z deformation. This allowed the stresses on the outlet deformation, causing the fluid to flow out of the sphere volume. The time dependant velocity profile is shown in Figure 4-18.

By way of comparison, the model contained water to enable validation against the physical rig. The dynamic viscosity for this model showed a different behaviour than that of blood. This will be explained later in the subject-specific velocity profile section. The chart generated in CFD-post is very different to that of the blood model. In particular, as the dynamic viscosity of the fluid was considered constant, the vortex generation was different from the blood especially with the location. These results are also different from the point of the location of the boundary conditions, as the inlet and outlet are on the same plane while in the blood model, they are on different horizontal planes.

The fluid flow behaviour, represented by the velocity vector magnitude during the iterative time steps, shows the importance of the vortex formation to produce the flow through the outlet. When FSI simulates the release phase, the velocity magnitude is decreasing through time. The velocity in the release phase is controlled by the pre-stressed model geometry and boundary conditions (Figure 4-19). The inlet diameter is larger than the outlet, hence the presence of the reverse flow location. Reverse flow was allowed in the simulation to avoid model instability. Reverse flow can occur when pressure gradients cause fluid to re-enter the domain at the location where the boundary condition is placed, due to the geometry.



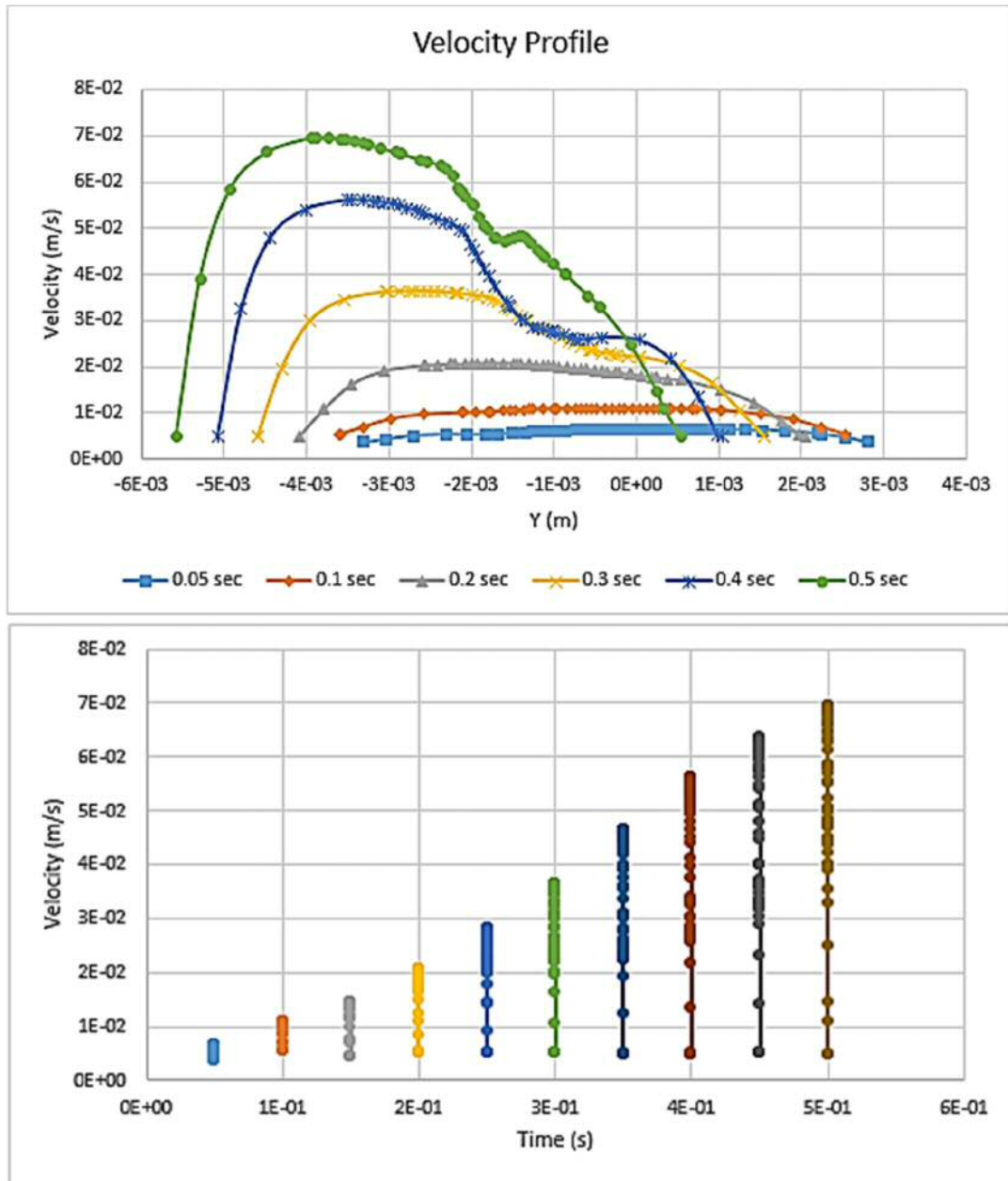


Figure 4-18 Velocity profile of the preliminary model during different time steps of the compression FSI stage. The graph on the top represents the velocity profile in accordance with the outlet position in the Y axis. The image below represents the outlet velocity in accordance with the time steps. The time steps data are colour coded for each time step showing increasing magnitude with each time step.

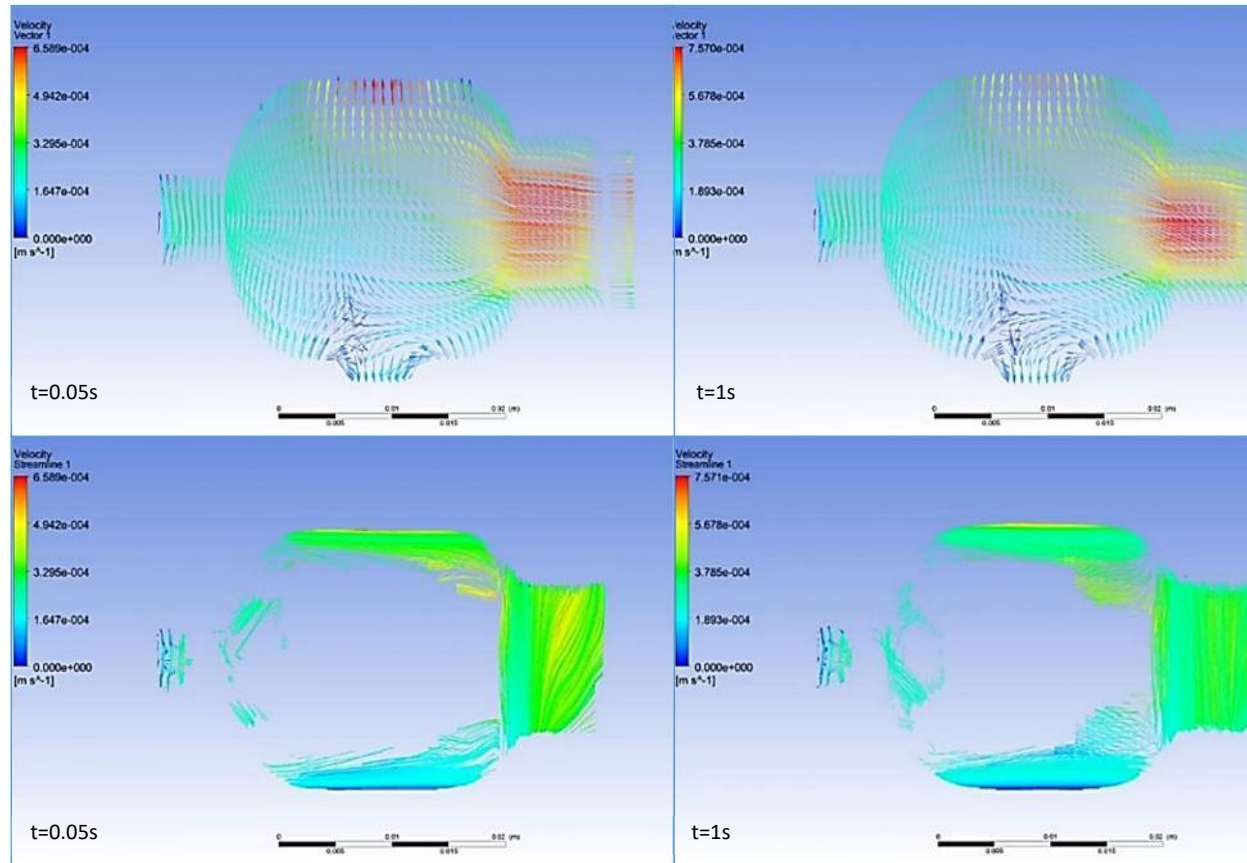


Figure 4-19 Velocity plane vectors and their streamline swirling strength map distribution in post CFD of the release stage of the FSI simulation. The velocity plane vectors map distribution and on below are the velocity streamline swirling strength map distribution in post CFD of the compression stage of the FSI simulation. The velocity is represented by vectors' increasing magnitude in the inlet indicated by the colour-coded map legend and the flow. The vortex formation is shown in the time steps.

Some flow reversal can be tolerated, but it will have an effect on mass-conservation and thus on convergence, and so it is highly recommended that it be minimized or eliminated. In this case, the convergence was monitored through the simulation; the amount of the reverse flow was minimal and the pre-stabilisation to the model reduced its effect on the convergence. As the outlet in the compression phase was placed further downstream, this reduced the amount of the reverse flow, but as in the release phase, the inlet is at the entrance boundary, so the reverse flow was higher than in the compression phase. As a result, care was taken to monitor the convergence of the simulation, and the area of the release was minimised in the structural side to reduce the effect of the reverse flow. Also, a better distribution of mesh sizes and elements leading up to the inlet usually reduced that too, but as the model mesh was inherited from the compression FSI, this option was not possible.

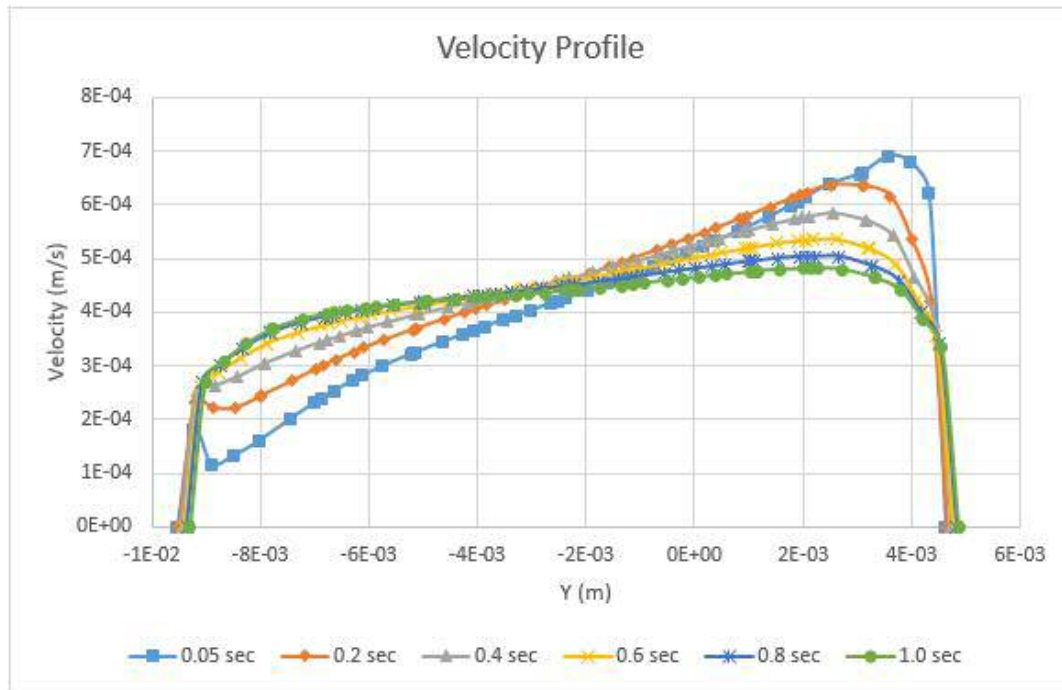


Figure 4-20 Velocity profile of the preliminary model during different time steps of the release FSI stage

In general, to produce a higher velocity magnitude, greater external pressure is required. This is done in two ways. It can be done first, by applying more displacement, which will conflict with the guidelines for the displacement required in the resuscitation and will cause damage to the hyperelastic material by causing extensive buckling of the surface and its fluid, meaning the mesh elements will fail. The other way of increasing the external pressure is by introducing multiple compressions and release steps. In this study, we have not attempted to exhaust all

possible solutions while considering that the resultant data are for a single compression. However, it is clear that the more realistic the geometry of the compressed sphere and boundaries are, the closer is the reached value to the required external pressure.

### ***Pressure Gradient and Wall Shear***

The fluid pressure gradient for the release FSI phase is less than the compression pressure distribution. In fact, depending on the total deformation of the geometry observed from the structural results, the release or inflation phase did not follow the pressure path generated in the compression phase. Although the resultant pressure from the outlet is negative compared to that of the inlet during the release phase, which is the sign from ANSYS for outflow pressure. However, the expected pressure gradient was different, and this is due to the limitation of the pre-stressed FSI modelling in ANSYS. In the preliminary model simulations, fewer steps were needed to distinguish different pressure paths especially in the release phase, as the pressure gradient was observed to be similar in multiple time steps during the simulation.

The results of the pressure distribution along the central XY plane are presented in Figure 4-21 to Figure 4-23. The general character of the pressure is associated with the pressure gradient vortices during the simulation. In this region before the outlet, owing to the powerful compression blood flow from the compression plates, the largest magnitudes of the pressure are detected during the later stages of the simulation.

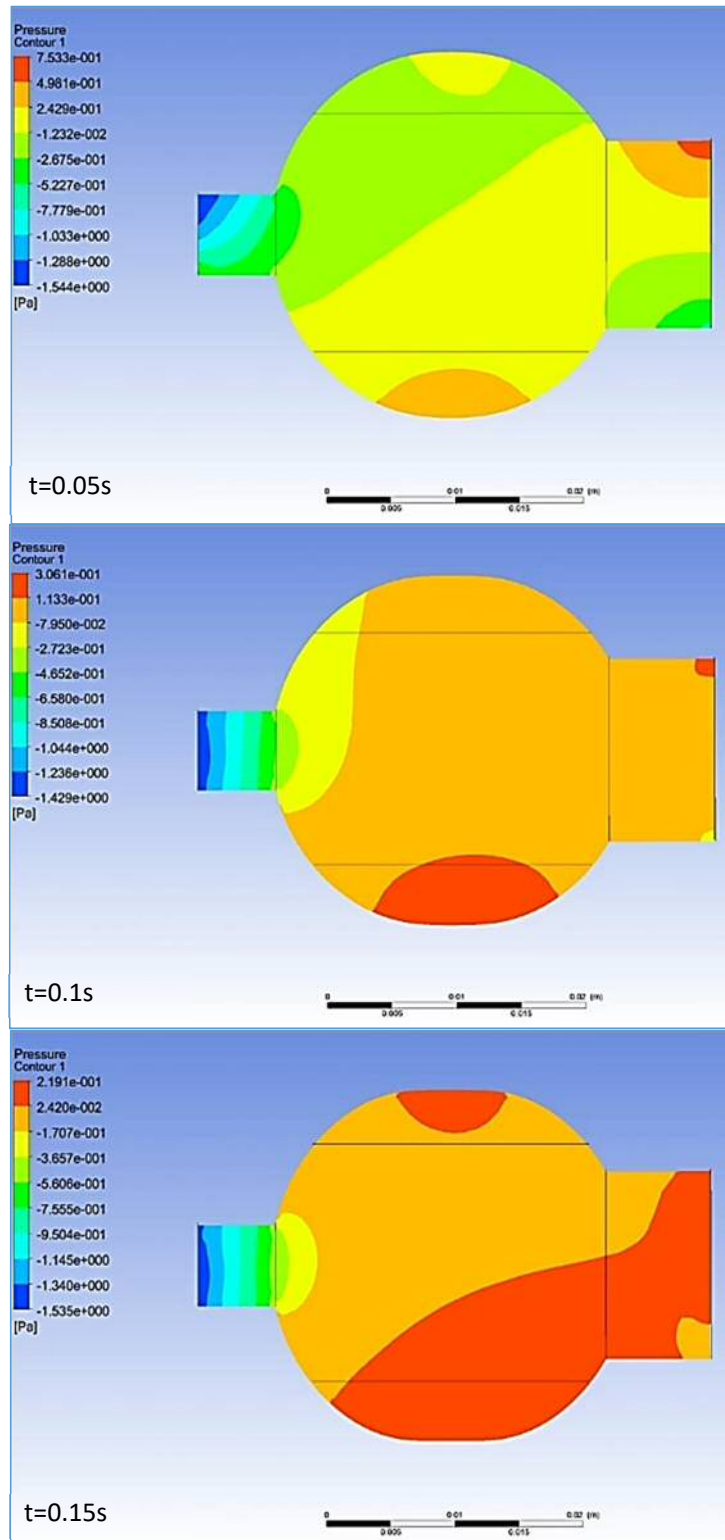


Figure 4-21 Pressure contour plane map distribution in post CFD of the compression stage FSI simulation for  $0 < t < 0.2$  sec. The pressure contour map distribution represented by increasing magnitude along the axis indicated by the colour-coded map legend and the flow. The vortex formation is shown during different time steps in different locations.

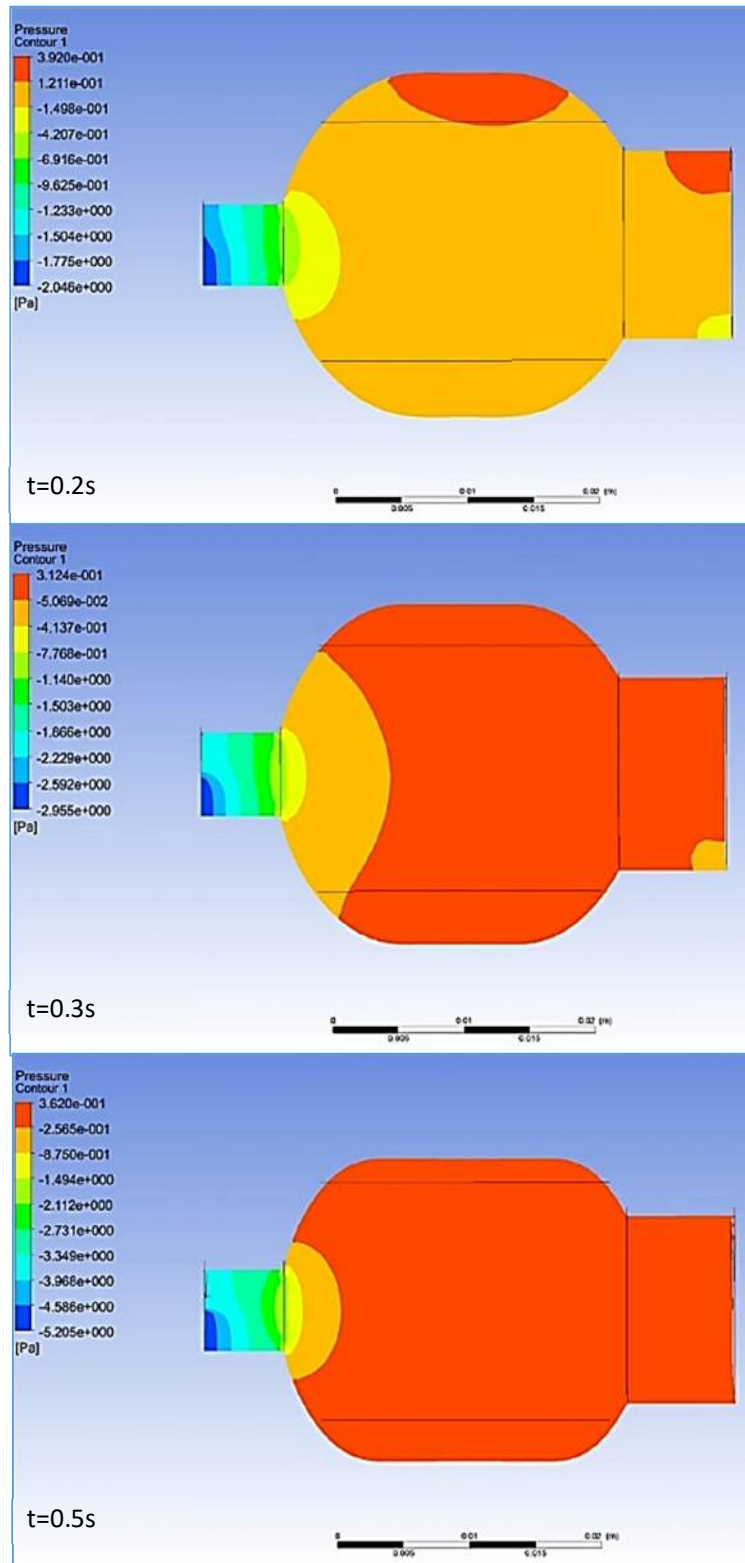


Figure 4-22 Pressure contour plane map distribution in post CFD of the compression stage FSI simulation for  $0.15 < t \leq 0.5$  sec. The pressure contour map distribution represented by increasing magnitude along the axis indicated by the colour-coded map legend and the flow. The vortex formation is shown during different time steps in different locations.

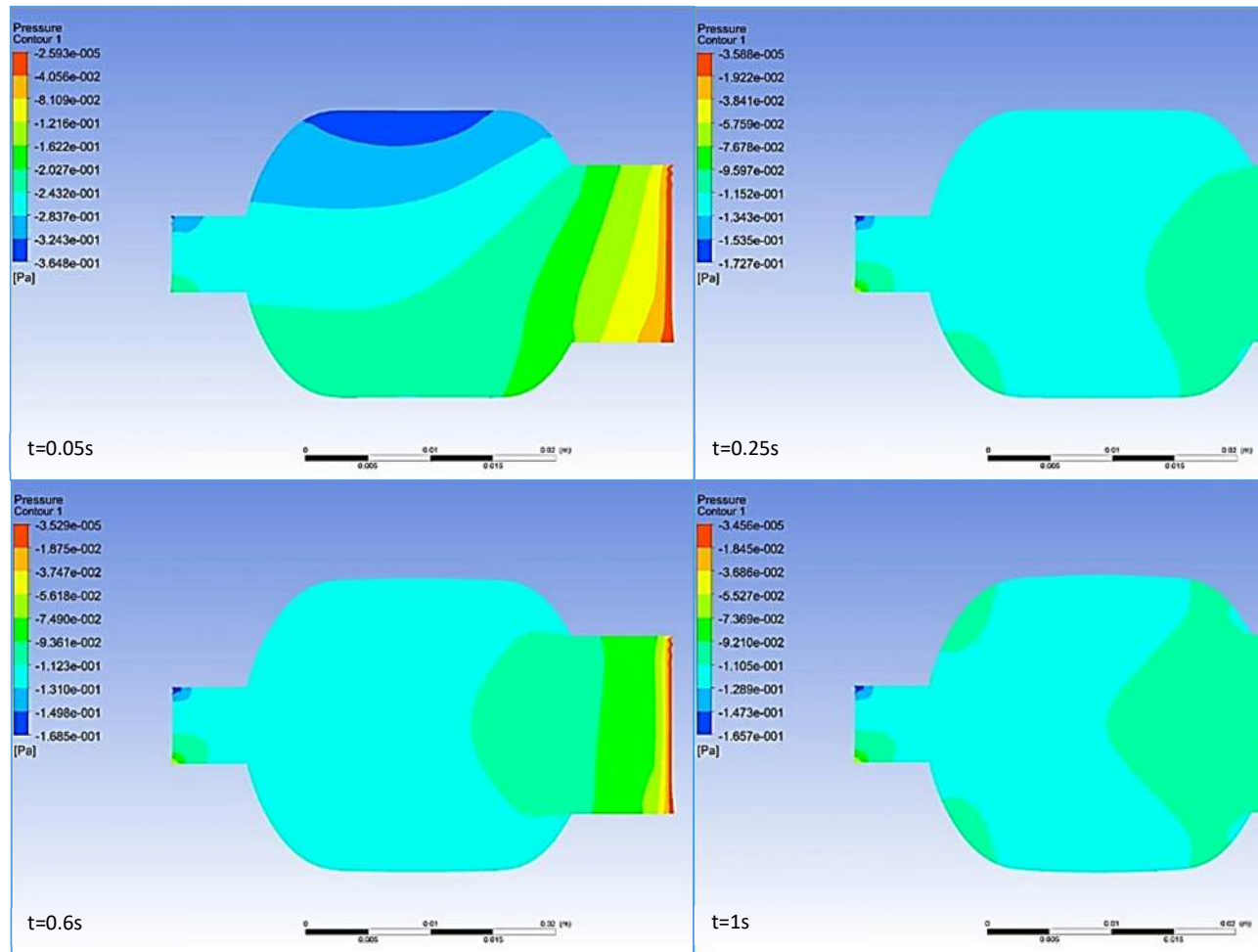


Figure 4-23 Pressure contour plane map distribution in post CFD of the release stage FSI simulation. The pressure contour map distribution magnitude along the axis indicated by the colour-coded map legend and the flow. The vortex formation is shown during different time steps in different

the outlet velocity has not reached its higher point. As the compression depth increases, the pressure gradient starts to change inside the sphere creating a vortex observed at  $t=0.1$  s near the bottom of the sphere and near the top at  $t=0.2$  s. Reaching the largest depth of the compression, the pressure increases in the whole region, forcing the outflow of the fluid through the outlet. The two formerly observed vortices, at  $t=0.35$  s to  $t=0.5$  s, are developed to include the whole sphere along with the inlet. During the release, a variation in pressure was observed and was recorded by an XY cross sectional plane. The changes in pressure distribution are shown for different time steps in Figure 4-23. At the start of the release, the lowest pressure was recorded in the top of the sphere. At  $t=0.25$  s, the pressure gradient started to increase to show its magnitude in the inlet where a vortex was observed nearby. At the end of the release, the pressure increased but remained lower than the pressure developed during the compression, thus forcing the fluid to flow through the pressure inlet.

Furthermore, WSS has also been computed to examine its influence on the wall motion. It was found that with the decline in the outflow velocity, WSS decreases and the magnitude increases during compression. The opposite happens during release (Figure 4-24 and Figure 4-25).



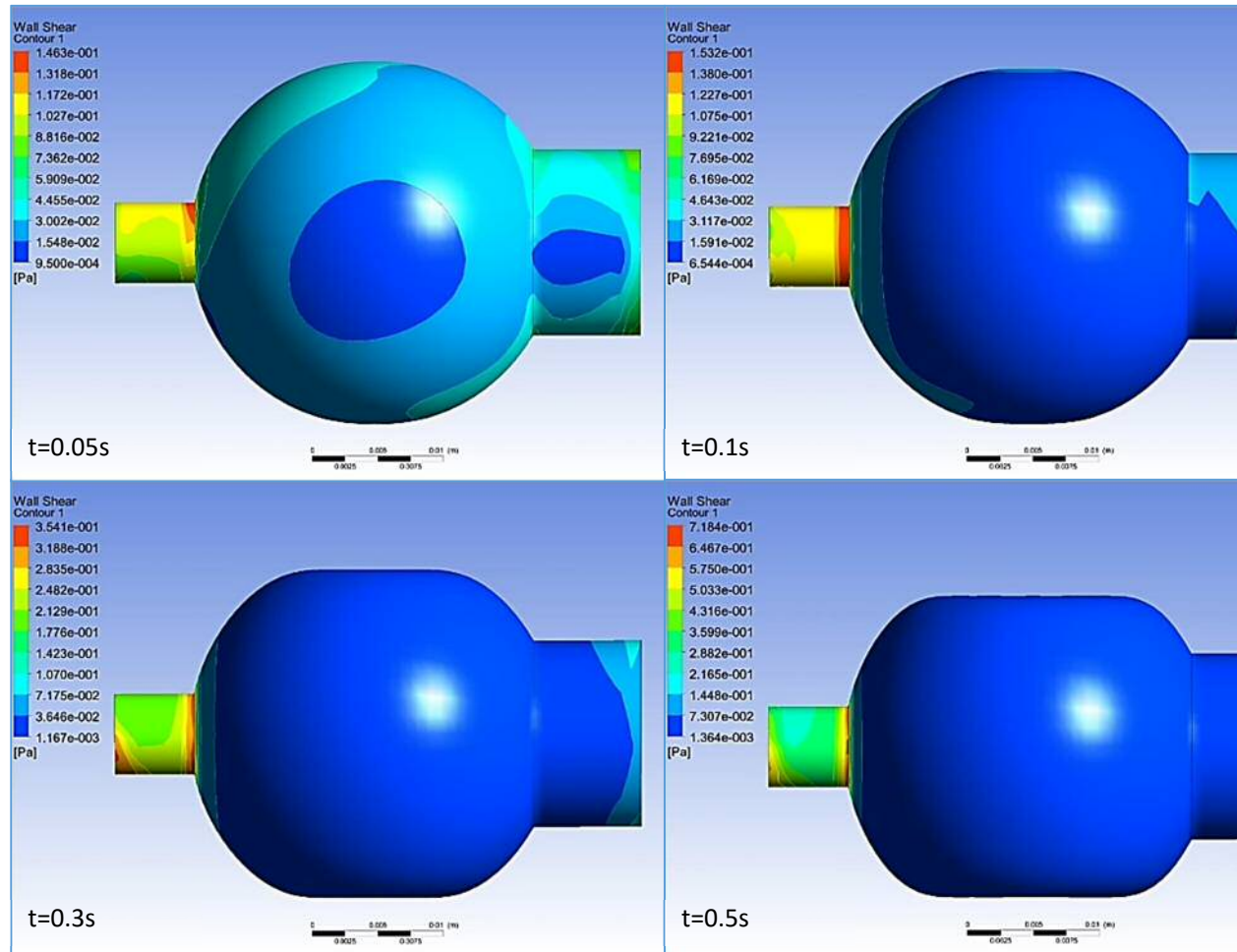


Figure 4-24 Wall shear map distribution in post CFD of the compression stage FSI simulation. The WSS contour map distribution is represented the fluid surface indicated by the colour-coded map legend and the flow. The gradient formation is shown during different time steps in different l

was observed to have increased. The inlet wall was observed to have the lowest WSS especially at the end of the compression, and this is due to the stagnation point. This phenomenon is more significant between  $t=0.3$  s and  $t=0.5$  s and is more obvious in the release phase FSI at the outlet-sphere junction. As shown in Figure 4-25, a gradual reduction in the WSS near the inlet wall magnitude was reported from at  $0.01 \text{ s} \leq t \leq 0.6 \text{ s}$  because of the flow deceleration. During the release phase, the outlet WSSs were steady throughout the simulation with a magnitude at the end of the boundary condition of the inlet and outlet.

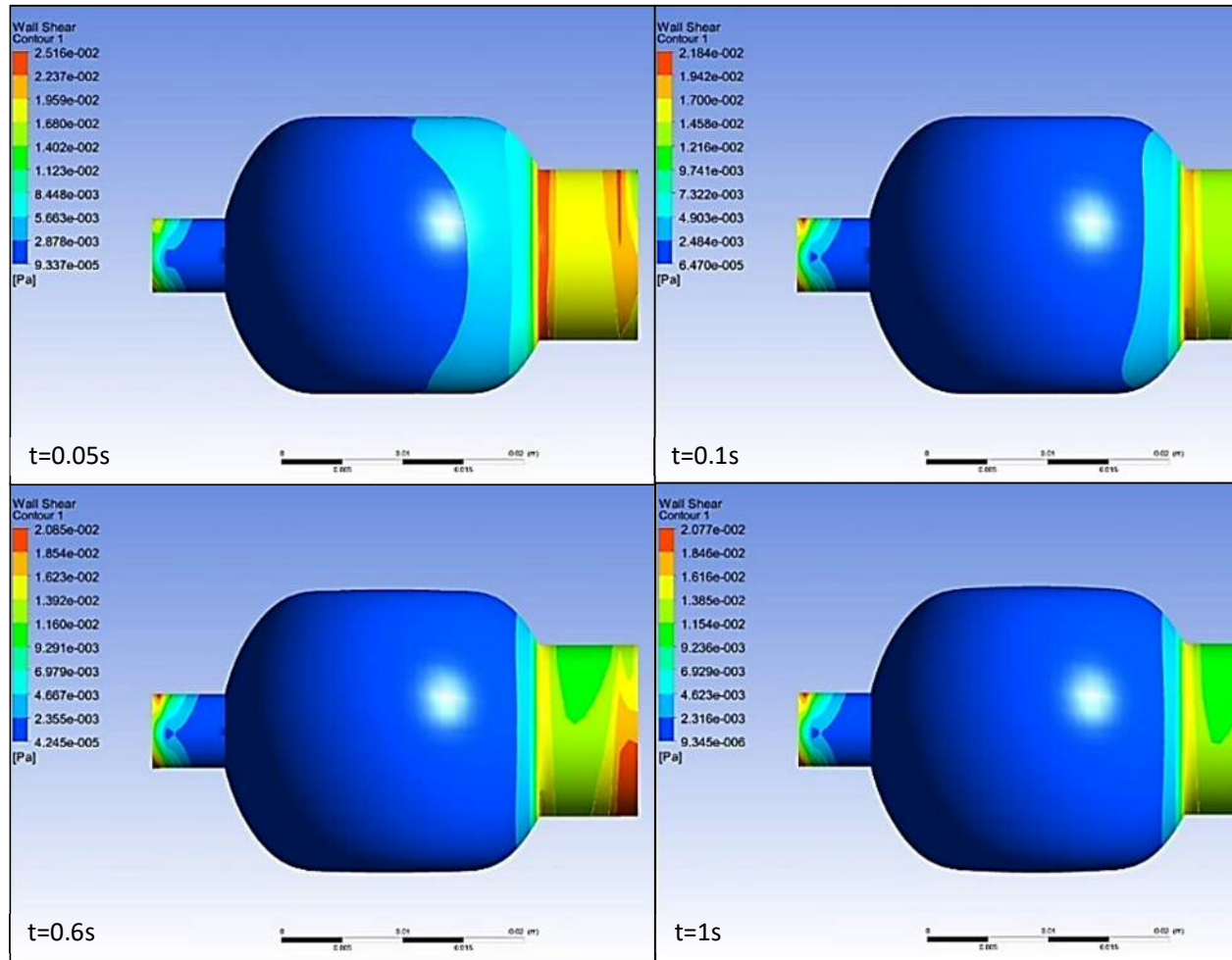


Figure 4-25 Wall shear map distribution in post CFD of the release stage FSI simulation. The WSS contour map distribution represented by increasing surface indicated by the colour coded map legend and the flow. The gradient formation is shown during different time steps in different locations.

maximum point throughout the compression simulation, but the distribution of the stress spread to all the defined contact regions. However, at the end of the simulation, the lowest stress was located at the centre of the sphere wall. Meanwhile, the stresses on the inlet and outlet remained the same throughout the simulation and recorded the minimum stress, as this region does not have any contact with the compressing plates. At  $t= 0.3$  s, the stress increases to include the upper and lower contacting surfaces while still recording the maximum value at the centre. After  $t=0.3$  s, the stress starts to spread beyond the contacting area with no separation between the sphere parts. This proves the connection type chosen for the surfaces as the increase stress did not cause the bonded contact separation (Figure 4-26 to Figure 4-29).

A similar analysis from Figure 4-28 and Figure 4-29, reveals that the maximum strains are at the point of the contact from the start of the simulation to  $t=0.3$  s. After this point, the maximum strains were recorded at the inlet-sphere connection. Meanwhile the minimum strain had a steady value recorded at the lateral surfaces of the sphere and although the stresses increased, but the lowest value stayed in this area. At  $t=0.2$  s, the strain starts to increase at the junction of the inlet to the sphere. The relation between the stress and strain during the simulation was plotted using a transient structural chart, which can be seen in Figure 4-8. As the strains increase, they remain at the low strain range of the tested material model for the preliminary and subject-specific simulation.

Results in this study include detailed flow patterns, and the results show a rich pattern of flow separations and vortex formation. An energy monitor reveals that the maximum energy dissipation occurs at the contact areas of the compressed sphere, as shown in Figure 4-30 and Figure 4-31. The area of the most strain energy is located on the contact area. This reduces the computational cost, reduces the areas of high strain throughout the simulation, and focuses the transfer of stresses to the fluid elements.

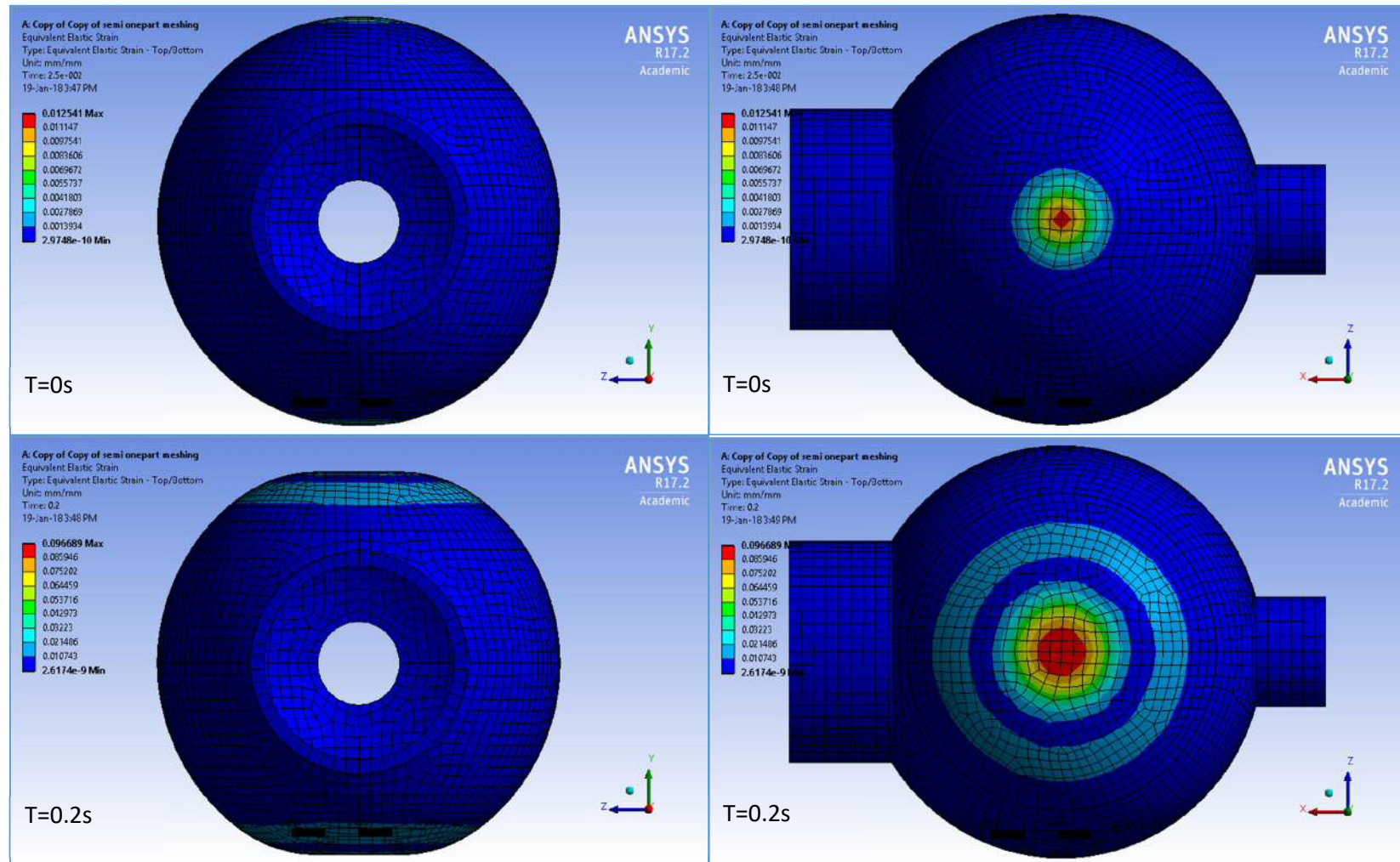


Figure 4-26 Equivalent Von-mises stress distribution map of the 1st stage FSI. On the left is the front view, and on the right is the top view for  $0 \leq t \leq 0.2$  sec.

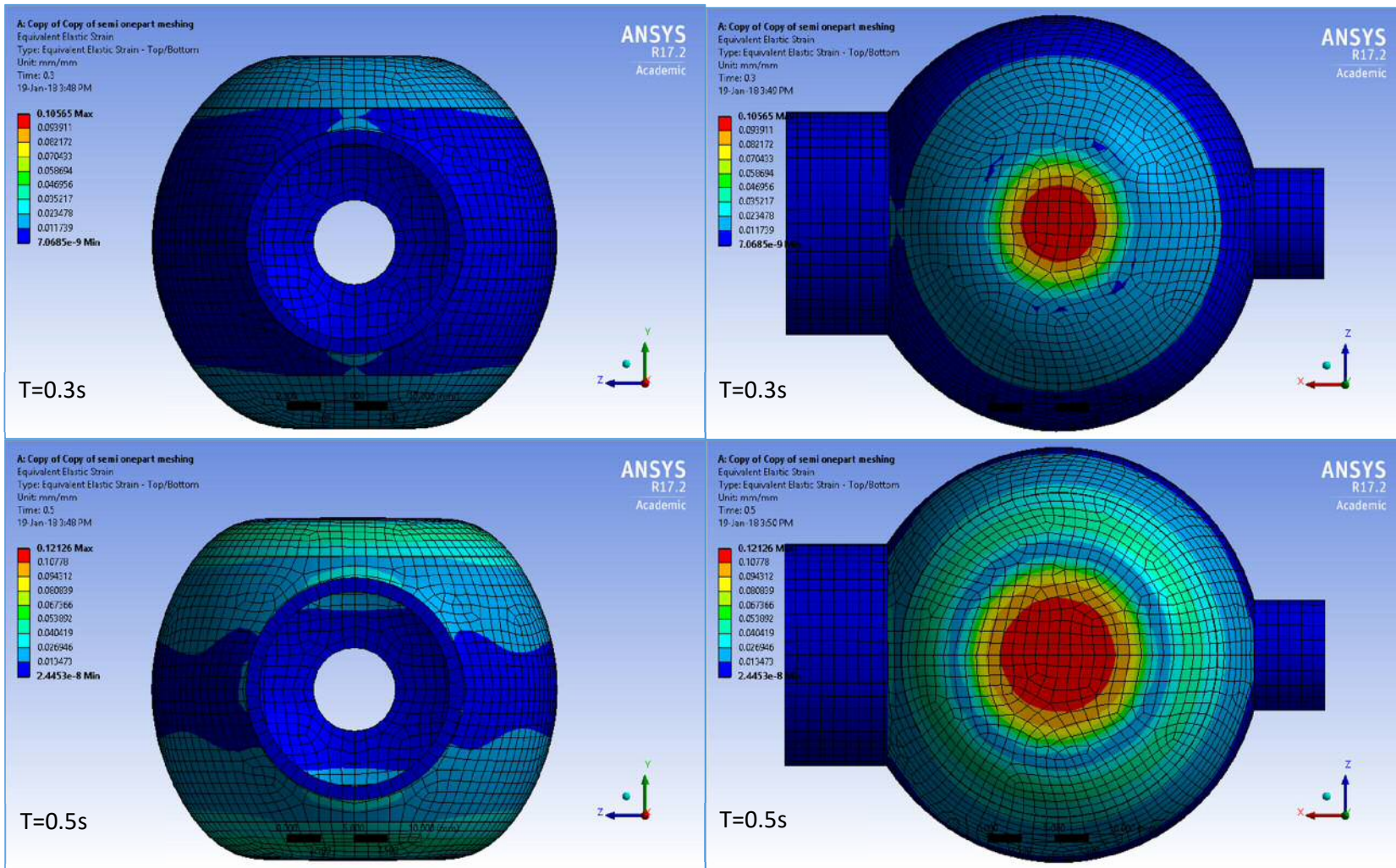


Figure 4-27 Equivalent Von-mises stress distribution map of the 1st stage FSI. On the left is the ZY vie (front view), and on the right is the XZ (top view) for  $0.3s \leq t \leq 0.5$  sec.

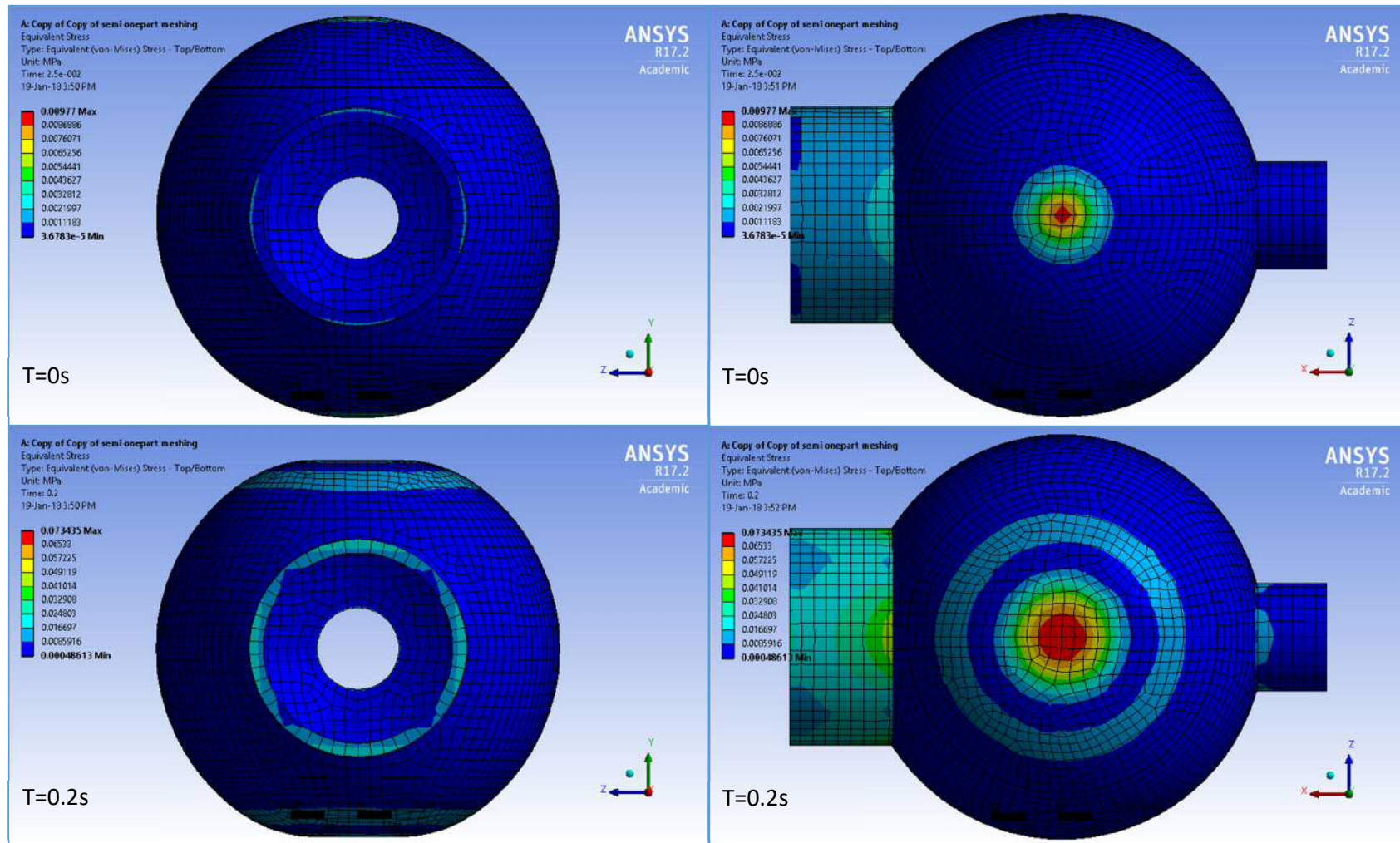


Figure 4-28 Equivalent elastic strain distribution map of the 1st stage FSI. On the left is the ZY vie (front view), and on the right is the XZ (top view) for  $0s \leq t \leq 0.2$  sec

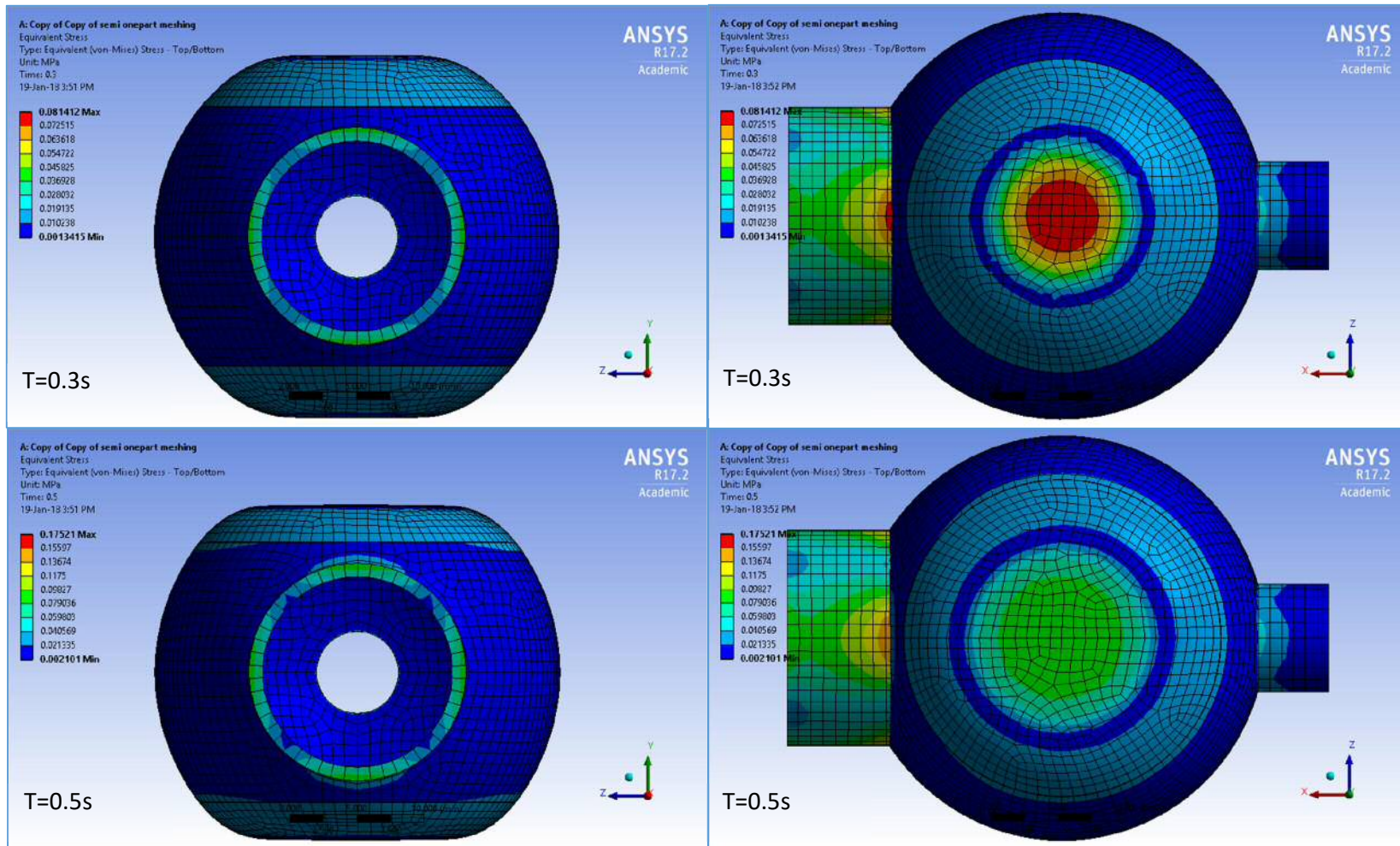


Figure 4-29 Equivalent elastic strain distribution map of the 1st stage FSI. On the left is ZY view (front view), and on the right is the XZ (top view) for  $0.3s \leq t \leq 0.5s$



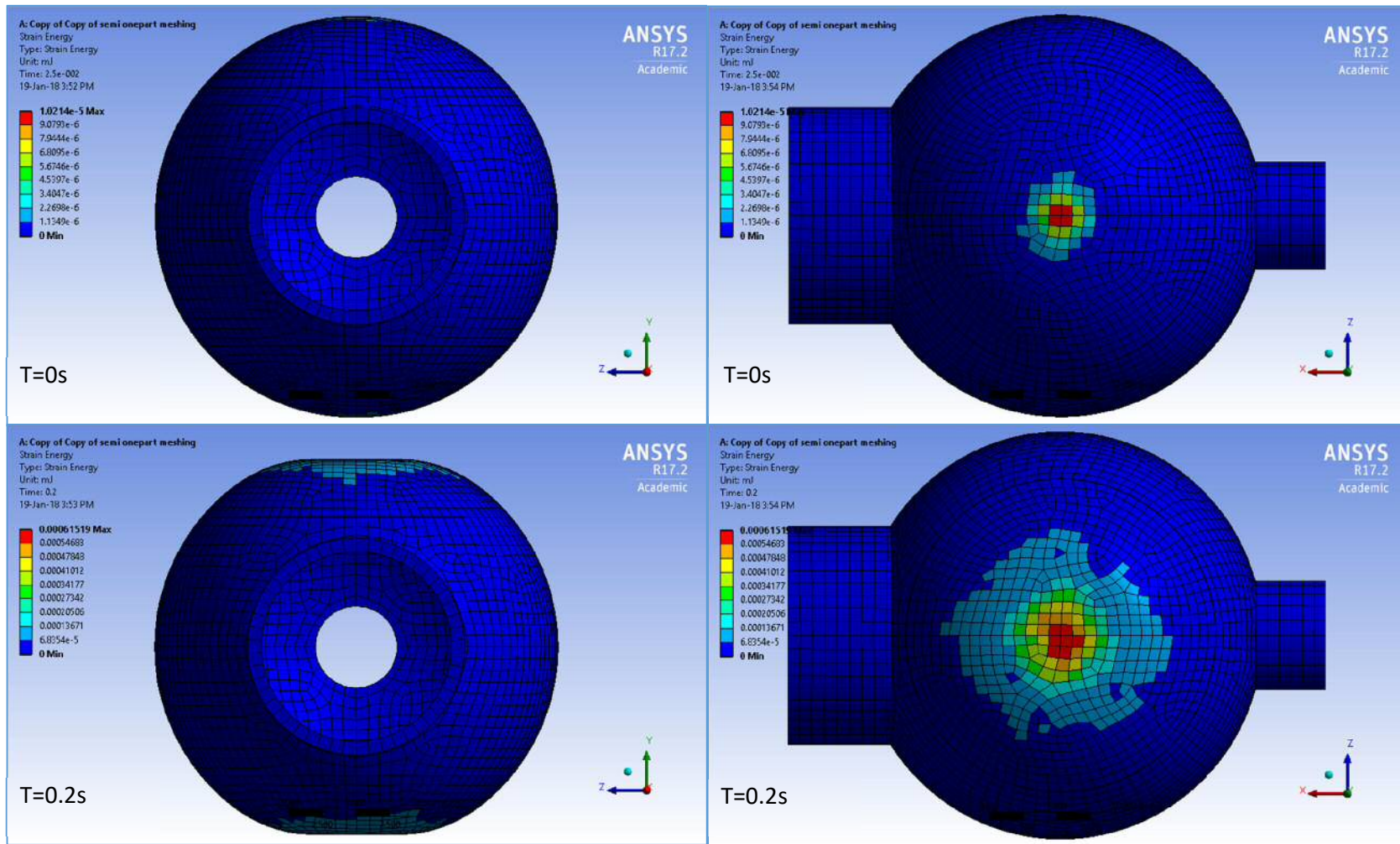


Figure 4-30 Strain energy distribution map of the 1st stage FSI. On the left is the front view ZY vie (front view), and on the right is the XZ (top view) for  $0 \leq t \leq 0.2$  sec

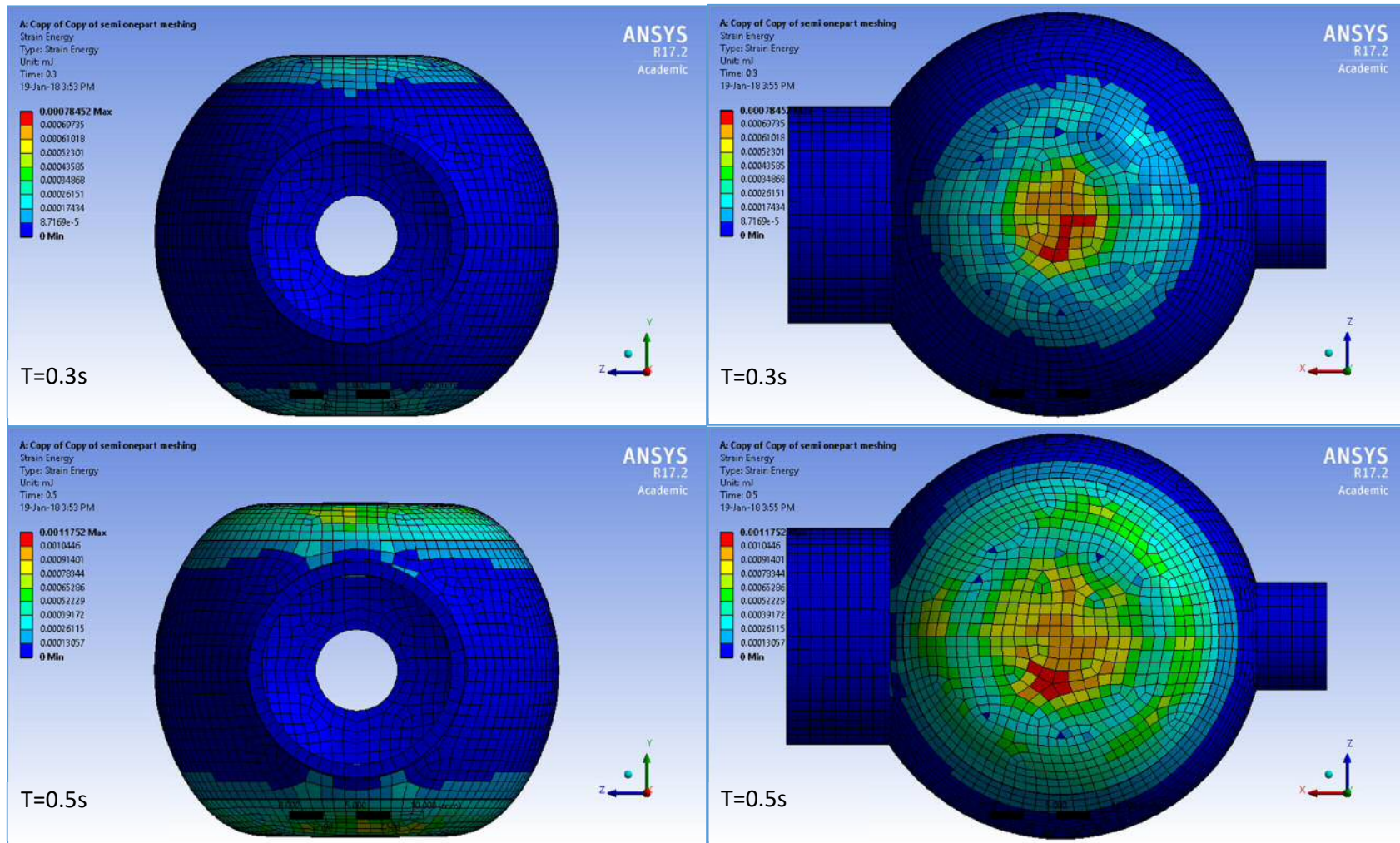


Figure 4-31 Strain energy distribution map of the 1st stage FSI. On the left is the front view ZY vie (front view), and on the right is the XZ (top view) for  $0.3s \leq t \leq 0.5$  sec

The 3D printed material was tested for mechanical properties to be used in the curve fitting of the hyperelastic model in the computational model in ANSYS. This step was done as part of the hyperelastic model computational validation process.

#### 4.2.6. Preliminary Model Validation

To validate the computational model, a physical model was designed using a 3D printed hyperelastic material. The data collected from the flow sensor was compared to the computational model using water material properties as the fluid and the curve fitted material model for the structural part. The Arduino software provides a tool to monitor the flow and the associated data required for the validation including the velocity. Usually, the Arduino software exports the collected data, but to facilitate the data collection procedure, a macro (PLX-DAQ) was used instead. This makes the monitoring of the data easier, and assessing the data during the experiment is faster. The Arduino code attached in the Appendix of this thesis shows the formulae used in the calculation of the velocities and flow rate at 0.1 s of the experiment time. The time step used was the same time step that was used in the computational model.

Unlike the velocity measurements shown in Figure 4-18, Figure 4-20 shows the velocity measured by the Arduino relating to time during the simulation. To validate that with the computational model, a pulsed velocity was measured in the computational post-CFD during the compression and release. Also, the Arduino keeps measurements of the fluid flow and hence of the inlet and outlet velocity throughout the experiment, as can be seen in Figure 4-32. The highest value of the computational simulation, as mentioned in section 4.2.4, shows good comparison to the measurement recorded in the flow sensor of 0.0784 m/s at the end of the compression period at  $t=0.5$  s.

Although the velocity magnitude was close in both cases, the velocity profile was different, and this is due to the calculated process used in ANSYS for averaging the element data through each iteration time (Figure 4-33). An additional factor of the velocity profile is the boundary conditions used in the computational results. As the valves used in the experiment were set to a higher value than one compression, the valves were replaced with sealing material to the inlet and outlet to allow the flow of the water during the experiment. The inlet velocity showed the same velocity profile as that obtained in the compression stage due to the same flow sensor characteristics.

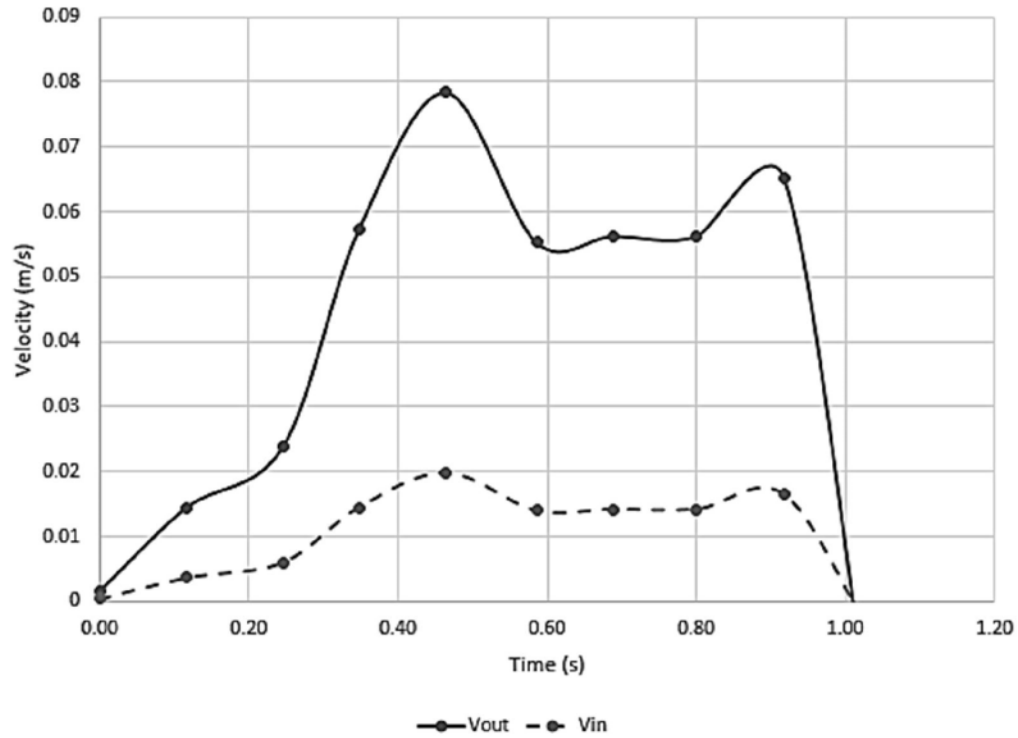


Figure 4-32 The inlet and outlet velocity profile obtained from the flow sensor in the validation rig design. The profile showing the velocity through the compression and release as the velocity is a function of flow rate

The inlet magnitude recorded a value higher than the value obtained from the computational model, as shown in Figure 4-33. The high magnitude of the inlet velocity refers to the flow generated by the release of the plate. This was done without the use of an external manual pump to replicate the process by the computational model. Also, the flow sensor records the flow through the whole compression, so the velocity was measured according to the flow sensor data, which is why the inlet and outlet velocity results were throughout the whole second unlike in the computational model, where it shows the inlet as a wall during the compression and the outlet as a wall during the release with zero velocity during the simulation.

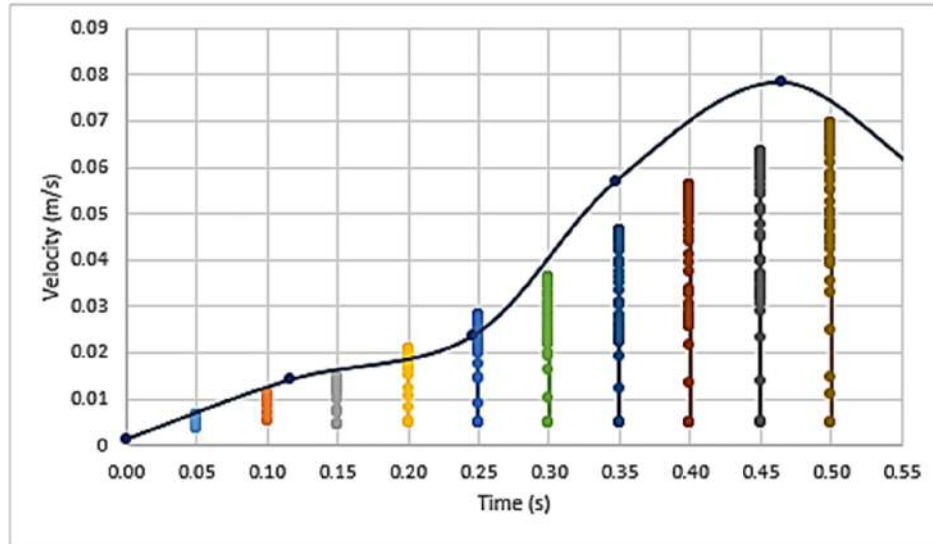


Figure 4-33 Velocity vs time of the validated computational model with the experimental data. The impulse results represents the data extracted from post-CFD in reference to the time of the computational simulation, while the velocity profile results are the data obtained from the flow sensor during the validation rig.

The manual pump was used only once before the first compression to fill the sphere and prepare the physical model for the compression of the fluid. If the manual pump were not used, the sphere would be empty and the compression would not result in a flow from the outlet. The experiment was set to 15 compressions with 1 compression and release in 1 second. This was used to accommodate the compression machine and the flow sensor criteria. The measured velocity was during the first compression of the experiment to validate the results with the same time step of the computational model. Consistent with findings in the total deformation of the transient structural (Figure 4-34 and Figure 4-35), the surface of the 3D printed sphere was deformed in the same regions, which gives a good indication of the choice of reduced contact surfaces of the computational model. The inlet and outlet of the structural FSI showed no deformation during the simulation due to the added constraints to the inlet and outlet, and that was the case in the physical model where the inlet and outlet were constrained by the attached tubing and hence no deformation occurred during the physical compression. Moreover, the outlet position was deformed during the compression, and that was the case during the compression phase of the computational model as outlet constraint was in the X, Y and rotational axis of the model.

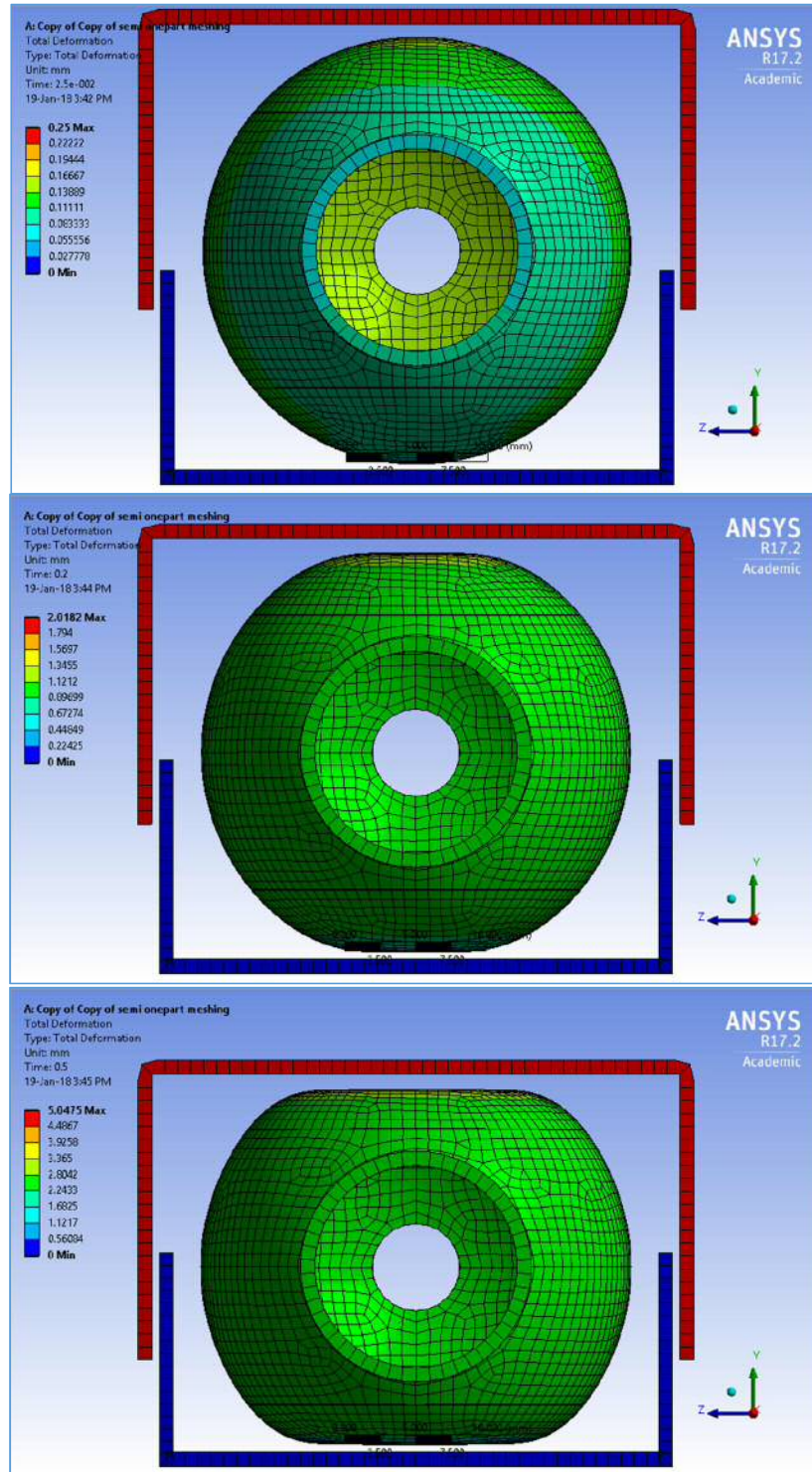


Figure 4-34 Total mesh deformation during the compression phase of the FSI simulation in transient structural in the YZ coordinate. The compression and support plates are shown as rigid shell surfaces during the compression and the colour coded distribution map represent the areas of element deformation characteristic during the compression.

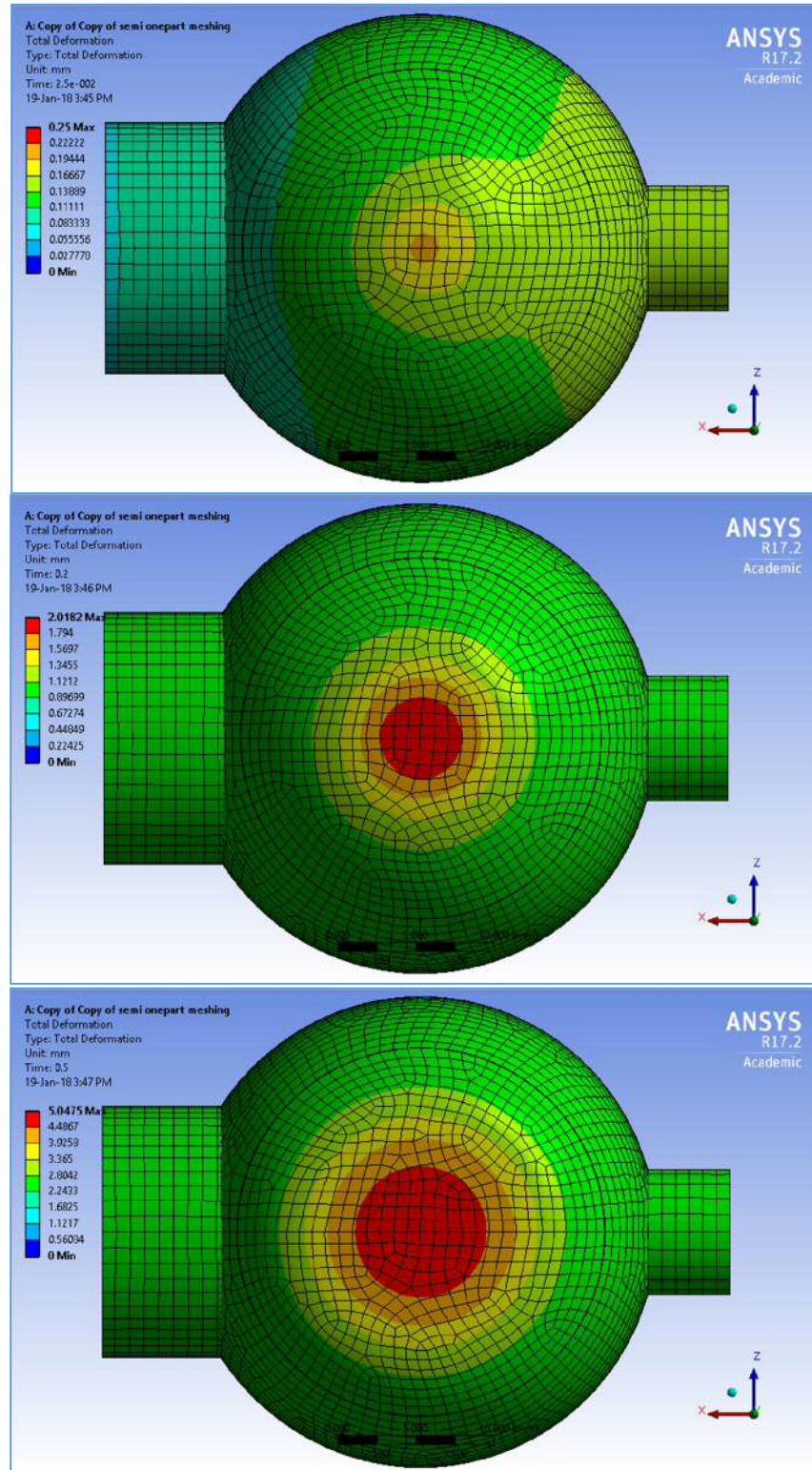


Figure 4-35 Total mesh deformation during the compression phase of the FSI simulation in transient structural in the ZX coordinate. The compression and support plates are shown as rigid shell surfaces during the compression and the colour coded distribution map represent the areas of element deformation characteristic during the compression.

From the experimental results, the present physical model agrees relatively well with the data from the computational model regarding the deformation of the structural part along with the velocity magnitude obtained in both models. The computational model, however, gives more potential to the design analysis, as the stress was not measured in the experimental rig, given that the DIC technique used in the previous material properties experiment will give data of the viewed area. However, it will be difficult to compare this with the stress obtained from the computational model, as the transient structural component measures the average of the deformed mesh elements of the entire geometry.

### **4.3. Subject-specific Model**

Blood flow has been traditionally represented using the incompressible Navier-Stokes equations in a fixed Eulerian frame of reference, and it can be accurately represented as an incompressible fluid whose constitutive behaviour is usually approximated by a non-Newtonian model. However, blood velocity and pressure fields can be greatly influenced by the motion of external or internal cardiovascular structures, such as the contracting cardiac muscle, moving heart valves, or deforming large arteries of the body. Characterisation of the mechanical behaviour of the moving vascular structure (usually in a Lagrangian frame of reference) and its interactions with the blood flow is necessary in cardiovascular modelling. Modelling the interactions between an incompressible blood flow and a deforming vascular structure represents one of the major challenges in the field of cardiovascular mechanics. In this section, subject-specific models (MRI and CT scan) are used as the next step for a better representation of the CPR process. The results of the compression outflow simulation are demonstrated in a series of images. The CFD data, Figure 4-36 to Figure 4-56, illustrate the evolution of blood flow through time. Transient blood wall stresses and strains are shown in Figure 4-59 to Figure 4-70.

#### **4.3.1. FE and post-CFD data**

To eliminate the inverse element mesh issue, each part of the interfacing surfaces were imported separately by setting the connection method in the FE package and in Fluent. Before the initiation of the simulation, the contact tool was used to identify the gap and penetration characteristics of the contacting elements. Reducing the contact area decreased the computational cost.



### **Post CFD Pressure Distribution**

Left ventricular lumen pressure is the dominant factor in force transduction between blood and tissue in the simulated cardiac physiology. To maintain the inflow and outflow of blood, average pressure within the left ventricular chamber is seen to decrease during the compression and increase during the release at the boundaries.

As Figure 4-36 to Figure 4-41 demonstrate, induction of blood flow out of the left ventricle induces a series of pressure waves, which travel predominantly axially down the vertical axis of the chamber. The decrease in the pressure is due to the increase in the velocity magnitude, which will be explained in the next section with the location of the predominant vortices of the fluid flow. As a consequence, the peak observed pressure moves throughout the compression phase as alterations in regions of red and blue, corresponding to highs and lows of pressure. During the compression, the pressure was recorded with a negative sign as an indication of the outflow of the fluid through the outlet and recorded its highest value at  $t=0.3$  s of 8.8Pa at the apex of the left ventricle. The lowest value of the pressure was recorded at the end of the compression with reverse flow in the entire geometry, and outflow at the centre of the outlet.

During the release phase of the simulation, the pressure was displayed as contours at the plane passing through the inlet and outlet and the pressure gradient streamlines. Due to the flow through the inlet, the pressure contours were decreasing, recording the highest value at the inlet boundary condition (Figure 4-39 to Figure 4-41).

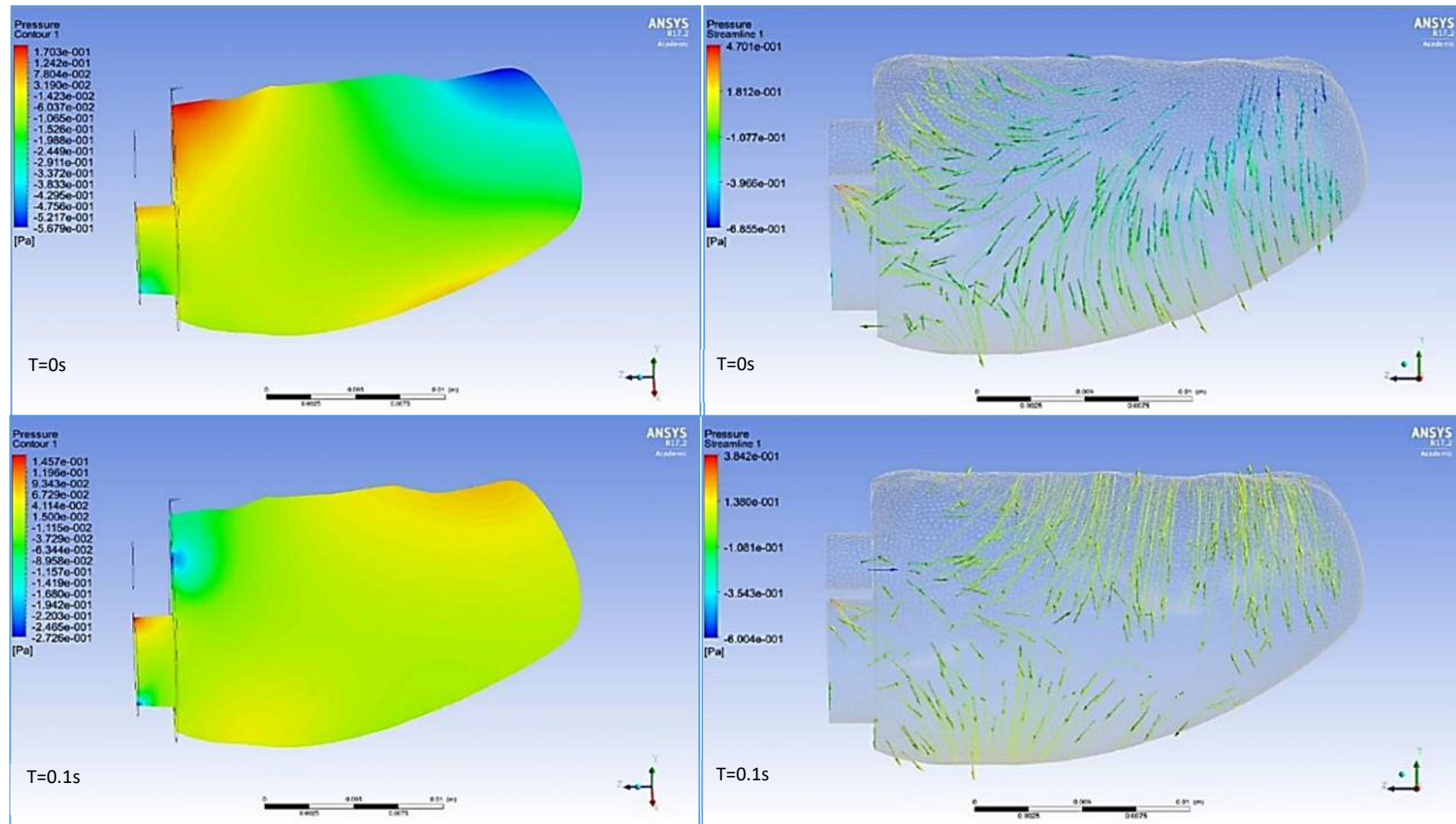


Figure 4-36 Pressure contour of the subject-specific fluid in the CFD post during the compression stage of FSI. On the right are the streamlines for those pressure gradients during different time steps throughout the simulation. The collected data are for  $0 \leq t \leq 0.1$  sec and the orientation is changed between the images for better representation of the data, the coordinate is indicated in the lower left corner for each image

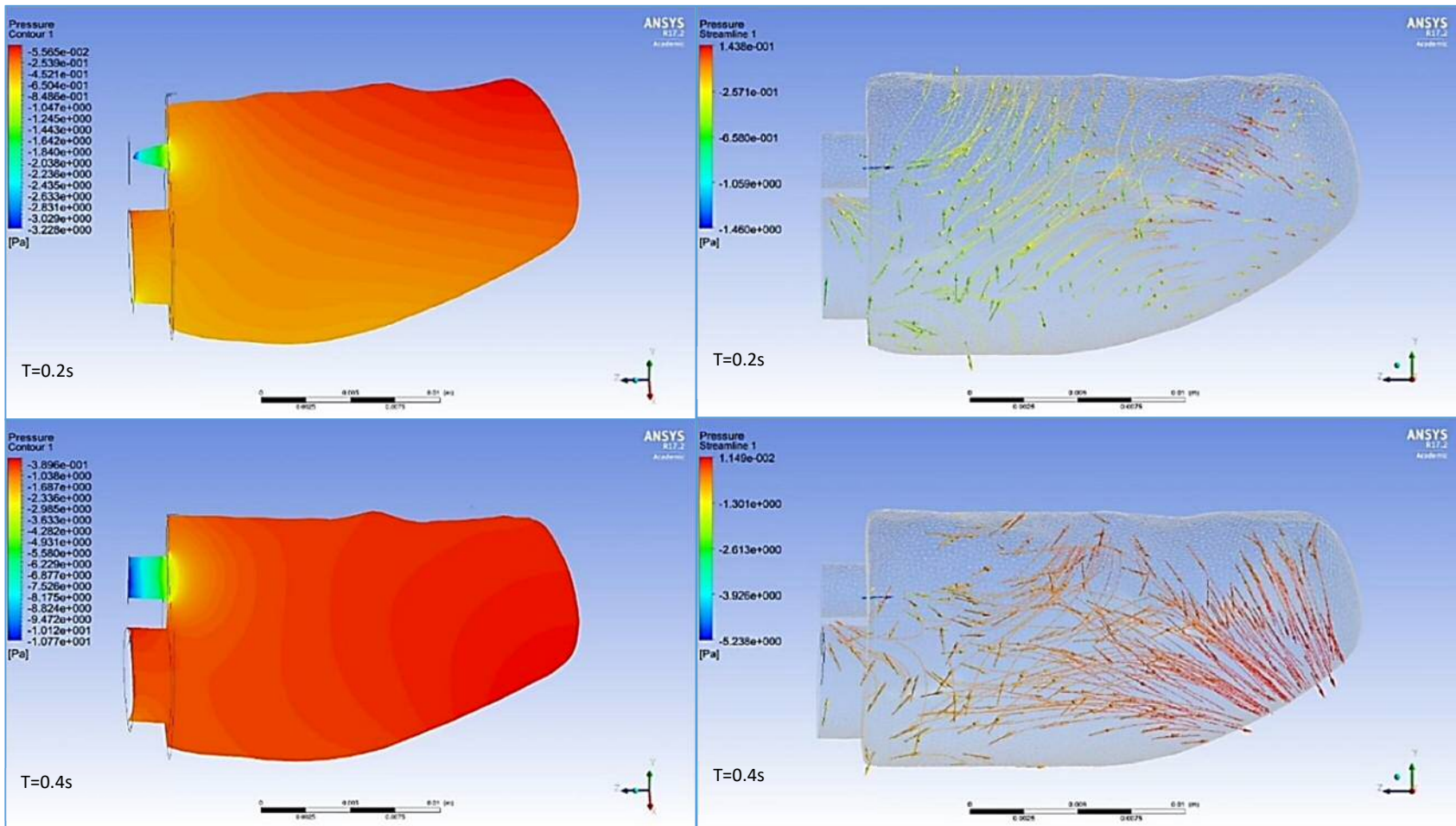


Figure 4-37 Pressure contour of the subject-specific fluid in the CFD post during the compression stage of FSI. On the right are the streamlines for those pressure gradients during different time steps throughout the simulation. The collected data are for  $0.2 \leq t \leq 0.4$  sec and the orientation is changed between the images for better representation of the data, the coordinate is indicated in the lower left corner for each image.

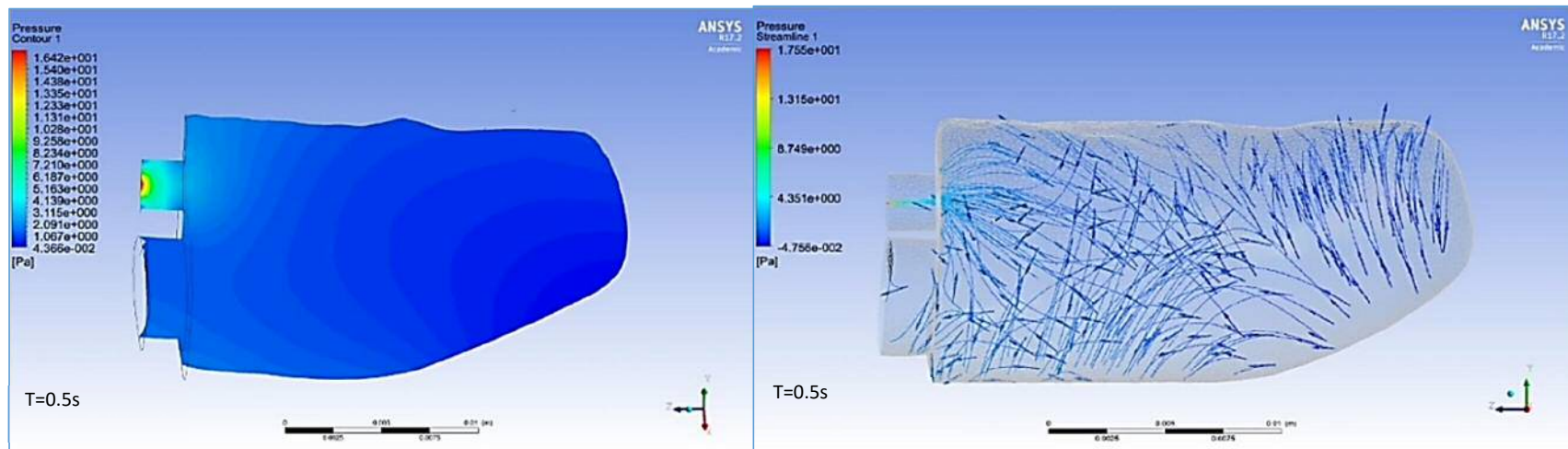


Figure 4-38 Pressure contour of the subject-specific fluid in the CFD post during the compression stage of FSI. On the right are the streamlines for those pressure gradients during different time steps throughout the simulation. The collected data are for  $t=0.5$  sec and the orientation is changed between the images for better representation of the data, the coordinate is indicated in the lower left corner for each image.

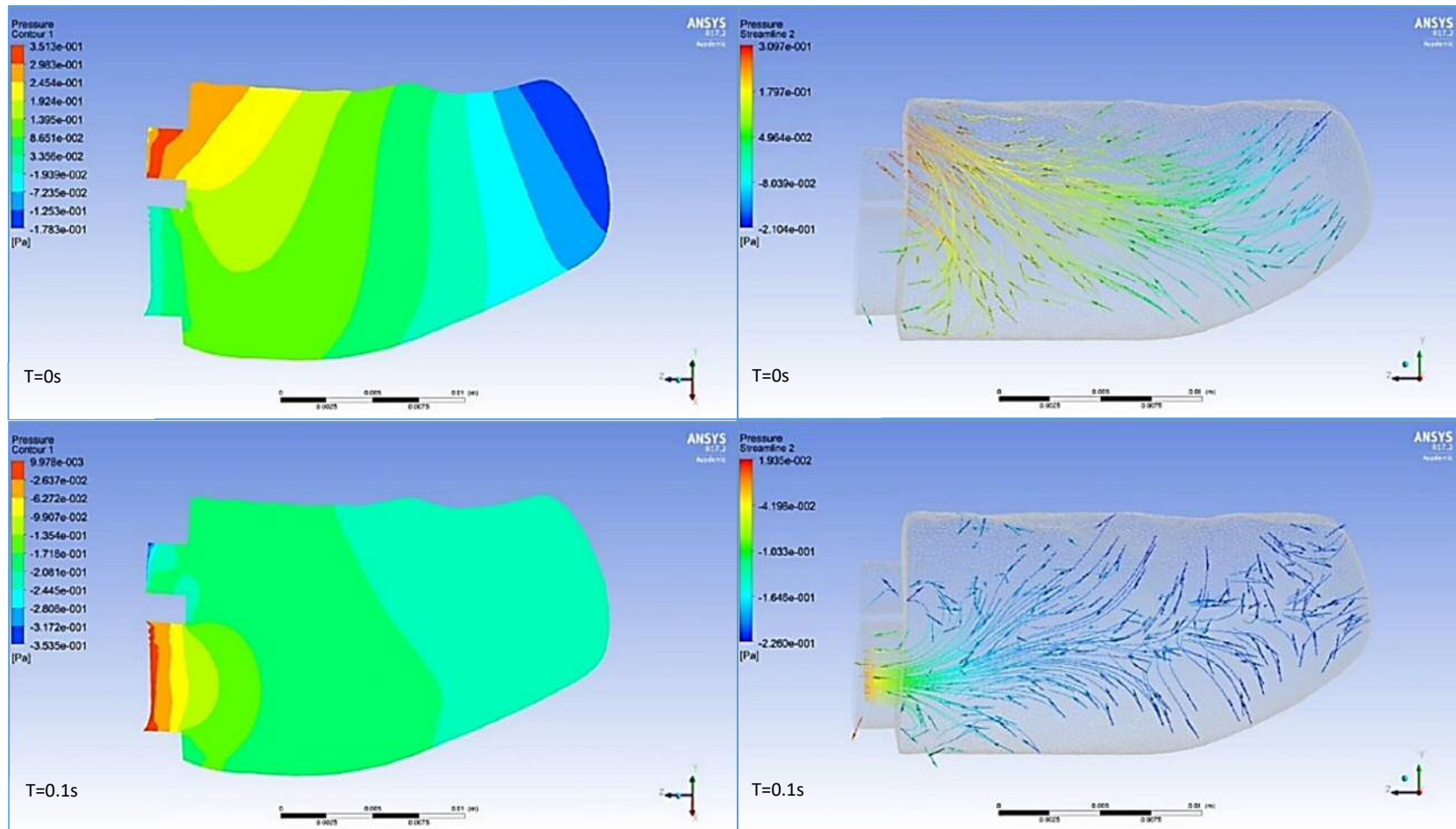


Figure 4-39 Pressure contour of the subject-specific fluid in the CFD post during the release stage of FSI. On the right are the streamlines for those pressure gradients during different time steps throughout the simulation. The collected data are for  $0 \leq t \leq 0.1$  sec and the orientation is changed between the images for better representation of the data, the coordinate is indicated in the lower left corner for each image.

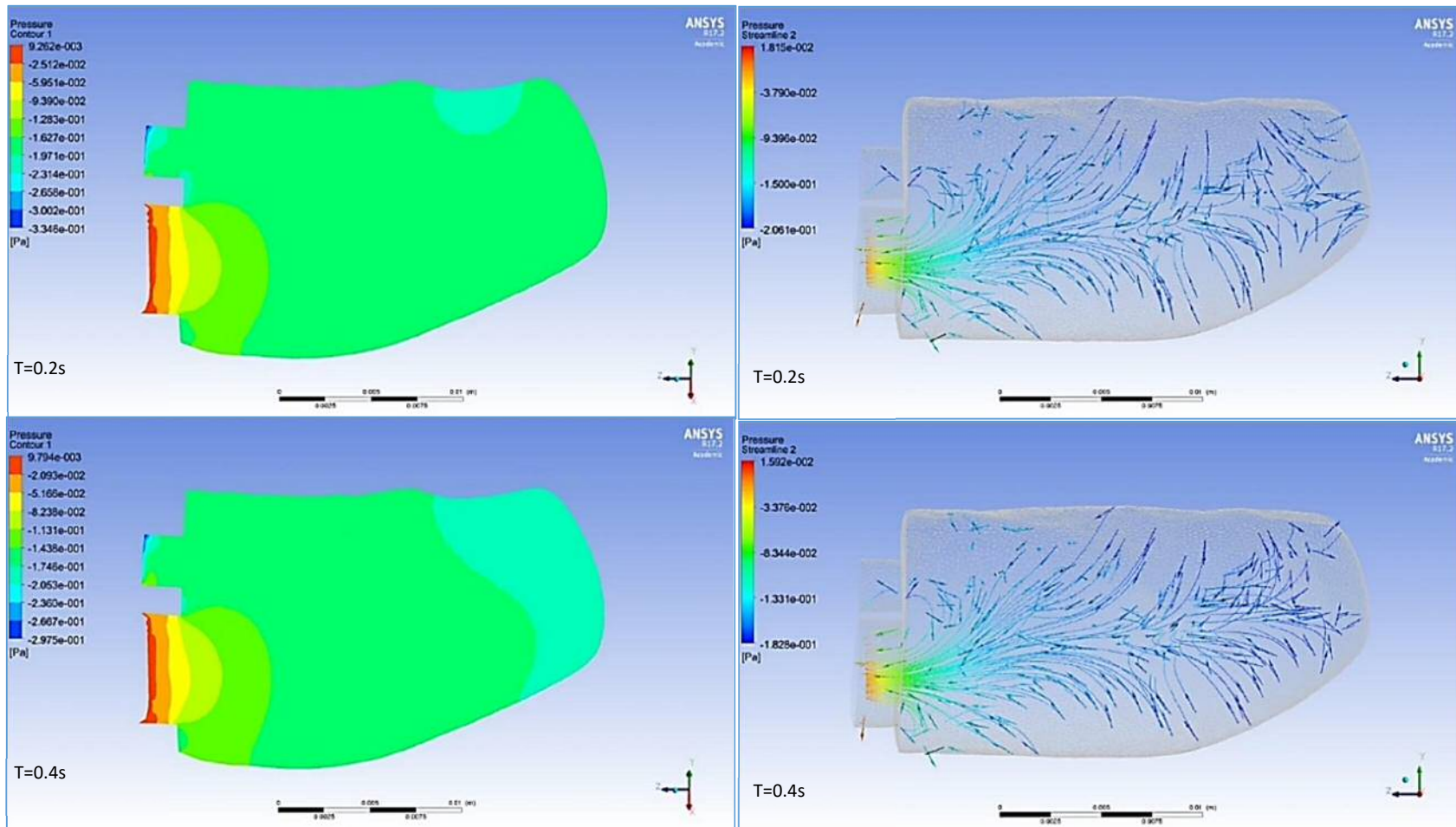


Figure 4-40 Pressure contour of the subject-specific fluid in the CFD post during the release stage of FSI. On the right are the streamlines for those pressure gradients during different time steps throughout the simulation. The collected data are for  $0.2s \leq t \leq 0.4$  sec and the orientation is changed between the images for better representation of the data, the coordinate is indicated in the lower left corner for each image.

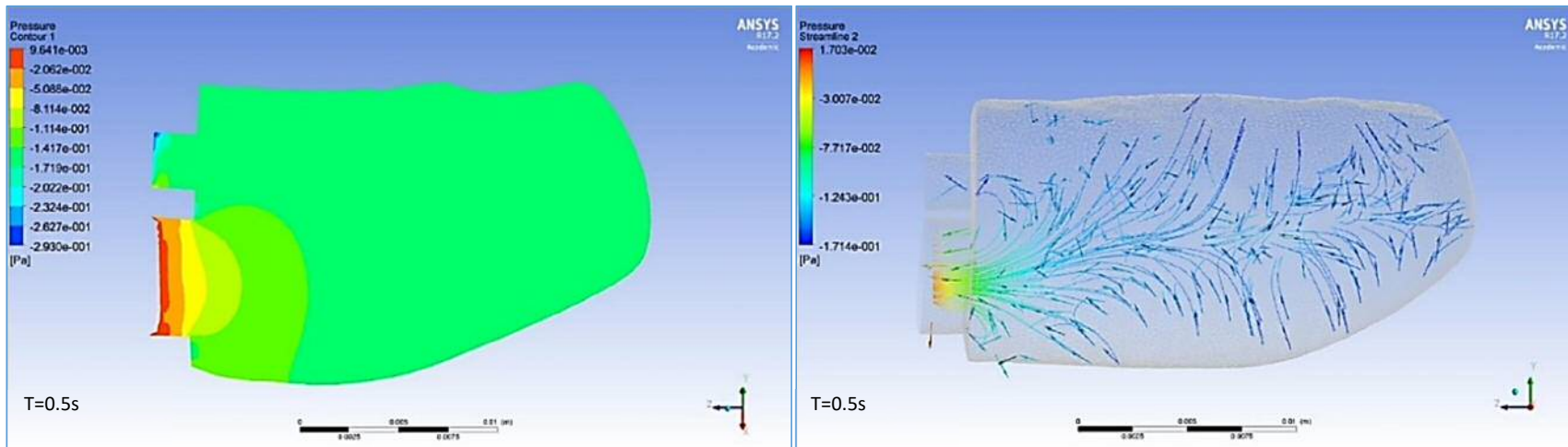


Figure 4-41 Pressure contour of the subject-specific fluid in the CFD post during the release stage of FSI. On the right are the streamlines for those pressure gradients during different time steps throughout the simulation. The collected data are for  $t=0.5$  sec and the orientation is changed between the images for better representation of the data, the coordinate is indicated in the lower left corner for each image.

### **Post CFD Velocity Distribution**

The velocity profiles over the compression and release period are presented in Figure 4-42 to Figure 4-53 in terms of flow pattern, direction, distribution magnitude, and stream lines. Because of dynamic changes in the blood flow behaviour at certain time steps during the simulation, the results are focused separately for the assigned time illustrated in these figures. The flow regime is presented by the velocity vectors and streamlines on the symmetric YZ plane. Three planes were chosen to present the velocity in order to focus on the vortices and streamlines at the boundary conditions. Two planes were located on the YZ orientation, but with different X+, each one passing through one of the boundary conditions (the outlet and inlet respectively). The third plane was oriented at the base of three points passing through inlet, outlet, and the apex of the LV geometry. The same planes were used in the compression and release FSI stages. As the blood flow is stabilized ( $t > 0.3$  s) with a magnitude of  $6.78e-2$  m/s, the velocity distributions (presented in Figure 4-43, Figure 4-45, and Figure 4-48) remain as a permanent pattern of blood flow for the rest of the simulation. However, the magnitude of the velocity at the outlet area obviously changes as a result of different flow rates from the pulsatile inflow.



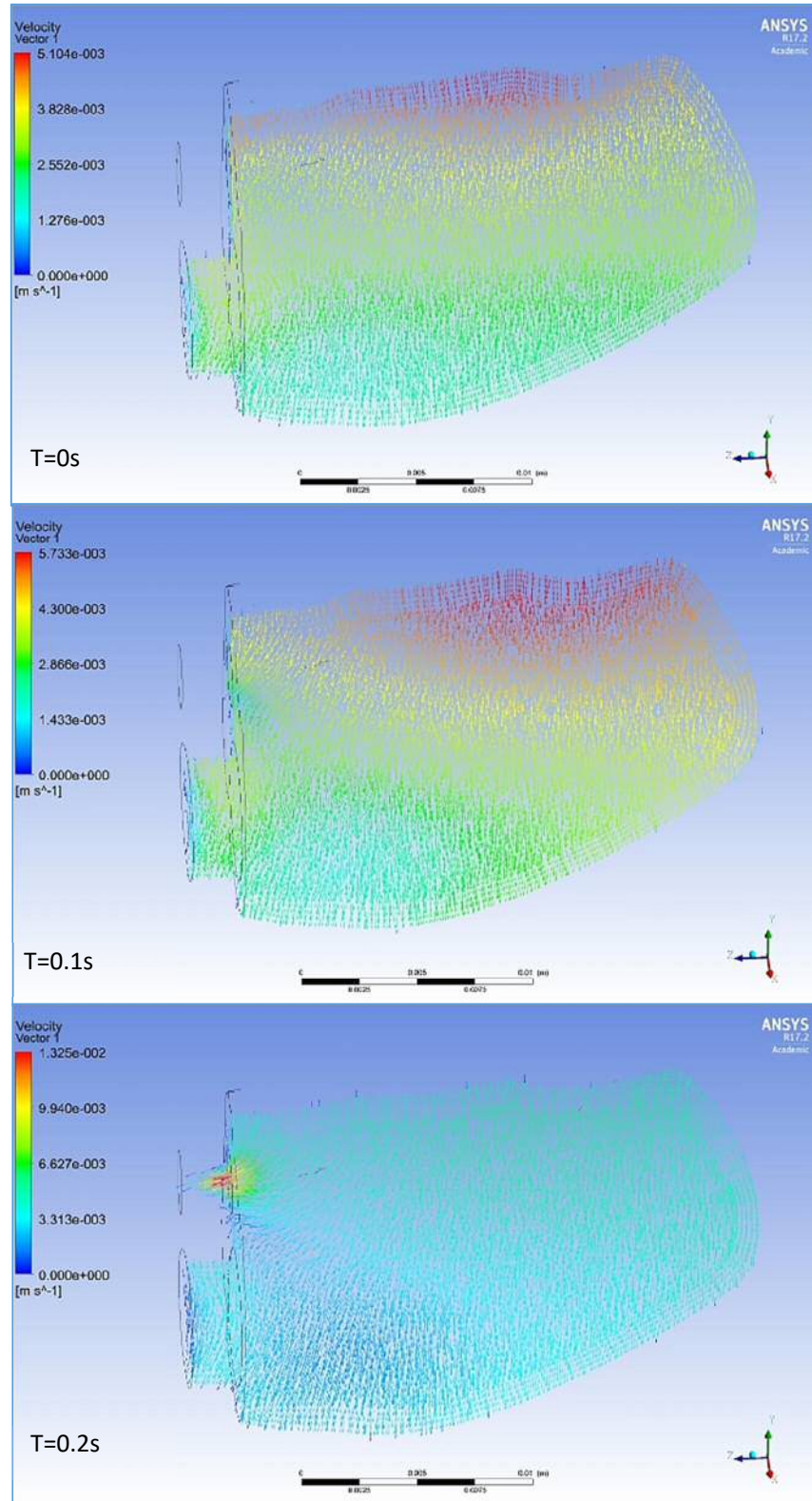


Figure 4-42 Velocity vectors for the fluid across the X+ three-point plane (inlet, outlet and apex plane) of the LV fluid in post CFD during 1st stage of FSI for  $0 \leq t \leq 0.2$  sec.

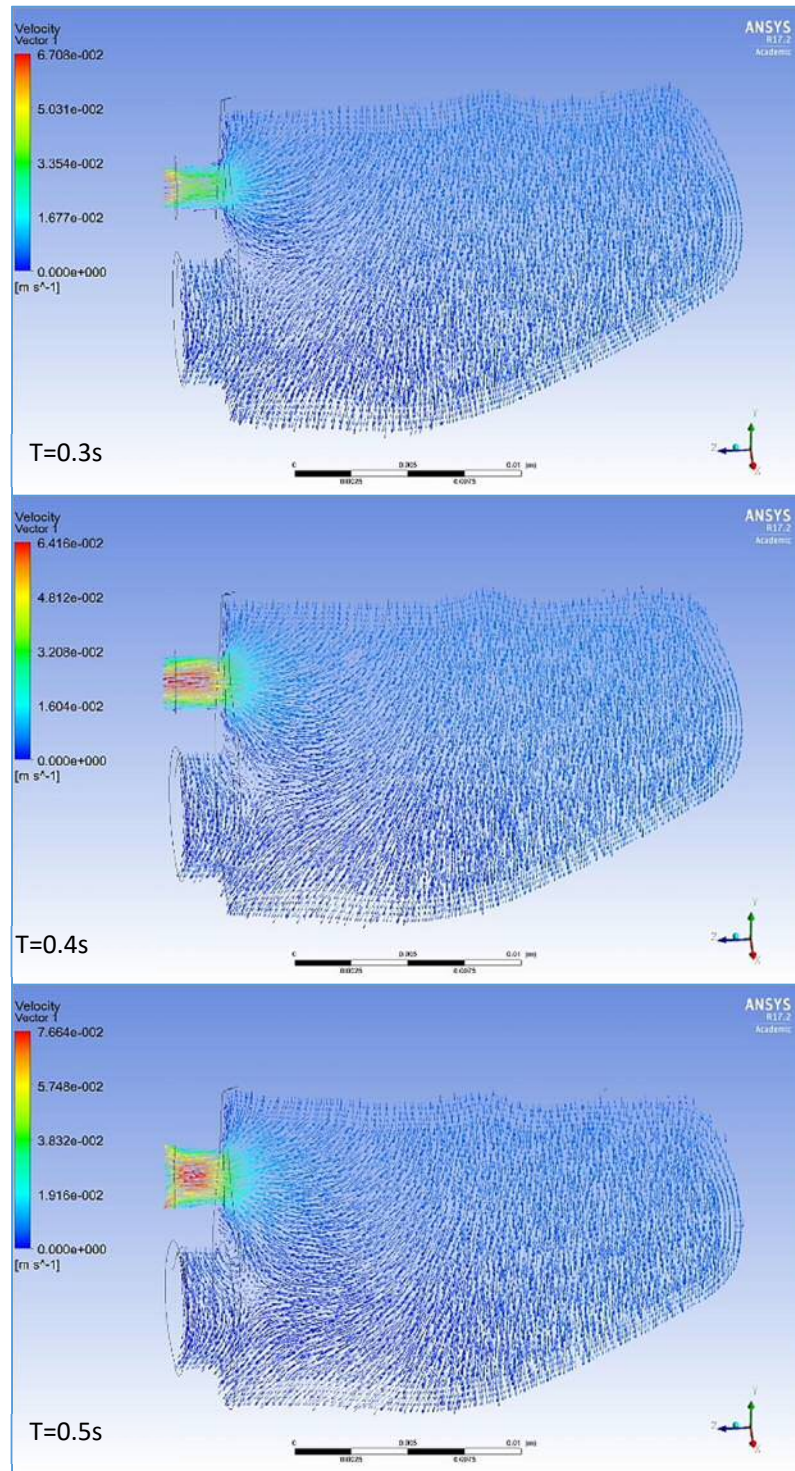


Figure 4-43 Velocity vectors for the fluid across the X+ three-point plane (inlet, outlet and apex plane) of the LV fluid in post CFD during 1st stage of FSI for  $0.3s \leq t \leq 0.5$  sec.

Generally, the blood velocity in a left ventricle during the compression phase causes a reverse flow and creates axial vortices in the apex and near the outlet (Lassilaa et al., 2012, Lemmon and Yoganathan, 2000, Moosavi et al., 2014, Doost et al., 2016, Saber et al., 2003). The character of a highly transient and disturbed flow field becomes most apparent in the YZ planes passing through the boundary conditions (Figure 4-44). At  $t=0.1$  s and  $t=0.2$  s, reverse flow is established in the outlet as a result of high-velocity flow through the outlet and low volume velocity in the plane.

The interaction between the reversed flow and the forward flow was finally balanced at  $t=0.3$  s, which caused a uniform recirculation zone at this point (Figure 4-45). The minimum velocity value was found to be behind the outlet area at the end of the compression (Figure 4-48). The velocity vectors show the velocity distribution in which a vortex appeared around the heel of the outlet boundary and another at the inferior wall of the LV. The first vortex started at  $t=0.1$  s and grew until the end of the compression while the second one appeared at the end of the compression, which can be more clearly seen in the outlet intersection plane shown in Figure 4-44 and Figure 4-46. In comparison to the inlet plane view, the vortex started at  $t=0.1$  s with a magnitude of  $5.733e-5$  m/s at the inferior wall of the LV, which is caused mainly by the forced reverse flow toward the inlet wall boundary. This vortex grew much larger through the duration of the simulation to split into two vortices with a low velocity compared to the high-velocity blood in the upper wall of the LV. This can be seen in the inlet intersection plane in Figure 4-46.

As the time progresses ( $t=0.3$  s), the vortex at the outlet grows and moves down backward because of the higher velocity. The minimum velocity was still found to be in the lower zone. A similar trend continues for the next time step at  $t=0.4$  s, where the effect for reverse flow is minimized. The velocity magnitude of  $7.664e-2$  m/s was recorded at the end of the simulation at  $t=0.5$  s.

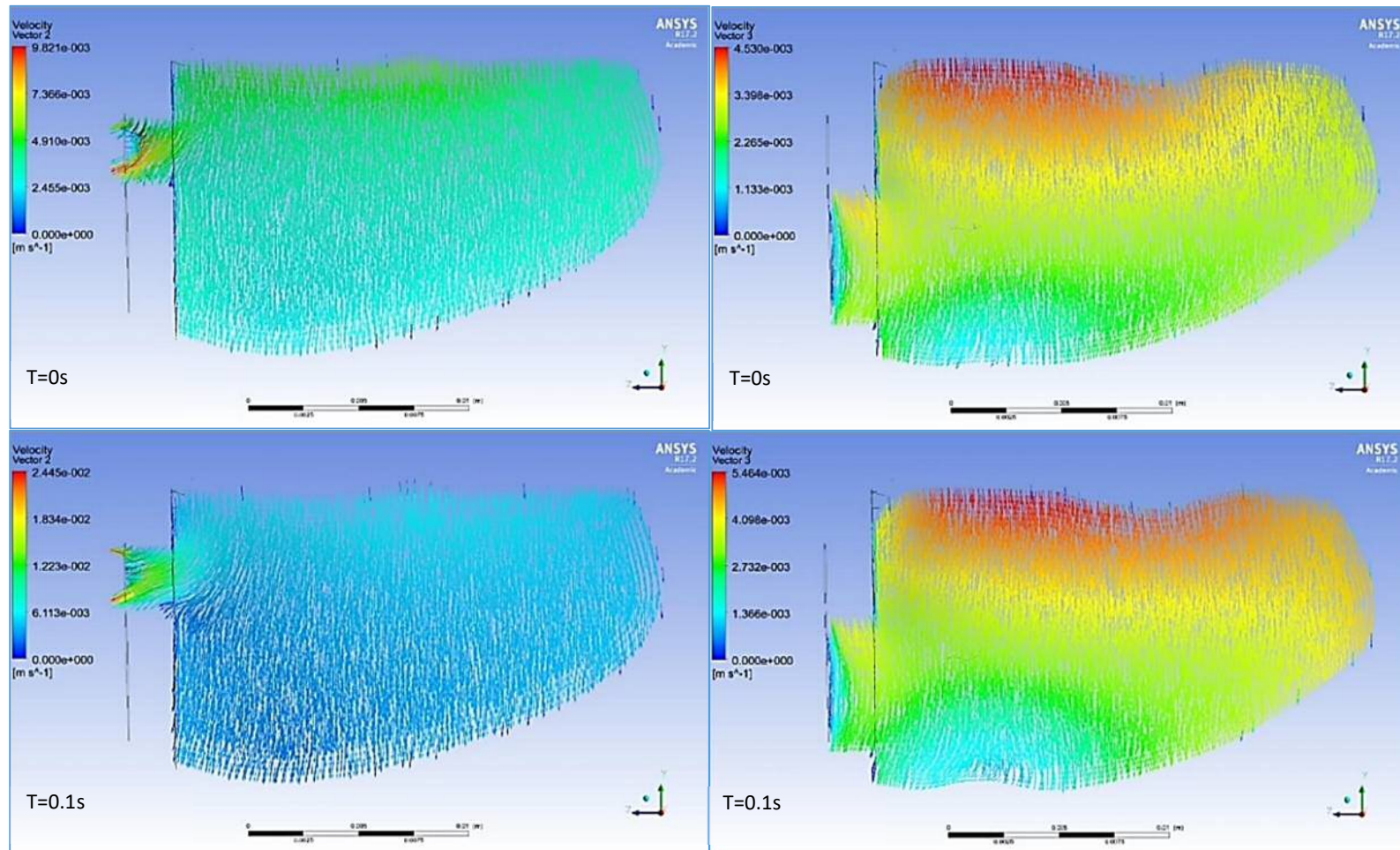


Figure 4-44 On the left, velocity vectors for the LV fluid across the outlet Y plane, and on the right, velocity vectors for the LV fluid across the inlet Y plane in CFD post during 1st stage of FSI for  $0 \leq t \leq 0.1$  sec.

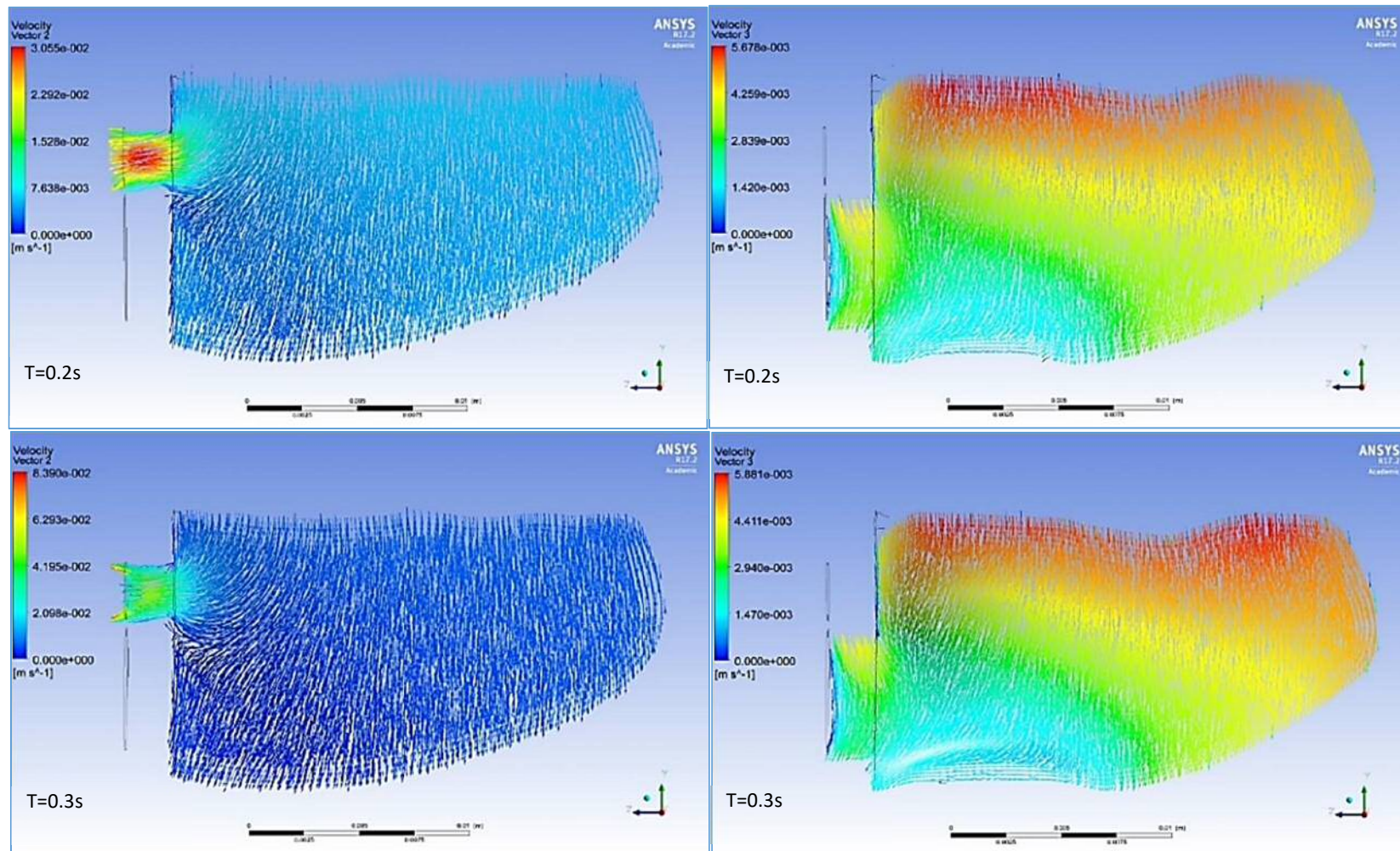


Figure 4-45 On the left, velocity vectors for the LV fluid across the outlet Y plane, and on the right, velocity vectors for the LV fluid across the inlet Y plane in CFD post during 1st stage of FSI for  $0.2s \leq t \leq 0.3$  sec.

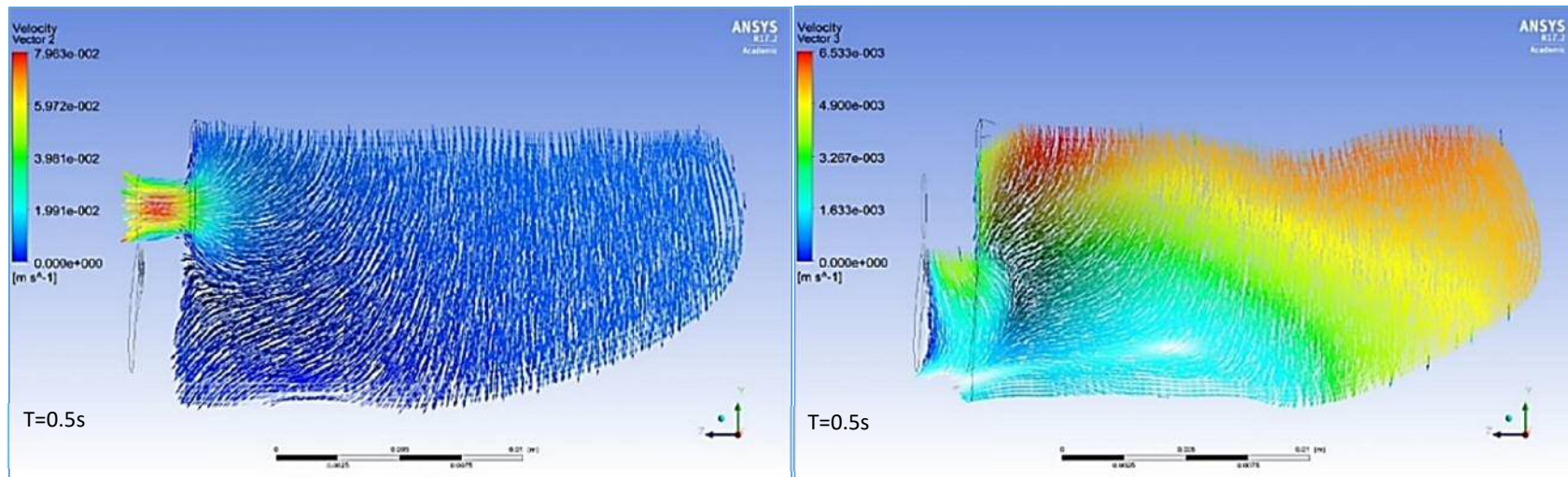


Figure 4-46 On the left, velocity vectors for the LV fluid across the outlet Y plane, and on the right, velocity vectors for the LV fluid across the inlet Y plane in CFD post during 1st stage of FSI for  $t=0.5$  sec.

For the time steps  $t > 0.4$  s, reversed flow ceases and forward flow is re-established toward the outlet (Figure 4-43 and Figure 4-45). The vectors data show the uniform flow near the wall of the LV during the compression through the inflation meshed area. This shows the laminar flow criteria of the blood flow through the geometry during the compression stage.

In the release phase of the simulation, the high velocities are found in the core of the inlet boundary conditions, which can be seen in Figure 4-49 and Figure 4-50. At  $t=0.1$  s and  $t=0.2$  s, reverse flow is established in the boundaries of the inlet, especially at the lower edge as a result of high-velocity flow through the outlet and low volume velocity in the plane. At  $t=0.3$  s, a vortex starts to be generated at the lower wall of the LV, and as is shown in Figure 4-52, the vortex is more prominent in the outlet plane while it seems to be split into two vortices in the inlet plane vectors. The interaction of these vortices forces the flow to move upward to the upper wall causing the velocity to increase at that area while maintaining a low value in the bottom.

In general, the left atrium and its pulmonary veins are commonly neglected for simulations of ventricular filling and mitral valve motion. During the cardiac cycle simulation, the imposed inlet profile is often approximated to a uniform pressure condition or some symmetric velocity profile across the mitral annulus. In this study, the inlet velocity profile is generated through the compression phase volume change and the imposed pressure and velocity from the compression stage of the FSI simulation. If more physiological representations of the atrium with venous inflows are included, atrial vortices will be generated. Those vortices will induce a non-uniform velocity profile across the mitral opening, which in turn, will influence the leaflets' dynamics and the intraventricular flow pattern.

In valve-less ventricles, the most observed phenomenon is the formation of an annular vortex ring behind the mitral orifice. The vortex ring penetrates the ventricle depending on the ratio of the mitral inlet to ventricular radius. Fluid injection across an orifice into a larger container can result in the generation of vortex rings if the ratio of orifice to cavity diameter is in a certain range (Shortland A. P. et al., 1996, Martinez-Legazpi et al., 2014).

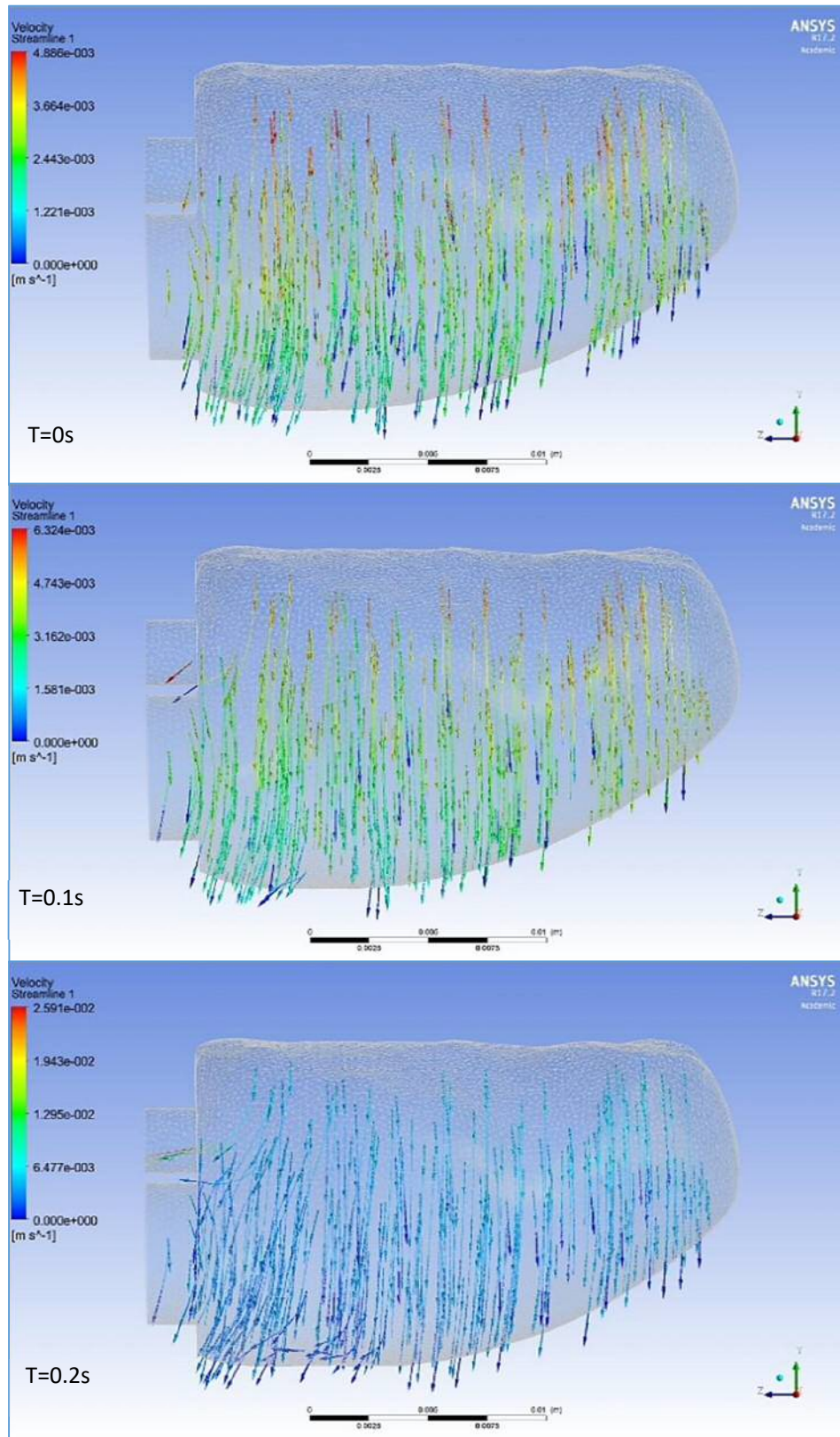


Figure 4-47 Velocity profile streamlines of the LV fluid in the CFD post during 1<sup>st</sup> stage of FSI for  $0 \leq t \leq 0.2$  sec.



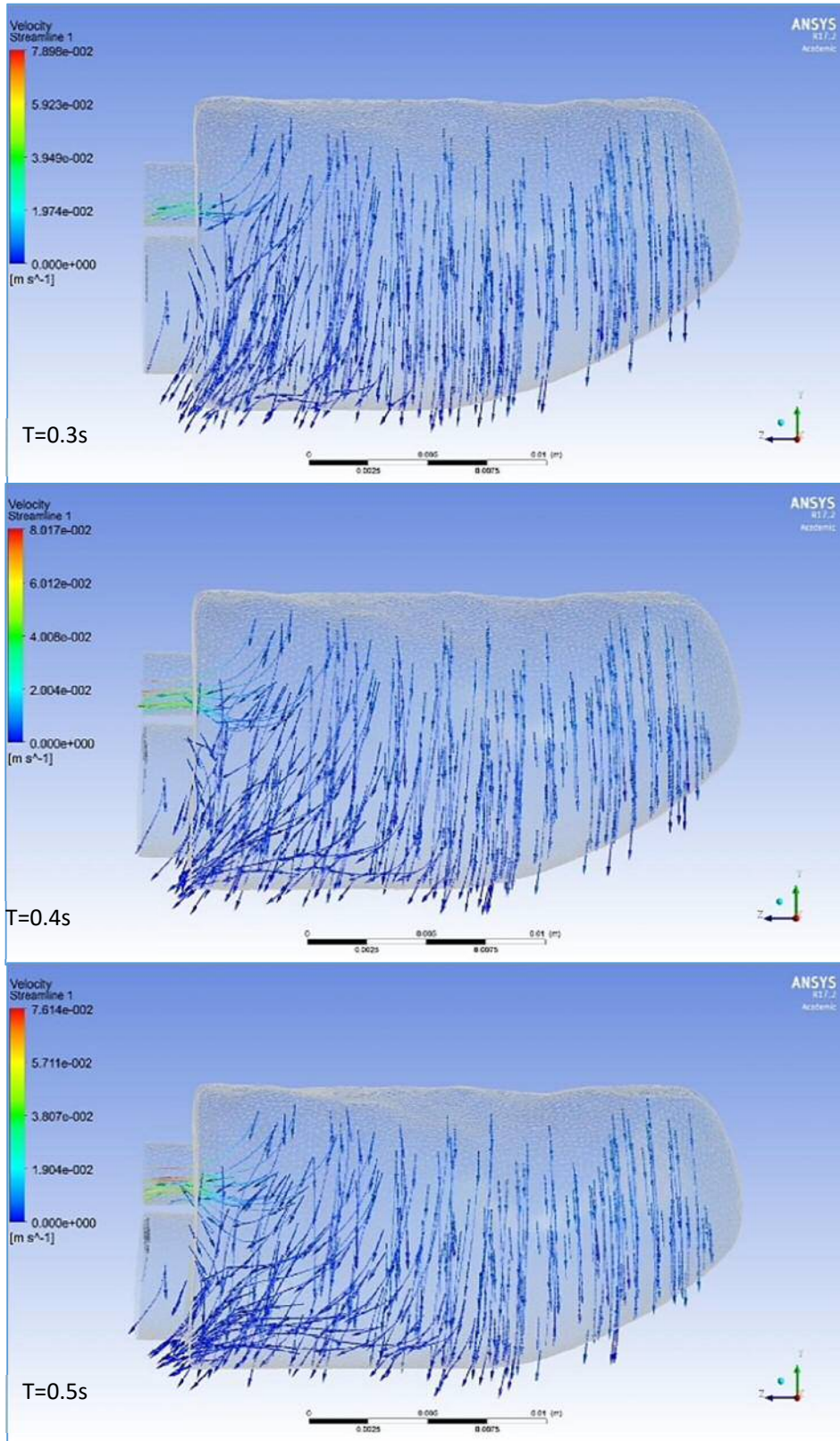


Figure 4-48 Velocity profile streamlines of the LV fluid in the CFD post during 1<sup>st</sup> stage of FSI for  $0.3 \leq t \leq 0.5$  sec.

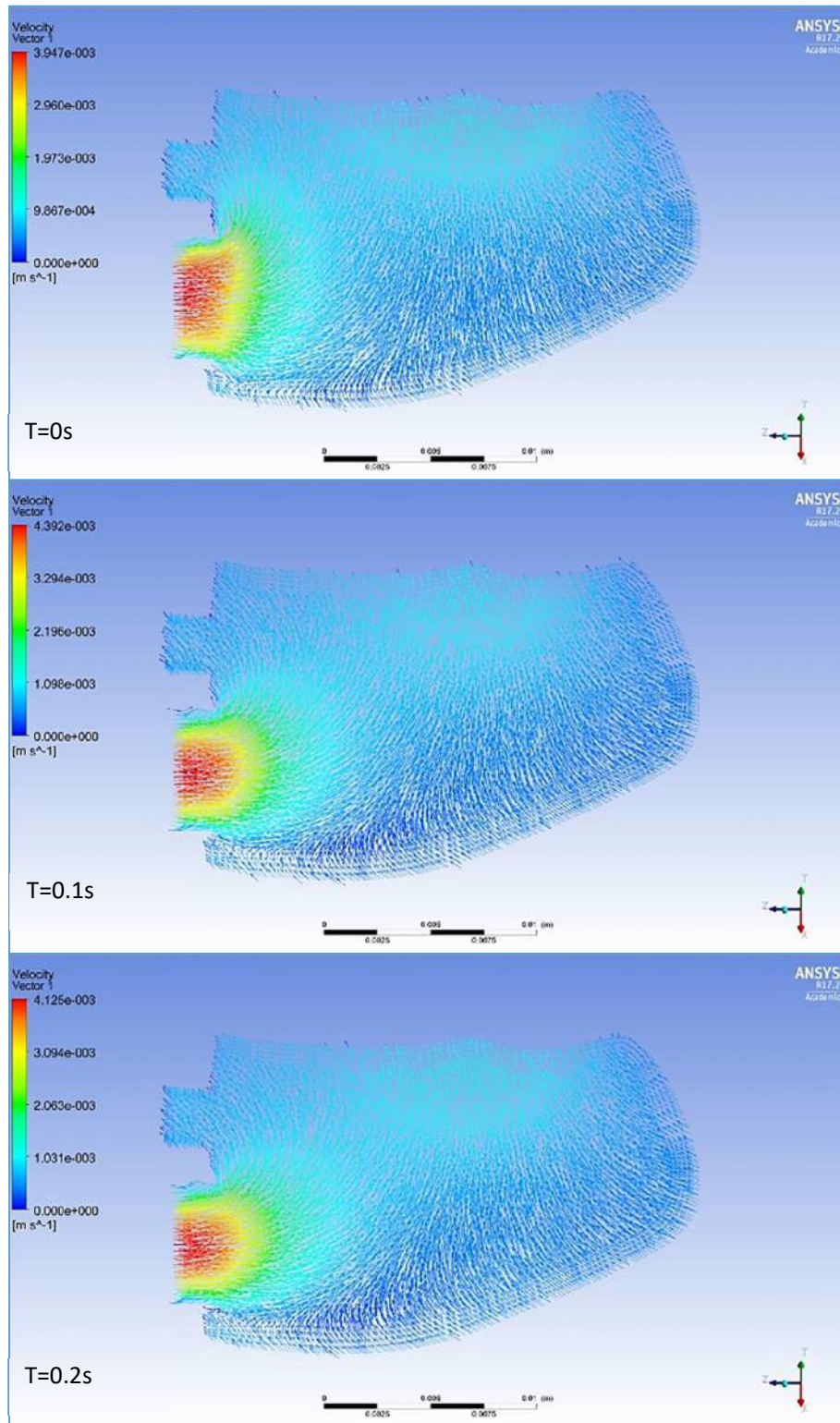


Figure 4-49 Velocity vectors for the fluid across the inlet and outlet plane of the LV fluid in CFD post during 2nd stage of FSI for  $0s \leq t \leq 0.2$  sec.

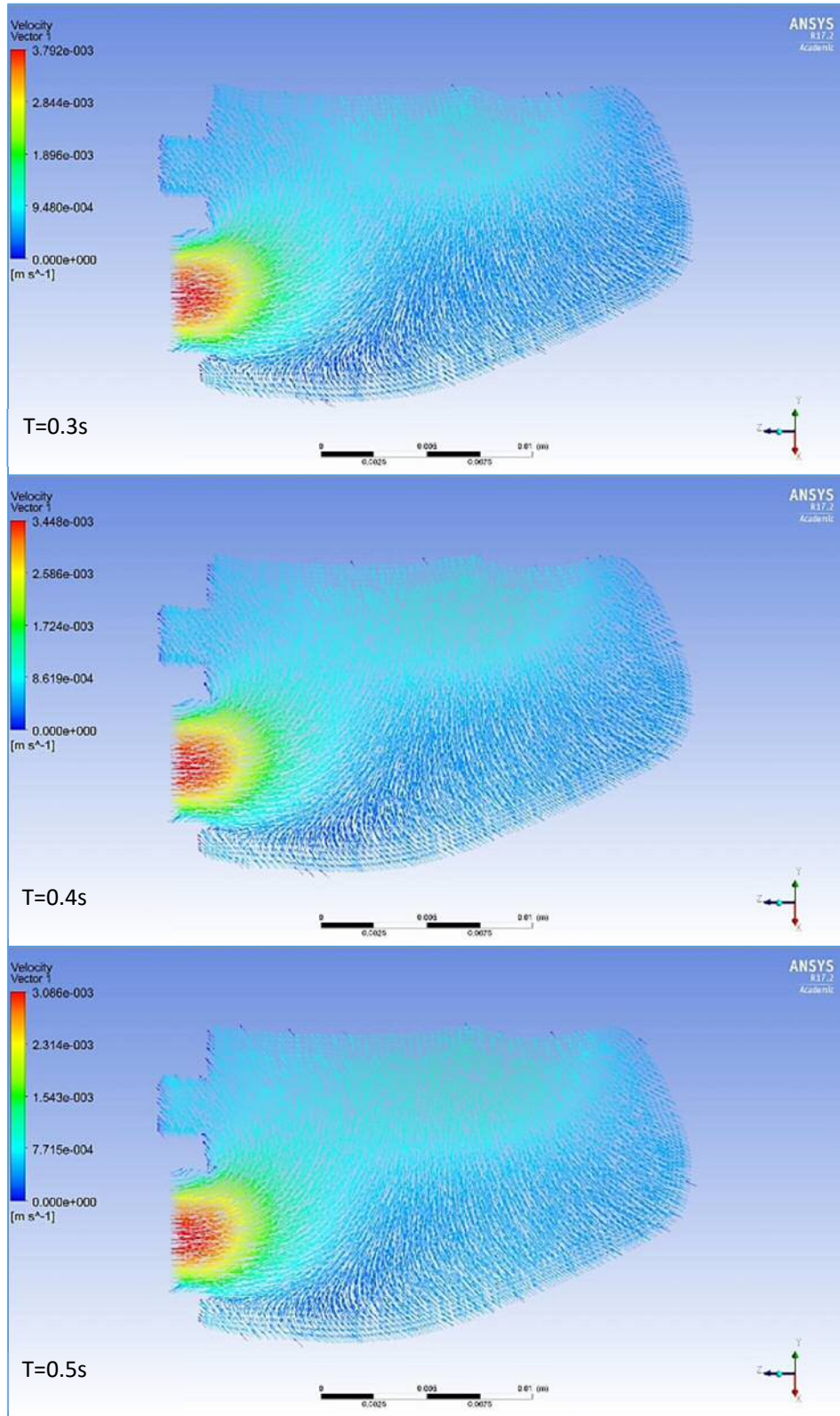


Figure 4-50 Velocity vectors for the fluid across the inlet and outlet plane of the LV fluid in CFD post during 2nd stage of FSI for  $0.3 \leq t \leq 0.5$  sec.

Moreover, the large vortex at the base of the LV is desirable due to the fact that the large vortex ring enhances the flow redirection toward the aorta by preserving the incoming blood flow momentum. The ratio of mitral inlet to ventricular radius will therefore play an important role in the formation and propagation of vortices during the LV filling phase, especially when no leaflets are present (Dahl, 2012). Experiments have shown that if the ratio is smaller than about 0.5, the propagation of vortex rings is possible. If the ratio is larger than 0.6, the vortices will be arrested or will not develop.

Figure 4-54 demonstrates the distribution of the velocity across the central axial line of the outlet boundary condition. During the initial time steps of the systolic phase ( $0.05 \text{ s} < t < 0.3 \text{ s}$ ), the velocity profiles are very low with the same profile shape. The maximum velocities are reported at  $t=0.3$  and  $0.4 \text{ s}$ . Similar results are shown in Figure 4-42 and Figure 4-43.

The shift of the velocity profile during the simulation is related to the change of position during the simulation, as the compression displacement depth increases as the blood volume is transferred according to the total mesh displacement. The flow becomes fully developed after this point with respect to time.

The outlet velocity profiles are generated with the inlet as a wall boundary condition with zero velocity. This indicates that the generated velocity in the outlet has the required velocity profile for the blood flow with a lower velocity magnitude compared to the cardiac cycle (Martinez-Legazpi et al., 2014).

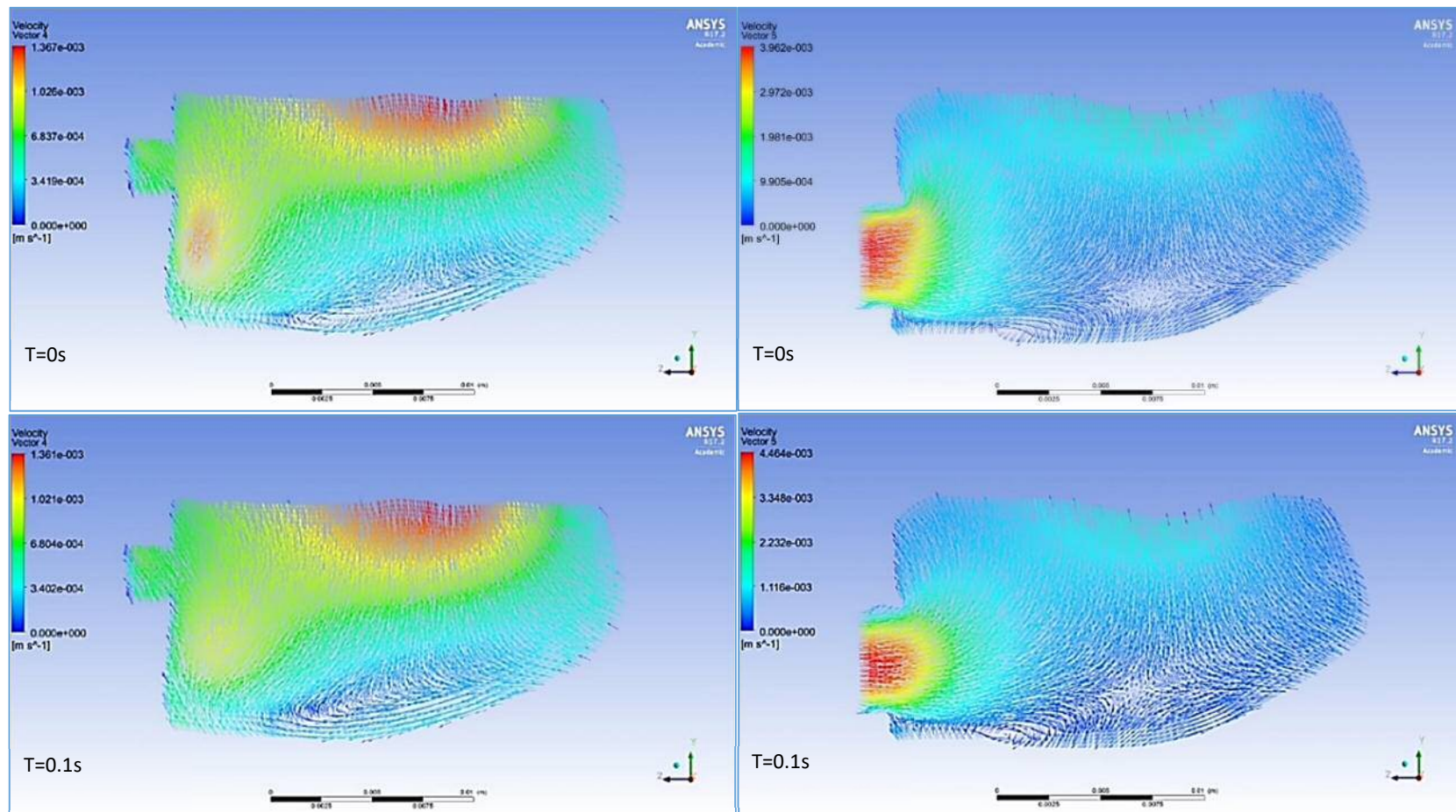


Figure 4-51 On the left are velocity vectors for the LV fluid across the outlet Y plane, and on the right, the velocity vectors for the LV fluid across the inlet Y plane in CFD post during the 2nd stage of FSI for  $0 \leq t \leq 0.1$  sec.

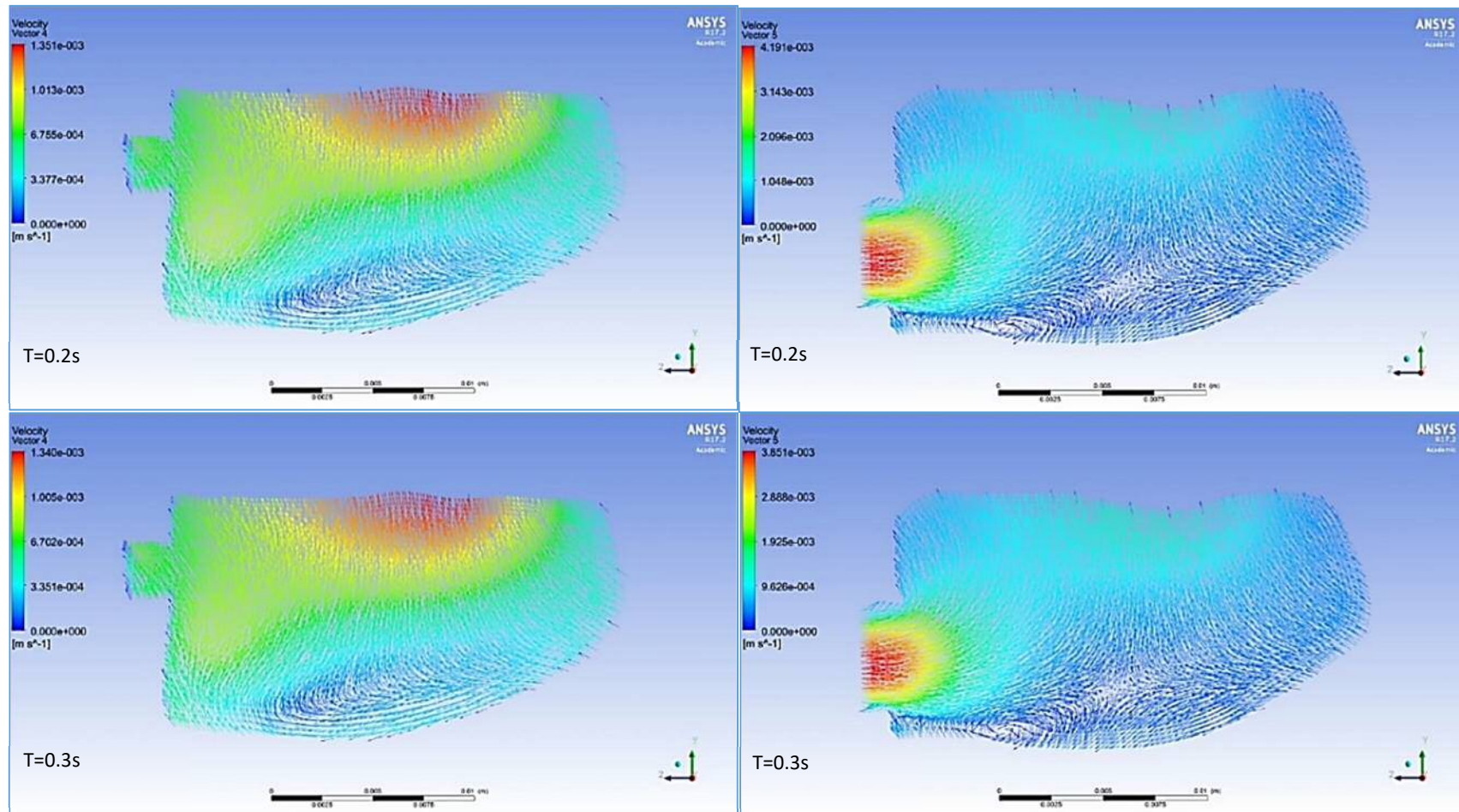


Figure 4-52 On the left are velocity vectors for the LV fluid across the outlet Y plane, and on the right, the velocity vectors for the LV fluid across the inlet Y plane in CFD post during the 2nd stage of FSI for  $0.2 \leq t \leq 0.3$  sec.

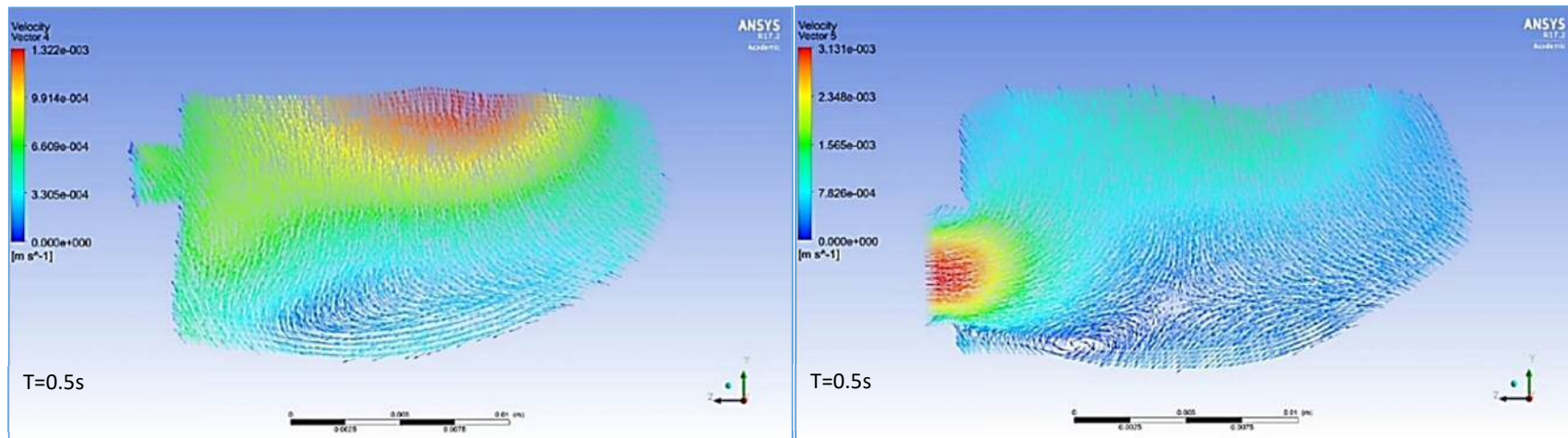


Figure 4-53 On the left are velocity vectors for the LV fluid across the outlet Y plane, and on the right, the velocity vectors for the LV fluid across the inlet Y plane in CFD post during the 2nd stage of FSI for  $t=0.5$  sec.

The stable pattern of flow is established as the flow accelerates from the upper deforming wall towards the outlet. Flow fields showed features of a quasi-steady laminar flow, and an almost symmetrical velocity profile is observed during the FSI simulation.

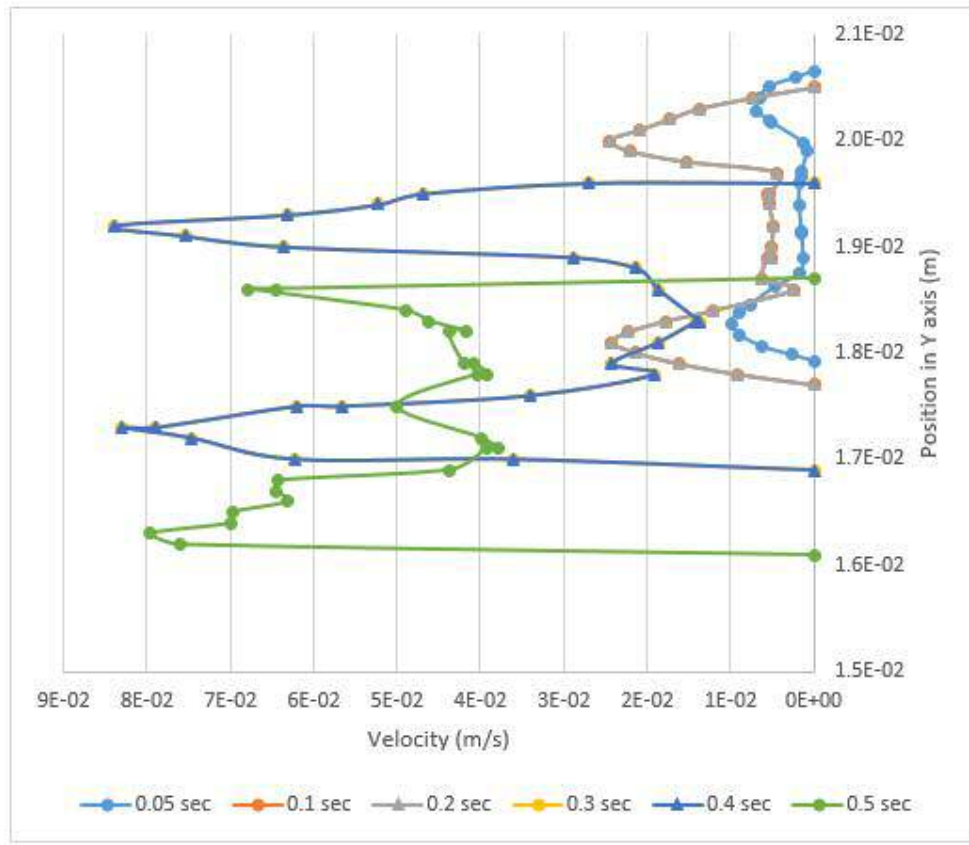


Figure 4-54 Velocity profile measured across the centre of the outlet of the LV at different times during the compression phase of FSI simulation

Figure 4-54 and Figure 4-55 demonstrate the variation of the velocity magnitudes in compression and release respectively at selected times. As can be observed, mostly, the velocity magnitudes of the model in the FSI stage have the same pattern. In the release FSI model, the velocity magnitude rises at the start of the simulation, and it starts to decrease after  $t=0.2$  s. This is caused by the steadiness of the vortex during that period of the simulation, and it can be seen in Figure 4-49 to Figure 4-53.

The velocity profile, however, agrees with the previous studies of the cardiac cycle velocity models (Doost et al., 2016, Hadi Wiputra et al., 2016). The generation of vortices in the release phase is observed to be less than in the compression model, and this is an indication of the limitation to the use of a pre-stressed model in ANSYS FSI. The velocity magnitude is seen to



be less than the velocity magnitude in the compression model, and this is in agreement with the LV behaviour to supply the systematic circulation with the required velocity and pressure. However, the velocity is still less than the velocity magnitude in the normal cardiac cycle, which requires multiple compressions to produce the efficient velocity to retain the normal physiology of the heart.

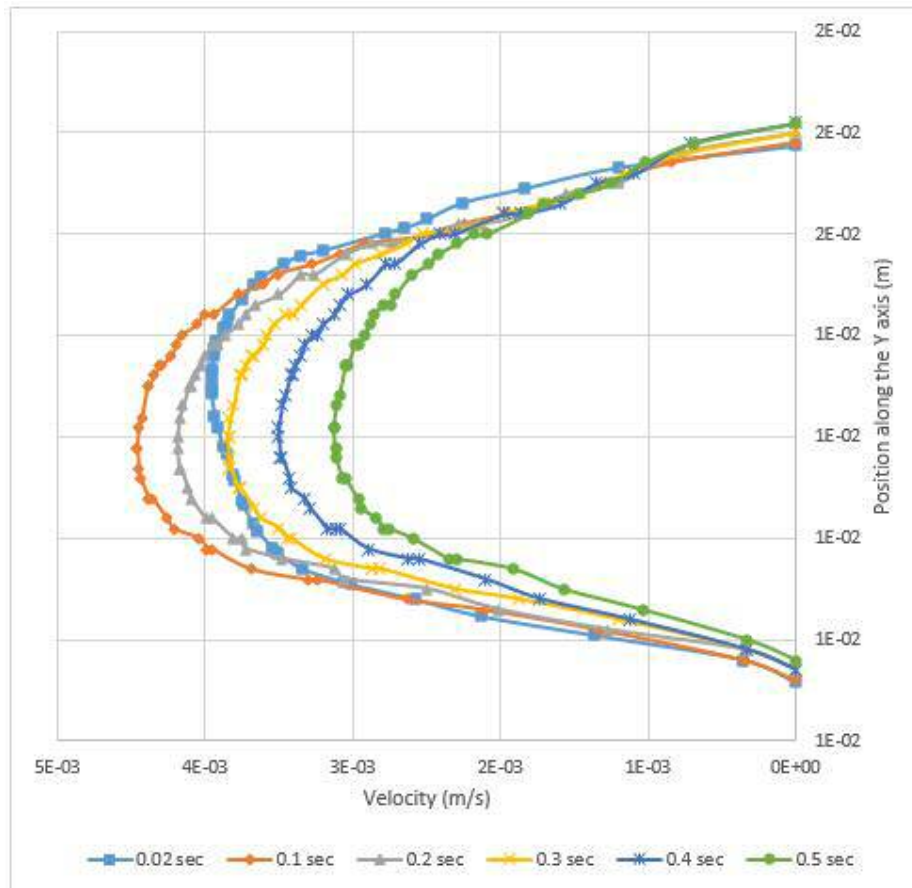


Figure 4-55 Velocity profile measured across the centre of the LV at different times during the release phase of the FSI simulation.

Figure 4-56 shows the dynamic viscosity vs the shear rate obtained in the compression and release FSI models. The results were extracted in the CFD post and were set prior to the simulation run. The viscosity profile is an indication of the blood model study by (Doost et al., 2016). Although in the simulation time, where  $t=0.3$  s, the viscosity profile drops, it is in agreement with the vortex formation found in Figure 4-42 to Figure 4-46, as mentioned previously.

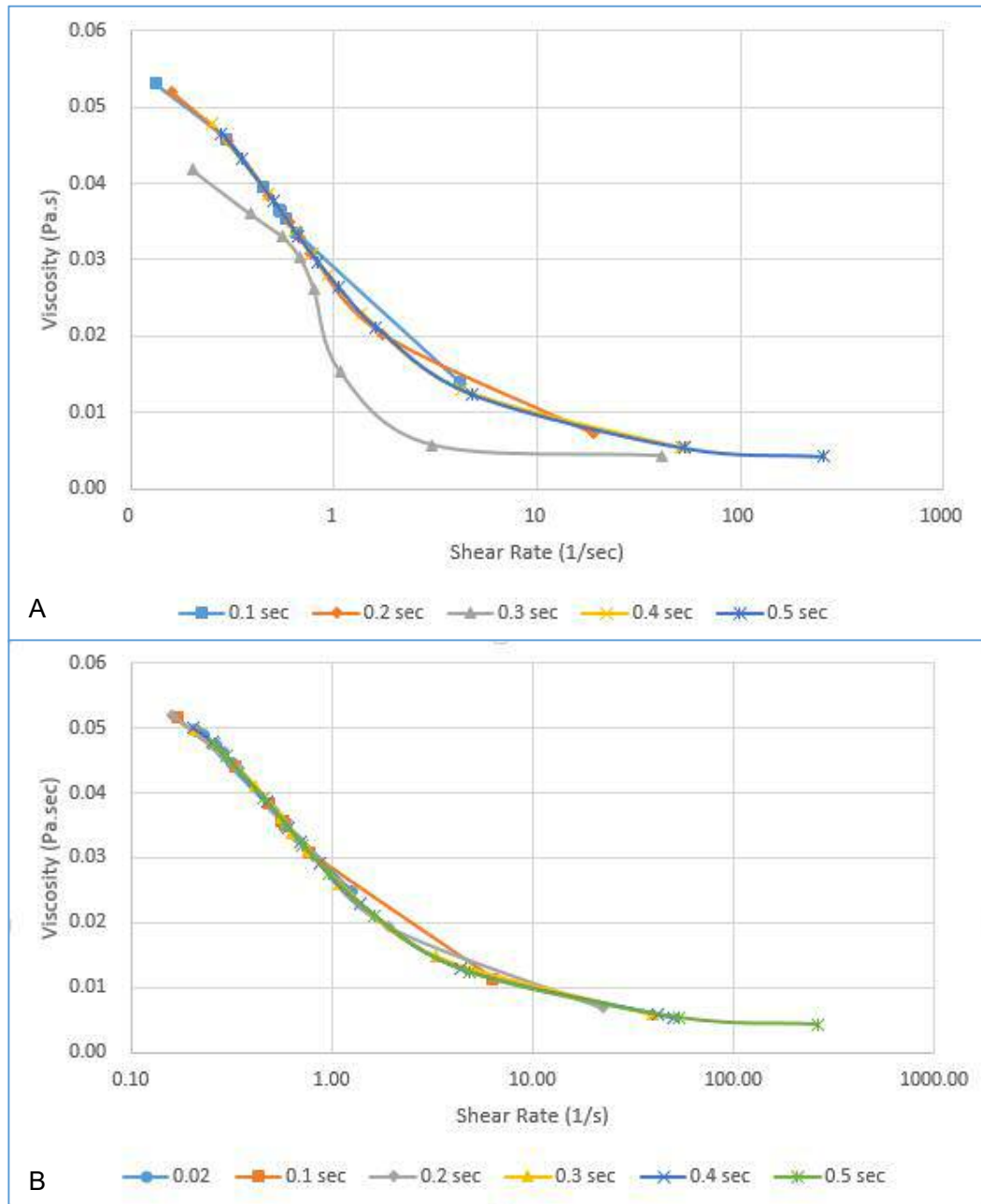


Figure 4-56 Dynamic viscosity vs shear rate for the Carreau fluid model (A) during the compression phase of the subject-specific FSI simulation, (B) during the release phase of the subject-specific FSI simulation

In summary, the model presented in this chapter can be regarded as a concrete example of how the methodology devised throughout the thesis can be effectively used to simulate cardiovascular compression as a first compression during CPR. At the same time, we also recognize that the results and analyses presented here are not enough to assess all the benefits and drawbacks of the proposed model. For instance, among the other aspects, a true

assessment of the model should include at least comparisons with (i) image data of the ventricular flow obtained from ultrasound infant data, (ii) measurements of flow rate and pressure waveforms in the right ventricle, and (iii) heart tissue material model with experimental tissue mechanical testing. Moreover, the presented methodology can be improved in several ways as is briefly discussed in the next chapter.

### **4.3.2. Structural Computational Data**

The performance evaluation of the model continues with extensive investigations on the dynamics of the structure, while considering the transferred fluid forces as the LV wall motion. In this regard, a summary of the fluid forces is imported in the form of pressure distribution. Accordingly, structural analysis is performed based on the results of total deformation, equivalent strain, and the Von Mises stress values at all synchronized time steps of the simulation. Such a selection of the variables relates to the interaction of the blood flow streams to the magnitudes and characteristics of wall deformation. Note that presentation of scalar magnitudes of multi-axial stress (Von Mises stress) is an appropriate choice as the constitutive model of the material was assumed to be anisotropic hyperelastic.

Total mesh (structure) deformation (TMD) is illustrated by contour plots in order to analyse the dominant direction of TMD as well as its maximum and minimum (Figure 4-57 and Figure 4-58). The TMD shows that the highest value on the upper contacting surface increases with each time step. Comparing the results with those of the shell heart model shows the exact areas of the deformation are still the contacting areas. The stresses and strains show different areas of interest representing the fluid forces transformed to the boundary conditions.

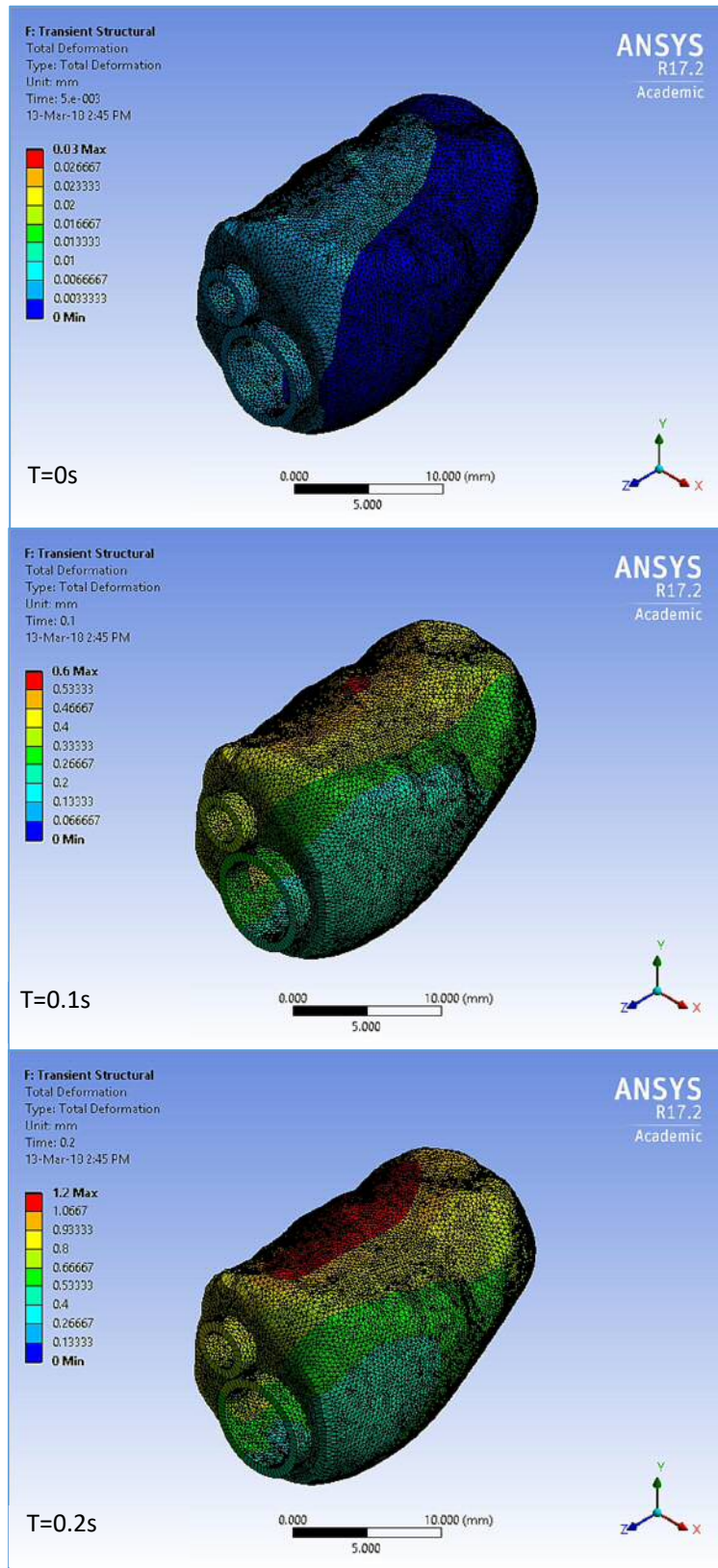


Figure 4-57 LV Total deformation distribution map of the 1<sup>st</sup> stage of FSI (isometric view) for  $0 \leq t \leq 0.2$  sec

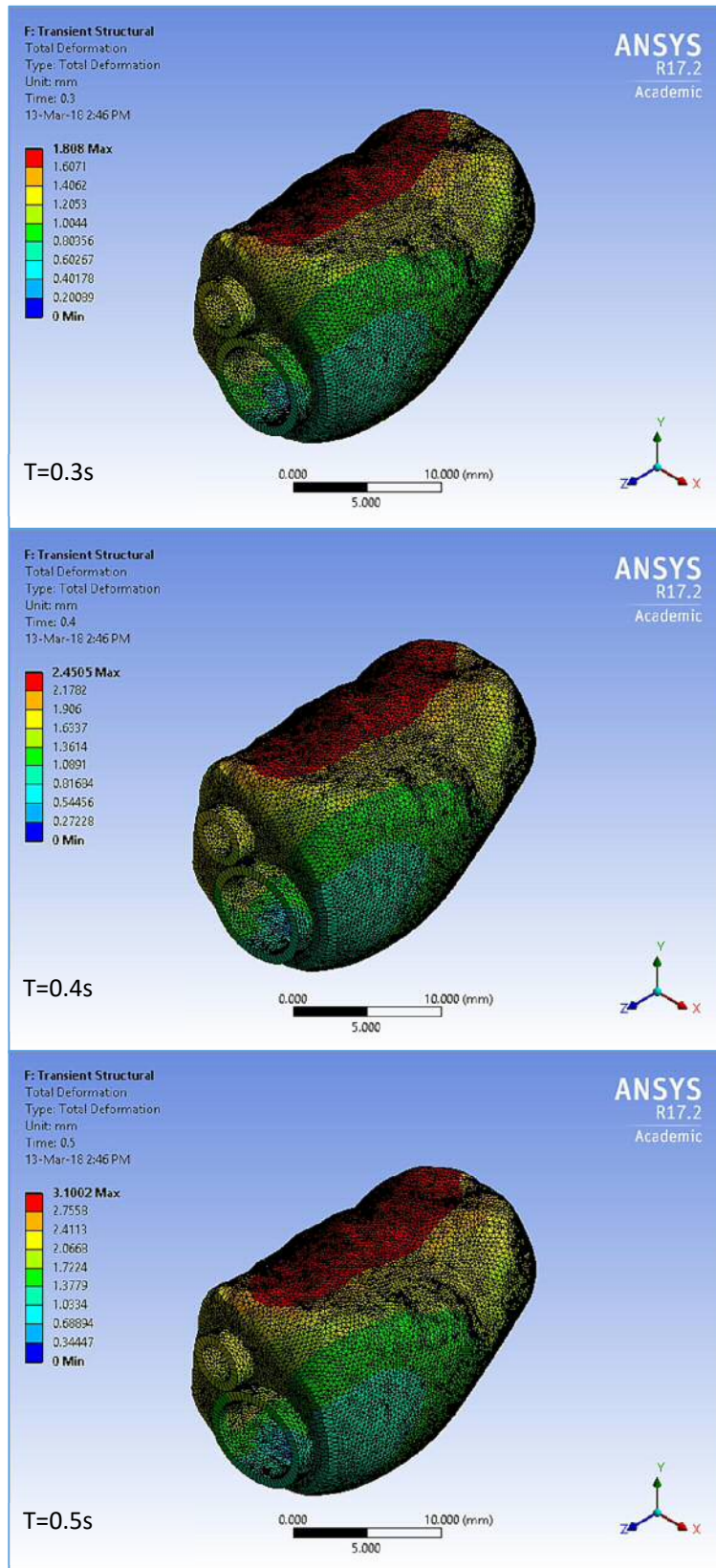


Figure 4-58 LV Total deformation distribution map of the 1<sup>st</sup> stage of FSI (isometric view) for  $0.3 \leq t \leq 0.5$  sec

The biological cardiac tissue, such as the left and right ventricle, consists of more than two families of collagen fibres and obeys orthotropic constitutive laws (Holzapfel and Ogden, 2009). As the orthotropic model requires computational coding to be adapted by the software used in this work, a hyperelastic model was used instead, which is a material model many researchers have used for the simulation of cardiac tissue. Results from the use of this model affect the stresses and strains of the left ventricle wall in the proposed model FSI. To study the effect of the fluid on the interacting wall of the LV during compression and release, stresses and strains were obtained from the CFD-post component of the FSI analysis system in ANSYS. Different from the preliminary model, the stresses and strains were represented as contours of the deforming wall during the various time steps of the simulation. The orientation of the results was located at the XY and ZX direction to better locate the stresses' and strains' maximum value change during the simulation time steps.

At the beginning of the simulation at  $t=0$  s, stresses are present at the top of the LV base, which is in compliance with the behaviour of the cardiac tissue material (Figure 4-59). As the compression starts, the magnitude of the stresses increases surrounding the base of the LV near the boundary conditions. The highest value of the stress was 0.362 kPa, as recorded on the upper wall near the outlet. As the compression displacement increases, the stresses on the wall increase, especially on the lateral wall of the LV. This is an improvement on the stress data collected from the shell heart model, as the stresses there were located at the area of contact, but in this FSI model, the actual stresses from the fluid were transferred to include the deforming wall. At  $t=0.4$  s, the Von-mises stress was distributed near the apex of the LV relating to the deformed geometry due to the compression and TMD occurring in the model during the simulation at this time step. At the end of the simulation, the maximum stress included the majority of the base and the inlet and outlet boundary wall due to the flow of fluid and the vortices generated at this stage of the compression. The TMD direction is predominantly normal to the cross sectional plane, and as this location circumferentially alters, the resultant TMD vectors gradually change their normal tangential direction at the lateral wall. This happened due to the distribution of velocity gradient presented previously in Figure 4-42. The highest value of the stress was at  $t=0.4$  s, where the value was 65.22 kPa. At this time, two large vortices were located the lower wall of the LV with the inlet vortex moving up to force the fluid to flow through the outlet; this vortex generated pressure on the wall of the LV, which increased the stress at this area. The vortex formation and the pressure distribution during compression was explained in the previous section, and the vortex referencing figures are seen in Figure 4-44 and Figure 4-47.

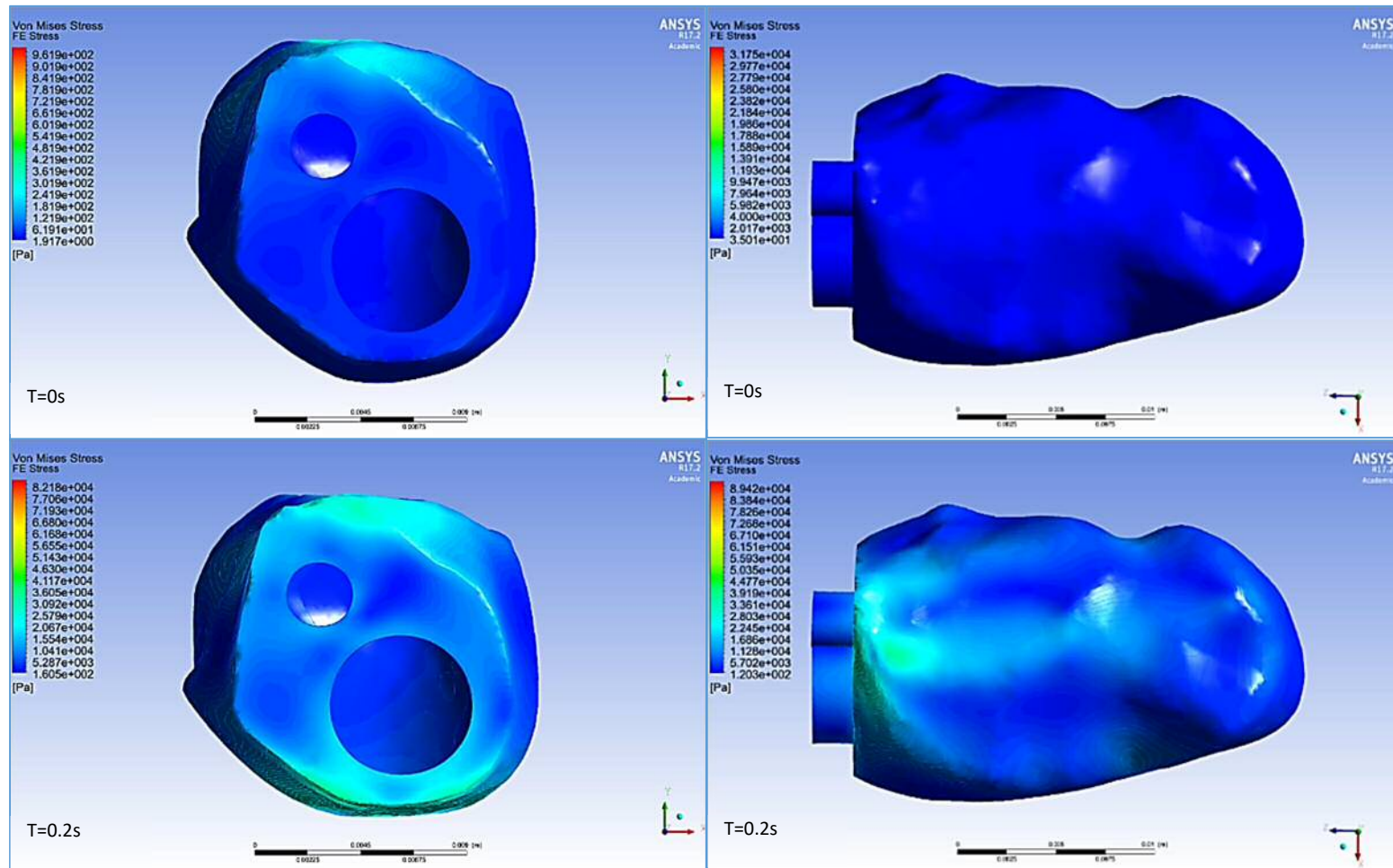


Figure 4-59 Subject-specific equivalent elastic stress distribution map in CFD post of the compression stage of FSI during multiple time steps. On the left are the XY (front view) and on the right are the ZX view for  $0 \leq t \leq 0.2$  sec.

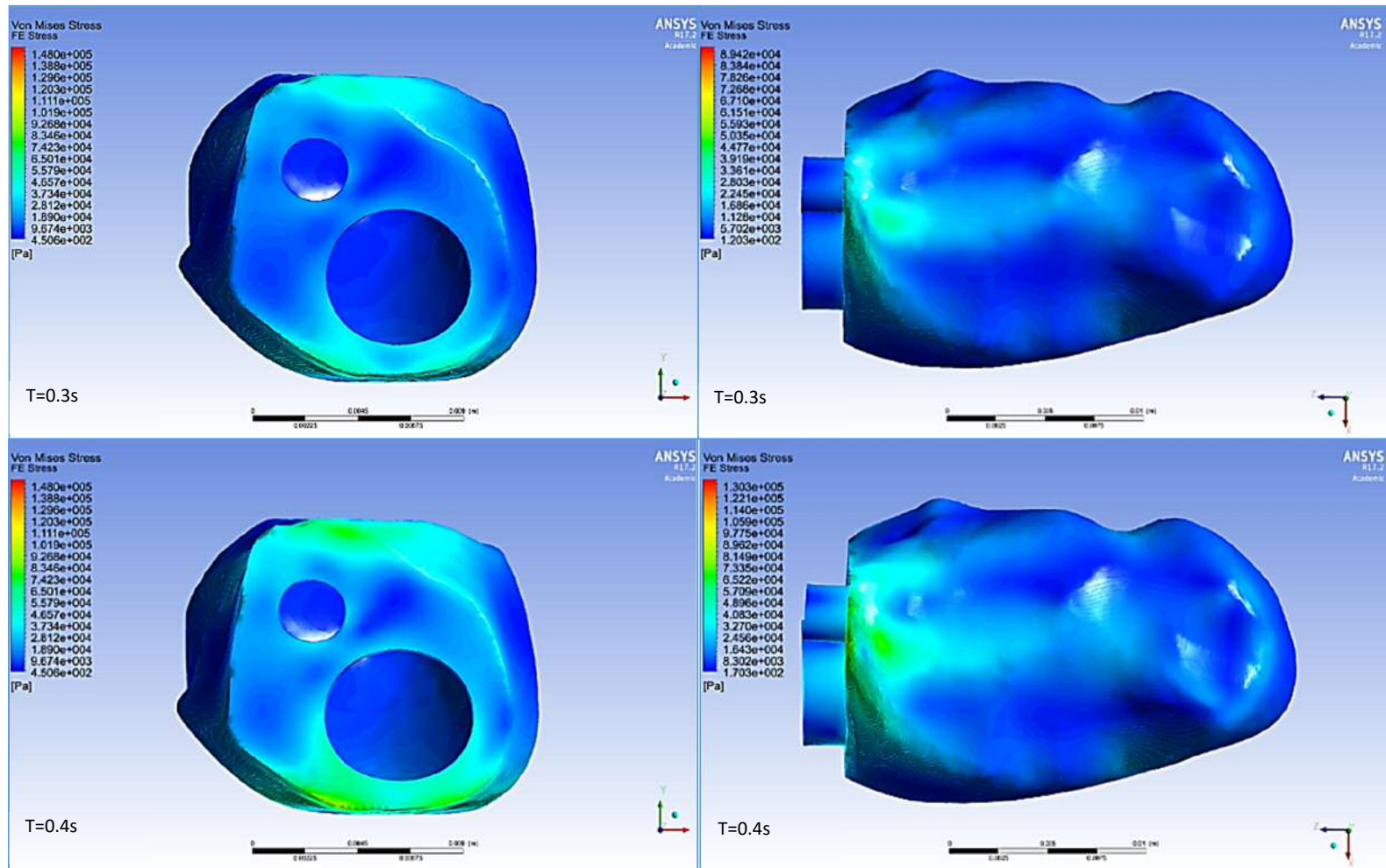


Figure 4-60 Subject-specific equivalent elastic stress distribution map in CFD post of the compression stage of FSI during multiple time steps. On the left are the XY (front view) and on the right are the ZX view for  $0.3 \leq t \leq 0.4$  sec.



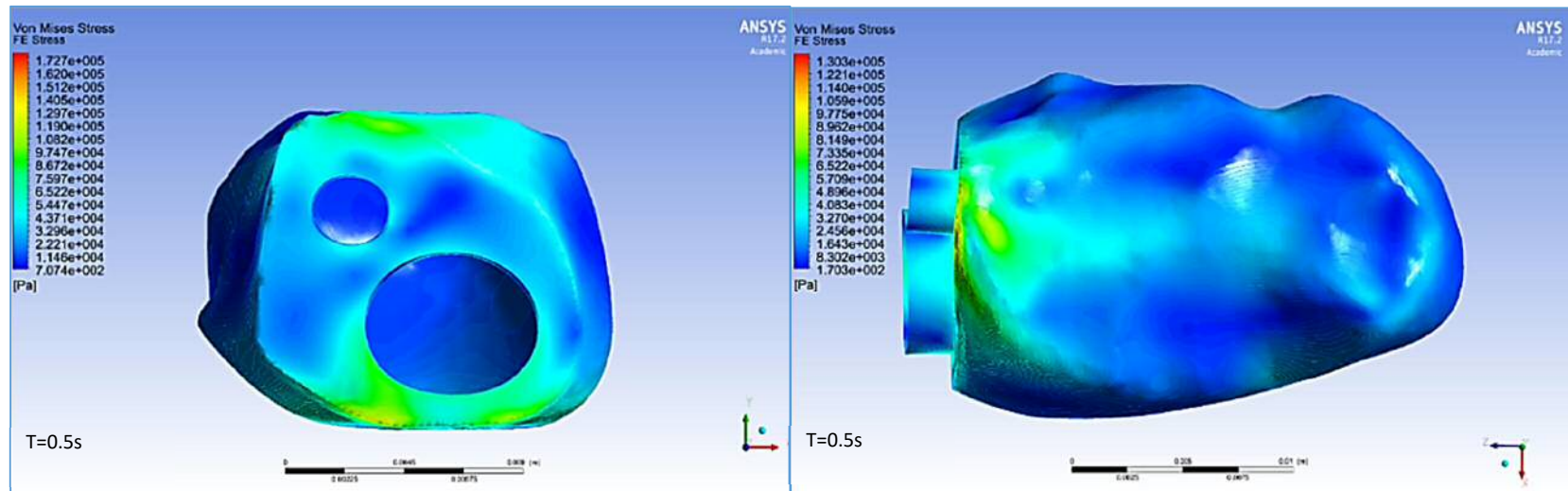


Figure 4-61 Subject-specific equivalent elastic stress distribution map in CFD post of the compression stage of FSI during multiple time steps. On the left are the XY (front view) and on the right are the ZX view for  $t=0.5$  sec.

that of the compression due to the second stage FSI dependence on the first stage, so the displacement of the upper wall is driven by the fluid flow through the inlet from the compliance of the wall during this phase. Reaching the end of the release phase simulation, the stresses are located to include the deforming wall with the base of the inlet and outlet, and the areas of maximum stress were still located near the apex of the LV.

The model strain was measured, and the results are presented in Figure 4-8. The strain of the computational compression was located within the lower biaxial strain range of the constitutive hyperelastic material model. Unlike in the preliminary model, the equivalent elastic strains of the deforming wall of the subject-specific model were measured in the post CFD component of the FSI model in the ANSYS analysis system, to show the effect of the FSI on the deformed wall and to show the variety of the data collection options in the simulation software. The orientation of the strain contours was chosen, such as the stress contours presenting the collected data at the XY and ZX orientations, to show the highest and lowest strains through the simulation time steps (Figure 4-65, Figure 4-66, and Figure 4-67).

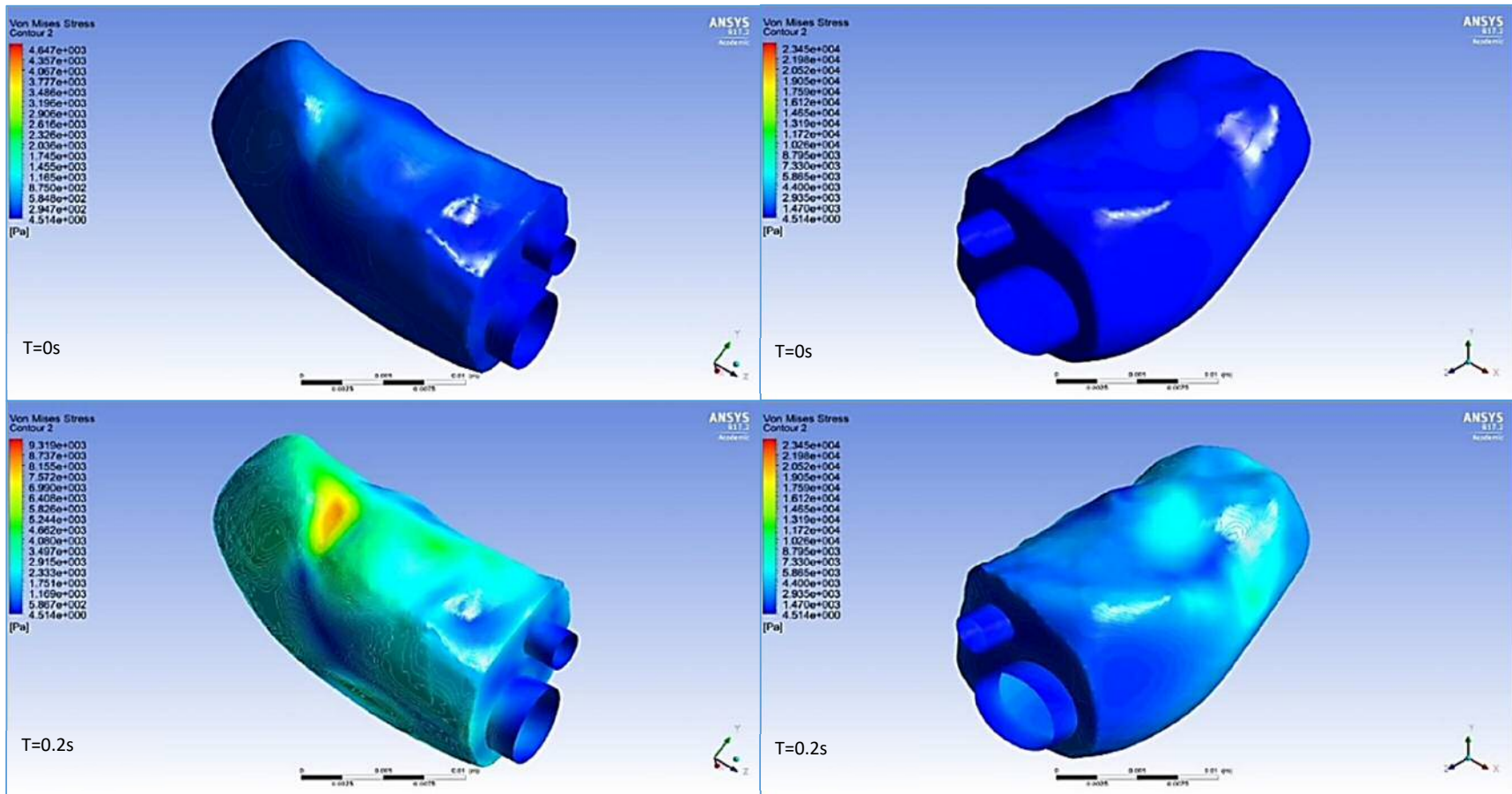


Figure 4-62 Subject-specific model equivalent elastic stress distribution map in CFD post of the release stage of FSI for different simulation times for  $0 \leq t \leq 0.2$  sec. The images on the right represent the isometric view and the opposite view is shown on the left.

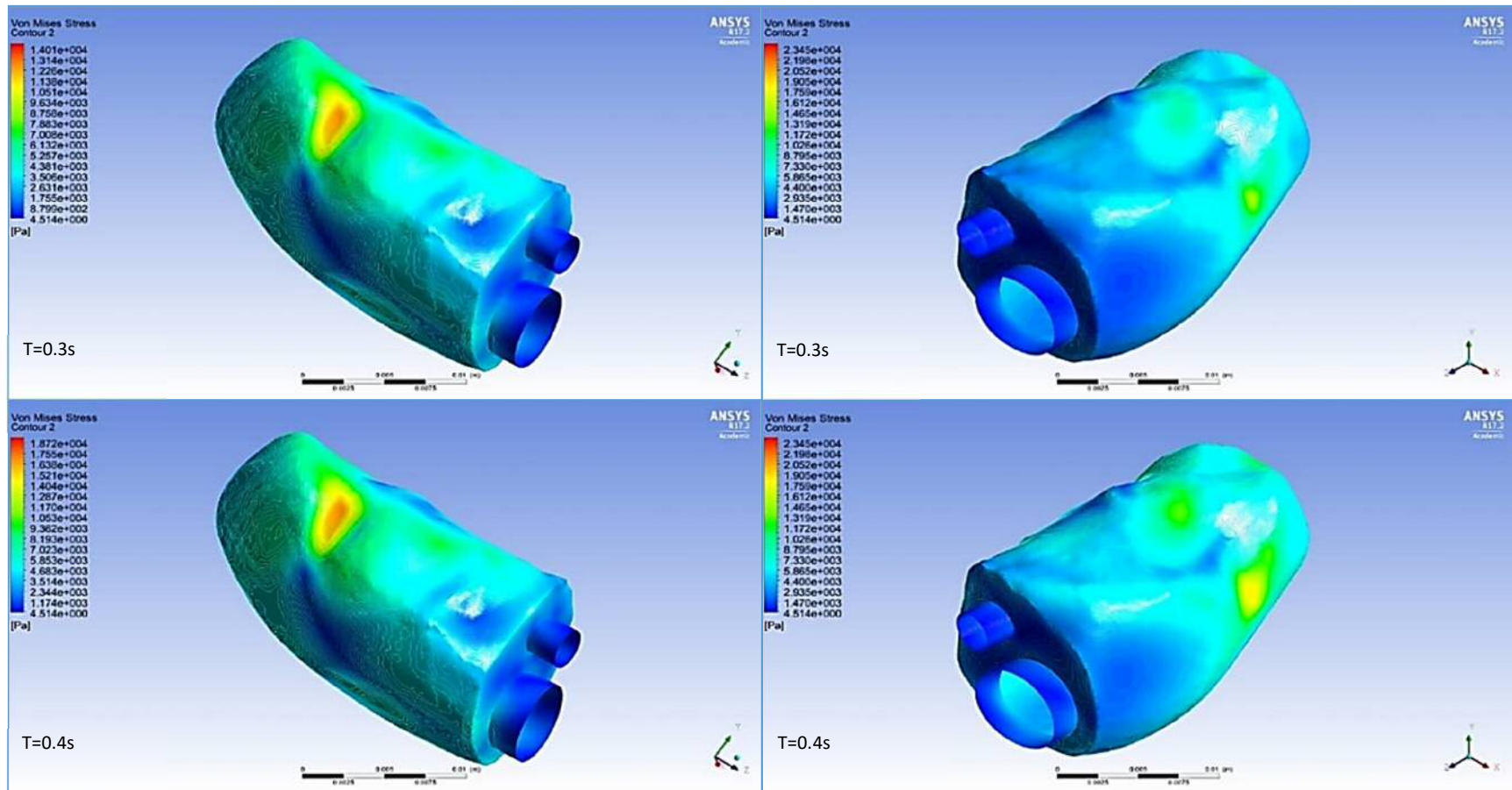


Figure 4-63 Subject-specific model equivalent elastic stress distribution map in CFD post of the release stage of FSI for different simulation times for  $0.3s \leq t \leq 0.4$  sec. The images on the right represent the isometric view and the opposite view is shown on the left.

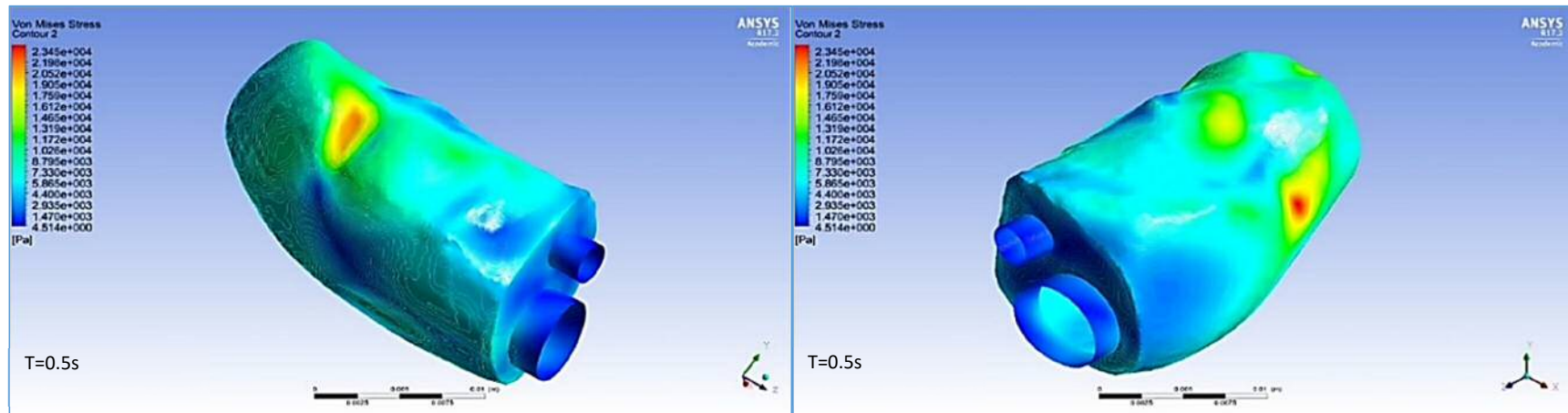


Figure 4-64 Subject-specific model equivalent elastic stress distribution map in CFD post of the release stage of FSI for different simulation times for  $t=0.5$  sec. The images on the right represent the isometric view and the opposite view is shown on the left.

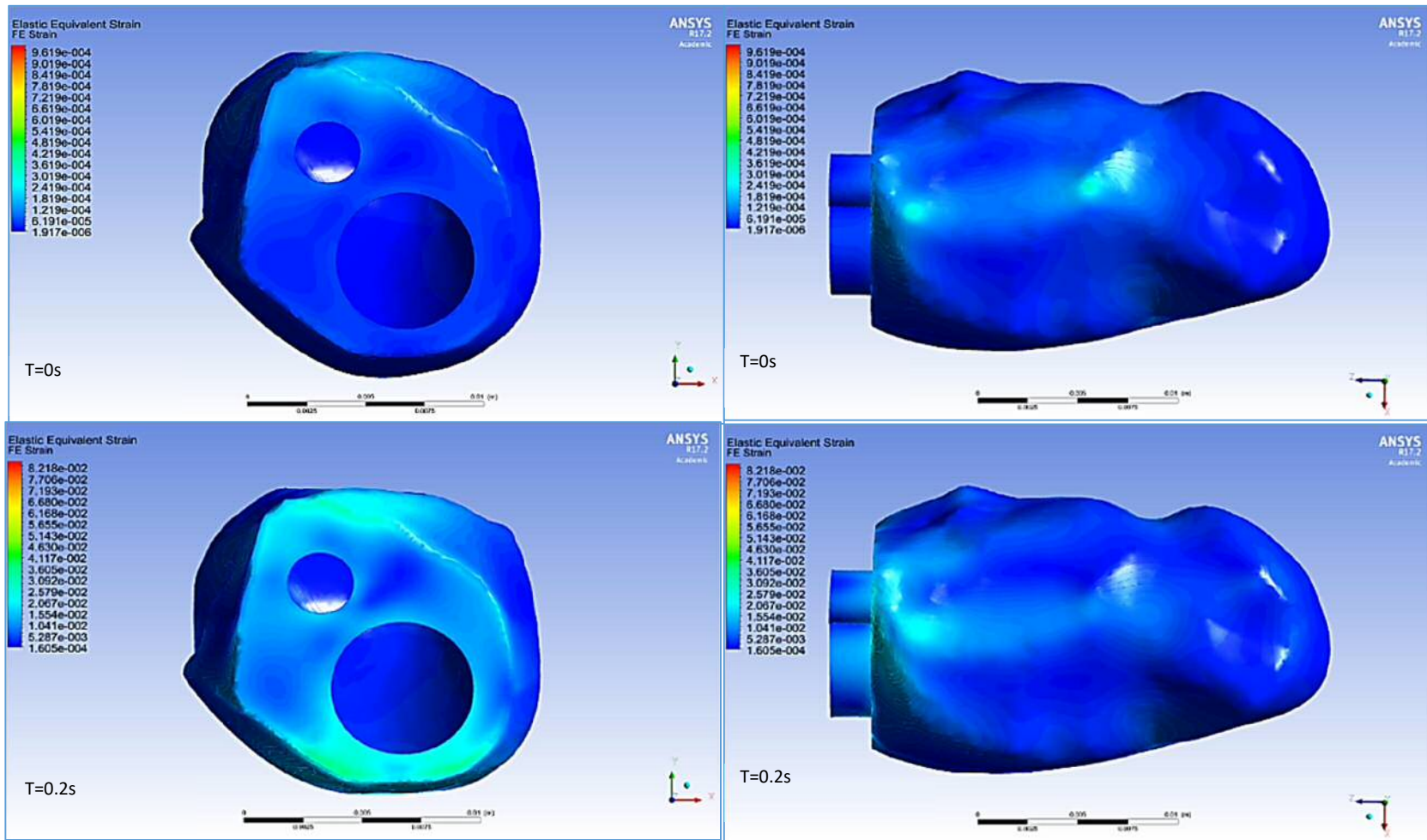


Figure 4-65 Subject-specific equivalent elastic strain distribution map in CFD post of the compression stage of FSI during multiple time steps for  $0s \leq t \leq 0.2$  sec. On the left are the XY (front view), and on the right, are the ZX view

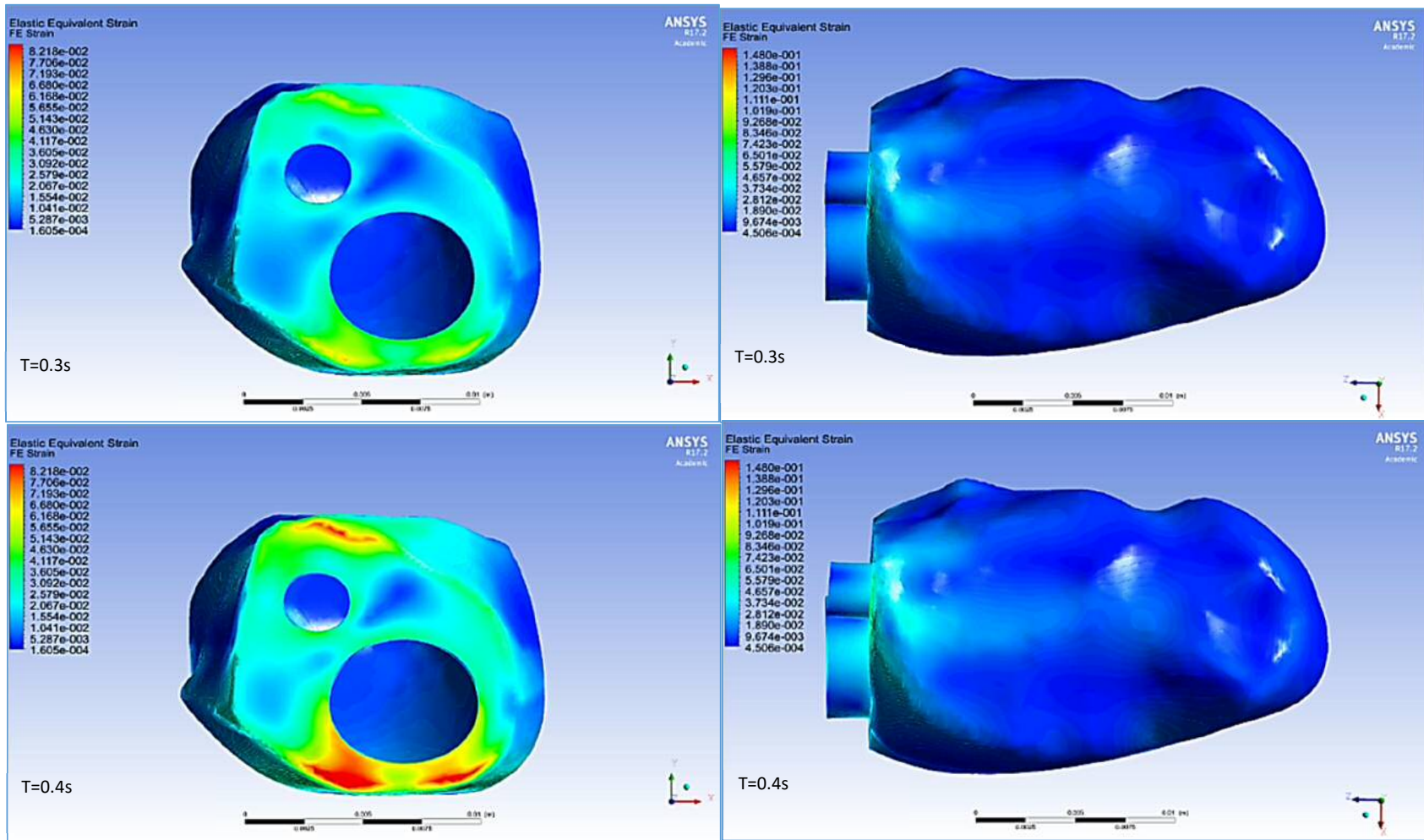


Figure 4-66 Subject-specific equivalent elastic strain distribution map in CFD post of the compression stage of FSI during multiple time steps for  $0.3 \leq t \leq 0.4$  sec. On the left are the XY (front view), and on the right, are the ZX view

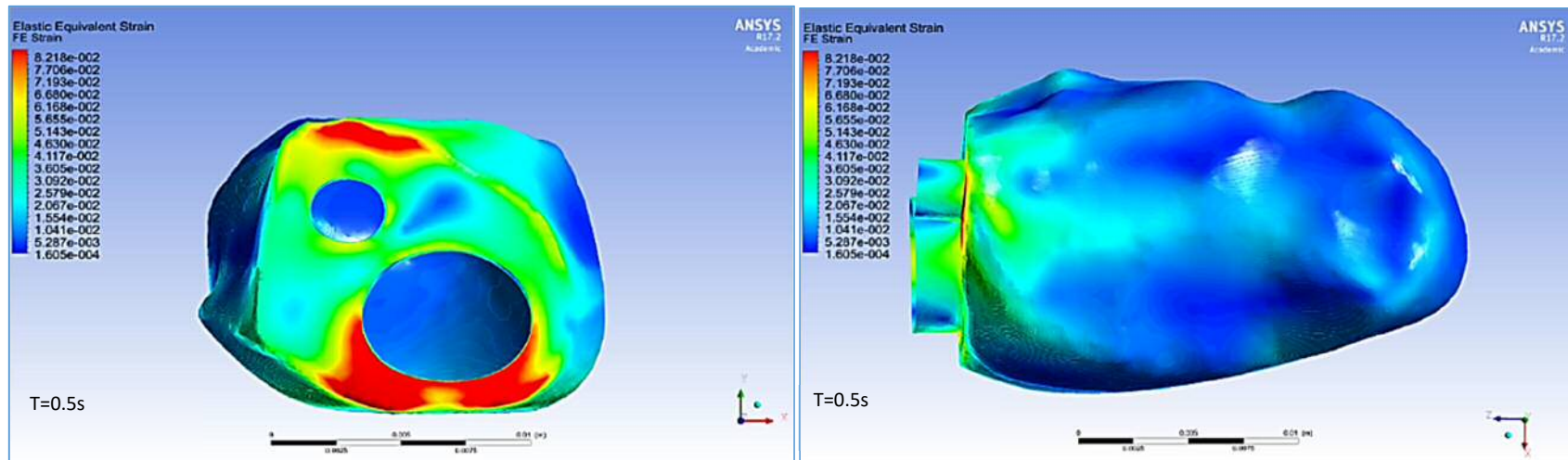


Figure 4-67 Subject-specific equivalent elastic strain distribution map in CFD post of the compression stage of FSI during multiple time steps for  $t=0.5$  sec. On the left are the XY (front view), and on the right, are the ZX view



dramatically through the rest of the simulation to reach 0.063% at the end of the simulation. Although the strains increased during the compression stage, they were still at the lower part of the biaxial strain profile of the material model, which validates the use of the hyperelastic material model curve fitting characteristics.

The reason for the compliance change is the sudden collapse of the wall due to the rapid compression. This material is more strongly constrained by the inlet and outlet boundaries and therefore these walls have a much stronger resistance to collapse until the external compression is sufficiently large. This occurred more in the preliminary model, as the boundaries were at each end of the model in contrast to their location in the subject-specific model.

During the release stage of the FSI (Figure 4-68, Figure 4-69, and Figure 4-70), the strains are shown in this figure at the same orientation as located for the stress, and once again, the strains were located at the same areas of interest as the stresses' distribution.

At the start of the release phase, the strains were very low, but at  $t=0.2$  s, rapid distribution of the strain contours could be seen starting from the apex reaching the base of the LV. The area of maximum strain was located near the apex, recording its maximum value of  $2.995e-2\%$  at the end of the simulation near the apex. The lowest values of the strains were at the inlet and outlet boundaries.

ANSYS has superior solvers for the structural analysis, and could be used to carry out all the simulations without using external coupling software with the fluent analysis system. Further compression to the LV with higher displacement showed a failed solution in the FSI and structural side. This is considered to be due to the software capacity, as the mesh size was reduced to a minimum value, and the step size was decreased.

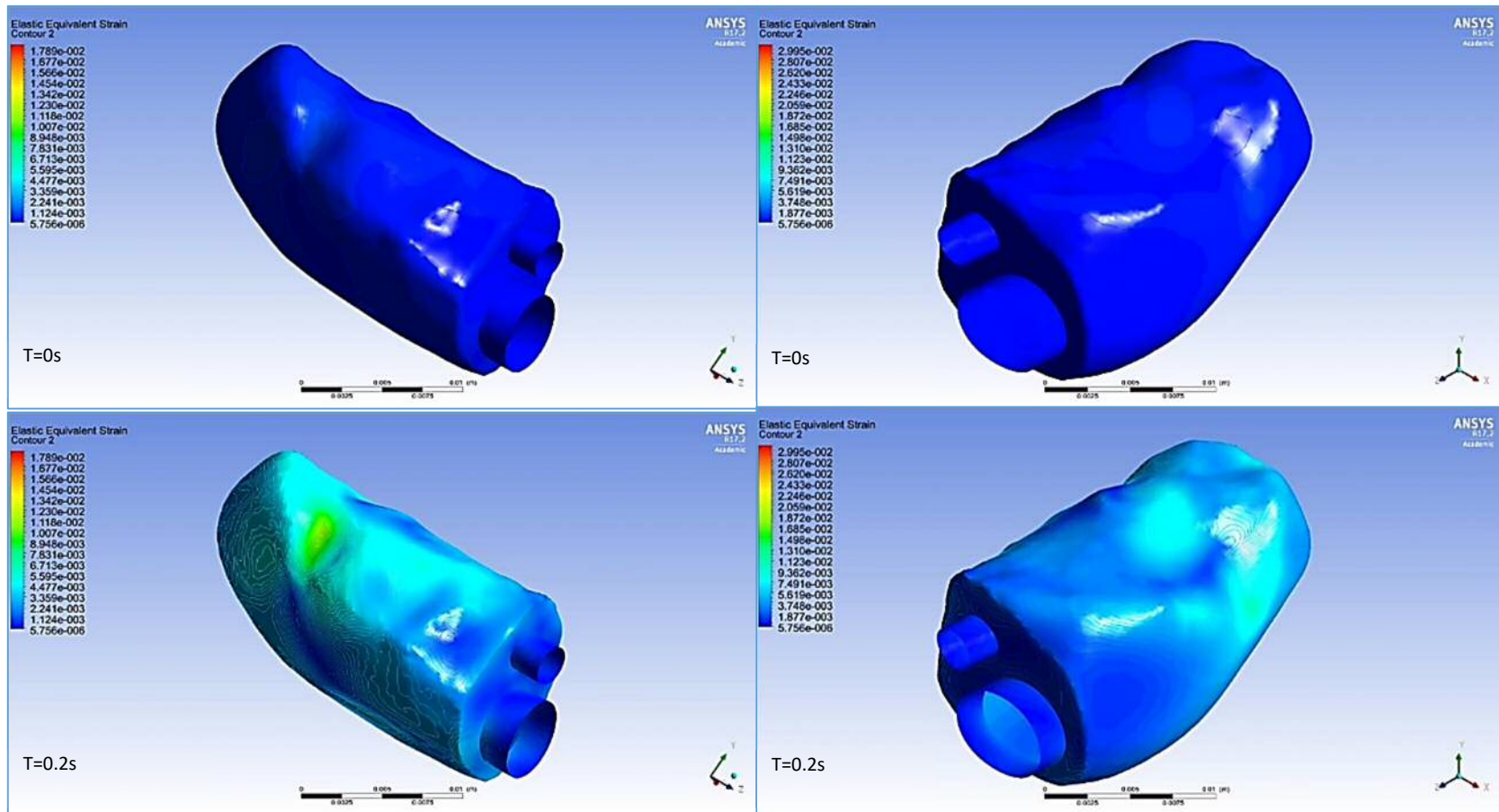


Figure 4-68 Subject-base model: Equivalent elastic strain distribution map in CFD post of the release stage of FSI different to the simulation time for  $0 \leq t \leq 0.2$  sec. The images on the right are for the isometric view, and those of the opposite view are shown on the left.

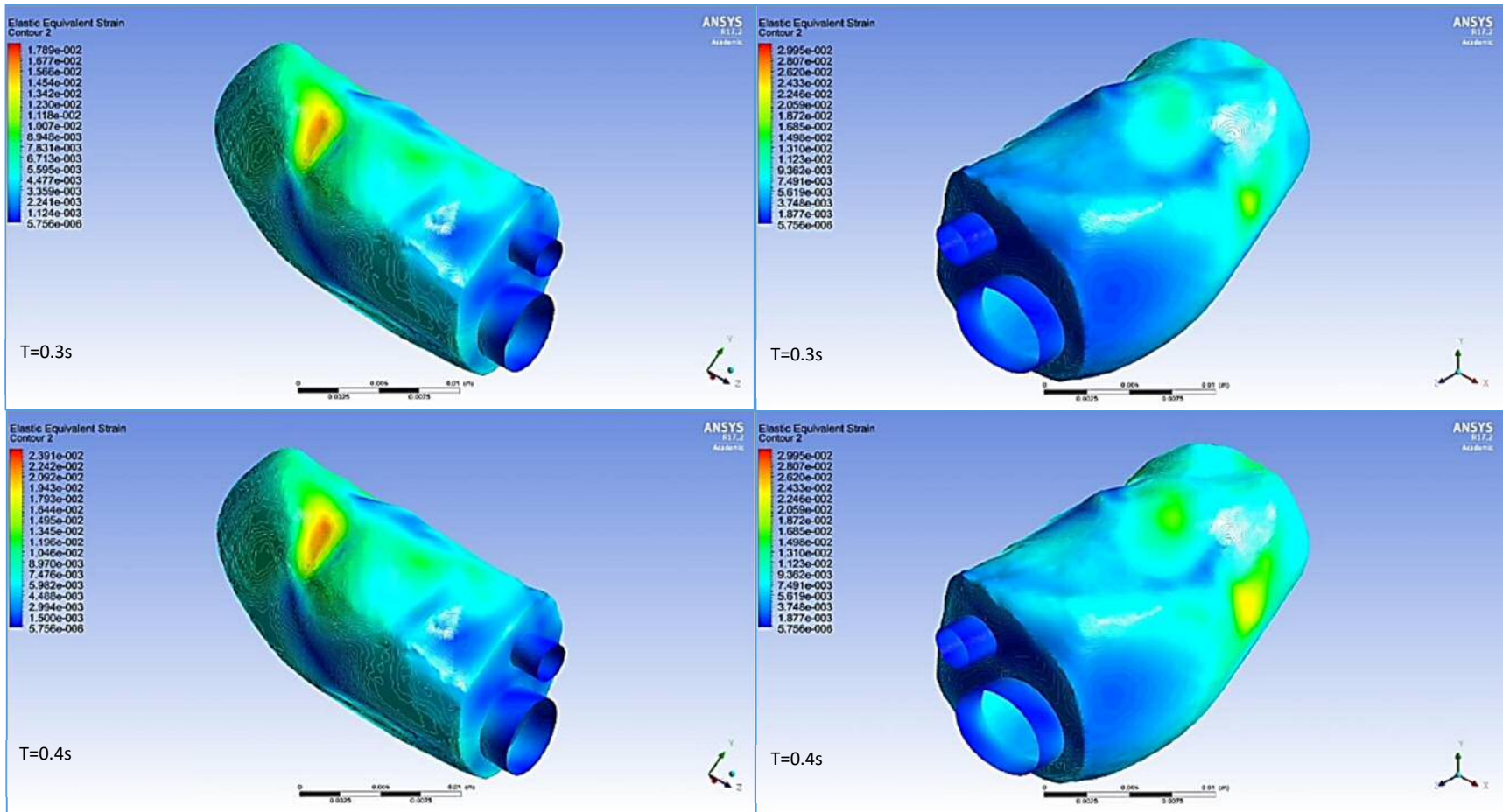


Figure 4-69 Subject-base model: Equivalent elastic strain distribution map in CFD post of the release stage of FSI different to the simulation time for  $0.3s \leq t \leq 0.4s$ . The images on the right are for the isometric view, and those of the opposite view are shown on the left.

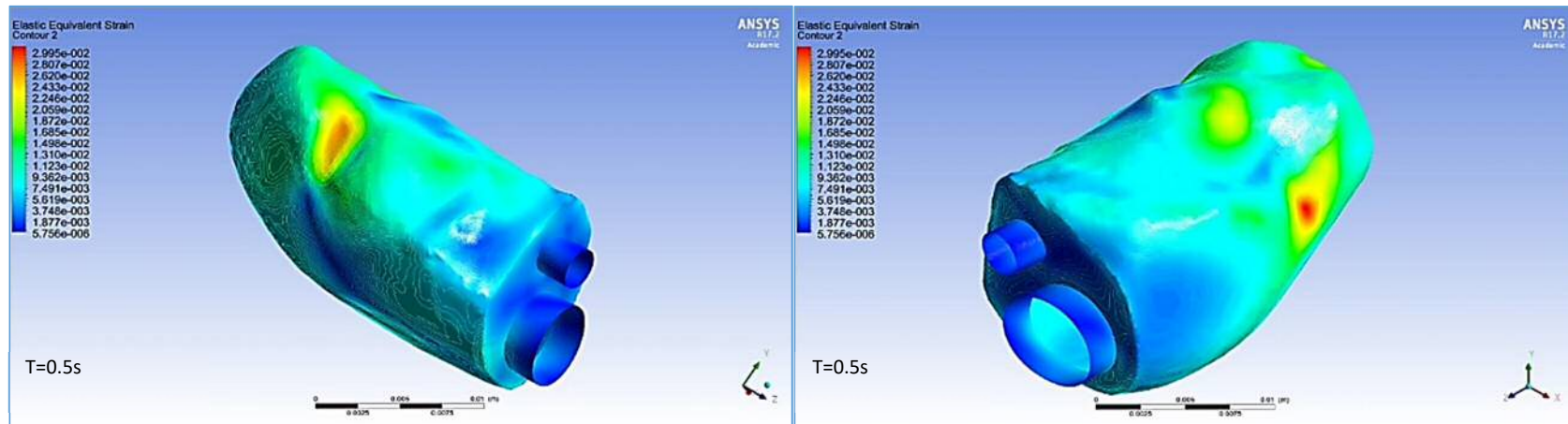


Figure 4-70 Subject-base model: Equivalent elastic strain distribution map in CFD post of the release stage of FSI different to the simulation time for  $t=0.5$  sec. The images on the right are for the isometric view, and those of the opposite view are shown on the left.

## Chapter 5. Technical Achievements and Limitations

### 5.1. Chapter Overview

In order to establish and design computational model as a platform, the quality of that model including convergence, boundary condition meshing and their related mapping as well as model stability, monitoring to those parameters should be performed throughout the running simulation. This step was performed to eliminate any causes of data shift or inconsistency due to software computational artefacts. This chapter also highlights the major findings and provides a set of limitations to the work undertaken in this study whilst providing directions for future studies.

- **Mesh Study:** The data transfer mapping quality assurance and the mesh study outcome, thus verifying the model's sensitivity quality.
- **Study Limitations:** Computational and experimental limitations Computational challenges and computational limitations of the proposed models.

## 5.2. Model mesh and Mapping Quality

Finite element, CFD, FSI modelling, and subject-specific meshing requirements include assigning and checking mesh quality metrics, integrating mesh control functions, investigating mesh independency, formulating appropriate mesh generation approaches, obtaining good mesh results and automating the mesh generation process. Mapping of contacting surfaces was also verified during the simulation to ensure the compatibility between the data transfer in the FSI surfaces. This section will discuss the data transfer mapping quality assurance and the mesh study outcome, thus verifying the model's sensitivity quality.

### 5.2.1. Mesh Sensitivity Study

A high-quality three-dimensional grid must be free of high-skewed elements. To verify the quality of the surface and volume mesh model, the quality range of each generated mesh element should be examined for stable simulations. The quality ranges of the metric parameters should not exceed certain critical average values; otherwise, high-skewed elements must be optimized and large spacing variations between adjacent cells minimized. This is achieved through an improved re-meshing of the domain and readjustment of the mesh parameters.

The velocity distribution, pressure profile, and WSS distribution within the XY plane were evaluated for six mesh configurations. The relative error of the mean-average wall shear within the XY plane decreased with mesh refinement from 21.4 % at the transition of the element size configuration, from 0.5 to 0.8, to 0.2 % at the transition, and from 0.5 to 0.55 %. The relative error of the pressure decreased by 30% at transition from 0.5 to 0.8, to by 0.2% at transition from 0.5 to 0.55. The velocity distribution was the most affected parameter of the element size, as it showed a reduction from over a 100% relative error at transition from 0.5 to 0.8, to a 0.39% relative error in the transition between the 0.5 to 0.55 element size configurations. This is an indication that velocity computation is more sensitive to mesh configuration than to pressure and wall shear computation. The obtained parameters for the idealized geometry are presented in Table 5-1.

Therefore, in the left ventricle, model meshing started from 0.5 mm element size as per the previous mentioned mesh study, then a 0.3 mm size was chosen in the model for better simulation results, as 0.5 was higher than the required element size for better mesh quality. The mesh quality of the idealized model was also studied to compare the mesh independent

parameters. Figure 5-1 shows that element size  $\leq 0.8$  mm has a steady mesh quality through the idealized model.

*Table 5-1 Results of dimensionless velocity, pressure, and wall shear and corresponding relative error (%) obtained at transitions between the different mesh element sizes in the idealized model*

<b>Element Size</b>	<b>Velocity</b>	<b>Pressure</b>	<b>Wall Shear</b>
0.5	4.53E-02	-5.12E+00	8.27E-02
0.55	4.54E-02	-5.11E+00	8.27E-02
0.6	4.70E-02	-4.11E+00	7.13E-02
0.65	4.78E-02	-4.10E+00	9.39E-02
0.7	7.35E-02	-4.08E+00	9.39E-02
0.75	9.10E-02	-3.74E+00	1.01E-01
0.8	1.09E-01	-3.59E+00	1.00E-01
<b>Transition from</b>	<b>Rel. V. Error</b>	<b>Rel. P. Error</b>	<b>Rel. W. Error</b>
0.5 to 0.55	-0.39%	0.24%	0.24%
0.5 to 0.6	-3.90%	19.75%	13.85%
0.5 to 0.65	-5.68%	19.92%	-13.52%
0.5 to 0.7	-62.50%	20.47%	-13.52%
0.5 to 0.75	-101.07%	27.01%	-21.91%
0.5 to 0.8	-141.07%	29.96%	-21.44%

The results presented in Table 5-1, Figure 5-1 and Figure 5-2 show that mesh-independency as assessed based on computed velocities is sufficient to establish mesh-independency for the preliminary model.

The results show the applied compression exerting the highest pressure on the walls of the sphere, and the velocity vectors show the vortices are near the inlet with little backflow due to the blood flow direction. Figure 5-2 shows the difference between the velocity profiles of two simulation step sizes. The image on the bottom of the figure shows that there is little difference in the velocity profiles, and the low value verifies that reducing the step size beyond this value will have a low impact on the results. The same procedure was used to verify the choice of the step size using a pressure contour.

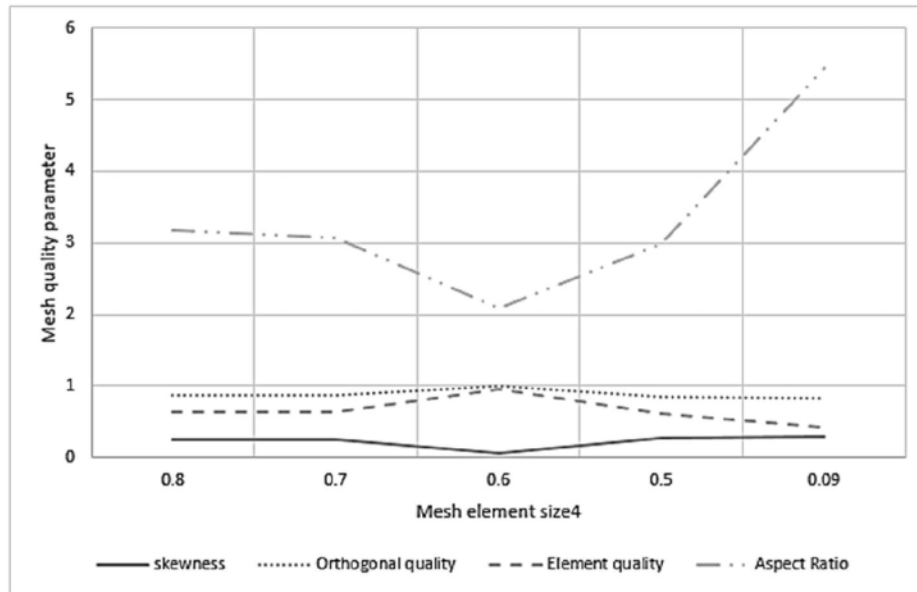


Figure 5-1 Mesh sensitivity for the preliminary model. The skewness, orthogonal quality, and element quality show steady values for mesh size between 0.8-0.09 mm. The aspect ratio will continue to increase with element size decrease.

Timestep independent simulations were reached using 0.025 step-size equally spaced time steps with 10 structural substeps. Figure 5-3 shows the difference in values between two step size simulations; the value illustrated on the bottom image shows the low difference value between the two simulations. Figure 5-2 and Figure 5-3 verify the step size used for the model simulation. For the LV model, the step size study started at 0.025 with a 0.3 mm mesh element size, but the complicated geometry added more instability to the LV model, which required the reduction in the step size to 0.005 for a better convergence; however, this increased the computational time. Therefore, the maximum step size was used to reduce the computational cost.

For all simulation types, the first step in creating the mesh is generating the boundary surface of the model. Therefore, surface meshes for both models (preliminary and LV) had to be generated. They were defined by the wall boundary, the lumen boundary, and the interface for the FE, the CFD, and the FSI applications, respectively. The surface meshes contain quad cells when used for FE for the preliminary model or CFD simulations, and tri cells if used for FSI simulations in the LV model. In both cases, the mesh generation is based on curvature and proximity size functions. The corresponding results are shown in Figure 3-2 and Figure 3-24.



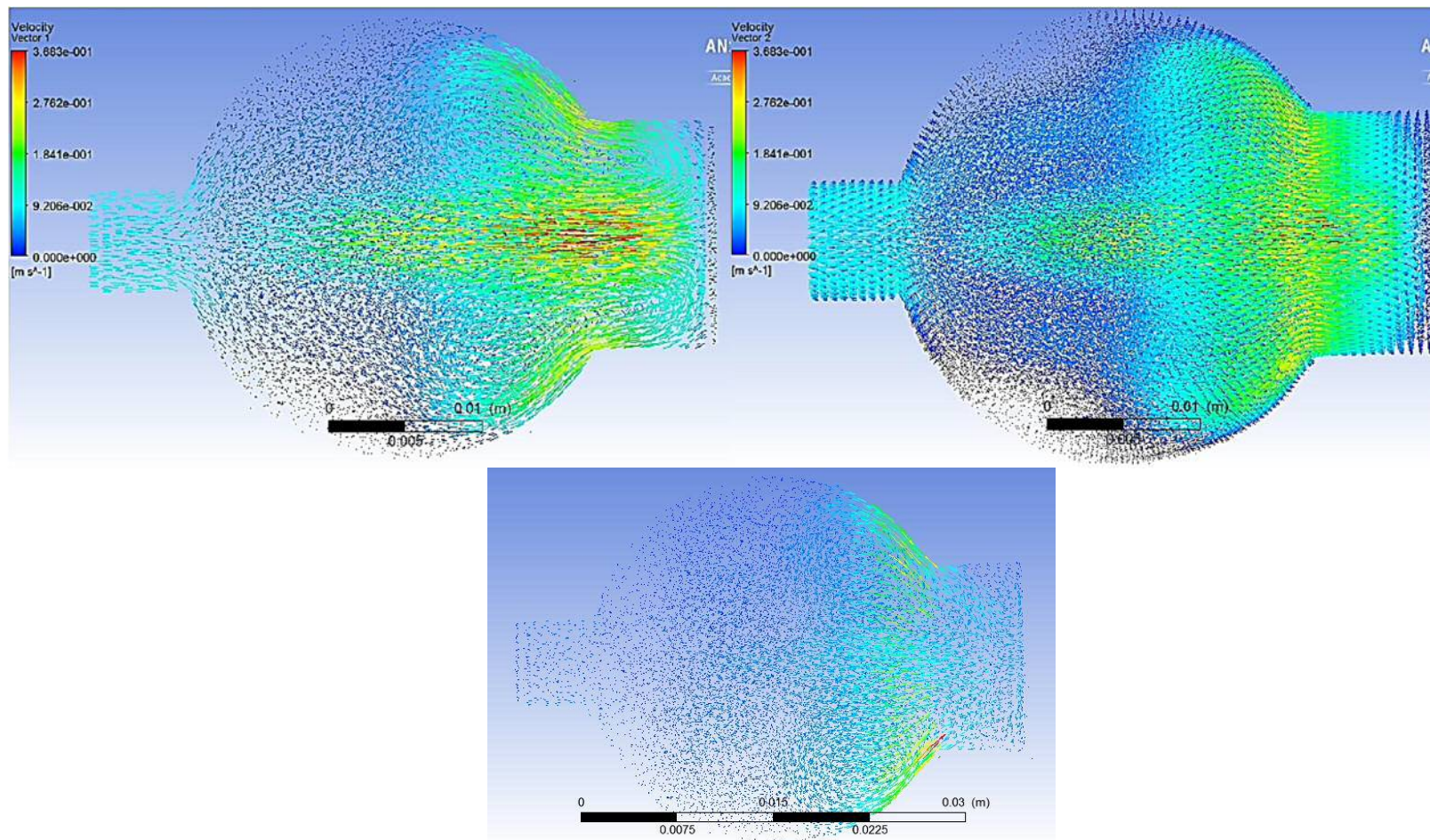


Figure 5-2 Velocity vector verification between different elements mesh and step size ANSYS16 Fluent. The images on the top represent velocity vectors of two-step size simulation results. The image on the bottom represents the difference between the two vectors.

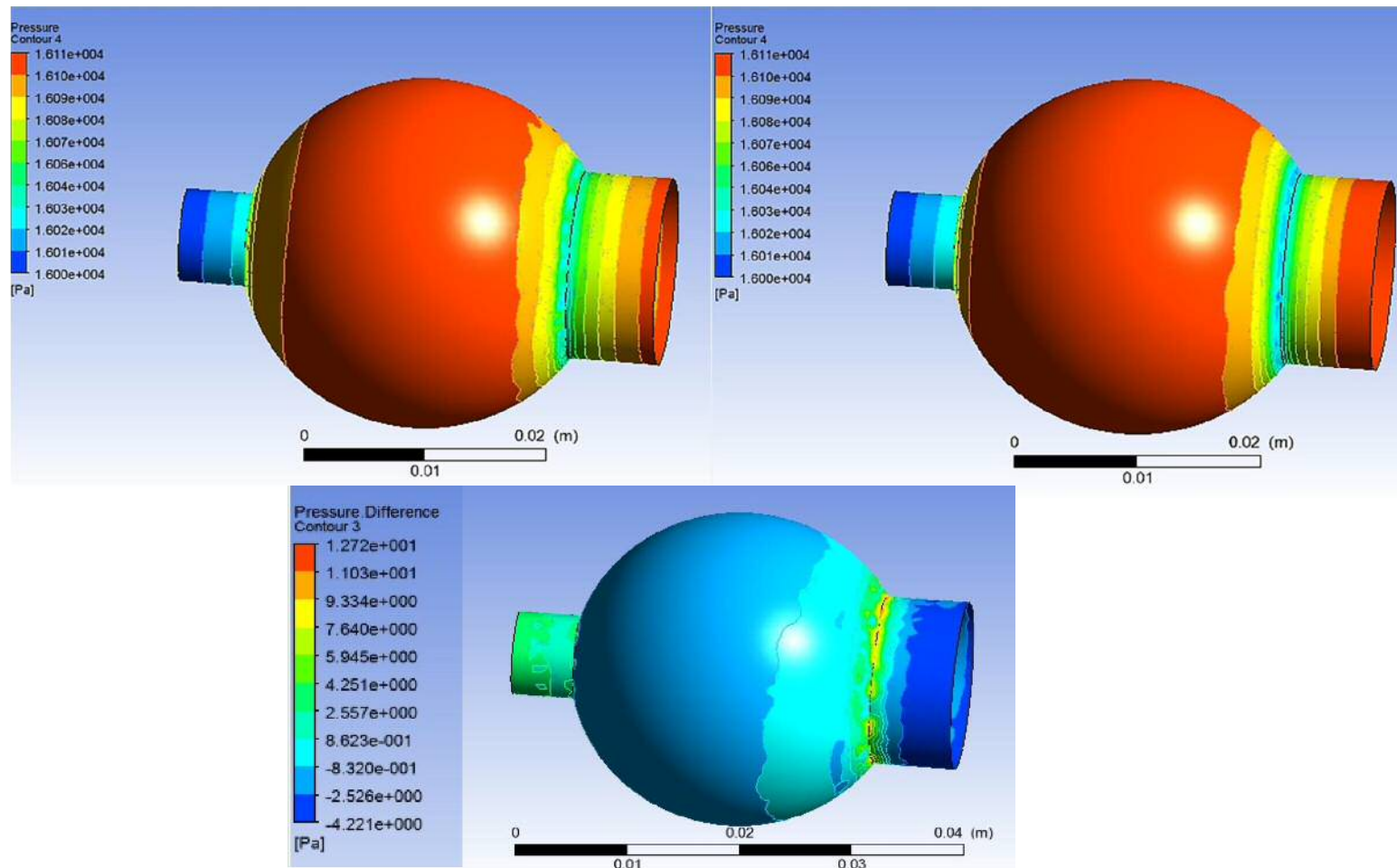


Figure 5-3 Pressure contour verification between different mesh elements and step size ANSYS16 Fluent: The images on the top represent pressure contours of two step-size simulation results. The image on the bottom represents the difference between the two contours.

### 5.2.2. Mapping Summary

As the issue of inverse volume error is common in FSI simulation, contacts between the structural parts of the FE was an important setting. To eliminate this issue, each part of the interfacing surfaces were taken separately by setting the connection method in the FE package and the fluid-structure connection in Fluent. Before the initiation of the simulation, the contact tool was used to identify the gap and penetration characteristics of the contacting elements.

#### ***Preliminary Model Mapping Summary***

Reducing the contact area decreases the computational cost, as can be seen in Figure 5-4 where the sphere has been identified as three parts; the upper and lower parts were considered contacting surfaces, and the middle part was connected to the inlet and outlet by the bonding connection.

The three-part sphere shape was grouped in ANSYS Design modeller to make sure that it is from the same material and there is no need to define the connection between the parts. This is an important step in the design, as during the simulation, if the parts are not grouped, they may dislocate when compression and release pressure occur or the pressure from the interfacing fluid interacts. The contact tool gives only the defined connection, and this is shown here with no penetration.

Figure 5-5 shows the mapping summary of the preliminary model. The mapping summary shows at the start of the simulation, and it is an indication of the model stability. The source and target surfaces of the FSI model are imported to a results component in ANSYS and should be set before the start of the simulation in the system coupling component. The mapping summary shows 100% mapped surfaces, and this is an indication that the data will be transferred between the two contacting surfaces during the FSI simulation.

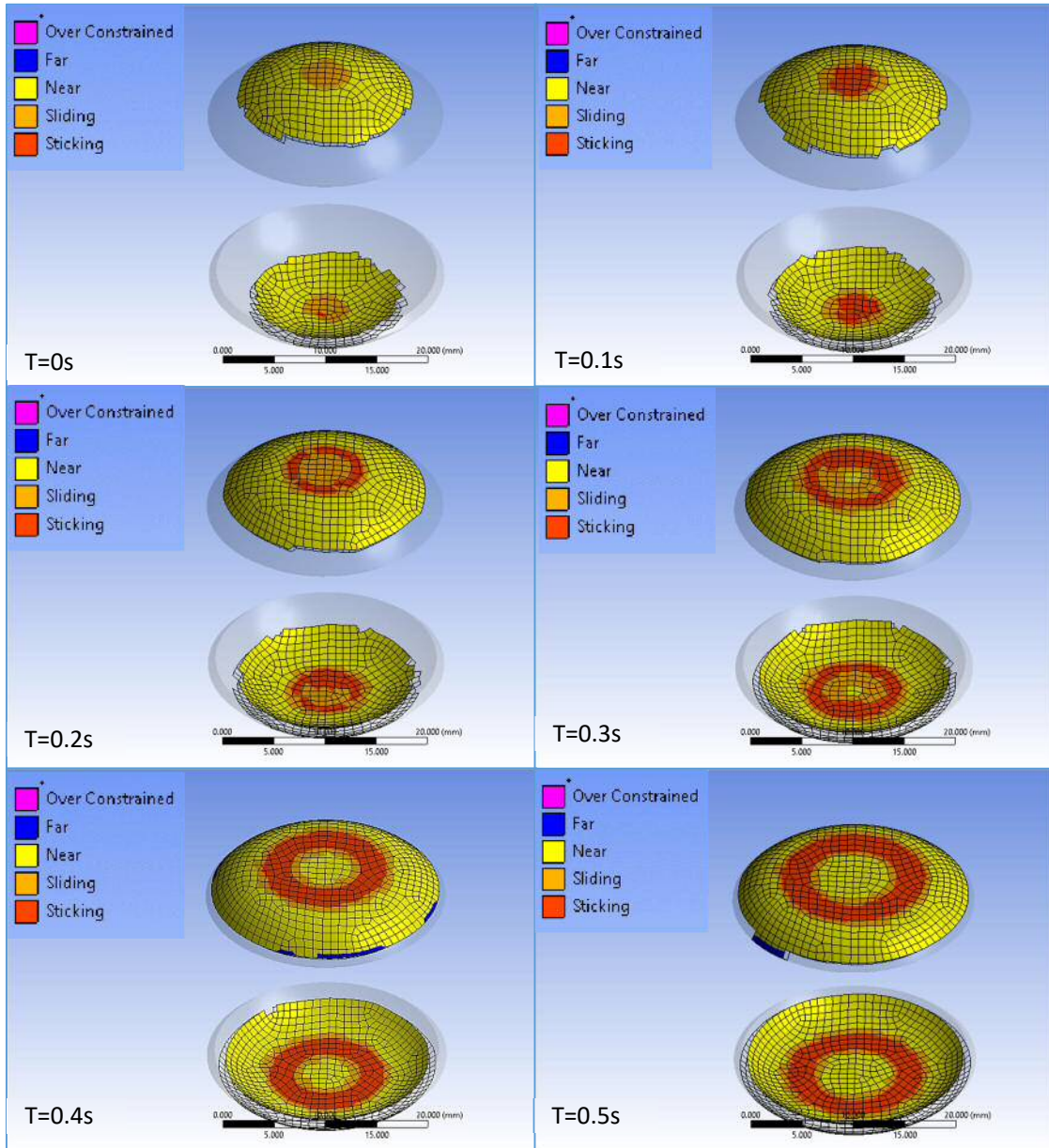


Figure 5-4 Contact status for the shell elements during the FSI simulation: During different time steps, the areas of contact are colour coded representing the elements close, far, penetration, and gap formation, which shows the lack of penetration elements during the simulation and the decrease of the gap between the compressing plates and the sphere surface.

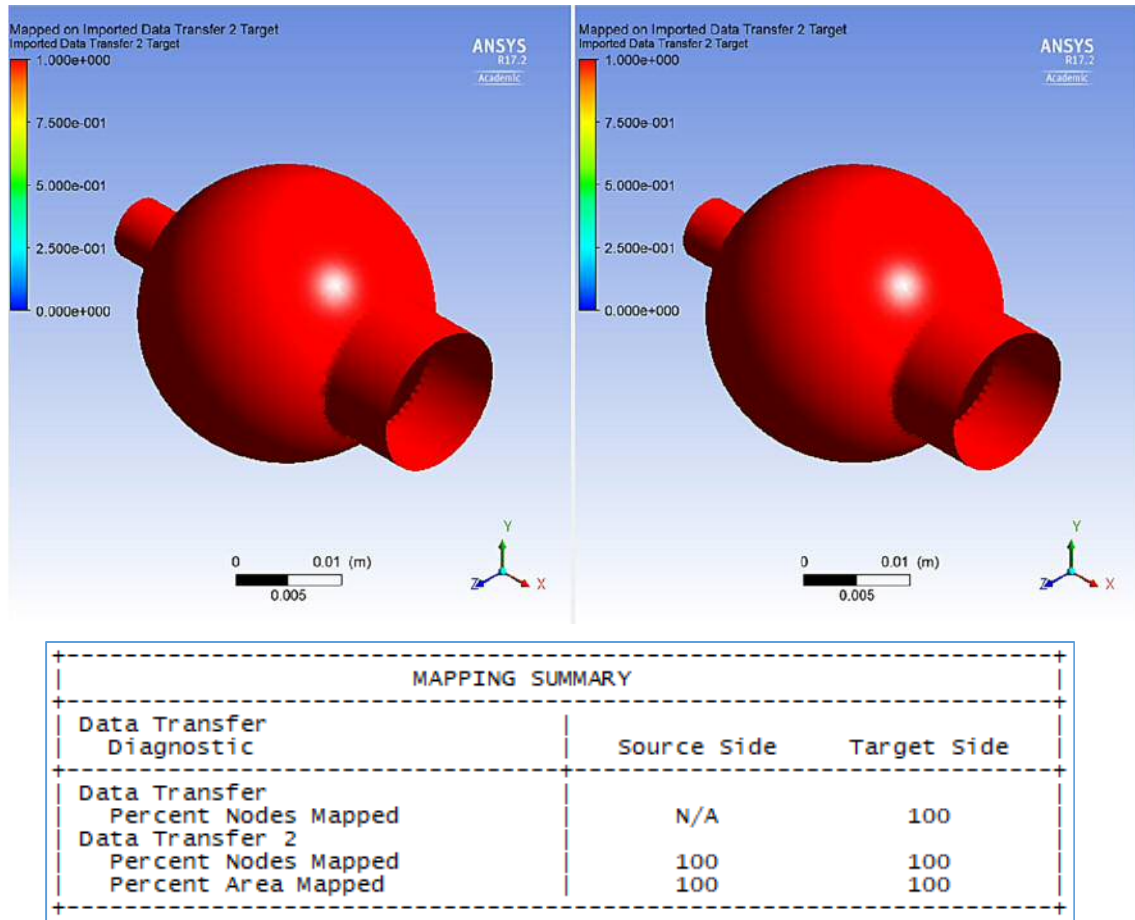


Figure 5-5 Mapping summary in the solution information of the preliminary model along with the source and target mapping compatibility: The similar colour surfaces show 100% compatibility as the unmapped surfaces would be indicated with blue coloured areas. The mapping summary is presented at the beginning of the simulation run showing 100% mapping between the source and target of the data transfer representing the structure and fluid in the FSI simulation.

### Subject-Specific Model Mapping Summary

The performance of the proposed model is evaluated and presented based on the fully converged computational results discussed in this chapter. The evaluation of the CPR compression technique has the major concern of getting a precise analysis of the flow characteristics during the full CPR procedure. This analysis requires breaking down the complex compression and release procedure into two two-way FSI simulations for one compression. A  $Y^+$  orientation is defined in the data collection of each simulation by locating the intersection between the boundary conditions in the fluid domain (post CFD) to better present the results in those planes which are parallel with the inflow velocity vectors. Based

on this orientation, clear images of 2D velocity streamlines are captured on various planar locations. The main reference planes are created in Cartesian coordinates, intersecting with the fluid flow boundaries in longitudinal YZ planes.

Figure 5-6 reveals the piglet heart CT scan using a lab-based Zeiss Xradia 520 (Carl Zeiss XRM, Pleasanton, CA, USA) X-ray. The images represent screenshots of the scanning video starting from (a) to (i). As can be seen, the heart was positioned in a cylinder to ensure it did not move during the scanning, and thus the orientation of the heart is not in the anatomical position as in the previous MRI scans. This meant rotating the 3D segmented model in 3-Matics to position the left ventricle in the expected anatomical position. This modification did not need to be done using the MRI scans, as the scans were of the whole anatomical chest, which positions the lungs and the heart in their accurate anatomical position. This also required the repositioning of the contained compression and fixed support plates in the FSI model. The rotation was done in 3-Matics, while repositioning according to the plates was done in ANSYS workbench; thus, this introduced a computational difficulty in mesh compatibility between the FE shell elements and the CFD fluid elements.

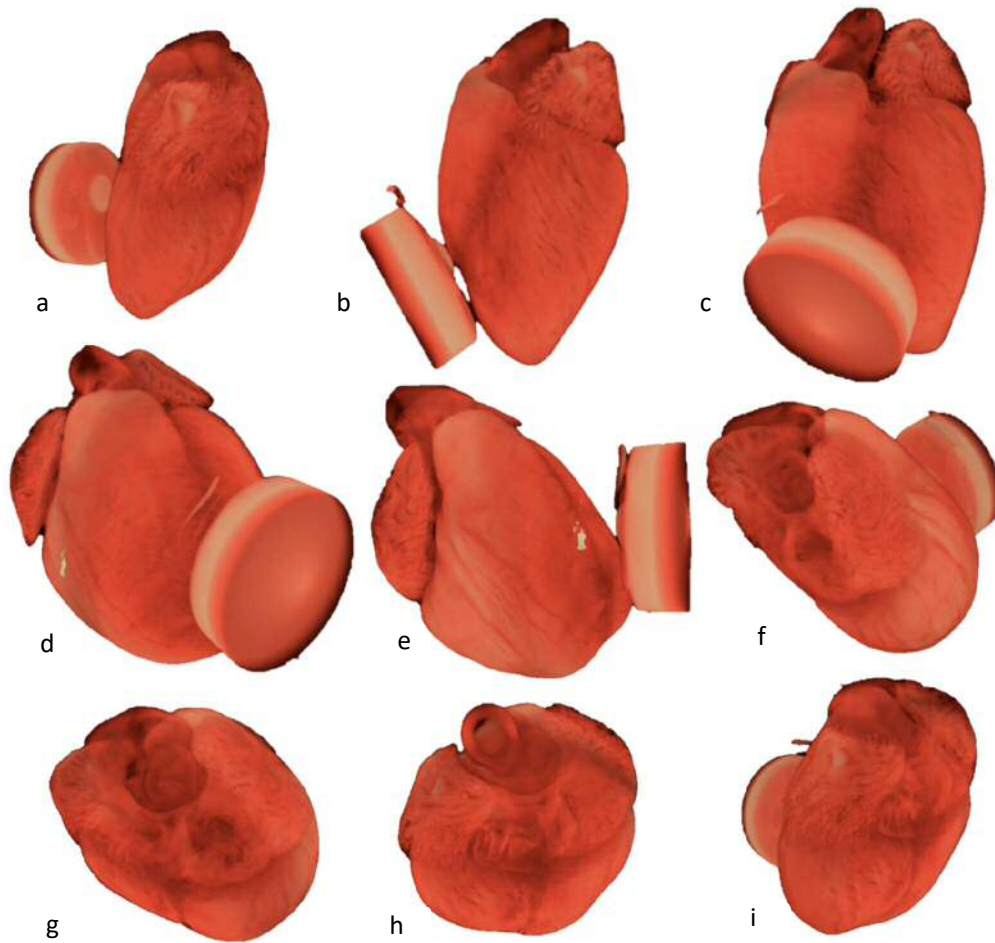


Figure 5-6 CT scans of piglet heart using a lab-based Zeiss Xradia 520 (Carl Zeiss XRM, Pleasanton, CA, USA) X-ray. The images represent screenshots of the scanning video starting from (a) to (i).

The compatibility was verified at the start of the simulation, as ANSYS monitoring shows the percentage of the source to target domains mapping summary, and during the simulation, this showed 100% mapping compatibility. Also, an execution control parameter was added in the expert setting, adding the *DumpInterfacemesh* property for both source and target. This property was examined using post CFD after each simulation to show the areas of incompatibility between the contacting surfaces of the fluid and structure until 100% compatibility was reached. This property was also used to examine the mesh quality, as it showed the weak mesh areas of the edges and boundary.

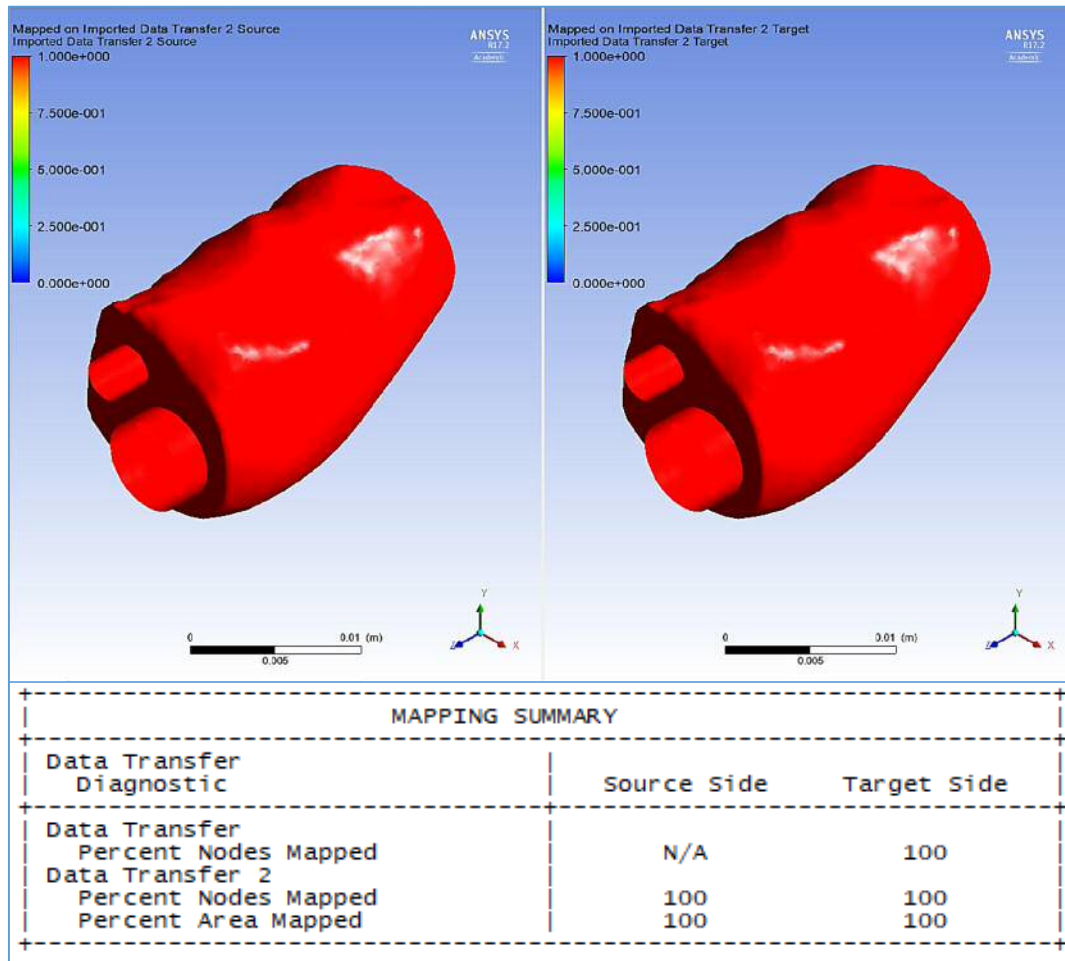


Figure 5-7 Coupling solution monitoring mapping summary and the mapping compatibility of the source and target of the structure and fluid contacting surfaces. The similarly coloured surfaces show 100% compatibility as the unmapped surfaces would be indicated with blue-coloured areas. The mapping summary is presented at the beginning of the simulation run, showing 100% mapping between the source and target of the data transfer representing the structure and fluid in the FSI simulation.

The mapping results in Figure 5-7 show 100% compatibility between the fluid and structure. As can be seen, the surface mapping was set from minimum to maximum, and the incompatible areas would show a blue colour in the case of incompatibility. As both the surfaces show the same colour without any areas of unmapped surfaces, this proves the 100% mapping between the contacting surfaces.



### 5.3. Computational Achievements

Capturing the pressure and velocity gradients across the left ventricle model and describing the stresses along the shell surface have been the main focus for developing the FSI method, as presented in Chapters 2 and 3. Although the method showed the potential to meet these two requirements in the various model problems proposed, several additional difficulties were encountered for the three-dimensional computational model of the left ventricle.

As the release phase was dependent on the first FSI, there were few modification possibilities to the boundary conditions. The second two-way FSI execution was also dependent on the first FSI. As the compression FSI needed development, the release was reset and the data cleared to follow the compression. That caused some issues with the mesh and step size sensitivity study, as the pre-stressed FSI needed to be reset after each modification, and each rerun of the simulation made it necessary to check the compatibility of the new modification. This also necessitated the rerun of the compression simulation to accommodate the dynamic mesh quality required by the second FSI.

The simulation time is an important factor for any computational model, as it reduces the computational cost. In this model, the required simulation time was reduced to a minimum without affecting the quality of the results; however, the simulation time for the largest mesh size and step size for the subject-specific model required over 10 hours, and thus any modification to the simulation parameters including structural and/or CFD required that amount of time to study its effect on the model.

The simulation running could be interrupted, but this adds to the data restart complication and the data saving process, and adds to the simulation time. This interruption process is explained in (ANSYS, 2018) and should be monitored so any interruptions of the software would not be saved, the simulation should be reset, and the run should be restarted; hence, signing off the workstation was not possible during the simulation.

A computational model needs to be stable before and during the simulation; any complication to the model may reduce this factor, and hence, convergence and complete data transfer between the fluid and structure will not occur. This issue was encountered in both computational models, as the material used was hyperelastic, and the fluid was considered non-Newtonian as the FSI model was already stable. All the improvement to the mesh quality increased the instability; hence, the trial and error

method to identify the correct stabilisation factor in Fluent added the time needed to design the working model.

The modelling process requires the use of multiple software programs for image segmentation, model design, model meshing, simulation, and material calibration. The use of multiple software programs introduced the issue of imported and exported files. Although in some of the software programs, it is mentioned that the files are compatible, working with these files demonstrated some incompatibility of the exported files, and even if the files were compatible, they needed further improvement before the export and after the import of the file into the new software. This was a major issue while importing the segmented geometry to ANSYS software, which required further improvement to the mesh in 3-Matics and in ANSYS after the file had been imported to the finite element modeller. This required modifying the workbench workflow design from the preliminary to the subject-specific model, as shown in Figure 3-13 and Figure 3-25. Including additional meshing and geometry components to the system coupling workflow always adds to the complexity of the simulation setting to be adapted to each analysis system component without losing the design's physical behaviour. This was also the case of importing the material model from MCalibration software to ANSYS as engineering data.

The major challenge in the design of the models was the meshing process. This arises from the compatibility issue mentioned earlier and from the compatibility of the fluid to solid contacting surfaces. The preliminary model mesh was used, as the geometry was shared, and both fluids and structures were meshed at the same time in the transient structural and at the pre Fluent meshing component. Although the meshing behaviour differed in the components, as each meshing relates to the material incorporated, the compatibility was monitored and recorded 100% at the start of each simulation. This issue was more complicated during the subject-specific model as the geometry is separate for both the fluid and structure due to the software compatibility issue mentioned before. This required further investigation of the meshing size and method. The meshing was monitored at the start of the simulation to show 100% compatibility between the source and target of the contacting surfaces.

There are several different factors that combine to affect the overall solution accuracy. In order of magnitude, those errors were considered throughout the simulation with the use of multiple surfaces and simulation monitoring:

- Round-off errors: Computer is working to a certain numerical precision
- Iteration errors: Difference between 'converged' solution and solution at iteration 'n'

- Solution errors: Difference between converged solution on current grid and 'exact' solution of model equations. 'Exact' solution: Solution on infinitely fine grid
- Model errors: Difference between 'exact' solution of model equations and reality (data or analytic solution)

## 5.4. Computational Model Limitations

The three-dimensional computational experiment, described in section 4.2.4, showed the development of a fluid pressure gradient in time. In this study, the FSI model fluid domain was fully divided by the wall boundary condition not allowing fluid to flow from one part to the other. In a heart valve problem, however, the valve does not cover the whole cross-sectional fluid area, as it has a small triangular opening in the middle. Although introducing the valve will improve the pressure gradient representation, it will add numerical complications to the FSI model, and so separate modelling is required for both the valves and the structural LV wall. The non-inclusion of the valves in the simulation was resolved by adding the second two-way FSI, which also added to the computational challenge.

The subject-specific model presented relies predominantly on idealized boundary conditions. For example, while in this model, the left ventricle wall was undistinguished from the septal wall, much more complex interactions exist within the human heart. The left ventricle wall is composed physically of both septal and epicardial surfaces. This surface composes the interior wall of the left ventricle and the right ventricle, which in turn, is in constant contact with the right ventricular blood flow. Moreover, the heart tissue wall is composed of three layers and has been numerically modelled by Holzapfel and Ogden (2009) and studied by Gultekin et al. (2016). This model requires computational coding for the numerical orthotropic curve fitting to be imported in the calibration software. This requires coding expertise that could not be acquired during the study and will be implemented in the subject-specific model in the future as a development of the existing model.

By modelling heart valves as the instantaneous opening or closing of the CFD model's inlet and outlet, our model deviated from the pressure-driven more-gradual valve opening and closing, thus causing errors in the velocity field near to the valves. However, we believe that some of the observations made are unlikely to change with or without these structures, such as the presence of vortex rings and the order of

magnitude of the wall shear stresses. Much previous work on adult ventricular fluid mechanics has been performed with simplifications such as ours. For example, several authors have modelled adult ventricles without heart valves (Cheng et al., 2005, Lemmon and Yoganathan, 2000, Watanabe et al., 2004), and their results still revealed much useful information. Thus, the current implementation is the first step in the scientific community's effort to understand infant cardiac fluid mechanics during CPR, with much room for future improvements.

It was also assumed that the area of the outlet and inlet does not change over time, which might give additional errors. However, while this error can be considerably small, (Lytle et al., 1985, Stewart et al., 1985) have reported that using the Doppler velocity alone with no consideration of valve-size changes over the cardiac cycle results in low errors in the flow rate for the aorta, mitral valve, and pulmonary arteries.

These limitations warrant extensive further research in both clinical imaging of the human infant heart and development of computational coding techniques, which could not be included in the current study.

## Chapter 6. Conclusion, Future Work and Research Contributions

### 6.1. Conclusion

The aim of this research was to investigate the effect of chest compression in infant CPR and establish a platform for computational model to investigate this effect. The coupled effects of flowing fluid and the heart wall during CPR was implemented by using a two-way fluid-structure interaction modelling of the left ventricle. The capability of two-way FSI modelling available in the commercial software ANSYS was used in this analysis and the following conclusions were drawn from this work:

- Two-way FSI provides a viable mechanism to further explore chest compression efficacy in infant CPR, based on the close comparison with the experimental data.
- Accurate simulation of blood velocity during LV expulsion provides opportunity to investigate new chest compression techniques that achieve an optimal value.
- Accurate representation of cardiac deformation provides new opportunities to explore the risk of iatrogenic trauma during chest compressions.
- Accuracy in simulating subject-specific geometries provides an investigative platform for exploring patient-specific cardiac interventions.

Those conclusions were based on the following computational and experimental findings:

- The velocity obtained from the experimental validation model agreed relatively well with that of the computational model giving the proposed model validity to be used in the investigation of the LV blood flow during compression (section 4.2.6, page 150).
- From the experimental results, the present physical model agrees relatively well with the data from the computational model regarding the deformation of the structural part along with the velocity magnitude obtained in both models (section 4.2.6, pages 151 and 152).

- Subject-specific model velocity profile of the blood flow from the outlet gave a similar velocity profile and magnitude as expected from a first compression of the left ventricle in a resting state (section 4.3.1, pages 177 and 178)
- The computational results demonstrated that the local apparent viscosity in non-Newtonian model had a high value near the boundary conditions and the middle of the LV. This viscosity profile agrees strongly with the literature blood non-Newtonian profile (section 4.3.1, page 179).
- The biaxial data showed that the stiffness of the 3D printed material was found to be lower than the tissue in the very low strain rate. However, the material was exposed to a loading strain relevant to its tested biaxial strain rate (section 4.2.2, page 115).
- The preliminary FSI model material experienced compression during the simulation; hence, the biaxial predicted data for the material is more significant for the choice of the hyperelastic material model (section 4.2.2, page 116).
- The proposed two-way FSI analysis of the problem was more sensitive to the meshes used in the fluid domain and finer meshes must be used for more complicated geometry, as expected (section 5.2.1, pages 200 and 201)

In summary, this research achieved the aim of implementing a fully coupled FSI method for the design and optimization of a porcine infant left ventricle during a simulated CPR compression. This model is considered a platform for investigating infant CPR chest compression parameter. Although the methods and results were validated by similar experimental work for the preliminary model and the literature, a more complicated model including the whole heart compartments and including the valves is recommended for further justifications. The following sections introduce a variety of improvements to the current computational method, and provide recommendations for the future directions in infant CPR modelling.

## 6.2. Future Work

The motivation for further research was found after extensive review about the existing limitations on the current model such as valve placement, mechanical material properties of the heart tissue. In this section, a brief overview is given outlining future directions for physiological modelling of the infant heart during CPR based on the work presented. A critical, and challenging, step is the validation of the future mechanical models for the simulation of heart function. As with many modelling efforts in biological systems, there are many potential avenues for model improvement. Finally, areas of interest and investigation are reviewed, illustrating the potential impact of these models.

### 6.2.1. Computational research needs

The advanced computational study of fluid structure interaction in left ventricle is facing, with exceptional degree of complexity in the modeling, and proposing an optimized design. As matter of fact, the existing methods up to date are not absolutely capable of precise predictions concerning hemodynamic and structural behavior of the infant heart model. Hence, an exclusive research is needed for enhancing the integration level between modeling endeavor and reality of the natural infant heart function.

In this regard, the first category of developments should suggest more efficient and accurate methods in data acquisition of the natural infant heart geometry. The available methods of MRI and CT scanning imaging are for animal heart and the available images for the human infant did not provide fine resolution image of the human organ. In addition, data processing and CAD rendering procedures are also a very time consuming step. The proposed modelling method, can be improved if more precise data is supplied. The technique reported by the current study relies on CT scan imaging for the FSI simulations. Structures such as the ventricular muscular texture, collagen fibres could not be clearly discerned. The thickness of the cardiac tissue varies through ventricle geometry and as the images were for already dead porcine, the heart structure was modified. For these reasons, we have not included these structures in the simulation, which would have inevitably limited the accuracy of our results.

Another major improvement is required in increasing the robustness of the computational algorithms in the area of multi domain coupling methods using multiple softwares. The meshing method for the CFD part of the FSI was faced with serious challenges, such as mesh adaptation techniques with large deformation and displacement occurring. Note that, the proper choice of dynamic meshing strategies is necessary to be employed, in which both the rate of convergence and precision of predictions are guaranteed. Current research used multi meshing routine to adapt to the compatibility between the segmenting and the simulating software for mesh updating, in which the skewness of fluid domain elements is continuously checked. Although the competency and accuracy of the applied method is verified, a very time consuming procedure of dynamic meshing is still the main challenge for future parametric studies. This is the major research required development of FSI algorithms, in which not only the expensive computational time and human effort is reduced, but also the inconsistencies of data exchange within the FSI scheme are eliminated.

A third class of improvements is related to the implementation of the cardiac tissue material orthotropic model. This research used a valid constitutive model hyperelastic 3D printed material properties as the constructive material. The dynamics of the proposed design is practically in agreement with the experimental data, however, additional investigation is recommended for the implementation of actual heart tissue orthotropic material model representing the numerical heart tissue model already available in literature. Although the cardiac tissue model is already presented in previous studies but the model requires advanced computational coding to be compatible in the simulating software which is a professional skill that could not be acquired during the time frame of the current study. Proposing an accurate orthotropic constitutive mode of the material, will offer more design optimization opportunities. Such a modification can broaden the range of design and optimization process.

The model presented in this study represent the effect of a single compression of the simulated CPR process. To study the effect of the CPR procedure, including multiple compressions according to the resuscitation guidelines in the model will give a comprehensive observation to the effectiveness of the factors influencing the predictability of this process. The current computational model could be validated against clinical data of blood flow parameters when the whole procedure is included in the model including the effect of the resuscitation breaths. This will definitely introduce a major complication to the model in terms of execution and modelling time and



coupling settings but will give validation opportunity to the actual procedure outcome. Hence, the need for a high performance computer is crucial to develop the model

### **6.2.2. Experimental research needs**

The present computational study of fluid structure interaction of cardiovascular component is validated by existing experimental preliminary model and results were validated against literature methodology and data. However, performing further validations is essential in order to explore the level of integrity between the evaluated performances and real values of structural and hemodynamical parameters. This will not only provide genuine feedback concerning the systematic approach undertaken for design and optimization, but also enhance the tailor made geometrical and material simplifications made on the proposed model.

The fundamental basis of experimental validation is to propose a robust and innovative left ventricle or human infant heart simulator as a 3D printed heart. Hence, identical geometrical representation that can be replicated in a experimental infant CPR manikin in order to evaluate and validate the performances of the proposed model. A 3D printed heart implementation in the manikin design can be used for future validation of manual compression and its effect on the flow using additional sensors of flow and pressure transducers to validate the existing subject-specific model.

Although using full blood in hemodynamical experiments is an ideal choice, much of the literatural experimental activities are using blood analogs. Therefore, future experimental research should consider the prospective of using the whole blood or any other resembling non-Newtonian analogs in which the effect of non-Newtonian rheology is not ignored. Such an approach may facilitates the identification of critical regions in which the non-Newtonian and mechanical properties of blood fluid are important (blood flow at valves boundary conditions).

The computational framework presented provides a potentially valuable tool for investigating aspects of cardiac physiology. The process of computational model validation is challenging and to develop a cardiac model often requires a substantial amount of data such as fibre orientation, material properties, and proper boundary condition. As a computational model, it is always considered as a simplification which, for many cardiac models, does not incorporate a large range of functional mechanisms. As a result of these complications, firm validation is improbable despite the significant advancements in MRI, Ct, Ultrasound and other assay measurements which can

provide comprehensive flow data and tissue movement. Due to the large number of factors which merge to produce observed heart function, it is impractical to truly validate a model with such simplifications. Perhaps a more reasonable approach is to assess model acceptability. Providing this knowledge, models can be effectively used to hypothesise functional behaviours within their window of applicability.

### **6.2.3. Prospective Simulations**

The application of fluid structure interaction analysis in the left ventricle design, can be extended from the current borders at compartment and organ level and focused more into complicated anatomical level. Including the thorax anatomical organs in the modeling approach can be utilized initially at including the valves and heart components in order to analyse damping effect of the layering structure. This is specifically vital on the aortic and pulmonary side of the heart as they are more connected to the cardiac cycle disturbance of the flow regimes. Hence, superior explanation can be offered for valve leaflet movement and their effect on the boundary condition.

### 6.3. Research Contributions

The research contributions listed below and are attached to this thesis in Appendix G. The published contributions to this thesis as follows:

- Samar Shaabeth, Allan Mason-Jones, Michael D Jones, Shwe P Soe, Peter S Theobald. *Development of an Infant Heart and Lung FEA Model for Optimizing Cardiopulmonary Resuscitation Performance*. 22nd Congress of the European Society of Biomechanics, July 10 - 13, 2016, Lyon, France.
- Faizan Ahmad, R. Prabhu, Jun Liao, Shwe Soe, Michael D Jones, Jonathan Miller, Parker Berthelson, Daniel Enge, Katherine M. Copeland, Samar Shaabeth, Richard Johnston, Ian Maconochie, Peter S. Theobald. *Biomechanical properties and microstructure of neonatal porcine ventricles*. Journal of the Mechanical Behavior of Biomedical Materials. Accepted 2018

## References

- AG, C. Z. 2018. *ZEISS International* [Online]. Available: <https://www.zeiss.com/microscopy/int/x-ray.html> [Accessed 2017].
- AGNEW, A. M., MOORHOUSE, K., KANG, Y. S., DONNELLY, B. R., PFEFFERLE, K., MANNING, A. X., LITSKY, A. S., HERRIOTT, R., ABDEL-RASOUL, M. & BOLTE, J. H. T. 2013. The Response Of Pediatric Ribs To Quasi-Static Loading: Mechanical Properties And Microstructure. *Ann Biomed Eng*, 41, 2501-14.
- AHMAD, F., PRABHU, R., LIAO, J., SOE, S., JONES, M. D., MILLER, J., BERTHELSON, P., ENGE, D., COPELAND, K. M., SHAABETH, S., JOHNSTON, R., MACONOCHIE, I. & THEOBALD, P. S. Unpublished. Biomechanical Properties And Microstructure Of Neonatal Porcine Ventricles. *Journal of the Mechanical Behavior of Biomedical Materials*. Cardiff University.
- ANNE L SOLEVÅG<sup>1</sup>, JORUNN MARIE MADLAND<sup>1</sup>, ESPEN GJÆRUM<sup>1</sup>, A. & BRITT NAKSTAD<sup>1</sup> 2012. Minute Ventilation At Different Compression To Ventilation Ratios, Different Ventilation Rates, And Continuous Chest Compressions With Asynchronous Ventilation In A Newborn Manikin.
- ANSYS, I. 2016. ANSYS Fluent Theory Guide. In: ANSYS, I. (ed.) *ANSYS Fluent Theory Guide*. U.S.A: ANSYS, Inc.
- ANSYS, I. 2018. *ANSYS software official website* [Online]. Available: <https://www.ansys.com/> [Accessed 2017].
- AREFIN, M. S. & MORSI, Y. S. 2014. Fluid Structure Interaction (FSI) Simulation Of The Left Ventricle (LV) During The Early Filling Wave (E-Wave), Diastasis And Atrial Contraction Wave (A-Wave). *Australas Phys Eng Sci Med*, 37, 413-23.
- AUGENSTEIN, K. F., COWAN, B. R., LEGRICE, I. J. & YOUNG, A. A. Estimation of Cardiac Hyperelastic Material Properties from MRI Tissue Tagging and Diffusion Tensor Imaging. 2006 Berlin, Heidelberg. Springer Berlin Heidelberg, 628-635.
- AVANZINI, A. & BATTINI, D. 2016. Integrated Experimental and Numerical Comparison of Different Approaches for Planar Biaxial Testing of a Hyperelastic Material. *Advances in Materials Science and Engineering*, 2016, 1-12.
- AXEL PRODUCTS, I. 2000. [www.axelproducts.com](http://www.axelproducts.com) *Compression or Biaxial Extension?* [Online]. Ann Arbor, MI, USA. [Accessed].

- BABBS, C. F., VOORHEES, W. D., FITZGERALD, K. R., HOLMES, H. R. & GEDDES, L. A. 1983. Relationship of Blood Pressure and Flow During CPR to Chest Compression Amplitude: Evidence for an Effective Compression Threshold.
- BAECK, K., LOPES, P. & VERSCHUEREN, P. 2017. Material Characterization Of Heartprint® Models And Comparison With Arterial Tissue Properties. Leuven, Belgium: Materialise NV.
- BARCLIFT, M. W. & WILLIAMS, C. B. 2012. Examining Variability In The Mechanical Properties Of Parts Manufactured Via Polyjet Direct 3d Printing.
- BARETTA, A., BAKER, H., KHAMBADKONE, S., HSIA, T.-Y., DUBINI, G., MIGLIAVACCA, F. & PENNATI, G. 2012. Patient-Specific Lumped Parameter Model of Single Ventricle Based on P-V Loop Analysis. *Journal of Biomechanics*, 45, S132.
- BASSOLS, A., COSTA, C., ECKERSALL, P. D., OSADA, J., SABRIA, J. & TIBAU, J. 2014. The Pig As An Animal Model For Human Pathologies: A Proteomics Perspective. *Proteomics Clin Appl*, 8, 715-31.
- BATCHELOR, G. K. 2000. *An Introduction to Fluid Dynamics*, Cambridge, Cambridge University Press.
- BEULEN, B. W. A. M. M., RUTTEN, M. C. M. & VAN DE VOSSE, F. N. 2009. A Time-Periodic Approach For Fluid-Structure Interaction In Distensible Vessels. *Journal of Fluids and Structures*, 25, 954-966.
- BIARENT, D., BINGHAM, R., EICH, C., LOPEZ-HERCE, J., MACONOCHIE, I., RODRIGUEZ-NUNEZ, A., RAJKA, T. & ZIDEMAN, D. 2010. European Resuscitation Council Guidelines for Resuscitation 2010 Section 6. Paediatric life support. *Resuscitation*, 81, 1364-88.
- BRUYAS, A. 2015. *Apport De La Fabrication Additive Multi-Mat'RIAUX Pour La Conception Robotique*. Docteur, Universit' de Strasbourg.
- BURKHART, T. A., ANDREWS, D. M. & DUNNING, C. E. 2013. Finite element modeling mesh quality, energy balance and validation methods: a review with recommendations associated with the modeling of bone tissue. *J Biomech*, 46, 1477-88.
- CHENG, Y., OERTEL, H. & SCHENKEL, T. 2005. Fluid-Structure Coupled CFD Simulation of the Left Ventricular Flow During Filling Phase. *Annals of Biomedical Engineering*, 33, 567-576.
- CHITRAKAR, S., CERVANTES, M. & THAPA, B. S. 2014. Fully Coupled FSI Analysis Of Francis Turbines Exposed To Sediment Erosion. *International Journal of Fluid Machinery and Systems*, 7, 101-109.

- CIFUENTES, A. O. & KALBAG, A. 1992. *A Performance Study of Tetrahedral and Hexahedral Elements in 3D Finite Element Structural Analysis*, IBM Thomas J. Watson Research Division.
- COSOLA, E., GENOVESE, K., LAMBERTI, L. & PAPPALETTERE, C. 2008. A General Framework For Identification Of Hyper-Elastic Membranes With Moiré Techniques And Multi-Point Simulated Annealing. *International Journal of Solids and Structures*, 45, 6074-6099.
- CRICK, S. J., SHEPPARD, M. N., HO, S. Y., GEBSTEIN, L. & ANDERSON, R. H. 1998. Anatomy Of The Pig Heart : Comparisons With Normal Human Cardiac Structure. *J. Anat.* , 193.
- CROCKER, L. E., DUNCAN, B. C., HUGHES, R. G. & URQUHART, J. M. 1999. Hyperelastic Modelling Of Flexible Adhesives Performance of Adhesive Joints Programme Project PAJ1 -Failure Criteria and their Application to Visco-Elastic/Visco-Plastic Materials. *NPL Report CMMT(A)*. National Physical Laboratory Teddington, Middlesex, UK.
- DAHL, S. K. 2012. *Numerical Simulations of Blood Flow in the Left Side of the Heart*. Philosophiae Doctor, Norwegian University of Science and Technology.
- DEAN, J. M., KOEHLER, R. C., SCHLEIEN, C. L., BERKOWITZ, I., MICHAEL, J. R., ATCHISON, D., ROGERS, M. C. & TRAYSTMAN, R. J. 1990. Age-related effects of compression rate and duration in cardiopulmonary resuscitation.
- DEAN, J. M., KOEHLER, R. C., SCHLEIEN, C. L., MICHAEL, J. R., CHANTAROJANASIRI, T., MARK C. ROGERS & TRAYSTMAN, R. J. 1987. Age-Related Changes In Chest Geometry During Cardiopulmonary Resuscitation.
- DOKOS, S., SMAILL, B. H., YOUNG, A. A. & LEGRICE, I. J. 2002. Shear Properties Of Passive Ventricular Myocardium. *Am J Physiol Heart Circ Physiol* 283.
- DOOST, S. N., ZHONG, L., SU, B. & MORSI, Y. S. 2016. The Numerical Analysis Of Non-Newtonian Blood Flow In Human Patient-Specific Left Ventricle. *Comput Methods Programs Biomed*, 127, 232-47.
- DRAKE, R. L., VOGL, W., MITCHELL, A. W. M., GRAY, H. & GRAY, H. 2010. *Gray's anatomy for students*, Philadelphia, PA, Churchill Livingstone/Elsevier.
- ERDEMIR, A., GUESS, T. M., HALLORAN, J., TADEPALLI, S. C. & MORRISON, T. M. 2012. Considerations for reporting finite element analysis studies in biomechanics. *J Biomech*, 45, 625-33.
- ESPA, S., BADAS, M. G., FORTINI, S., QUERZOLI, G. & CENEDESE, A. 2012. A Lagrangian Investigation Of The Flow Inside The Left Ventricle. *European Journal of Mechanics - B/Fluids*, 35, 9-19.

- FITZHUGH, R. 1961. Impulses And Physiological States In Theoretical Models Of Nerve Membrane. *Biophys. J.*, 1, 445–466.
- FORMAGGIA, L., MOURA, A. & NOBILE, F. 2007. On The Stability of The Coupling Of 3D and 1D Fluid-Structure Interaction Models for Blood Flow Simulations. *ESAIM: Mathematical Modelling and Numerical Analysis*, 41, 743-769.
- GEMSENSORSINC. Turbine Flow Rate Sensor FT-110 Series. *In*: LTD, G. S. (ed.). UK.
- GERRIT J. NOORDERGRAAF, TAMMO J. DIJKEMA, WIL J.P.M. KORTSMIT, WIL H.A. SCHILDERS, GERT J. SCHEFFER & NOORDERGRAAF, A. 2005. Modeling in Cardiopulmonary Resuscitation: Pumping the Heart. *Cardiovascular Engineering: An International Journal*, 5.
- GULTEKIN, O., SOMMER, G. & HOLZAPFEL, G. A. 2016. An Orthotropic Viscoelastic Model For The Passive Myocardium: Continuum Basis And Numerical Treatment. *Comput Methods Biomech Biomed Engin*, 19, 1647-64.
- HADDAD, S. M. & SAMANI, A. 2017. A novel micro-to-macro approach for cardiac tissue mechanics. *Comput Methods Biomech Biomed Engin*, 20, 215-229.
- HADI WIPUTRA, CHANG QUAN LAI, GUAT LING LIM, JOEL JIA WEI HENG, LAN GUO, SANAH MERCHANT SOOMAR, HWA LIANG LEO, ARIJIT BIWAS, CITRA NURFARAH ZAINI MATTAR & YAP, C. H. 2016. Fluid Mechanics of Human Fetal Right Ventricles From Image-Based Computational Fluid Dynamics Using 4d Clinical Ultrasound Scans. *Am J Physiol Heart Circ Physiol*, 311, H1498-H1508.
- HALPERIN, H. R., PARADIS, N., ORNATO, J. P., ZVIMAN, M., LACORTE, J., LARDO, A. & KERN, K. B. 2004. Cardiopulmonary Resuscitation With A Novel Chest Compression Device In A Porcine Model Of Cardiac Arrest: Improved Hemodynamics And Mechanisms. *J Am Coll Cardiol*, 44, 2214-20.
- HAZER, D. 2009. *Automated Patient-Specific Modeling of Blood Flow and Vessel Wall Mechanics in Aortic Pathology*. PhD, Fridericana zu Karlsruhe.
- HAZER, D., UNTERHINNINGHOFEN, R., KOSTRZEWA, M., KAUCZOR, H.-U., DILLMANN, R. & RICHTER, G.-M. 2006a. Wall Shear Stress Simulations in a CT Based Human Abdominal Aortic Model *Jahrestagung der Deutschen Gesellschaft für Computer- und Roboterassistierte Chirurgie CURAC*. Germany.
- HAZER, D., UNTERHINNINGHOFEN, R., KOSTRZEWA, M., KAUCZOR, H. U., DILLMANN, R. & RICHTER, G. M. 2006b. A Workflow for Computational Fluid Dynamics Simulations using Patient-Specific Aortic Models *International*

- Congress on FEM Technology with 2006 German ANSYS Conference.* Schwabenlandhalle Stuttgart/Fellbach, Germany.
- HELLEVIK, L. R., DAHL, S. K. & SKALLERUD, B. A Frst Approach Towards Patient-Specific 2D FSI-Simulation Of Mitral Valve Dynamics During Diastolic filling. Fourth national conference on Computational Mechanics, 2007 2007 Trondheim.
- HOLZAPFEL, G. A. & OGDEN, R. W. 2009. Constitutive Modelling Of Passive Myocardium: A Structurally Based Framework For Material Characterization. *Philos Trans A Math Phys Eng Sci*, 367, 3445-75.
- IGLESIAS, J. M., LOPEZ-HERCE, J., URBANO, J., SOLANA, M. J., MENCIA, S. & DEL CASTILLO, J. 2010. Chest Compressions Versus Ventilation Plus Chest Compressions In A Pediatric Asphyxial Cardiac Arrest Animal Model. *Intensive Care Med*, 36, 712-6.
- INSTITUTION, T. B. S. 2012. Rubber, vulcanized or thermoplastic — Determination of tensile stress-strain properties. UK.
- IONASEC, R. I., VOIGT, I., GEORGESCU, B., WANG, Y., HOULE, H., VEGA-HIGUERA, F., NAVAB, N. & COMANICIU, D. 2009. Patient-Specific Modeling and Quantification of the Aortic and Mitral Valves from 4D Cardiac CT and TEE. *IEEE*.
- JANELA, J., MOURA, A. & SEQUEIRA, A. 2010. A 3D Non-Newtonian Fluid–Structure Interaction Model For Blood Flow In Arteries. *Journal of Computational and Applied Mathematics*, 234, 2783-2791.
- JIM DAY, POWERTRAIN, G. & KURT MILLER 2000. Equibiaxial Stretching of Elastomeric Sheets, An Analytical Verification of Experimental Technique. *Axel Products, Inc*.
- KESY, A. & KOTLINKSI, J. 2010. Mechanical Properties Of Parts Produced By Using Polymer Jetting Technology. *Archives of Civil and Mechanical Engineering*, 10.
- KRITTIAN, S. B., LAMATA, P., MICHLER, C., NORDSLETTEN, D. A., BOCK, J., BRADLEY, C. P., PITCHER, A., KILNER, P. J., MARKL, M. & SMITH, N. P. 2012. A Finite-Element Approach To The Direct Computation Of Relative Cardiovascular Pressure From Time-Resolved Mr Velocity Data. *Med Image Anal*, 16, 1029-37.
- KRUTÍLEK, D. & RAIDA, Z. Optimal meshing for high-frequency analysis of realistic structure. 2015 Conference on Microwave Techniques (COMITE), 22-23 April 2015 2015. 1-4.
- KUNDU, P. K. & COHEN, I. M. 2008. *Fluid Mechanics*, Academic Press.



- KUNTZ, M. & MENTER, F. R. 2004. Simulation Of Fluid-Structure Interactions In Aeronautical Applications. *European Congress on Computational Methods in Applied Sciences and Engineering*.
- KUNZ, J. & STUDER, M. 2006. Determining the Modulus of Elasticity in Compression via the Shore A Hardness. *Kunststoffe international*, 2006, 92-94.
- LALLY, C., A.J.REID & PRENDERGAST, P. J. 2004a. Elastic Behavior of Porcine Coronary Artery Tissue Under Uniaxial and Equibiaxial Tension. *Annals of Biomedical Engineering*, 32, 1355–1364.
- LALLY, C., REID, A. J. & PRENDERGAST, P. J. 2004b. Elastic Behavior of Porcine Coronary Artery Tissue Under Uniaxial and Equibiaxial Tension. *Annals of Biomedical Engineering*, 32, 1355-1364.
- LASSILAA, T., MALOSSI, A. C. I., STEVANELLA, M., VOTTA, E., REDAELLI, A. & DEPARIS, S. 2012. Multiscale fluid-structure interaction simulation of patient-specific left ventricle fluid dynamics with fictitious elastic structure regularization. *Wiley InterScience*.
- LELOVAS, P. P., KOSTOMITSOPOULOS, N. G. & XANTHOS, T. T. 2014. A Comparative Anatomic and Physiologic Overview of the Porcine Heart. *Journal of the American Association for Laboratory Animal Science*, 53, 432–438.
- LEMMON, J. D. & YOGANATHAN, A. P. 2000. Three-Dimensional Computational Model of Left Heart Diastolic Function With Fluid–Structure Interaction. *Journal of Biomechanical Engineering*, 122.
- LI, Z., KINDIG, M. W., SUBIT, D. & KENT, R. W. 2010. Influence Of Mesh Density, Cortical Thickness And Material Properties On Human Rib Fracture Prediction. *Med Eng Phys*, 32, 998-1008.
- LIAGHAT, T. 2014. *Two-Way Fluid-Structure Coupling In Vibration And Damping Analysis Of An Oscillating Hydrofoil*. Diplôme De Maîtrise Ès Sciences Appliquées, Université De Montréal.
- LIU, Y., PEKKAN, K., JONES, S. C. & YOGANATHAN, A. P. 2004. The Effects of Different Mesh Generation Methods on Computational Fluid Dynamic Analysis and Power Loss Assessment in Total Cavopulmonary Connection. *Journal of Biomechanical Engineering*, 126, 594.
- LYTLE, B. W., COSGROVE, D. M., GILL, C. C., STEWART, R. W., GOLDING, L. A., GOORMASTIC, M., TAYLOR, P. C. & LOOP, F. D. 1985. Mitral Valve Replacement Combined With Myocardial Revascularization: Early And Late Results For 300 Patients, 1970 To 1983. *Circulation*, 71, 1179-1190.
- MACONOCHIE, I. K., BINGHAM, R., EICH, C., LOPEZ-HERCE, J., RODRIGUEZ-NUNEZ, A., RAJKA, T., VAN DE VOORDE, P., ZIDEMAN, D. A., BIARENT, D.

- & PAEDIATRIC LIFE SUPPORT SECTION, C. 2015. European Resuscitation Council Guidelines for Resuscitation 2015: Section 6. Paediatric life support. *Resuscitation*, 95, 223-48.
- MAHER, K. O., BERG, R. A., LINDSEY, C. W., SIMSIC, J. & MAHLE, W. T. 2009. Depth Of Sternal Compression And Intra-Arterial Blood Pressure During CPR In Infants Following Cardiac Surgery. *Resuscitation*, 80, 662-4.
- MAO, W., CABALLERO, A., MCKAY, R., PRIMIANO, C. & SUN, W. 2017. Fully-coupled fluid-structure interaction simulation of the aortic and mitral valves in a realistic 3D left ventricle model. *PLOS ONE*, 12, e0184729.
- MARTIN, P., THEOBALD, P., KEMP, A., MAGUIRE, S., MACONOCHIE, I. & JONES, M. 2013a. Real-Time Feedback Can Improve Infant Manikin Cardiopulmonary Resuscitation By Up To 79%--A Randomised Controlled Trial. *Resuscitation*, 84, 1125-30.
- MARTIN, P. S., KEMP, A. M., THEOBALD, P. S., MAGUIRE, S. A. & JONES, M. D. 2013b. Do Chest Compressions During Simulated Infant Cpr Comply With International Recommendations? *Arch Dis Child*, 98, 576-81.
- MARTIN, P. S., KEMP, A. M., THEOBALD, P. S., MAGUIRE, S. A. & JONES, M. D. 2013c. Does A More "Physiological" Infant Manikin Design Effect Chest Compression Quality And Create A Potential For Thoracic Over-Compression During Simulated Infant Cpr? *Resuscitation*, 84, 666-71.
- MARTINEZ-LEGAZPI, P., BERMEJO, J., BENITO, Y., YOTTI, R., PEREZ DEL VILLAR, C., GONZALEZ-MANSILLA, A., BARRIO, A., VILLACORTA, E., SANCHEZ, P. L., FERNANDEZ-AVILES, F. & DEL ALAMO, J. C. 2014. Contribution Of The Diastolic Vortex Ring To Left Ventricular Filling. *J Am Coll Cardiol*, 64, 1711-21.
- MATSHES, E. W. & TREVENEN, C. 2011. Infant Heart Dissection In A Forensic Context: Babies Are Not Just Small Adults. *Acad Forensic Pathol.*, 1, 156-165.
- METHTHANANDA, I. M., PARKER, S., PATEL, M. P. & BRADEN, M. 2009. The Relationship Between Shore Hardness Of Elastomeric Dental Materials And Young's Modulus. *Dent Mater*, 25, 956-9.
- MEYER, F., DECK, C. & EISENACH, A. 2011. Child Advanced Safety Project For European Roads.
- MIHALEF, V., IONASEC, R., WANG, Y., ZHENG, Y., GEORGESCU, B. & COMANICIU, D. Patient-Specific Modeling Of Left Heart Anatomy, Dynamics And Hemodynamics From High Resolution 4D CT. 2010 IEEE International Symposium on Biomedical Imaging: From Nano to Macro, 14-17 April 2010 2010. 504-507.

- MOORE, J. P. & WILLIAMS, C. B. 2012. Fatigue Characterization Of 3D Printed Elastomer Material. *23rd, Annual international solid freeform fabrication symposium*. Austin, TX.
- MOOSAVI, M. H., FATOURAEE, N., KATOOZIAN, H., PASHAEI, A., CAMARA, O. & FRANGI, A. F. 2014. Numerical Simulation Of Blood Flow In The Left Ventricle And Aortic Sinus Using Magnetic Resonance Imaging And Computational Fluid Dynamics. *Comput Methods Biomech Biomed Engin*, 17, 740-9.
- MOREIRA, D. C. & NUNES, L. C. S. 2013. Comparison of simple and pure shear for an incompressible isotropic hyperelastic material under large deformation. *Polymer Testing*, 32, 240-248.
- NAGUMO, J., ARIMOTO, S. & YOSHIKAWA, S. An Active Pulse Transmission Line Simulating Nerve Axon. *Proc. IRE*, 1962. 2061–2070.
- NEURAUTER, A., NYSAETHER, J., KRAMER-JOHANSEN, J., EILEVSTJONN, J., PAAL, P., MYKLEBUST, H., WENZEL, V., LINDNER, K. H., SCHMOLZ, W., PYTTE, M., STEEN, P. A. & STROHMENGER, H. U. 2009. Comparison of mechanical characteristics of the human and porcine chest during cardiopulmonary resuscitation. *Resuscitation*, 80, 463-9.
- NORDSLETTEN, D. *Fluid - Solid Coupling for the Simulation of Left Ventricular Mechanics*. University of Oxford.
- NORDSLETTEN, D., MCCORMICK, M., KILNER, P. J., HUNTER, P., KAY, D. & SMITH, N. P. 2011a. Fluid-solid coupling for the investigation of diastolic and systolic human left ventricular function. *International Journal for Numerical Methods in Biomedical Engineering*, 27, 1017-1039.
- NORDSLETTEN, D. A., NIEDERER, S. A., NASH, M. P., HUNTER, P. J. & SMITH, N. P. 2011b. Coupling multi-physics models to cardiac mechanics. *Prog Biophys Mol Biol*, 104, 77-88.
- OERTEL, H. & KRITTIAN, S. (eds.) 2012. *Modelling the Human Cardiac Fluid Mechanics*.
- OGDEN, R. W. 1972a. Large Deformation Isotropic Elasticity – On The Correlation Of Theory And Experiment For Incompressible Rubberlike Solids. *Proceedings Of The Royal Society A Mathematical, Physical And Engineering Sciences*, 326.
- OGDEN, R. W. 1972b. Large Deformation Isotropic Elasticity: On The Correlation Of Theory And Experiment For Compressible Rubberlike Solids. *Proceedings Of The Royal Society A Mathematical, Physical And Engineering Sciences*, 328.
- OLIVEIRA, B. L. D. & SUNDNES, J. Comparison of Tetrahedral and Hexahedral Meshes for Finite Element Simulation of Cardiac Electro-Mechanics. VII

- European Congress on Computational Methods in Applied Sciences and Engineering, 2016. National Technical University of Athens.
- OPENSHAW, P., EDWARDS, S. & HELMS, P. 1984. Changes in rib cage geometry during childhood. *Thorax*, 39, 624-627.
- ORNATO, J. P. & PEBERDY, M. A. 2005. *Cardiopulmonary Resuscitation*, Humana Press, Totowa, N.J.
- PALMIERI, G., CHIAPPINI, G., SASSO, M. & PAPALINI, S. Hyperelastic Materials Characterization by Planar Tension Tests and Full-field Strain Measurement. SEM Annual Conference, 2009 Albuquerque New Mexico USA. Albuquerque New Mexico USA.
- PANTON, R. L. 2005. *Incompressible Flows*, Academic Press.
- PEARSON EDUCATION, I. 2010. *Intro to the Heart* [Online]. Available: <https://antranik.org/intro-to-the-heart/> [Accessed 2017].
- PEARSON, I. & PICKERING, M. 2001. The determination of a highly elastic adhesive's material properties and their representation in "Finite element analysis. *Finite Elements in Analysis and Design*, 37, 221-232.
- PETERS, J. & IHLE, P. 1990a. Mechanics Of The Circulation During Cardiopulmonary Resuscitation Pathophysiology And Techniques (Part I). *Intensive Care Med* 16, 20-27.
- PETERS, J. & IHLE, P. 1990b. Mechanics Of The Circulation During Cardiopulmonary Resuscitation Pathophysiology And Techniques (Part II). *Intensive Care Med*, 16, 20-27.
- RAMOS, A. & SIMOES, J. A. 2006. Tetrahedral versus hexahedral finite elements in numerical modelling of the proximal femur. *Med Eng Phys*, 28, 916-24.
- RIVLIN, R. S. 1948. Large elastic deformations of isotropic materials IV. further developments of the general theory. *Philosophical Transactions of the Royal Society of London. Series A, Mathematical and Physical Sciences*, 241, 379-397.
- ROBINSON, M., SOE, S., JOHNSTON, R., BUREK, R., MCSHANE, G., ADAMS, R., HANNA, B. & THEOBALD, P. Unpublished. Mechanical Characterization of Additively Manufactured Elastomeric Structures for High Strain Rate Applications. Cardiff University.
- ROTTENBERG, E. M. 2014. The Critical Need For Further Research And Development Of Abdominal Compressions Cardiopulmonary Resuscitation. *Am J Emerg Med*, 32, 931-4.
- RS Arduino Uno Datasheet and manual. In: RADIONONS, R. (ed.).

- RUDIHOFF, M. T., MAUGHAN, W. L., EFFRON, M., FREUND, P. & WEISFELDT, M. L. 1980. Mechanisms Of Blood Flow During Cardiopulmonary Resuscitation. *Circulation*, 61, 345-352.
- SABER, N. R., WOOD, N. B., GOSMAN, A. D., MERRIFIELD, R. D., YANG, G.-Z., CHARRIER, C. L., GATEHOUSE, P. D. & FIRMIN, D. N. 2003. Progress Towards Patient-Specific Computational Flow Modeling of the Left Heart via Combination of Magnetic Resonance Imaging with Computational Fluid Dynamics. *Annals of Biomedical Engineering*, 31, 42-52.
- SANDOZ, B., VAJDA, E., ALONZO, F., BRUYERE, K. & BERMOND, F. 2011. The Mechanics Of The In Vivo Infant And Toddler Trunk During Respiratory Physiotherapy. *Clin Biomech (Bristol, Avon)*, 26, 535-42.
- SASSO, M. & AMODIO, D. 2006. Development of a Biaxial Stretching Machine for Rubbers by Optical Methods.
- SASSO, M., PALMIERI, G., CHIAPPINI, G. & AMODIO, D. 2008. Characterization of hyperelastic rubber-like materials by biaxial and uniaxial stretching tests based on optical methods. *Polymer Testing*, 27, 995-1004.
- SASSO, M., PAPALINI, S., CHIAPPINI, G. & PALMIERI, G. 2007. Characterization of Time-Dependent Materials by Biaxial Stretching Tests.
- SCAMPOLI, S. System Coupling 14.0 – Two- way FSI with ANSYS FLUENT and ANSYS Mechanical. ANSYS Regional Conference, 2012.
- SEIBERT, H., SCHEFFER, T. & DIEBELS, S. 2014. Biaxial Testing of Elastomers - Experimental Setup, Measurement and Experimental Optimisation of Specimen's Shape. *Technische Mechanik*, 34, 72 – 89.
- SHAHZAD, M., KAMRAN, A., SIDDIQUI, M. Z. & FARHAN, M. 2015. Mechanical Characterization and FE Modelling of a Hyperelastic Material. *Materials Research*, 18, 918-924.
- SHORTLAND A. P. , A., B., JARVIS J. C., HENRY F. S. , IUDICELLO F., W., C. M. & S., S. 1996. Formation And Travel Of Vortices In Model Ventricles: Application To The Design Of Skeletal Muscle Ventricles *Journal of Biomechanics*, 29, 503-511.
- SILBERNAGL, S. & LANG, F. 2000. *Color Atlas of Pathophysiology.*, Stuttgart, New York, Thieme.
- SOMMER, G., SCHRIEFL, A. J., ANDRA, M., SACHERER, M., VIERTLER, C., WOLINSKI, H. & HOLZAPFEL, G. A. 2015. Biomechanical properties and microstructure of human ventricular myocardium. *Acta Biomater*, 24, 172-92.
- STANDARDIZATION, I. O. F. 2005. Rubber, vulcanized or thermoplastic — Determination of tensile stress-strain properties. *ISO 37:2005(E)*. Switzerland.

- STANDARDS, B. 2011. Rubber, vulcanized or thermoplastic — Determination of compression stress-strain properties. British Standards.
- STEPHENSON, R. S., BOYETT, M. R., HART, G., NIKOLAIDOU, T., CAI, X., CORNO, A. F., ALPHONSO, N., JEFFERY, N. & JARVIS, J. C. 2012. Contrast Enhanced Micro-Computed Tomography Resolves The 3-Dimensional Morphology Of The Cardiac Conduction System In Mammalian Hearts. *PLoS One*, 7, e35299.
- STEWART, W. J., JIANG, L., MICH, R., PANDIAN, N., GUERRERO, J. L. & WEYMAN, A. E. 1985. Variable effects of changes in flow rate through the aortic, pulmonary and mitral valves on valve area and flow velocity: Impact on quantitative doppler flow calculations. *Journal of the American College of Cardiology*, 6, 653-662.
- SWART, G. L., MATEER, J. R., DEBEHNKE, D. J., JAMESON, S. J. & OSBORN, J. L. 1994. The Effect of Compression Duration on Hemodynamics during Mechanical High-impulse CPR. *ACADEMIC EMERGENCY MEDICINE*, 1, 430-437.
- TAKAHASHI, H. & FROST, H. M. 1966. Age and Sex Related Changes in the Amount of Cortex of Normal Human Ribs. *Acta Orthopaedica*, 37, 122-130.
- TANG, D., YANG, C., GEVA, T. & DEL NIDO, P. J. 2008. Patient-specific MRI-based 3D FSI RV/LV/patch models for pulmonary valve replacement surgery and patch optimization. *J Biomech Eng*, 130, 041010.
- TSAI, A., COATS, B. & KLEINMAN, P. K. 2012. Stress Profile Of Infant Rib In The Setting Of Child Abuse: A Finite Element Parametric Study. *J Biomech*, 45, 1861-8.
- UDRIȘTE, M. A. & NEAGU, A. 2010. Aspects Of Thorax Biomechanics And Their Implications In Improving Cardiopulmonary Resuscitation Techniques. *Romanian J. Biophys*, 20, 193-201.
- VERESS, A. I., GULLBERG, G. T. & WEISS, J. A. 2005. Measurement of Strain in the Left Ventricle during Diastole with cine-MRI and Deformable Image Registration. *Journal of Biomechanical Engineering*, 127, 1195-1207.
- VERESS, A. I., WEISS, J. A., KLEIN, G. J. & GULLBERG, G. T. Quantification of 3D left ventricular deformation using hyperelastic warping: comparisons between MRI and PET imaging. *Computers in Cardiology*, 22-25 Sept. 2002 2002. 709-712.
- WANG, L., QUANT, R. & KOLIOS, A. 2016. Fluid structure interaction modelling of horizontal-axis wind turbine blades based on CFD and FEA. *Journal of Wind Engineering and Industrial Aerodynamics*, 158, 11-25.

- WATANABE, H., SUGIURA, S., KAFUKU, H. & HISADA, T. 2004. Multiphysics Simulation Of Left Ventricular Filling Dynamics Using Fluid-Structure Interaction Finite Element Method. *Biophysical Journal*, 87, 2074-85.
- YANG, K. H., HU, J., WHITE, N. A. & KING, A. I. 2006. Development of Numerical Models for Injury Biomechanics Research: A Review of 50 Years of Publications in the Stapp Car Crash Conference. *Stapp Car Crash Journal*, 50, 429-490.
- YANNOPOULOS, D., MCKNITE, S., AUFDERHEIDE, T. P., SIGURDSSON, G., PIRRALLO, R. G., BENDITT, D. & LURIE, K. G. 2005. Effects of Incomplete Chest Wall Decompression During Cardiopulmonary Resuscitation on Coronary and Cerebral Perfusion Pressures in A Porcine Model of Cardiac Arrest. *Resuscitation*, 64, 363-72.
- ZHONG, L., SU, B., ZHANG, J. M., LEO, H. L. & TAN, R. S. 2013. Fsi Simulation Of Intra-Ventricular Flow In Patient-Specific Ventricular Model With Both Mitral And Aortic Valves. *Conf Proc IEEE Eng Med Biol Soc*, 2013, 703-6.
- ZUERCHER, M., HILWIG, R. W., RANGER-MOORE, J., NYSAETHER, J., NADKARNI, V. M., BERG, M. D., KERN, K. B., SUTTON, R. & BERG, R. A. 2010. Leaning during chest compressions impairs cardiac output and left ventricular myocardial blood flow in piglet cardiac arrest. *Crit Care Med*, 38, 1141-6.

## **Appendix A. Simulation Quality Assurance**

### **Preliminary Model Simulation Monitoring**

To determine the quality of the computational model, convergence and stability were monitored throughout the running simulation. This step was performed to eliminate any causes of data shift or inconsistency due to software computational artefacts. Three types of monitoring were used to examine the convergence of the model in the structural, fluid, and system coupling components of ANSYS software. The monitoring charts were a measure of the convergence of the model at each iteration step and/or cumulative iteration time. Slow or “bad” convergence was monitored through the simulation at initial time steps to reduce the computational cost and abort the simulation. This was done to modify the setting for better convergence and stabilisation for the model as well.

In the transient structural component, displacement, force, and momentum convergence were monitored with reference to the cumulative iteration time (Figure A-1).



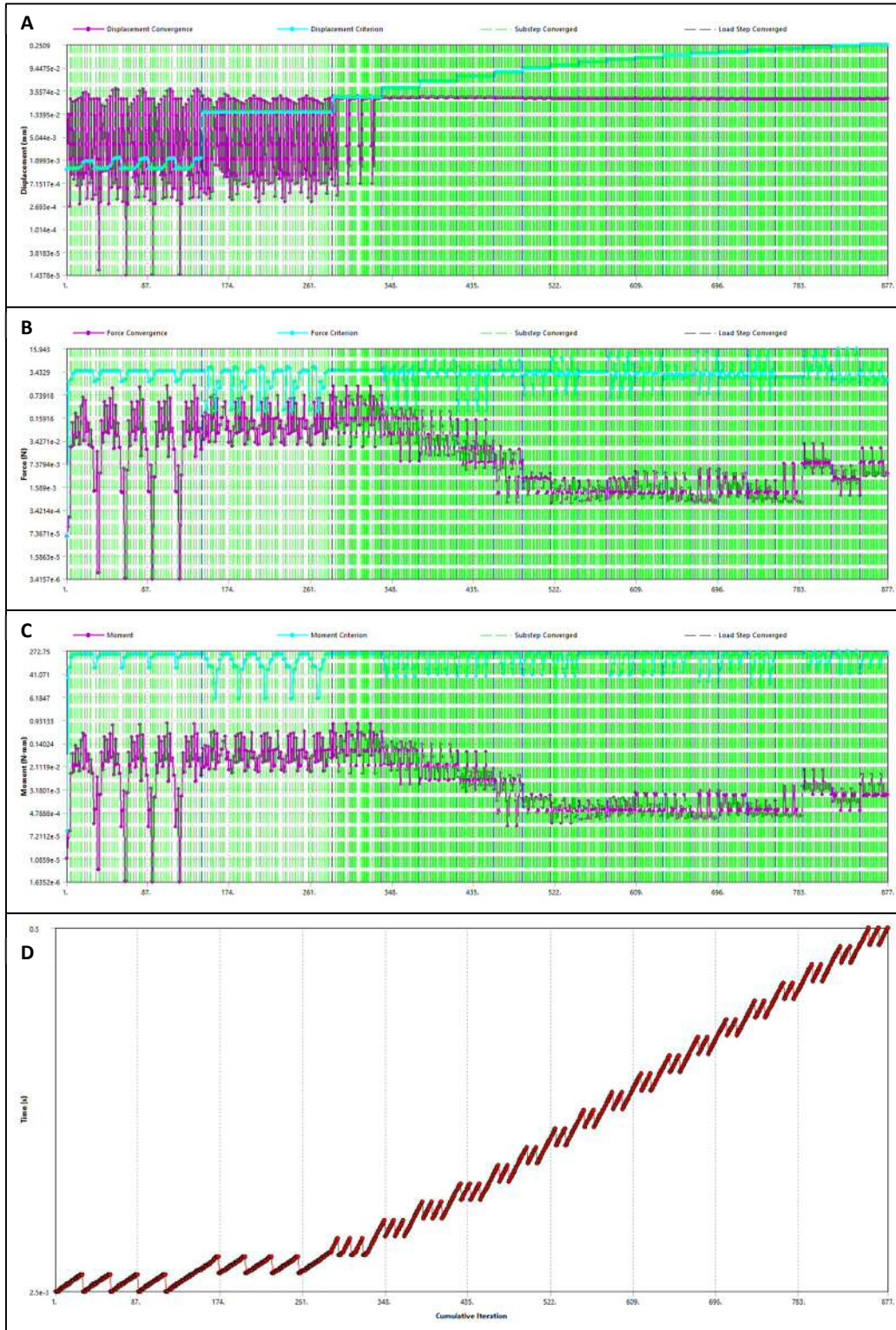


Figure A-1 Solution information for the FE analysis of the FSI simulation: A) Displacement convergence, B) Force convergence, C) Momentum convergence, D) Cumulative iteration time where all the above results projected on

The final simulation charts are presented in this appendix showing the successful, stable, and converged models. Sub steps were also indicated in the monitoring charts and were represented as vertical lines to determine the current time step during the simulation. This is useful in the case of any interruption to the simulation, as the restart was set before the run, and the model will reiterate the simulation at any sub step interruption time. The convergence was obtained faster after the onset of the compression, and convergence happened at each step during the simulation of the FSI preliminary model, as can be seen in Figure A-1.

In Fluent, residual stresses and surface monitoring were used to measure the convergence and stability of the simulated model. Convergence throughout the simulation is evident via the residual stress monitor supported by the static pressure and velocity magnitude convergence shown in Figure A-2. The surface monitoring was set prior to the execution of the simulation in order for it to be saved in the same file path to be studied later on or during the simulation. The surface monitoring data indicate the required time stepping in both FE and CFD. In Fluent, the iteration stepping follows the time step set in the system coupling component of the FSI simulation; thus, monitoring the convergence gives an indication not only of the CFD but of the FSI convergence as well.

The CFD number of iterations was reduced to a minimum of four iteration per time step to enhance the convergence and reduce the computational cost. Reducing the number further would have introduced an issue of very fast interaction between the dynamic elements of mesh between the interacting surfaces causing the interfacing problem. This was obvious in the velocity magnitude monitoring chart, but it was necessary to use more CPU for the simulation instead of facing the interfacing issue as well as using parallel simulation with six cores for the CFD and two for the structural. The other monitors showed the same convergence criteria for the simulation, which indicates good convergence during the simulation. These surface monitors were also used to indicate the stabilisation factor quantity needed to stabilise the model, as the model was interrupted to change the stabilisation factor and reset.

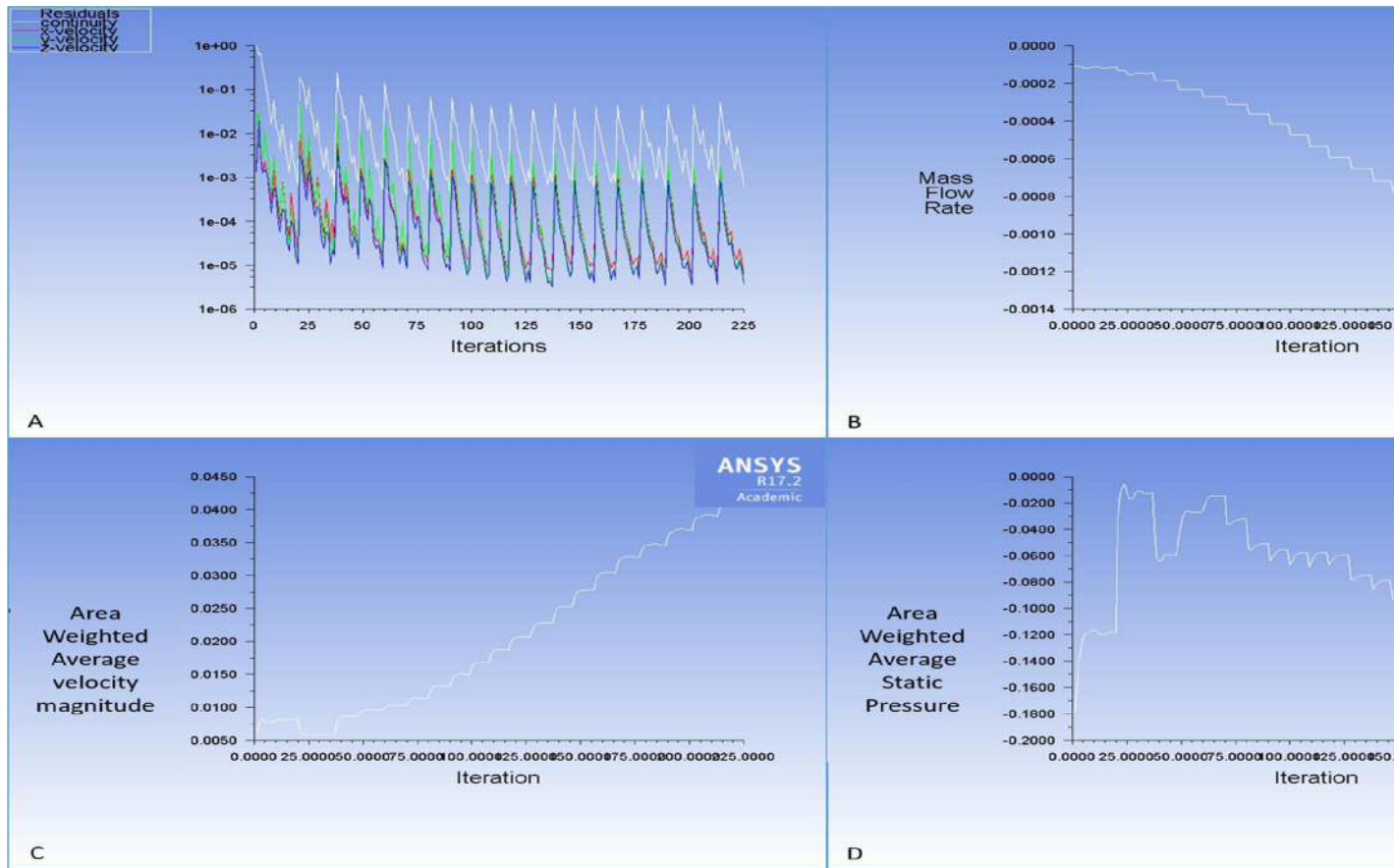


Figure A-2 FLUENT simulation monitoring. A) Scaled residuals, B) Mass flow rate on the outlet, C) Area weighted average of the velocity magnitude, D) Area weighted average of the pressure on the deforming wall

This procedure is the only way to examine the required stabilisation factor for better simulation, and as the factor range starts from 1 to 1000, it introduced a simulation challenge and added to the time needed for the running simulation to be assessed.

The third monitoring chart was used to examine the co-simulation process of the structure and fluid simulation at the same time and to observe the data transfer behaviour between the contacting surfaces of the model. As the model implements hyperelastic material with incompressible fluid model, the model is already unstable, and the first initialising step shows an enhanced stability afterwards due the enhanced stability factor and data transfer convergence. Figure A-3 shows the convergence of the two data transfers, and it indicates that the simulation converged in each step.

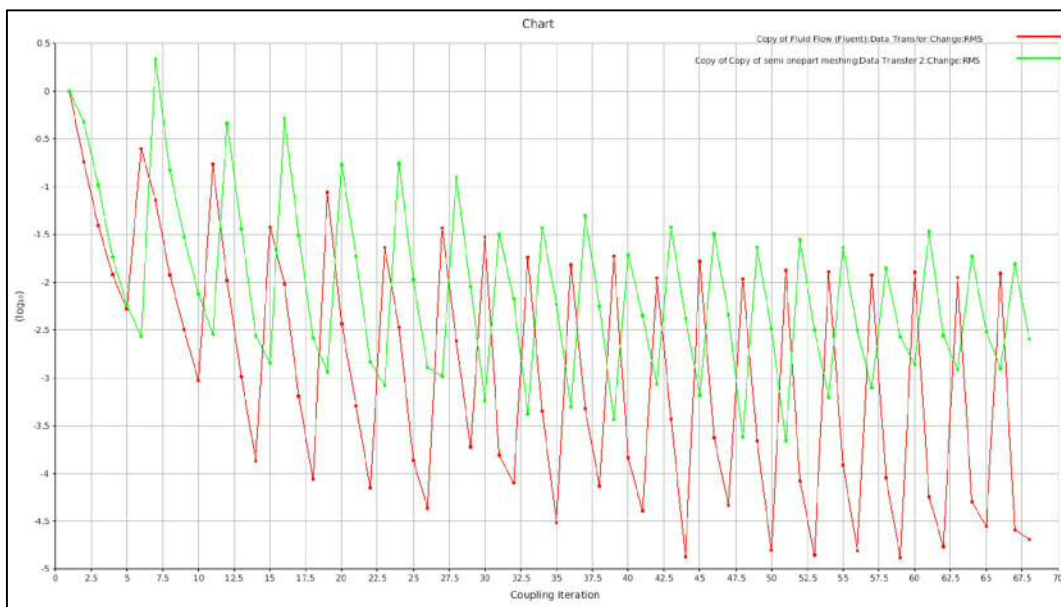


Figure A-3 System coupling monitor chart for the transient structural and Fluent flow during the simulation (compression stage)

## Subject-Specific Model Simulation Monitoring

In the subject specific model, the same monitoring charts were used to examine the convergence and stability of the model simulation for structural, CFD, and FSI components. During the 2-way FSI simulation, there were some noticeable differences of the convergence quality between the compression and release phases of the FSI. During the structural monitoring, sub stepping was not introduced, and that was obvious in the lack of the sub stepping indicators; hence, any interruption of the simulation would require a restart of the simulation FSI time-step iteration. The successful model structural monitoring charts are shown in Figure A-4 and Figure A-5. Three graphs of the displacement, force, and momentum

of the average elements for the model in accordance with the cumulative iterations were observed during the simulation. Convergence in the late part of the simulation was observed to be faster and in consequence of the early part associated with the initiation of the compression and release of the model. Also, the number of steps used was higher than the number used in the preliminary model; that was used for stabilisation purposes, as can be seen in the relating figures. As the model geometry is complicated, stabilisation was required for better convergence, and this is evident in the monitoring charts.

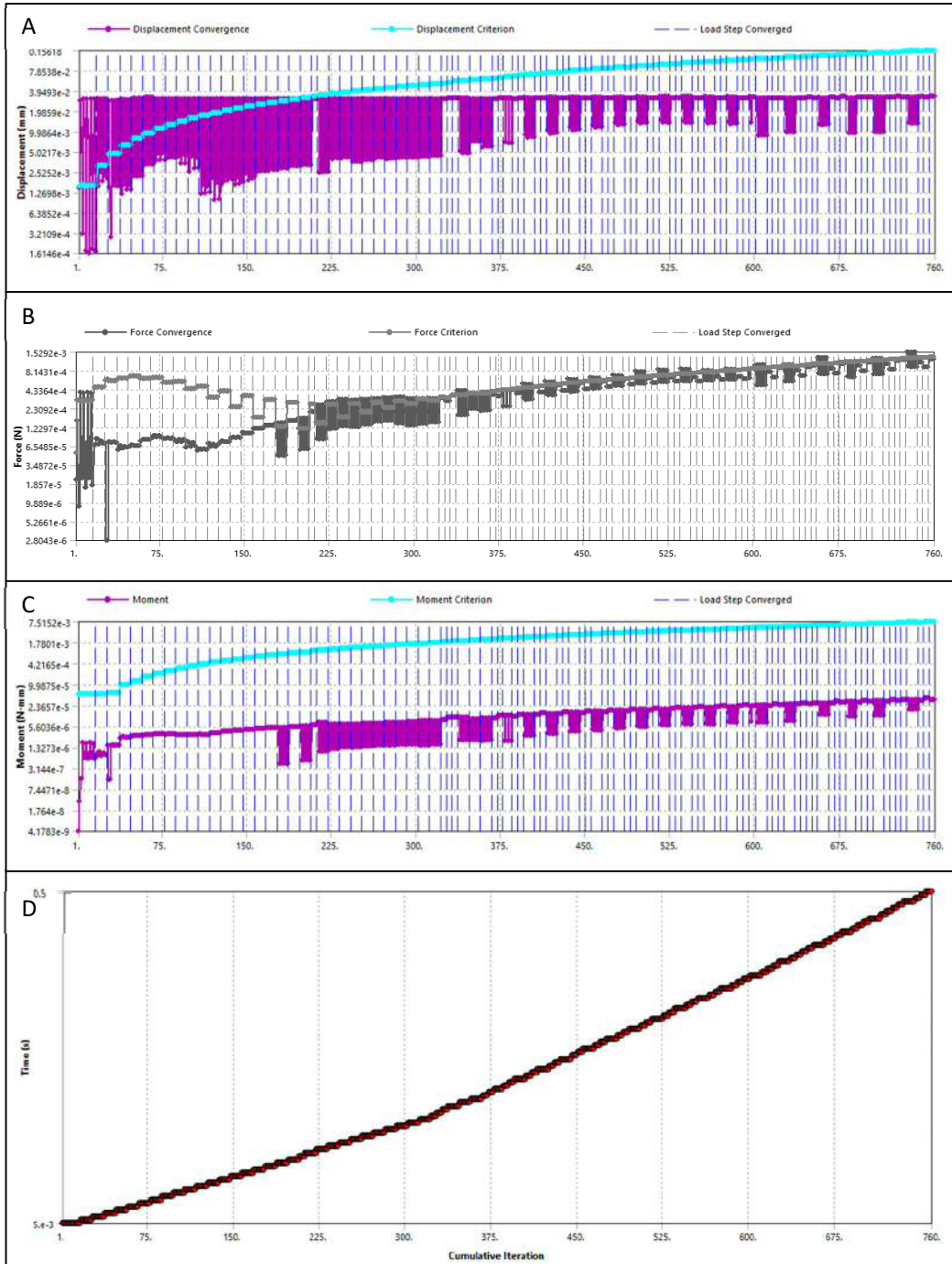


Figure A-4 Solution information for the FE analysis of the FSI simulation (1<sup>st</sup> stage): A) Displacement convergence, B) Force convergence, C) Momentum convergence, D) Cumulative iteration time where all the above results projected on

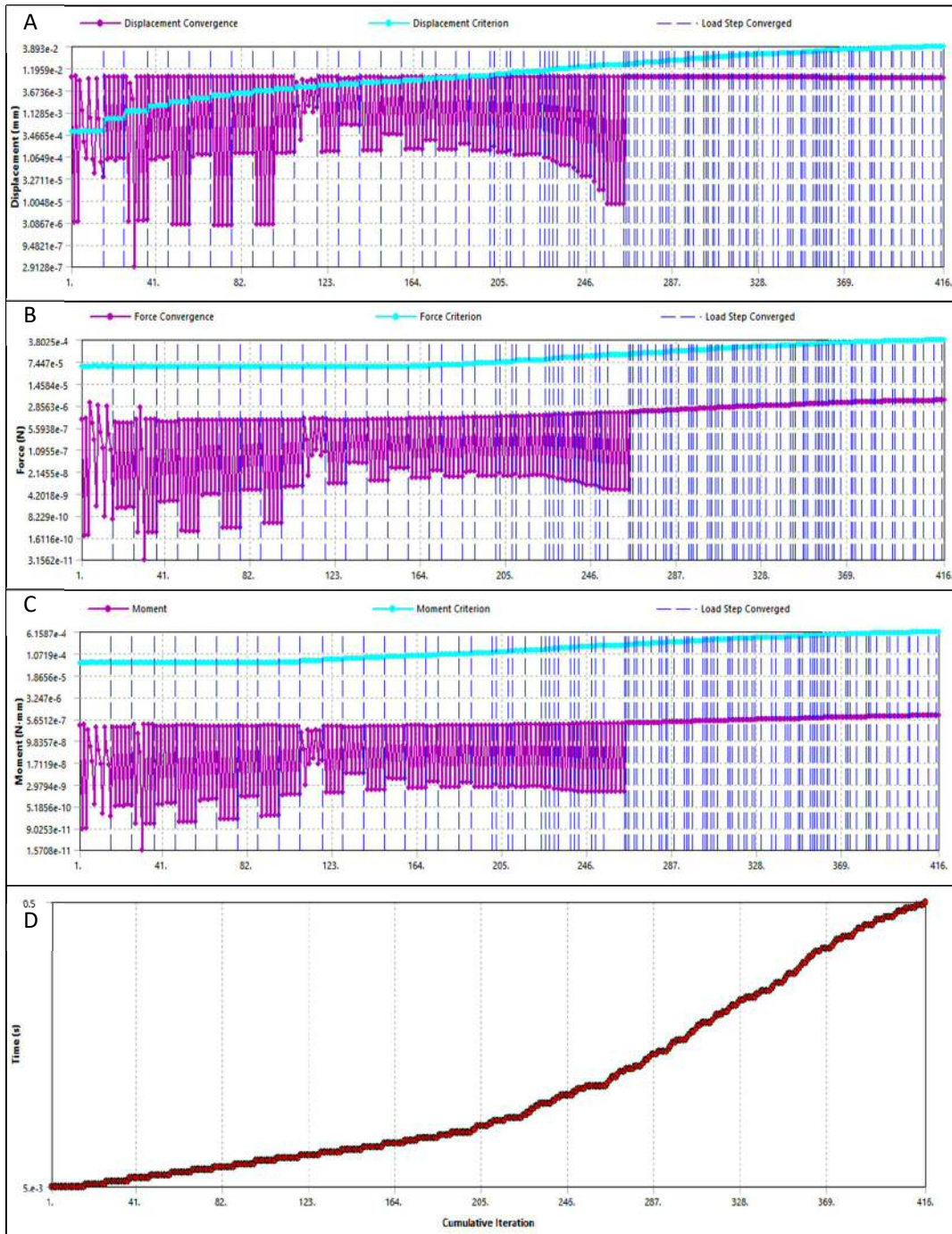


Figure A-5 Solution information for the FE analysis of the FSI simulation (2<sup>nd</sup> stage): A) Displacement convergence, B) Force convergence, C) Momentum convergence, D) Cumulative iteration time where all the above results projected on

The FSI simulation monitoring of the subject-specific model, good and fast convergence after the point of compression, especially after the 220 coupling iteration, and the convergence remain steady throughout the rest of the simulation. By projecting that on the FE and CFD monitoring, it can be seen that this happened also in the same period of time. The coupling monitoring charts for compression and release are found in Figure A-6 and Figure A-7.

In the release phase of the FSI modelling, the convergence is happening at more points than in the compression phase, and this is due to the reduced amount of forced dynamic elements mesh. However, the convergences are shorter in amplitude, which gives an indication of the slower convergence between two data transfers. This could have had a significant impact if the CFD monitoring graphs had a convergence issue, but as can be seen in Figure A-9, the area weighted average for the pressure and velocity gives high convergence values with low CPU usage of even less than the quantity used in the preliminary model.

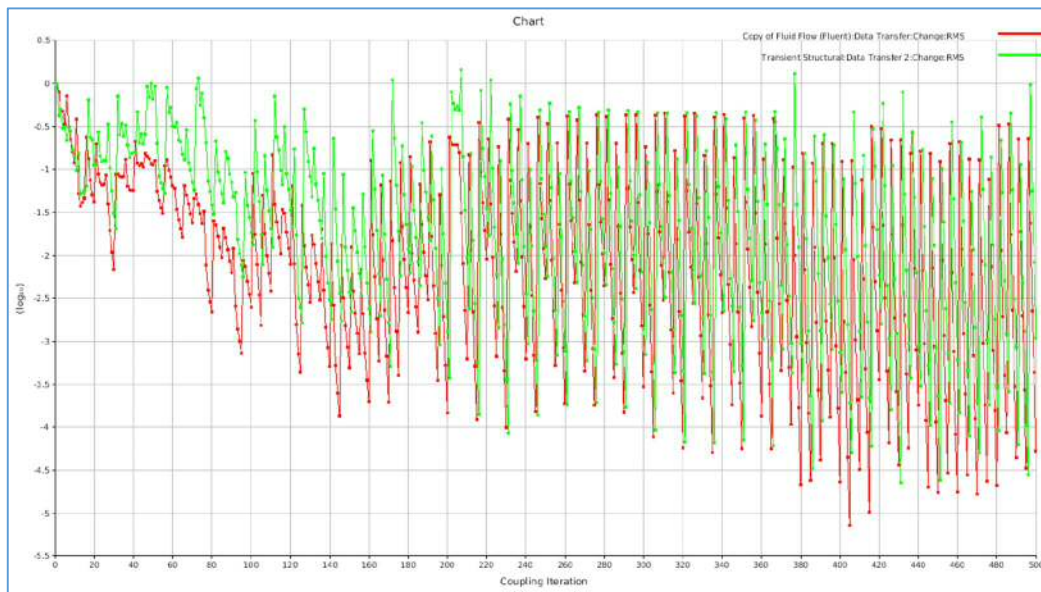


Figure A-6 LV System coupling monitor chart for the transient structural and Fluent flow during the simulation

For the CFD part, convergence was monitored using residual stresses along the model during the simulation along with different surface monitoring. Successful convergence throughout the simulation was observed using the surface monitoring. The residual is one of the most fundamental measures of an iterative solution's convergence, as it directly quantifies the error in the solution of the system of equations. In a CFD analysis, the residual measures the local imbalance of a conserved variable in each control volume. Therefore, every cell in the model has its own residual value for each of the equations being solved (Figure A-8 and Figure A-9).



In an iterative numerical solution, the residual will never be exactly zero. However, the lower the residual value is, the more numerically accurate is the solution. Each CFD code has its own procedure for normalizing the solution residuals.

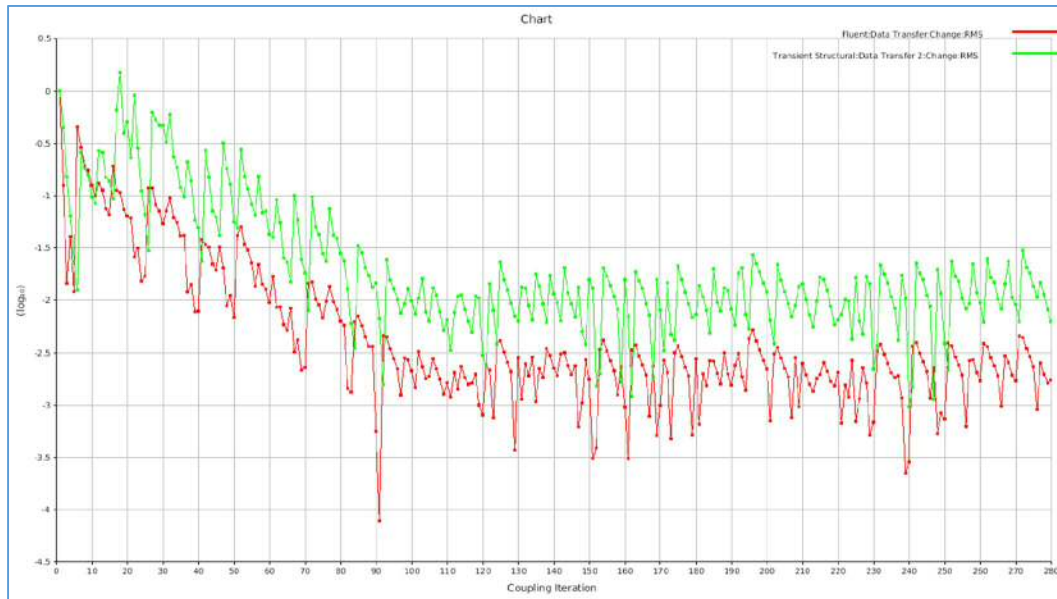


Figure A-7 LV System coupling monitor chart for the transient structural and Fluent flow during the simulation (2<sup>nd</sup> stage)

The value of the stabilisation factor was chosen according to an optimisation method based on the changes to the surface monitoring graphs. As can be seen, there are differences between the surface monitoring of the subject-specific and the preliminary model. This is caused by the high stabilisation factor used in this model. As the geometry is complicated, the model becomes more unstable, and as the shell geometry was imported from 3-Matics, the .iges file type introduced multiple surface elements. This led to the need to design the topological separation of the whole surface and to reduce the area of contact between the LV surface and the contacting plates. This topological connections add complexity to the geometry. All those reasons required high value for the stabilisation factor and were a priority in the simulation setting. Although with lower values of the factor, there was a convergence monitored in Fluent, it was not enough to stabilise the model. This was observed as the simulation was interrupted with error regarding the negative volume mesh in the fluid side of the FSI. This issue was removed when the stabilisation factor choice reached 800. As there is no exact number required or recommended for the choice, relying on the trial and error method is the only option recommended by the software manufacturers.

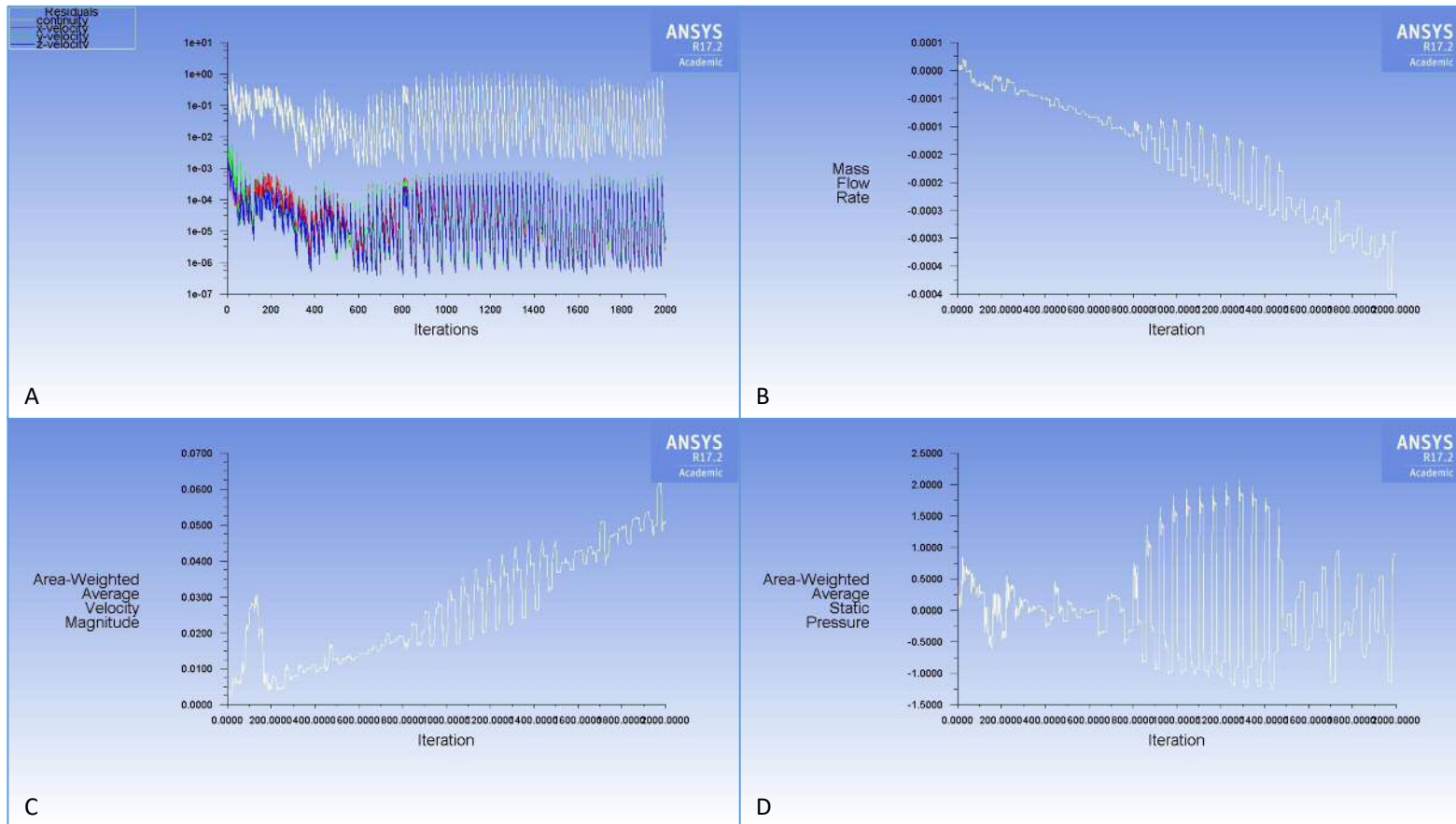


Figure A-8 LV FLUENT simulation monitoring: A) Scaled residuals, B) Mass flow rate on the outlet, C) Area weighted average of the velocity magnitude on the outlet, D) Area weighted average of the pressure on the deforming wall.

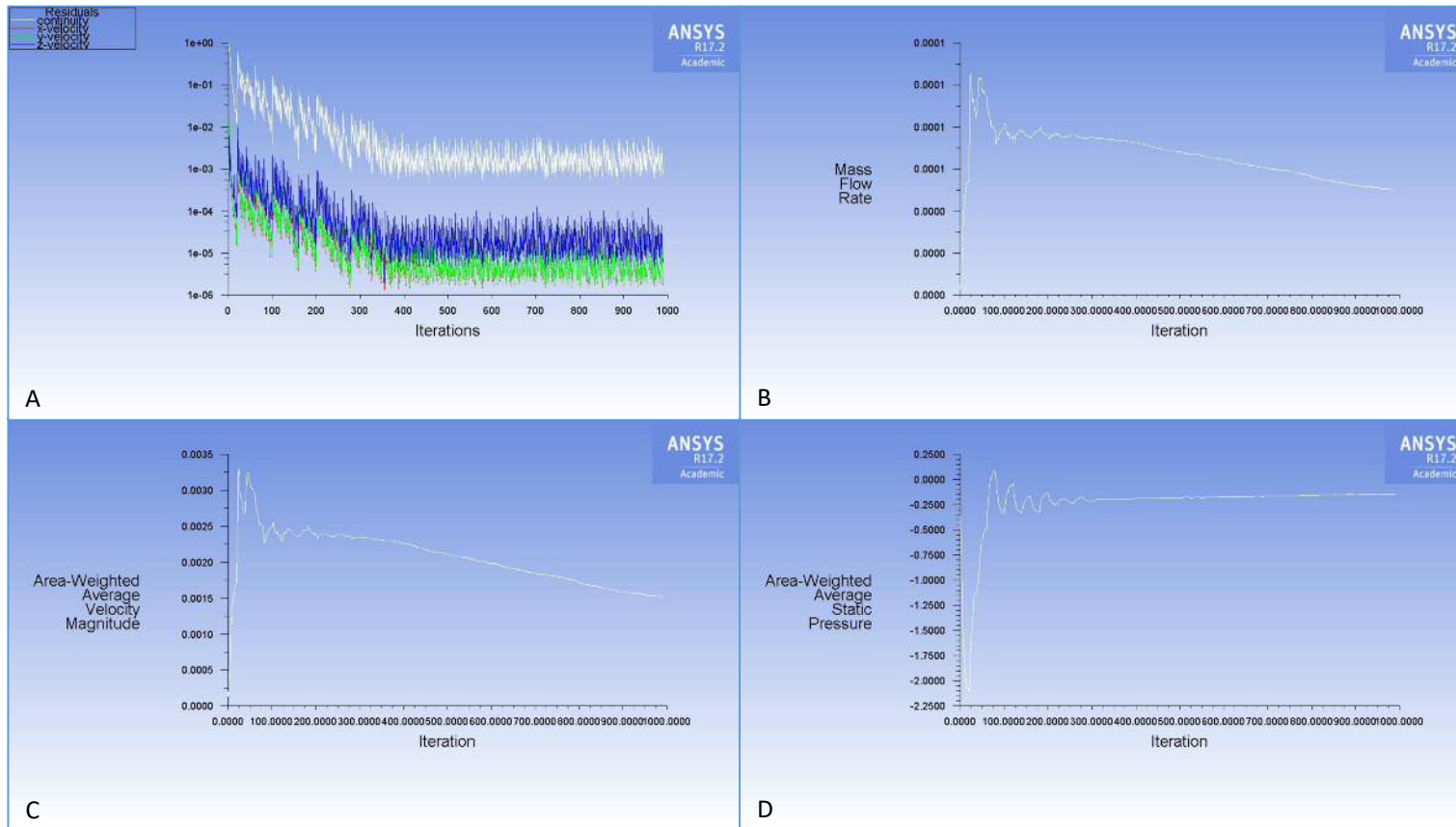


Figure A-9 LV FLUENT simulation monitoring (2<sup>nd</sup> stage): A) Scaled residuals, B) Mass flow rate on the outlet, C) Area weighted average of the velocity magnitude on the outlet, D) Area weighted average of the pressure on the deforming wall.

## Appendix B. Arduino UNO Technical Specifications

### Power

The Arduino Uno can be powered via the USB connection or with an external power supply. The power source is selected automatically.

External (non-USB) power can come either from an AC-to-DC adapter (wall-wart) or battery. The adapter can be connected by plugging a 2.1mm center-positive plug into the board's power jack. Leads from a battery can be inserted in the Gnd and Vin pin headers of the POWER connector.

The board can operate on an external supply of 6 to 20 volts. If supplied with less than 7V, however, the 5V pin may supply less than five volts and the board may be unstable. If using more than 12V, the voltage regulator may overheat and damage the board. The recommended range is 7 to 12 volts.

The power pins are as follows:

- VIN. The input voltage to the Arduino board when it's using an external power source (as opposed to 5 volts from the USB connection or other regulated power source). You can supply voltage through this pin, or, if supplying voltage via the power jack, access it through this pin.
- 5V. the regulated power supply used to power the microcontroller and other components on the board. This can come either from VIN via an on-board regulator, or be supplied by USB or another regulated 5V supply.
- 3V3. A 3.3 volt supply generated by the on-board regulator. Maximum current draw is 50 mA.
- GND. Ground pins.

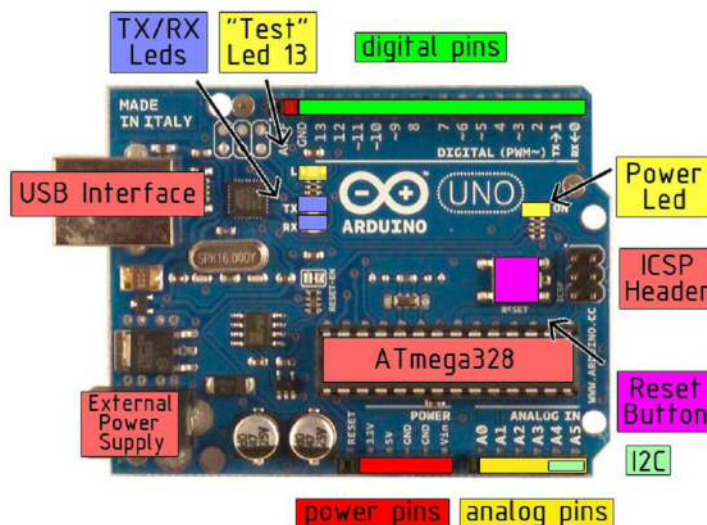


Figure B1 Arduino UNO board specifications (RS)

## Memory

The Atmega328 has 32 KB of flash memory for storing code (of which 0, 5 KB is used for the boot loader); it has also 2 KB of SRAM and 1 KB of EEPROM (which can be read and written with the EEPROM library).

*Table B1 Arduino Uno summary specifications*

<b>Microcontroller</b>	Microcontroller
<b>Operating Voltage</b>	Operating Voltage
<b>ATmega328</b>	ATmega328
<b>5V</b>	5V
<b>Input Voltage (recommended) 7-12V</b>	Input Voltage (recommended) 7-12V
<b>Input Voltage (limits)</b>	Input Voltage (limits)
<b>Digital I/O Pins</b>	Digital I/O Pins
<b>6-20V</b>	6-20V
<b>Analog Input Pins</b>	Analog Input Pins
<b>DC Current per I/O Pin</b>	DC Current per I/O Pin
<b>DC Current for 3.3V Pin</b>	DC Current for 3.3V Pin
<b>Flash Memory</b>	Flash Memory

## Input and Output

Each of the 14 digital pins on the Uno can be used as an input or output, using `pinMode()`, `digitalWrite()`, and `digitalRead()` functions. They operate at 5 volts. Each pin can provide or receive a maximum of 40 mA and has an internal pull-up resistor (disconnected by default) of 20-50 kOhms. In addition, some pins have specialized functions:

- **Serial:** 0 (RX) and 1 (TX). Used to receive (RX) and transmit (TX) TTL serial data. These pins are connected to the corresponding pins of the ATmega8U2 USB-to-TTL Serial chip.
- **External Interrupts:** 2 and 3. These pins can be configured to trigger an interrupt on a low value, a rising or falling edge, or a change in value. See the `attachInterrupt()` function for details.
- **PWM:** 3, 5, 6, 9, 10, and 11. Provide 8-bit PWM output with the `analogWrite()` function.
- **SPI:** 10 (SS), 11 (MOSI), 12 (MISO), 13 (SCK). These pins support SPI communication, which, although provided by the underlying hardware, is not currently included in the Arduino language.
- **LED:** 13. There is a built-in LED connected to digital pin 13. When the pin is HIGH value, the LED is on, when the pin is LOW, it's off.

The Uno has 6 analog inputs, each of which provide 10 bits of resolution (i.e. 1024 different values). By default they measure from ground to 5 volts, though is it possible to change the upper end of their range using the AREF pin and the `analogReference()` function. Additionally, some pins have specialized functionality:

- I<sup>2</sup>C: 4 (SDA) and 5 (SCL). Support I<sup>2</sup>C (TWI) communication using the Wire library.

There are a couple of other pins on the board:

- AREF. Reference voltage for the analog inputs. Used with `analogReference()`.
- Reset. Bring this line LOW to reset the microcontroller. Typically used to add a reset button to shields which block the one on the board.

## Communication

The Arduino Uno has a number of facilities for communicating with a computer, another Arduino, or other microcontrollers. The ATmega328 provides UART TTL (5V) serial communication, which is available on digital pins 0 (RX) and 1 (TX). An ATmega8U2 on the board channels this serial communication over USB and appears as a virtual com port to software on the computer. The '8U2 firmware uses the standard USB COM drivers, and no external driver is needed. However, on Windows, an \*.inf file is required.

The Arduino software includes a serial monitor which allows simple textual data to be sent to and from the Arduino board. The RX and TX LEDs on the board will flash when data is being transmitted via the USB-to-serial chip and USB connection to the computer (but not for serial communication on pins 0 and 1).

A SoftwareSerial library allows for serial communication on any of the Uno's digital pins.

The ATmega328 also support I<sup>2</sup>C (TWI) and SPI communication. The Arduino software includes a Wire library to simplify use of the I<sup>2</sup>C bus.

## Programming

The Arduino Uno can be programmed with the Arduino software (download). Select "Arduino Uno w/ATmega328" from the Tools > Board menu (according to the microcontroller on your board). For details.

The ATmega328 on the Arduino Uno comes preburned with a bootloader that allows you to upload new code to it without the use of an external hardware programmer. It communicates using the original STK500 protocol (reference, C header files).

You can also bypass the bootloader and program the microcontroller through the ICSP (In-Circuit Serial Programming) header.

The ATmega8U2 firmware source code is available . The ATmega8U2 is loaded with a DFU bootloader, which can be activated by connecting the solder jumper on the back of the board (near the map of Italy) and then resetting the 8U2. You can then use Atmel's FLIP software (Windows) or the DFU programmer (Mac OS X and Linux) to load a new firmware. Or you can use the ISP header with an external programmer (overwriting the DFU bootloader).

## Automatic (Software) reset

Rather than requiring a physical press of the reset button before an upload, the Arduino Uno is designed in a way that allows it to be reset by software running on a connected computer. One of the hardware flow control lines (DTR) of the ATmega8U2 is connected to the reset line of the ATmega328 via a 100 nanofarad capacitor. When this line is asserted (taken low), the reset line drops long enough to reset the chip. The Arduino software uses this capability to allow you to upload code by simply pressing the upload button in the Arduino environment. This means that the bootloader can have a shorter timeout, as the lowering of DTR can be well-coordinated with the start of the upload.

This setup has other implications. When the Uno is connected to either a computer running Mac OS X or Linux, it resets each time a connection is made to it from software (via USB). For the following half-second or so, the bootloader is running on the Uno. While it is programmed to ignore malformed data (i.e. anything besides an upload of new code), it will intercept the first few bytes of data sent to the board after a connection is opened. If a sketch running on the board receives one-time configuration or other data when it first starts, make sure that the software with which it communicates waits a second after opening the connection and before sending this data.

The Uno contains a trace that can be cut to disable the auto-reset. The pads on either side of the trace can be soldered together to re-enable it. It's labeled "RESET-EN". You may also be able to disable the auto-reset by connecting a 110 ohm resistor from 5V to the reset line.

## USB Overcurrent Protection

The Arduino Uno has a resettable polyfuse that protects your computer's USB ports from shorts and overcurrent. Although most computers provide their own internal protection, the fuse provides an extra layer of protection. If more than 500 mA is applied to the USB port, the fuse will automatically break the connection until the short or overload is removed.

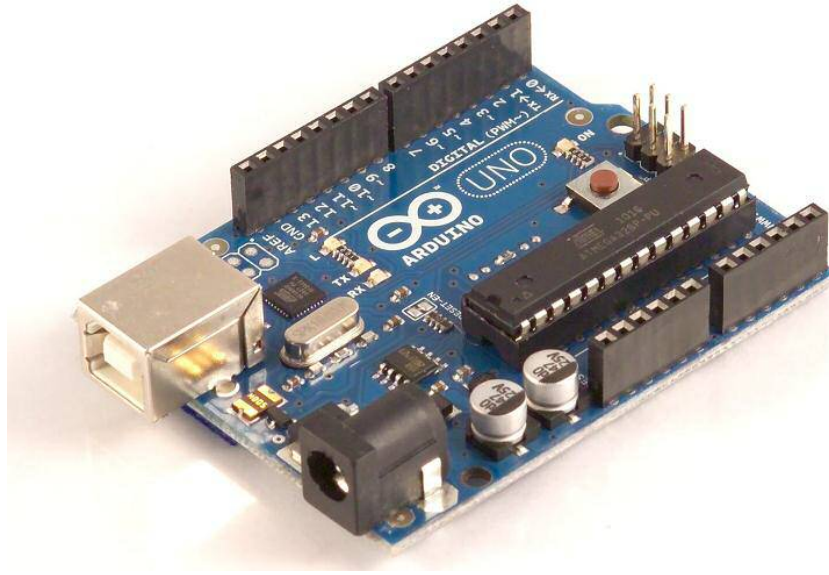


*Figure B2 Arduino Uno Physical characteristics view (RS)*

## Physical Characteristics

The maximum length and width of the Uno PCB are 2.7 and 2.1 inches respectively, with the USB connector and power jack extending beyond the former dimension. Three screw holes allow the board to be attached to a surface or case. Note that the distance between digital pins 7 and 8 is 160 mil (0.16"), not an even multiple of the 100 mil spacing of the other pins.



## Appendix C.

### Arduino Sensor Code

```

/*
Gems FT-110 Liquid flow rate sensor

*/

byte statusLed = 13;

byte sensorInterrupt = 0; // 0 = digital pin 2
byte sensorPin = 2;

// The hall-effect flow sensor outputs approximately 24 pulses per second per
// litre/minute of flow.
float calibrationFactor = 24;

volatile byte pulseCount;

float flowRate;
float velocityinlet;
float velocityoutlet;
unsigned int flowMilliLitres;
unsigned long totalMilliLitres;

unsigned long oldTime;

void setup()
{

  // To initialize a serial connection for reporting values to the host
  Serial.begin(38400);

  pulseCount = 0;
  flowRate = 0.0;
  velocityoutlet = 0.0;
  velocityinlet = 0.0;
  flowMilliLitres = 0;
  totalMilliLitres = 0;
  oldTime = 0;

  // The Hall-effect sensor is connected to pin 2 which uses interrupt 0.
  // Configured to trigger on a FALLING state change (transition from HIGH
  // state to LOW state)
  attachInterrupt(sensorInterrupt, pulseCounter, FALLING);
  Serial.println("CLEARDATA"); //clears up any data left from previous projects
  Serial.println("LABEL,Time,Timer,Flow Rate (L/min),Current liquid Flowing (ml/Sec),Output
Liquid Quantity (ml),Velocity outlet (m/sec),Velocity Inlet (m/Sec)");
  //LABEL is used so excel knows the next things will be the names of the columns
  //(instead of Acolumn you could write Time for instance)

```

```

Serial.println("RESETTIMER"); //resets timer to 0
}

/**
 * Main program loop
 */
void loop()
{
  if((millis() - oldTime) > 100) // Only process counters once per 0.1 second
  {
    // Disable the interrupt while calculating flow rate and sending the value to
    // the host
    detachInterrupt(sensorInterrupt);

    // Because this loop may not complete in exactly 0.1 second intervals we calculate
    // the number of milliseconds that have passed since the last execution and use
    // that to scale the output. We also apply the calibrationFactor to scale the output
    // based on the number of pulses per second per units of measure (litres/minute in
    // this case) coming from the sensor.
    flowRate = ((1000.0 / (millis() - oldTime)) * pulseCount) / calibrationFactor;

    // To get the velocity from flow rate divide by outlet then inlet area depending
    // on the radius (4.33, 8.62) mm
    // v(m/sec)=Q(l/min)/(pi((r in m)^2)*1.6667e-5)
    // 1.6667e-5 is the conversion of Q(l/min) to Q (m3/sec)
    velocityoutlet = flowRate * 0.283;
    velocityinlet = flowRate * 0.0714;

    // The time this processing pass was executed. Because we've disabled interrupts
    // the millis() function won't actually be incrementing right at this point,
    // but it will still return the value it was set to just before interrupts went away.
    oldTime = millis();

    // Divide the flow rate in litres/minute by 60 to determine how many litres have
    // passed through the sensor in this 0.1 second interval, then multiply by 1000 to
    // convert to millilitres.
    flowMilliLitres = (flowRate / 60) * 1000;

    // Add the millilitres passed in this second to the cumulative total
    totalMilliLitres += flowMilliLitres;

    unsigned int frac;
    unsigned int fracvo;
    unsigned int fracvi;

    // Print the flow rate for this 0.1 second in litres / minute
    Serial.print("Flow rate: ");
    Serial.print(int(flowRate)); // Print the integer part of the variable
    Serial.print("."); // Print the decimal point
    // Determine the fractional part. The 1000 multiplier gives us 3 decimal place.
    frac = (flowRate - int(flowRate)) * 1000;
  }
}

```

```

Serial.print(frac, DEC); // Print the fractional part of the variable
Serial.print("L/min");

// Print the number of litres flowed in this 0.1 second
Serial.print(" Current Liquid Flowing: "); // Output separator
Serial.print(flowMilliLitres);
Serial.print("mL/Sec");

// Print the cumulative total of litres flowed since starting
Serial.print(" Output Liquid Quantity: "); // Output separator
Serial.print(totalMilliLitres);
Serial.println("mL");

// Print the velocity in the outlet for this 0.1 second in m/s
Serial.print("Velocity outlet: ");
Serial.print(int(velocityoutlet)); // Print the integer part of the variable
Serial.print("."); // Print the decimal point
// Determine the fractional part. The 1000 multiplier gives us 3 decimal place.
fracvo = (velocityoutlet - int(velocityoutlet)) * 1000;
Serial.print(fracvo, DEC); // Print the fractional part of the variable
Serial.print("m/s");

// Print the velocity in the inlet for this 0.1 second in m/s
Serial.print("Velocity inlet: ");
Serial.print(int(velocityinlet)); // Print the integer part of the variable
Serial.print("."); // Print the decimal point
// Determine the fractional part. The 10 multiplier gives us 3 decimal place.
fracvi = (velocityinlet - int(velocityinlet)) * 1000;
Serial.print(fracvi, DEC); // Print the fractional part of the variable
Serial.print("m/s");

Serial.print("DATA,TIME,TIMER,");

Serial.print(int(flowRate)); // Print the integer part of the variable
Serial.print("."); // Print the decimal point
// Determine the fractional part. The 1000 multiplier gives us 3 decimal place.
frac = (flowRate - int(flowRate)) * 1000;
Serial.print(frac, DEC); // Print the fractional part of the variable

Serial.print(int(velocityoutlet)); // Print the integer part of the variable
Serial.print("."); // Print the decimal point
// Determine the fractional part. The 10 multiplier gives us 3 decimal place.
fracvo = (velocityoutlet - int(velocityoutlet)) * 1000;
Serial.print(fracvo, DEC); // Print the fractional part of the variable

Serial.print(int(velocityinlet)); // Print the integer part of the variable
Serial.print("."); // Print the decimal point
// Determine the fractional part. The 10 multiplier gives us 3 decimal place.
fracvi = (velocityinlet - int(velocityinlet)) * 1000;
Serial.print(fracvi, DEC); // Print the fractional part of the variable

Serial.print(",");

```

```
Serial.print(flowMilliLitres);
Serial.print(", ");
Serial.print(totalMilliLitres);
Serial.print(", ");

Serial.println(); //println is added to the last command so it knows to go
//into the next row on the second run
delay(100); //add a delay

// Reset the pulse counter so we can start incrementing again
pulseCount = 0;

// Enable the interrupt again now that we've finished sending output
attachInterrupt(sensorInterrupt, pulseCounter, FALLING);
}
}

/*
Interrupt Service Routine
*/
void pulseCounter()
{
  // Increment the pulse counter
  pulseCount++;
}
```

## Appendix D.

### Nickel-Plated Brass Non-Return Valves Datasheet

These nickel-plated brass adjustable non-return valves, suitable for harsh environments, allow compressed air to flow in one direction and prevent flow in the other. This product incorporates precise adjustment of opening pressure for greater flexibility.

Table D1 Technical Characteristics of the one-way valves

<b>Compatible Fluid</b>	Compressed air					
<b>Working Pressure</b>	0 to 12 bar					
<b>Working Temperature</b>	-20°C to +80° C					
<b>Cracking Pressure</b>	Threads			0 to 4 Turns (value given as an example only)		
	M5x0.8 – G1/8 – G1/4			1 to 0.10 bar		
	G3/8			1 to 0.15 bar		
	G1/2			1 to 0.20 bar		
<b>Max. Tightening Torques</b>	Threads	M5x0.8	G1/8	G1/4	G3/8	G1/2
	daN.m	0.16	0.8	1.2	3	3.5

Adjustment and locking of the non-return valve cracking pressure with two different Allen keys prevents the settings from being accidentally changed.

### Regulations

- DI: 2002/95/EC (RoHS)
- RG: External Components: 21CFR (FDA) (seal: § 177.2600, nickel: §184.1537, grease: NSF H1)
- RG: 1935/2004 (external surface flow  $\geq 0.02$  litre per hour)
- DI: 2006/42/EC (external surface Ra < 0.8  $\mu\text{m}$ )
- RG: 1907/2006 (REACH)

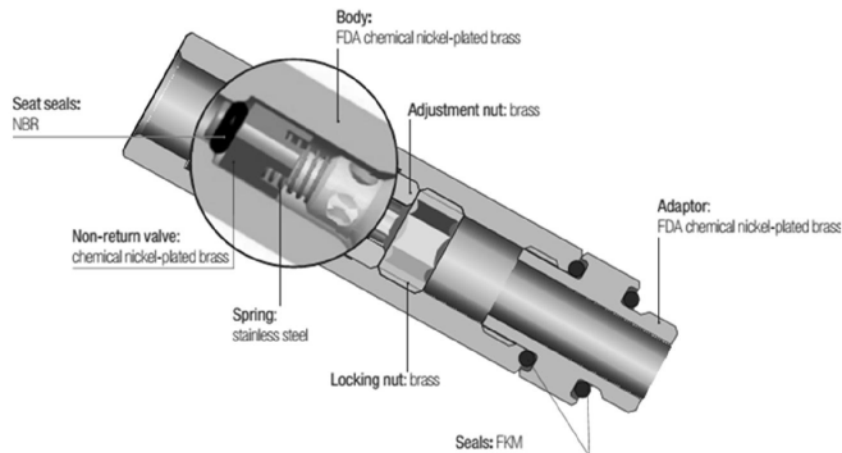


Figure D1 Component Materials for the silicone-free one-way valve

## Appendix E.

### Turbine Flow Rate Sensor Data sheet

Gems FT-110 hall-effect turbine flow rate sensor is ideal for OEM applications involving low flow liquid monitoring. The low cost coupled with 1/2% repeatability makes it an ideal candidate for replacing dispensing timer systems. Unlike existing timing systems, turbine technology is not influenced by changes in system pressure caused by aging filters. The sensor's standard power and output specifications make it easy to retrofit to existing controllers.

### Installation

### Specifications and Dimensions

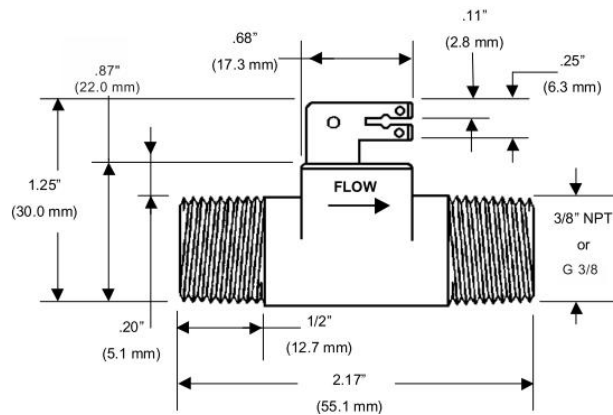


Figure E1 Flow sensor dimensions (Space Terminal Connection Shown) (GemsSensorsInc.)

**3/8" NPT Units:** Apply a sparse amount of thread sealant (Permatex "No More Leaks"®) or Teflon® tape to male threads. Insure that sealant does not enter into the turbine and bearing internal area. Hand-tighten unit in place. Turn an additional 1/4 turn to provide seal. If seal leaks, turn an additional 1/4 turn until leak stops. Do not exceed one additional turn total.

**G 3/8 Units:** G 3/8 units mate with a flat face seal washer (90 shore EPDM, 0, 5 mm ID, 14, 5 mm OD, 2, 0 mm thick) similar to a garden hose arrangement. This arrangement requires no sealants; hand-tightening should be sufficient for sealing.

Table E1 Flow sensors Specifications

Wetted Parts	<b>Body:</b> Nylon 12/ <b>Turbine:</b> Nylon 12 Composite/ <b>Bearings:</b> PTFE/15% Graphite
Operating Pressure	200 psi
Burst Pressure	2500 psi
Operating Temperature	-4° to 212°F (-20° to 100°C)
Viscosity	32 to 81 SSU (.8 - 16 Centistokes)
Filter	< 50 Microns
Input Power	5-24 VDC @ 8 mA
Output	NPN Sinking Open Collector @ 50 mA, Max.
Accuracy	± 3% of Rdg. Normal Range
Repeatability	0.5% FS Normal Range
Electrical Connection	Spade Terminals .110/.248 X .031" (2.8/6.3 X .8 mm) or 1 Meter Cable

### Electrical/Output Signal

The output signal is a square wave signal, whose frequency varies linearly with flow rate. An external pull-up resistor (user-supplied) is required to insure that the open collector will sink less than 50 mA.

Gems' cable and connector can be ordered as follows:

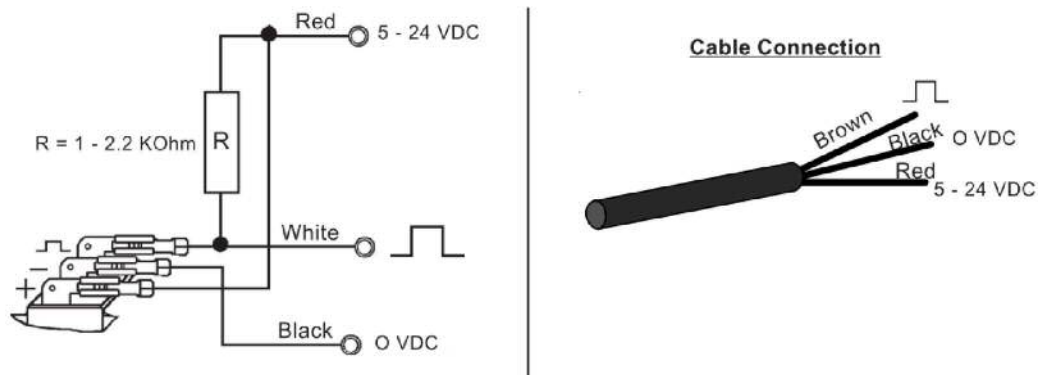


Figure E2 Wiring diagrams Part#173941: 3Ft. Cable assembly (on the left). Part#173942: 10 Ft. Cable assembly (on the right). (GemsSensorsInc.)

# Appendix F. PolyJet Materials Data Sheet



## PolyJet Materials Data Sheet

### MATERIALS SIMULATING ENGINEERING PLASTICS

DIGITAL ABS, GREEN (RGD5160-DM, RGD5161-DM) MADE OF RGD515 & RGD535 [DIGITAL ABS, IVORY (RGD5130-DM, RGD5131-DM) MADE OF RGD515 & RGD531					
	ASTM	UNITS	METRIC	UNITS	IMPERIAL
Tensile strength	D-638-03	MPa	55-60	psi	8000-8700
Elongation at break	D-638-05	%	25-40	%	25-40
Modulus of elasticity	D-638-04	MPa	2600-3000	psi	375,000-435,000
Flexural Strength	D-790-03	MPa	65-75	psi	9,500-11,000
Flexural Modulus	D-790-04	MPa	1700-2200	psi	245,000-320,000
HDT, °C @ 0.45MPa	D-648-06	°C	58-68	°F	136-154
HDT, °C @ 0.45MPa after thermal post treatment procedure A	D-648-06	°C	82-90	°F	180-194
HDT, °C @ 0.45MPa after thermal post treatment procedure B	D-648-06	°C	92-95	°F	198-203
HDT, °C @ 1.82MPa	D-648-07	°C	51-55	°F	124-131
Izod Notched Impact	D-256-06	J/m	65-80	ft lb/inch	1.22-1.50
Tg	DMA, E=	°C	47-53	°F	117-127
Shore Hardness (D)	Scale D	Scale D	85-87	Scale D	85-87
Rockwell Hardness	Scale M	Scale M	67-69	Scale M	67-69
Polymerized density	ASTM D792	g/cm3	1.17-1.18		

HIGH TEMPERATURE MATERIAL (RGD525)					
	ASTM	UNITS	METRIC	UNITS	IMPERIAL
Tensile strength	D-638-03	MPa	70-80	psi	10,000-11,500
Elongation at break	D-638-05	%	10-15	%	10-15
Modulus of elasticity	D-638-04	MPa	3200-3500	psi	465,000-510,000
Flexural Strength	D-790-03	MPa	110-130	psi	16,000-19,000
Flexural Modulus	D-790-04	MPa	3100-3500	psi	450,000-510,000
HDT, °C @ 0.45MPa	D-648-06	°C	63-67	°F	145-163
HDT, °C @ 0.45MPa after thermal post treatment procedure A	D-648-06	°C	75-80	°F	167-176
HDT, °C @ 1.82MPa	D-648-07	°C	55-57	°F	131-135
Izod Notched Impact	D-256-06	J/m	14-16	ft lb/inch	0.262-0.300
Water Absorption, %	D-570-98 24hr	%	1.2-1.4	%	1.2-1.4
Tg	DMA, E=	°C	62-65	°F	144-149
Shore Hardness D	Scale D	Scale D	87-88	Scale D	87-88
Rockwell Hardness	Scale M	Scale M	78-83	Scale M	78-83
Polymerized density	ASTM D792	g/cm3	1.17-1.18		
Ash content	USP281	%	0.38-0.42	%	0.38-0.42

### MATERIALS SIMULATING STANDARD PLASTICS

TRANSPARENT MATERIALS RGD720					
	ASTM	UNITS	METRIC	UNITS	IMPERIAL
Tensile strength	D-638-03	MPa	50-65	psi	7250-9450
Elongation at break	D-638-05	%	15-25	%	15-25
Modulus of elasticity	D-638-04	MPa	2000-3000	psi	290,000-435,000
Flexural Strength	D-790-03	MPa	80-110	psi	12000-16000
Flexural Modulus	D-790-04	MPa	2700-3300	psi	390,000-480,000
HDT, °C @ 0.45MPa	D-648-06	°C	45-50	°F	113-122
HDT, °C @ 1.82MPa	D-648-07	°C	45-50	°F	113-122
Izod Notched Impact	D-256-06	J/m	20-30	ft lb/inch	0.375-0.562
Water Absorption	D-570-98 24hr	%	1.5-2.2	%	1.5-2.2
Tg	DMA, E=	°C	48-50	°F	118-122
Shore Hardness (D)	Scale D	Scale D	83-86	Scale D	83-86
Rockwell Hardness	Scale M	Scale M	73-76	Scale M	73-76
Polymerized density	ASTM D792	g/cm3	1.18-1.19		
Ash content	USP281	%	0.01-0.02	%	0.01-0.02

Find material properties for color materials on the Color Digital Materials Data Sheet.

TRANSPARENT MATERIALS VEROCLEAR RGD810					
	ASTM	UNITS	METRIC	UNITS	IMPERIAL
Tensile strength	D-638-03	MPa	50-65	psi	7250-9450
Elongation at break	D-638-05	%	10-25	%	10-25
Modulus of elasticity	D-638-04	MPa	2000-3000	psi	290,000-435,000
Flexural Strength	D-790-03	MPa	75-110	psi	11000-16000
Flexural Modulus	D-790-04	MPa	2200-3200	psi	320,000-465,000
HDT, °C @ 0.45MPa	D-648-06	°C	45-50	°F	113-122
HDT, °C @ 1.82MPa	D-648-07	°C	45-50	°F	113-122
Izod Notched Impact	D-256-06	J/m	20-30	ft lb/inch	0.375-0.562
Water Absorption	D-570-98 24hr	%	1.1-1.5	%	1.1-1.5
Tg	DMA, E=	°C	52-54	°F	126-129
Shore Hardness (D)	Scale D	Scale D	83-86	Scale D	83-86
Rockwell Hardness	Scale M	Scale M	73-76	Scale M	73-76
Polymerized density	ASTM D792	g/cm3	1.18-1.19		
Ash content	USP281	%	0.02-0.06	%	0.02-0.06



RIGID OPAQUE MATERIALS					
VEROGRAY RGD850, VEROBLOCKPLUS RGD875, VEROWHITEPLUS RGD835, VEROYELLOW RGD836, VEROCYAN RGD841, VEROMAGENTA RGD851					
	ASTM	UNITS	METRIC	UNITS	IMPERIAL
Tensile strength	D-638-03	MPa	50-65	psi	7250-9450
Elongation at break	D-638-05	%	10-25	%	10-25
Modulus of elasticity	D-638-04	MPa	2000-3000	psi	290,000-435,000
Flexural Strength	D-790-03	MPa	75-110	psi	11000-16000
Flexural Modulus	D-790-04	MPa	2200-3200	psi	320,000-465,000
HDT, °C @ 0.45MPa	D-648-06	°C	45-50	°F	113-122
HDT, °C @ 1.82MPa	D-648-07	°C	45-50	°F	113-122
Izod Notched Impact	D-256-06	J/m	20-30	ft lb/inch	0.375-0.562
Water Absorption	D-570-98 24hr	%	1.1-1.5	%	1.1-1.5
Tg	DMA, E-	°C	52-54	°F	126-129
Shore Hardness (D)	Scale D	Scale D	83-86	Scale D	83-86
Rockwell Hardness	Scale M	Scale M	73-76	Scale M	73-76
Polymerized density	ASTM D792	g/cm3	1.17-1.18	Scale M	73-76
Ash content VeroGray, VeroWhitePlus	USP281	%	0.23-0.26	%	0.23-0.26
Ash content VeroBlockPlus	USP281	%	0.01-0.02	%	0.01-0.02

SIMULATED POLYPROPYLENE MATERIALS					
DURUS WHITE RGD430					
	ASTM	UNITS	METRIC	UNITS	IMPERIAL
Tensile strength	D-638-03	MPa	20-30	psi	2900-4350
Elongation at break	D-638-05	%	40-50	%	40-50
Modulus of elasticity	D-638-04	MPa	1000-1200	psi	145,000-175,000
Flexural Strength	D-790-03	MPa	30-40	psi	4350-5800
Flexural Modulus	D-790-04	MPa	1200-1600	psi	175,000-230,000
HDT, °C @ 0.45MPa	D-648-06	°C	37-42	°F	99-108
HDT, °C @ 1.82MPa	D-648-07	°C	32-34	°F	90-93
Izod Notched Impact	D-256-06	J/m	40-50	ft lb/inch	0.749-0.937
Water Absorption	D-570-98 24hr	%	1.5-1.9	%	1.5-1.9
Tg	DMA, E-	°C	35-37	°F	95-99
Shore Hardness (D)	Scale D	Scale D	74-78	Scale D	74-78
Rockwell Hardness	Scale M	Scale M	no data	Scale M	no data
Polymerized density	ASTM D792	g/cm3	1.15-1.17		
Ash content	USP281	%	0.10-0.12	%	0.1-0.12

RIGUR RGD450					
	ASTM	UNITS	METRIC	UNITS	IMPERIAL
Tensile strength	D-638-03	MPa	40-45	psi	5800-6500
Elongation at break	D-638-05	%	20-35	%	20-35
Modulus of elasticity	D-638-04	MPa	1700-2100	psi	246,000 - 305,000
Flexural Strength	D-790-03	MPa	52-59	psi	7500 - 8500
Flexural Modulus	D-790-04	MPa	1500-1700	psi	217,000 - 246,000
HDT, °C @ 0.45MPa	D-648-06	°C	49-54	°F	120-129
HDT, °C @ 1.82MPa	D-648-07	°C	45-50	°F	113-122
Izod Notched Impact	D-256-06	J/m	30-35	ft lb/inch	0.561-0.656
Tg	DMA, E-	°C	48-52	°F	118-126
Shore Hardness (D)	Scale D	Scale D	80-84	Scale D	80-84
Rockwell Hardness	Scale M	Scale M	58-62	Scale M	58-62
Polymerized density	ASTM D792	g/cm3	1.20-1.21		
Ash content	USP281	%	0.3-0.4	%	0.3-0.4

RIGID OPAQUE MATERIALS					
VEROBLUE RGD840					
	ASTM	UNITS	METRIC	UNITS	IMPERIAL
Tensile strength	D-638-03	MPa	50-60	psi	7250-8700
Elongation at break	D-638-05	%	15-25	%	15-25
Modulus of elasticity	D-638-04	MPa	2000-3000	psi	290,000-435,000
Flexural Strength	D-790-03	MPa	60-70	psi	8700-10200
Flexural Modulus	D-790-04	MPa	1900-2500	psi	265,000-365,000
HDT, °C @ 0.45MPa	D-648-06	°C	45-50	°F	113-122
HDT, °C @ 1.82MPa	D-648-07	°C	45-50	°F	113-122
Izod Notched Impact	D-256-06	J/m	20-30	ft lb/inch	0.375-0.562
Water Absorption	D-570-98 24hr	%	1.5-2.2	%	1.5-2.2
Tg	DMA, E-	°C	48-50	°F	118-122
Shore Hardness (D)	Scale D	Scale D	83-86	Scale D	83-86
Rockwell Hardness	Scale M	Scale M	73-76	Scale M	73-76
Polymerized density	ASTM D792	g/cm3	1.18-1.19		
Ash content	USP281	%	0.21-0.22	%	0.21-0.22

RUBBER-LIKE MATERIALS					
TANGOBLOCKPLUS FLX980 AND TANGOPLUS FLX930					
	ASTM	UNITS	METRIC	UNITS	IMPERIAL
Tensile strength	D-412	MPa	0.8-1.5	psi	115-220
Elongation at break	D-412	%	170-220	%	170-220
Compressive set	D-395	%	4-5	%	4-5
Shore Hardness (A)	D-2240	Scale A	26-28	Scale A	26-28
Tensile Tear resistance	D-624	Kg/cm	2-4	Lb/in	18-22
Polymerized density	ASTM D792	g/cm3	1.12-1.13		

TANGOBLOCK FLX973					
	ASTM	UNITS	METRIC	UNITS	IMPERIAL
Tensile strength	D-412	MPa	1.8-2.4	psi	115-350
Elongation at break	D-412	%	45-55	%	45-55
Compressive set	D-395	%	0.5-1.5	%	0.5-1.5
Shore Hardness (A)	D-2240	Scale A	60-62	Scale A	60-62
Tensile Tear resistance	D-624	Kg/cm	3-5	Lb/in	18-24
Polymerized density	ASTM D792	g/cm3	1.14-1.15		

TANGOGRAY FLX950					
	ASTM	UNITS	METRIC	UNITS	IMPERIAL
Tensile strength	D-412	MPa	3-5	psi	435-725
Elongation at break	D-412	%	45-55	%	45-55
Compressive set	D-395	%	0.5-1.5	%	0.5-1.5
Shore Hardness (A)	D-2240	Scale A	73-77	Scale A	73-77
Tensile Tear resistance	D-624	Kg/cm	8-12	Lb/in	50-60
Polymerized density	ASTM D792	g/cm3	1.16-1.17		



The data included in this brochure is for your information purposes only and should not be considered specific advice to any particular customer project. Each customer is responsible for the design, functioning and all other decisions with regards to its particular projects and systems. The sale and provision of the products described in this brochure are subject to terms and conditions outlined in Stratasys' selling policies, contracts between the parties or Stratasys' Terms and Conditions of Sale. This brochure is not intended to and does not enlarge or add to any such contract or terms.  
 © 2014, 2015 Stratasys Ltd. All rights reserved. Stratasys, Stratasys logo, Objet, For a 3D World, Objet24, Objet30, Objet 30 Pro, Objet30 OTHedDesk, Objet Studio, Quadra, QuadraTempo, FullCure, SHR, Eden, Eden250, Eden260, Eden260V, Eden 330, Eden350, Eden350V, Eden500V, Job Manager, CADMatrix, Connex, Objet260 Connex, Connex350, Connex500, Objet1000, Figur, Alaris, Alaris30, PolyLog, TangoBlack, TangoGrey, TangoPlus, TangoBlockPlus, VeroBlue, VeroBlack, VeroBlockPlus, VeroClear, VeroDent, VeroGray, VeroWhite, VeroWhitePlus, Durus, Digital Materials, PolyJet, PolyJet Matrix, Digital ABS and ObjetGreen are trademarks or registered trademarks of Stratasys Ltd. and/or its subsidiaries or affiliates and may be registered in certain jurisdictions. All other trademarks belong to their respective owners. MSS\_PU\_PUMaterialsDataSheet\_EN\_0815

## Appendix G.

## Research Contributions

### DEVELOPMENT OF AN INFANT HEART AND LUNG FE MODEL FOR OPTIMIZING CARDIOPULMONARY RESUSCITATION PERFORMANCE

Samar Shaabeth, Allan Mason-Jones, Michael D Jones, Shwe P Soe, Peter S Theobald

Cardiff School of Engineering, Cardiff University, Cardiff, Wales, UK

#### Introduction

Simulations of blood flow have gained a great relevance in the understanding of the human cardiovascular system. Cardiac pathologies, such as atherosclerosis or aneurysms, are closely related to blood flow characteristics, such as areas of flow reversal or low and oscillatory shear stress. Therefore, a detailed understanding of the local haemodynamics can have useful application and the developments in the acquisition of medical data and the evolution in the performance of recent computers have made it possible to deliver patient specific information on the blood flow behavior [1]. This project ultimately aims to develop a fluid-structure interaction (FSI) model capable of simulating cardiopulmonary resuscitation (CPR) - the physical compression of the chest during cardiac arrest. International resuscitation guidelines are updated every 5 years to describe the optimal technique for manually circulating blood [2]; however, it is striking that these guidelines generally rely upon animal-based data when advising on the most effective techniques for use on children (obvious ethical and emotive constraints prevent gathering of data from human cases).

This paper represents the initial steps in developing a simplified model, simulating this complex procedure, to improve knowledge of the normal blood flow during CPR, that will ultimately help to understand the assessment of patients with cardiovascular abnormalities and to improve that performance of infant.

#### Method and Results

The time dependent geometry of the infant heart and lungs were segmented from MRI images of an infant chest using Mimics 18.0 and 3-Matics 10.0 software shown in figure 1. The lungs and a simplified model of the heart, during cardiac arrest, was exported to ANSYS 16.0 FE modeler. The model will then be compressed as per the latest (2015) resuscitation guidelines and the force applied as a vector of 254.8N [3] on force patches and a fixed support on the support surface patches. Body sizing was set with a 1mm element size and an independent patching tetrahedron was used as the meshing method for the concentration on the curvature for the full assembly (figure 2). The material properties for the lungs and the heart were considered as isotropic materials and assigned for each part in the engineering data [4]. The equivalent stress and the total deformation for the whole assembly was measured.

The results provide an indication of the stresses distributed when applying the CPR compression force on the lungs and how the lung deformation compresses the left side of the heart.

These results, combined with those of the CFD analysis using ANSYS Fluent, will be investigated further to get the FSI analysis providing important insight into the parameters critical for performing more complex modelling.

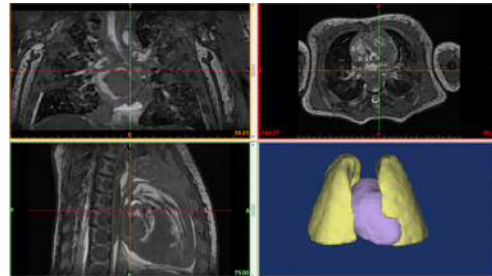


Figure 1: MIMICS 18.0 3D segmentation of the heart and lung of 8 weeks old infant.

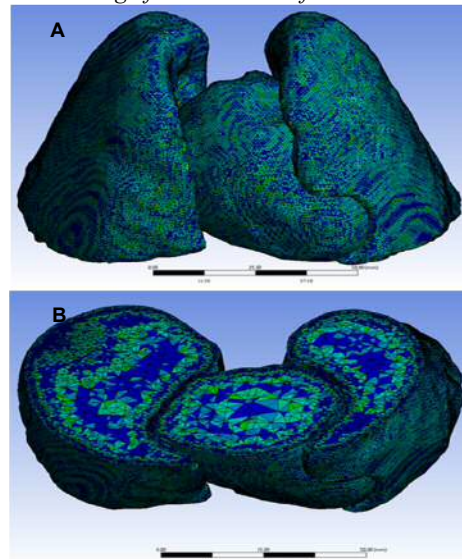


Figure 2: A: Infant heart and lung mesh in ANSYS 16.0, B: Meshed model transverse section

#### References

1. H. Oertel, Modelling the Human Cardiac Fluid Mechanics, 4<sup>th</sup> edition, 2012
2. Ian K. M., et al, European Resuscitation Council Guidelines for Resuscitation 2010 Section 6. Paediatric life support, Resuscitation 95 (2015) 223–248 2015
3. Martin PS., et al. Arch Dis Child, 98:576–581, 2013.
4. Meyer et al., Child Advanced Safety Project For European Roads, 2011.



## Biomechanical properties and microstructure of neonatal porcine ventricles

Faizan Ahmad<sup>1</sup>, R. Prabhu<sup>2</sup>, Jun Liao<sup>2,3\*</sup>, Shwe Soe<sup>1</sup>, Michael D Jones<sup>1</sup>, Jonathan Miller<sup>2</sup>, Parker Berthelson<sup>2</sup>, Daniel Enge<sup>4</sup>, Katherine M. Copeland<sup>3</sup>, Samar Shaabeth<sup>1</sup>, Richard Johnston<sup>5</sup>, Ian Maconochie<sup>6</sup>, Peter S. Theobald<sup>1\*</sup>

<sup>1</sup> School of Engineering, Cardiff University, UK;

<sup>2</sup> Centre for Advanced Vehicular Systems and Department of Biological Engineering, Mississippi State University, US;

<sup>3</sup> Department of Bioengineering, The University of Texas at Arlington, US;

<sup>4</sup> University of the Cumberland, US;

<sup>5</sup> College of Engineering, Swansea University, UK;

<sup>6</sup> Imperial College NHS Healthcare Trust, UK.

### Corresponding author:

Jun Liao, PhD, FAHA  
Associate Professor,  
Department of Bioengineering,  
University of Texas at Arlington,  
500 UTA BLVD, Suite 353,  
Arlington, TX 76010,  
Phone: (817) 272-6779  
Email: jun.liao@uta.edu

Peter S Theobald, PhD  
Bioengineering Research Group  
Cardiff School of Engineering, Cardiff University,  
Queens Buildings,  
The Parade, Newport Road,  
Cardiff, CF243AA, UK,  
Phone (44) 2920 874726  
Email: TheobaldPS@cardiff.ac.uk

## Highlights

- Maturation increases the stiffness of cardiac tissue when comparing our neonatal data to that describing the mature porcine heart.
- Neonatal tissue exhibits non-linear, anisotropic, and heterogeneous behaviour.
- The neonatal porcine cardiac tissue is one-half the uniaxial stiffness, one-third the biaxial stiffness, and one-fourth the simple shear stiffness, of equivalent mature tissue.
- The anterior walls are stiffer than the posterior walls, in both ventricles.

## Abstract

Neonatal heart disorders represent a major clinical challenge, with congenital heart disease alone affecting 36,000 new-borns annually within the European Union. Surgical intervention to restore normal function includes the implantation of synthetic and biological materials; however, a lack of experimental data describing the mechanical behaviour of neonatal cardiac tissue is likely to contribute to the relatively poor short- and long-term outcome of these implants. This study focused on characterising the mechanical behaviour of neonatal cardiac tissue using a porcine model, to enhance the understanding of how this differs to the equivalent mature tissue. The biomechanical properties of neonatal porcine cardiac tissue were characterised by uniaxial tensile, biaxial tensile, and simple shear loading modes, using samples collected from the anterior and posterior walls of the right and left ventricles. Histological images were prepared using Masson's trichrome staining, to enable assessment of the microstructure and correlation with tissue behaviour. The mechanical tests demonstrated that the neonatal cardiac tissue is non-linear, anisotropic, viscoelastic and heterogeneous. Our data provide a baseline describing the biomechanical behaviour of immature porcine cardiac tissue. Comparison with published data also indicated that the neonatal porcine cardiac tissue exhibits one-half the stiffness of mature porcine tissue in uniaxial extension testing, one-third in biaxial extension testing, and one-fourth stiffness in simple shear testing; hence, it provides an indication as to the relative change in characteristics associated with tissue maturation. These data may prove valuable to researchers investigating neonatal cardiac mechanics.

**Keywords:** Neonatal porcine hearts, cardiac mechanics, congenital heart diseases, passive mechanical behaviour, age-dependent variations.

## 1. Introduction

Congenital heart disease (CHD) annually affects approximately 36,000 new-borns within the European Union [1, 2], and describes a series of structural cardiac disorders, including ventricular and atrial septal defects. Multi-physics modelling and the development of new synthetic materials are innovative approaches seeking to positively influence the clinical outcomes; however, an acute lack of data describing the biomechanical behaviour of neonatal cardiac tissue, twinned with the structural changes to the tissue during maturing, is potentially limiting the effectiveness of these novel techniques.

The adult cardiac tissue is known to exhibit highly complex behaviour, including non-linearity and anisotropy [3-10], as a consequence of its intricate structure [11-15]. Critically, ventricular wall functionality differs between the adult and neonate, as the latter can only increase the cardiac output by increasing the heart rate (although only limited), whereas the adult heart can also increase stroke volume [16, 17]. The neonate heart also has a greater fraction of fibrous tissue to contractile tissue, than an adult [16, 17], whilst there is variation in the collagen fibril density, and mono-nucleated and bi-nucleated cell concentrations [18-20]. Increasing age is also associated with changes in the cardiac matrix, and an increase in collagen fibril crosslinking and assembly [21]. No experimental data exists to quantify neonate tissue, however, meaning simulations adopt and/or scale adult data, incorporating an unknown level of error [21-24].

Computational modelling is increasingly used in adult cardiology to understand the behaviour of structural components, enabling the simulation of normal and pathophysiological conditions and leading to new interventions [25-31]. A lack of appropriate data to describe neonatal tissue limits the widespread use and effectiveness of sophisticated techniques, to investigate neonatal-based disorders. Surgical intervention, aiming to restore normal function, includes the implantation of synthetic materials to mimic natural tissue behaviour [32-34]; however, the relatively poor short- and long-term outcomes may be partly associated with the scant literature describing neonatal cardiac biomechanics. This lack of knowledge may also be contributing to the relatively limited success of biological scaffolds [35, 36]; hence, enhanced knowledge of tissue behaviour to achieve more effective designs has the potential to positively influence CHD mortality and morbidity [36].

We thus aim to systematically quantify the biomechanical properties of neonatal right and left ventricles, using an accepted neonatal porcine animal model [37-44]. These

biomechanical data are consolidated with histological imaging, to provide a comprehensive analysis of tissue from the right and left ventricle free walls (RVFW, LVFW). This study will provide baseline data describing the behaviour of neonatal porcine tissue and, through comparison to equivalent mature data, will also be able to provide an insight into the effect of maturation on tissue behaviour. Such data may then prove useful to those researchers investigating immature cardiac tissue mechanics and the clinicians/bioengineers exploring new intervention techniques in congenital heart diseases.

## 2. Materials and methods

### 2.1. Materials

Forty-three, one-day-old neonatal porcine hearts (Yorkshire) were acquired from a local abattoir house in Mississippi, from donor piglets mass: 2.0 – 2.2kg, length: 0.35 – 0.48m. The deceased piglets all appeared fully developed, meaning that they were most likely to have died from hypoxia either during or immediately after, farrowing (i.e. birth). All donor's hearts were presumed to be healthy, pending subsequent inspection. The piglets were collected within hours of their death and transported to the Tissue Bioengineering Laboratory at the Mississippi State University, stored in ice-cooled boxes at 4°C. The hearts were then promptly dissected out and visually examined for any macroscopic damage or disruption, with any that failed this assessment being excluded from further investigation. The anterior and posterior aspects of the LVFW and RVFW were then identified (Fig. 1), before defining the FSN-coordinate system as the fibre axis (F), defined as the mean-fibre direction as observed by the external surface texture; the sheet axis (S), defined as the direction transverse to the fibre axis within the layer; the sheet-normal axis (N), defined as the direction perpendicular to both the fibres and layers [9, 10, 45]. In this study, the fibre axis (F) is described as the 'mean-fibre direction' (MFD), and sheet-normal axis (N) as the 'cross fibre direction' (CFD) [10]. Such a method is inherently subjective, though was performed in a manner consistent with previous studies [9, 10].

Uniaxial extension testing samples were dissected from twenty hearts. Ten randomly selected hearts had samples of dimensions 20mm (l) x 10mm (w) x 3mm (t) dissected, with the longest dimension aligned to the MFD. The remaining 10 hearts were used to harvest samples in the CFD (Fig. 2 (a), (b) & (c)). All 20 samples were then trimmed using a cutting punch, achieving a traditional dog-bone shape and a 5mm minimum width. For biaxial extension analysis, five samples (15 x 15 x 3mm) were dissected using a square-shaped cutting punch from the LVFW, and a further five hearts used for RVFW samples (Fig. 2 (d) & (e)). Each sample was dissected such that the presumed MFD and CFD were consistent with the x- and y-axes of the cutter. A similar approach, though smaller cutter (3 x 3 mm), was adopted to dissect tissue for shear analysis. These were collected from the anterior and posterior aspects of the LVFW and RVFW, dissected from the equatorial regions of 5 hearts (Fig. 2 (f) & (g)). The final eight hearts were used for histological analysis (Fig. 1). Thirty-two cubic samples (5 x 5 x 5 mm) were dissected using a square-shaped cutter from the equatorial regions of the anterior and posterior aspects of LVFW and RVFW (Fig. 1). In this



instance, a coordinate system was established that ensured consistent orientation of the cutter, as this analysis served to quantify the relative fibre alignment. Hence, the cutter was always aligned with the vertical axis of the heart, defined as passing through the apex and base.

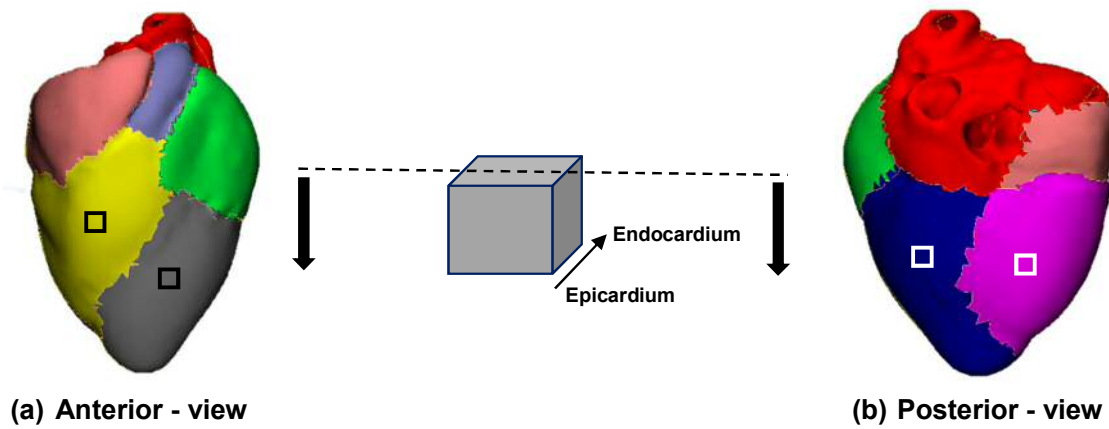


**Fig.1.** Three-dimensional schematic model of the neonatal porcine heart. **(a)** Anterior view: LVFW = Grey region, RVFW = Yellow region. **(b)** Posterior view: LVFW = blue region, RVFW = pink region. Squares represent the location of dissecting histological samples ( $5 \times 5$  mm), which were then sectioned in the plane perpendicular to the transmural direction.

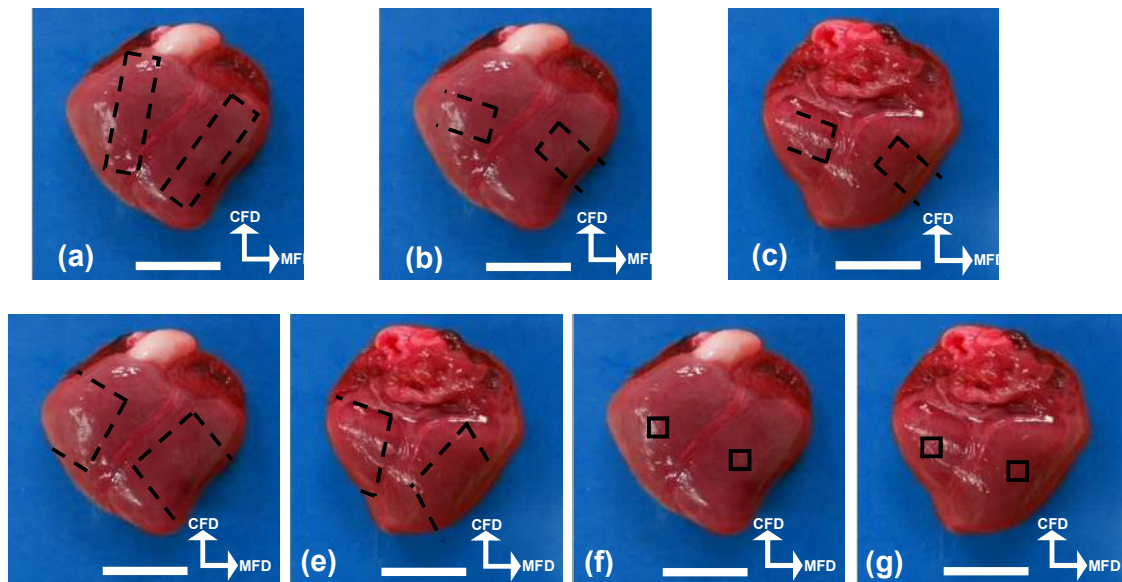


**Fig. 2.** Schematic representation of the samples harvested from the neonatal porcine heart. Samples were dissected aligned to the ‘mean fibre direction’ (MFD) and ‘cross fibre direction’ (CFD), determined by observing the external features of the organ. **(a)** Uniaxial CFD samples are dissected from the anterior aspect of the LVFW and RVFW. **(b) & (c)** Uniaxial MFD samples extend from the anterior to posterior aspect of the LVFW and RVFW. **(d) & (e)** Biaxial (square) samples extended from the anterior to posterior aspects of the LVFW and RVFW. **(f) & (g)** Simple shear samples were dissected from the equatorial region of both the anterior and posterior aspects of the LVFW and RVFW. Scale bar = 12 mm.

## 2.2. Methods

The directional anisotropy of the LVFW and RVFW tissue was investigated at different deformation states, via four independent protocols. Biomechanical testing was completed within 12h of birth, to produce data from fresh tissue.

### 2.2.1. Microstructural analysis

All 32 samples were fixed in 4% paraformaldehyde for 48h and then in 70% glutaraldehyde. Samples were then processed through a standard histological preparation protocol, including being dehydrated in graded alcohol, cleared with xylene and then embedded within paraffin wax. Each block was cut perpendicular to the transmural direction, with a 2mm deep section selected for analysis (Fig. 1). A standard Masson's trichrome staining protocol was performed, with the sections finally mounted with Permount. The Masson's trichrome stain identified muscle fibres in red, and collagen fibres light blue.

### 2.2.2. Uniaxial extension test

Both ends of the dog-bone-shaped samples were wrapped in emery paper and clamped into the stainless steel grips of a uniaxial testing machine (Mach-1; Biosyntech, MN). This produced samples with a dimension of approximately 15mm (l) x 5mm (w) x 3mm (t), with five measurements taken with digital callipers. Each sample was preconditioned with 10 cycles at 10% strain, before being loaded to failure at 1.5 mms<sup>-1</sup> ramp speed. Engineering stress was computed by normalising the applied force to the initial cross-sectional area, and engineering strain calculated by normalising the displacement to the initial gauge length. Mean peak stress, which describes the stress of failure, was then calculated from these data for the MFD and CFD samples. The last preconditioning cycle was used to quantify the myocardial hysteresis (to account for energy dissipation due to the viscoelastic behaviour), dividing the area enclosed by the loading and unloading curves (energy dissipation) by the area beneath the loading curve (energy input).

### 2.2.3. Biaxial extension test

Biaxial mechanical properties were investigated using a biaxial testing system, described in detail elsewhere [46, 47]. The square samples, which had been dissected with the observed MFD and CFD aligned with the x- and y-axes were then mounted onto the machine using surgical sutures. Five thickness measurements were collected at different locations, using a digital calliper, to determine an average dimension. The samples were then immersed in 37°C PBS. Ten preconditioning cycles were performed before the data were collected for analyses. The specimens were stretched by applying a 30 N/m tension in the MFD ( $T_{\text{MFD}}$ ) and CFD ( $T_{\text{CFD}}$ ) at 0.5  $\text{mms}^{-1}$ . Tissue deformation was measured via a charge-coupled device camera (National Instrument, IMAQ CCD, Austin, TX), tracking the relative position of four reference points placed in a  $2 \times 2$  array. In-house Labview code (National Instrument, Version 6, Austin, TX) was used to control the stepper motors and record the applied forces and tissue strain.

### 2.2.4. Simple shear test

Simple shear tests focussed on the relative shearing and sliding of the myocardial tissues. Simple shear tests involved mounting the tissue in custom-built shear plates which, in turn, were mounted in the Mach 1 testing machine (Biosyntech, MN) and submerged in PBS at 37°C. Regional anisotropy was investigated using  $3 \times 3 \times 3$  mm cubic specimens that had been dissected such that the MFD and CFD were consistent with the x and y-axes. Tissue samples were mounted between the two shear plates using minimal cyanoacrylate. They were sheared in the FS plane along the MFD and then the NS plane along the CFD, following identification of these planes representing the extremes of shear behaviour in the adult porcine LVFW myocardium [9]. The tissue was exposed to positive and negative shear at 10% and incrementally increased to a maximum 50%, at a loading rate of 0.02  $\text{mms}^{-1}$ .

## 2.3. Data analysis

### 2.3.1. Fibre orientation and surface area calculations from histological images

The Fourier components analysis method quantified the fibre orientation from histological images of the 4 heart regions, using the Fiji/Image J (NIH, USA) software and the 'Directionality' plug-in (<https://imagej.net/Directionality>) [48]. Data from histological images

enabled identification of the 'preferred' fibre orientation direction (i.e. the histogram peak). This peak was then fitted with a Gaussian function, reporting the preferred fibre orientation [49, 50]. A custom MATLAB code was also adopted to quantify the surface area ratio of collagen to myocyte fibres, using image thresholding based on RGB (red, green and blue) values [51].

### 2.3.2. Uniaxial and biaxial tensile tests

Engineering stresses in MFD ( $P_{11}$ ) and CFD ( $P_{22}$ ) are calculated as the ratio of the applied force and the initial cross-sectional area. Strains in the MFD ( $\epsilon_1$ ) and CFD ( $\epsilon_2$ ) are computed as the ratio of the displacement and the initial gauge length.

$$P_{11} = \frac{f_1}{A_1}, \quad P_{22} = \frac{f_2}{A_2}, \quad (1)$$

$$\epsilon_1 = \frac{x_1}{X_1}, \quad \epsilon_2 = \frac{x_2}{X_2},$$

Where: ( $x_1, x_2$ ) are the displacements; ( $X_1, X_2$ ) are the initial gauge lengths.

### 2.3.3. Simple shear test

Shear stress ( $\tau$ ) is the ratio of the shear force  $f$  and the shear area  $a = L^2$ ; hence, this calculation represents the relative in-plane displacement of two parallel layers of this cubic specimen. The amount of shear  $\gamma$  ranges from 0.1 – 0.5 in increments of 0.1, whilst the separation distance (side length) for the cubic specimen was  $L \sim 3$  mm.

$$\gamma = \frac{\Delta L}{L}, \quad \tau = \frac{f}{L^2}, \quad (2)$$

Where:  $\Delta L$  represents the shear displacement.

### 2.3.4. Statistical analysis

All values are reported as the mean  $\pm$  standard deviation (SD), where a  $p$ -value less than 0.05 was considered as statistically significant. One-way analysis of variances (ANOVA) was performed along with Tukey HSD post hoc test to quantify the statistical significance of the anterior and posterior aspects of both ventricles. All statistical analyses were conducted in SPSS 20.0.

### 3. Results

#### 3.1. Microstructural analysis

Representative images from the microscopic examination are presented showing the overall fibre orientation in the anterior and posterior aspects of the LVFW and RVFW (Fig. 3). These samples were collected aligned to the vertical axis of the heart (defined as passing through the apex and base). The images indicate that the fibre direction in the anterior LVFW are more aligned to the horizontal, and posterior the vertical axes, respectively. Indeed, the alignment of fibres with either the horizontal or vertical appears stronger in the LVFW than the RVFW. The Fourier component analysis quantifies these alignments and confirms that the fibres in the anterior and posterior LVFW are more aligned to the horizontal and vertical axes of the heart. Conversely, fibres in the anterior and posterior RVFW are aligned nearer diagonally (Table 1), though the former has less intercellular space (Figs. 3 (c) & (d)). The ratio of collagen to myocyte fibres was highest in the LVFW posterior, and lowest in the RVFW anterior, regions (Table 2). The average in-plane (x, y) principal (preferred) fibre orientation of the LVFW and RVFW are stated in Table 1.

Collagen / myocyte	LV (A)	(SD)	LV (P)	(SD)	RV (A)	(SD)	RV (P)	(SD)
Transmural - plane	0.10	(0.5)	0.20	(0.6)	0.03	(0.3)	0.08	(0.4)

**Table 2**

The average surface area ratio of collagen to myocyte for RVFW and LVFW in the anterior (n = 16) and posterior (n = 16) aspects. Histological specimens were examined in the plane perpendicular to the transmural direction, using custom MATLAB code.

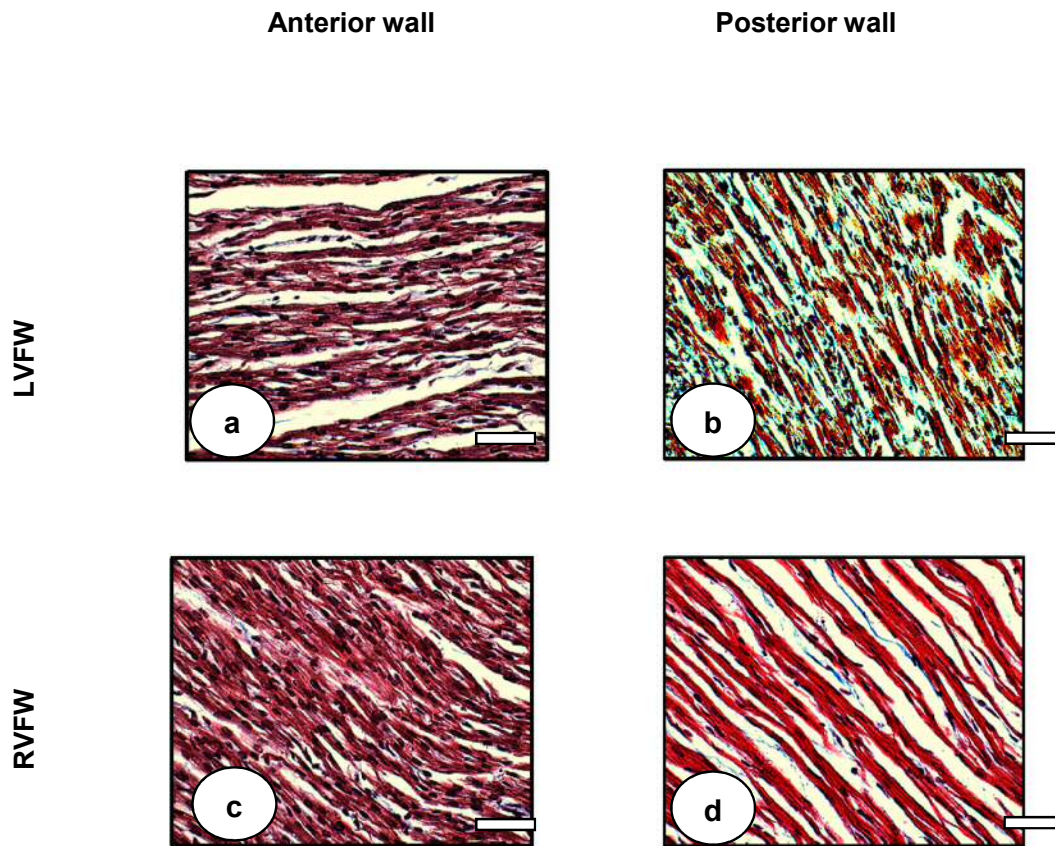


**Fig. 3.** Masson's trichrome staining images of the neonatal porcine heart sectioned from the plane perpendicular to the transmural direction and viewed at  $\times 40$  magnification. **(a)** LVFW anterior, demonstrating circumferentially aligned fibres. **(b)** LVFW posterior, describing longitudinally aligned fibres. The RVFW anterior **(c)** and posterior **(d)** aspects demonstrated almost symmetrical fibre alignment, with the former having greater concentration and alignment of muscle fibres as reported in Table.2. Principal or preferred fibre angles are detailed in Table.1. Scale bar =  $50\mu\text{m}$ .

Heart regions	Preferred fibre orientation $\mu$ ( $^{\circ}$ )	(SD)	Coefficient of determination $R^2$	(SD)
LVFW (A)	4.19	(0.6)	0.96	(0.4)
LVFW (P)	-60.98	(0.7)	0.98	(0.6)
RVFW (A)	-40.77	(0.2)	0.98	(0.7)
RVFW (P)	-44.01	(0.4)	0.98	(0.6)

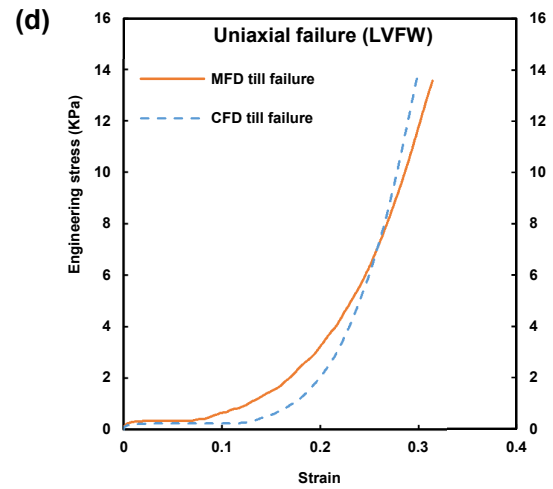
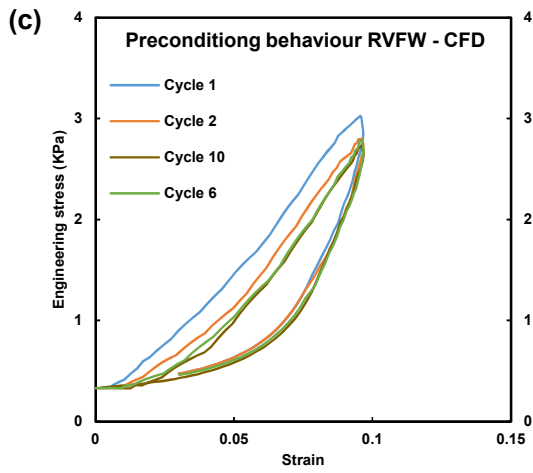
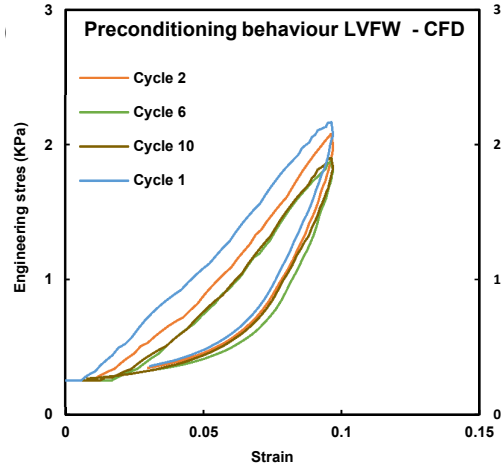
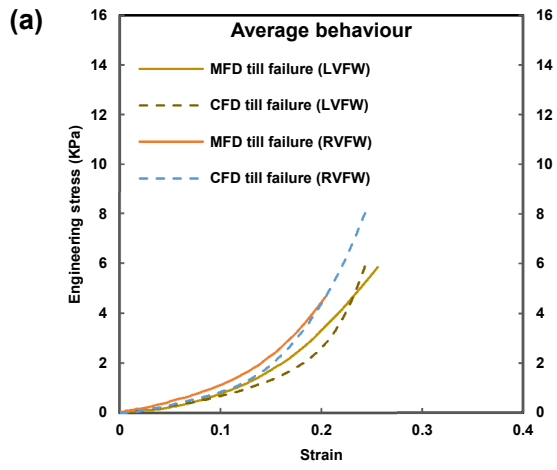
**Table 1**

The average in-plane ( $x$ ,  $y$ ) principal fibre orientation parameter and coefficient of determination  $R^2$  'goodness of fit' for RVFW and LVFW in the anterior ( $n = 16$ ) and posterior ( $n = 16$ ) aspects. Histological specimens were examined in the plane perpendicular to the transmural direction, using Fourier components analysis method ( $n = 32$ ).

### 3.2. Uniaxial extension behaviour

The mean uniaxial behaviour of the LVFW and RVFW in extension is presented in Fig. 4 (a), with the data describing a non-linear, anisotropic, viscoelastic (hysteresis – formation) response in all regions. Ten preconditioning cycles were performed, with both the LVFW and RVFW demonstrating the greatest change in behaviour during the first two cycles (Fig. 4 (b) & (c)). It is evident from Figs. 4 (a), (d), (e) & (f) that the MFD was stiffer than the CFD in the strain range 0 to  $\sim 0.20$ , but that the CFD becomes stiffer than the MFD after  $\sim 0.20$  for both ventricles. The RVFW is consistently the stiffer of the two ventricles. The energy dissipation and failure stresses are reported in Tables. 3 & 4. The data in Figs. 4 (a) – (f) demonstrate similar trends, though there is a significant difference between the RVFW and LVFW peak stresses ( $p = 0.001$ ) and between MFD and CFD ( $p = 0.0001$ ).





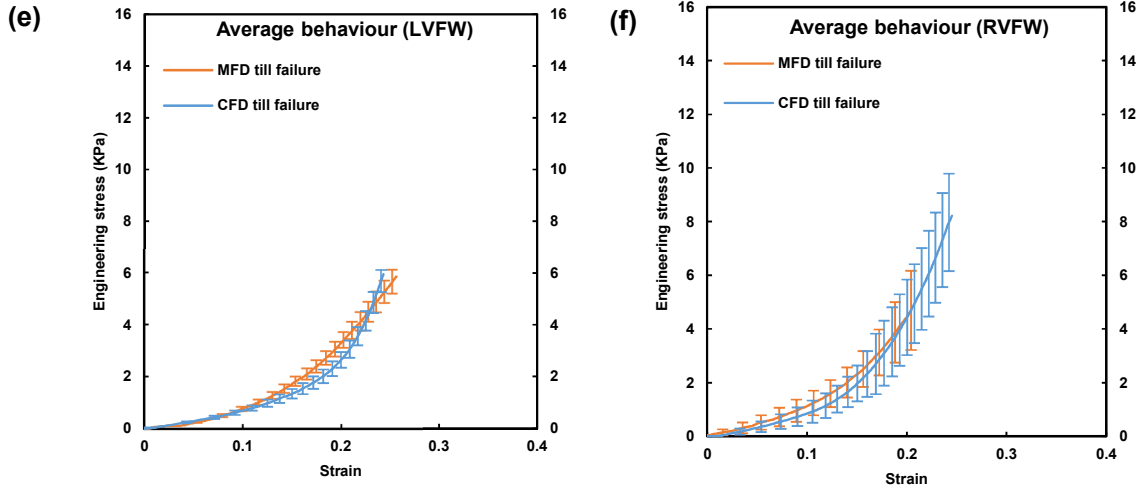


**Fig. 4.** (a) Average ‘uniaxial behaviour’ of LVFW & RVFW until failure (n = 5). (b) – (c) Uniaxial cyclic behaviour of LVFW and RVFW in CFD. (d) Representing passive ‘uniaxial behaviour’ of LVFW until failure. Mean curves of the LVFW (e) and RVFW (f) (n = 5). Standard deviation indicated by error bars.

Hysteresis area				
Heart regions	MFD	(SD)	CFD	(SD)
LVFW	91	(112)	80	(82)
RVFW	54	(108)	43	(93)

**Table 3**

Average hysteresis area ( $J/m^3$ ) of neonatal porcine LVFW and RVFW for uniaxial testing at 20% strain in MFD and CFD.

Heart regions	MFD	(SD)	CFD	(SD)
LVFW	5.84	(0.4)	5.95	(0.4)
RVFW	4.69	(1.4)	8.22	(1.8)

**Table 4**

Average failure stress values (KPa) for neonatal LVFW and RVFW for uniaxial testing; the specimens were stretched until failure. Mean  $\pm$  SD stress values are plotted in Figs. 4 (e) and 4 (f).

### 3.3. Biaxial extension behaviour

The biaxial mechanical representatives (Engineering stress vs stretch) were investigated at  $30 \text{ Nm}^{-1}$ :  $30 \text{ Nm}^{-1}$  tension ranges (Fig. 5). RVFW and LVFW possess non-linear, anisotropic and viscoelastic (hysteresis formation) mechanical responses (Figs. 5 (a) – (b)). The RVFW is stiffer, whilst the LVFW demonstrates greater viscoelasticity. The MFD exhibits stiffer behaviour and greater viscoelasticity in both ventricles, than the CFD (Figs. 5 (a) – (d)). The LVFW exhibits mechanical cross-coupling between the MFD and CFD as demonstrated in Fig. 5(a). The energy dissipation and peak Engineering stresses are presented in Tables. 5 & 6. A significant difference exists between the RVFW and LVFW peak Engineering stresses in MFD ( $p = 0.0001$ ) and CFD ( $p = 0.0001$ ).

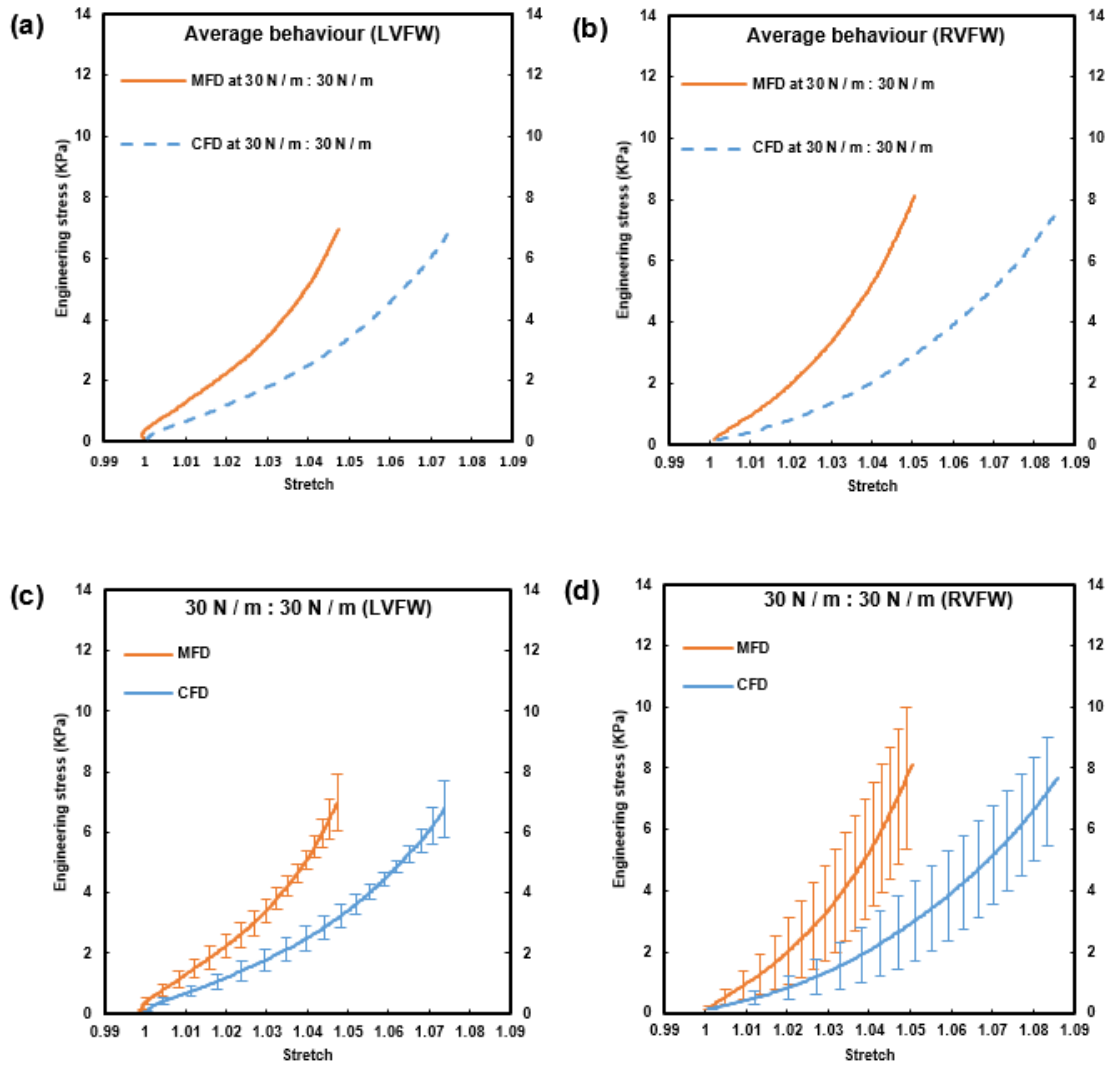


**Fig. 5.** (a) The average biaxial behaviour of LVFW, with negative strain indicating possible in-plane mechanical cross-coupling between the MFD-CFD ( $n = 5$ ). (b) Average biaxial behaviour of RVFW ( $n = 5$ ). Mean 'biaxial' curves of the (c) LVFW and (d) RVFW ( $n = 5$ ). Error bars describe the standard deviation.

---

Hysteresis area

---

Heart regions	MFD	(SD)	CFD	(SD)
LVFW	51	(121)	19	(76)
RVFW	48	(128)	23	(67)

---

**Table 5**

Average hysteresis area ( $J/m^3$ ) of neonatal porcine LVFW and RVFW for biaxial testing at (30:30) N / m in MFD and CFD.

---

Heart regions	MFD	(SD)	CFD	(SD)
LVFW	6.97	(0.9)	6.77	(0.9)
RVFW	8.11	(2.3)	7.67	(1.8)

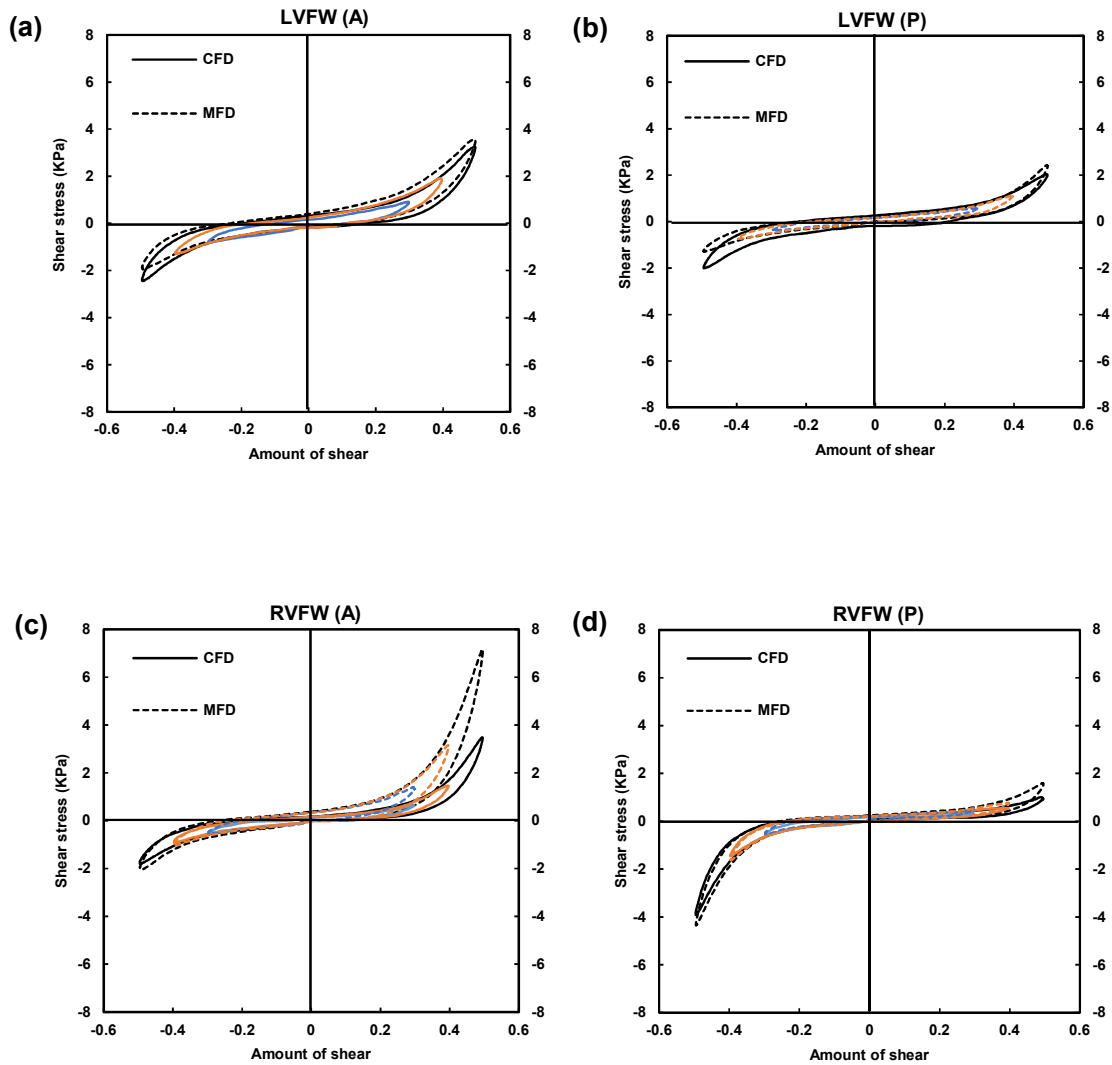
---

**Table 6**

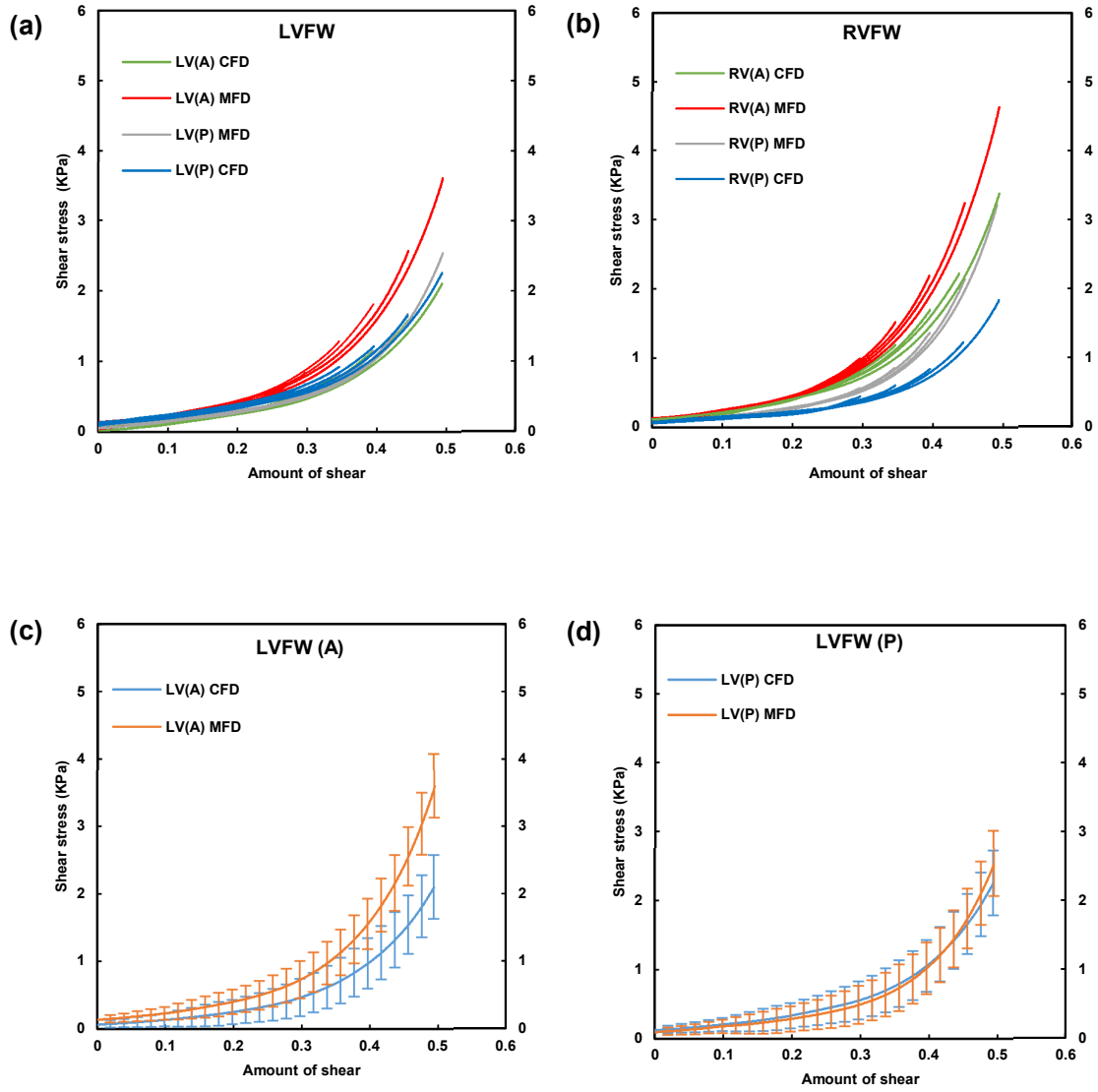
Average peak Engineering stress values (KPa) for neonatal porcine LVFW and RVFW for biaxial testing at (30:30) N / m in MFD and CFD. Mean  $\pm$  SD stress values are plotted in figs. 5 (c) and 5 (d).

### 3.4. Simple shear behaviour

Hysteresis formation (energy dissipation) is prominently evident throughout the cyclic shearing behaviour, with both ventricles demonstrating increased shear (Fig. 6). The anterior walls appear stiffer with greater energy dissipation than the posterior walls of both ventricles, whilst the MFD is stiffer than the CFD (Fig. 7 (a) – (b)). The RVFW exhibits asymmetrical behaviour, possessing greater stiffness in the positive direction anteriorly and negative direction posteriorly. Conversely, both aspects of the LVFW exhibit consistent behaviour in both directions (Fig. 6). The energy dissipation and peak shear stresses are described in Tables. 7, 8 & 9. The influence of fibre direction is described in (Figs. 7 (a) – (f)), whilst variations in tissue behaviour are identified statistically via a one-way ANOVA and Tukey HSD post hoc test (Table. 10).



**Fig.6.** Demonstrating passive 'simple shear' behaviour of the anterior and posterior aspects of the LVFW & RVFW in the MFD and CFD, at increments of 0.3 (blue curve), 0.4 (orange curve) and 0.5 (black curve). The positive y-axis represents the positive direction of myocardial shearing. **(a)** LVFW – anterior. **(b)** LVFW – posterior. **(c)** RVFW – anterior. **(d)** RVFW – posterior.





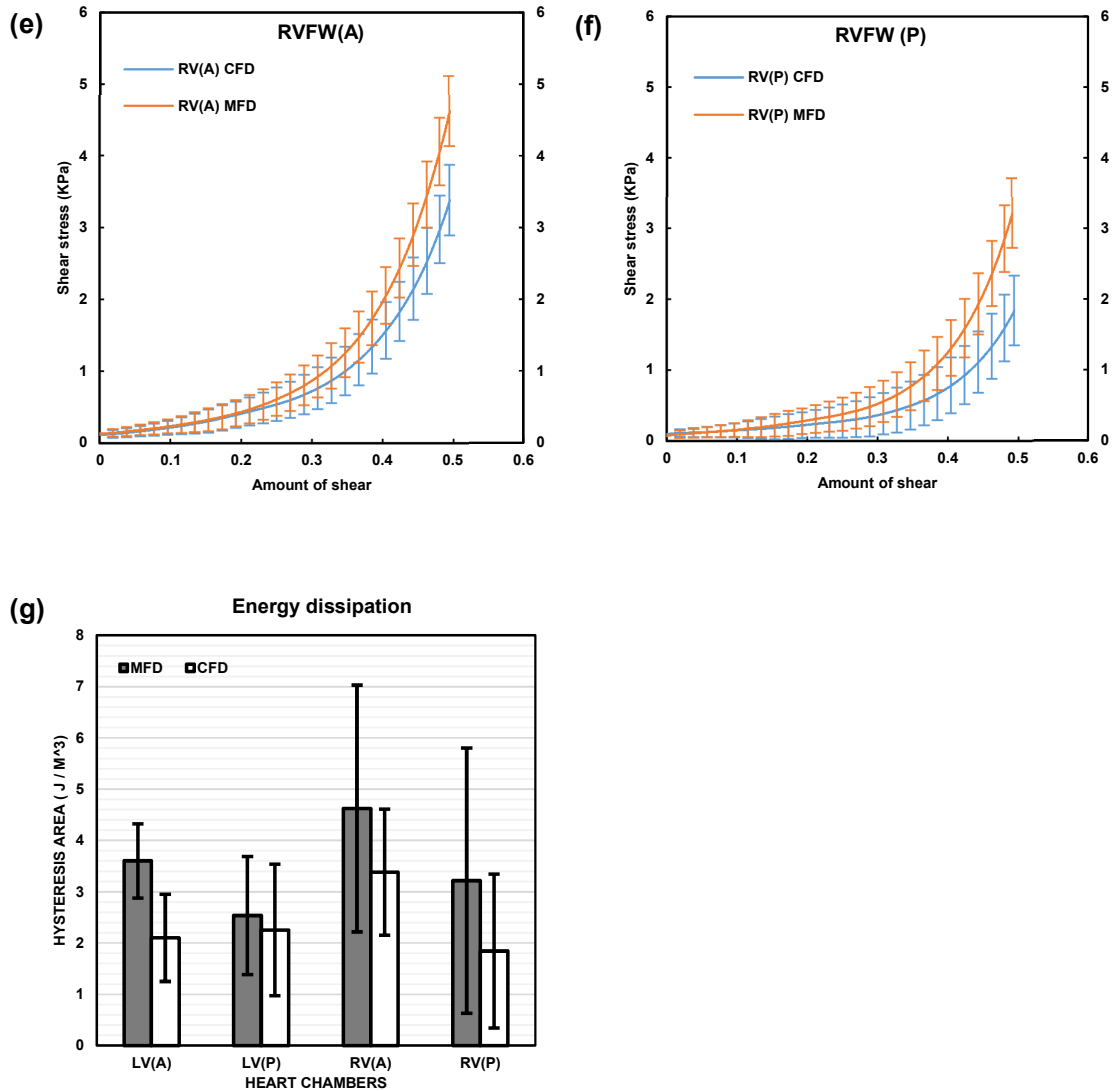


**Fig. 7.** ‘Mean simple shear behaviour’ of anterior and posterior aspect of the LVFW (a) and the RVFW (b), in the MFD and CFD at increments of 0.1, 0.2, 0.3, 0.4 & 0.5 (n = 5). LVFW anterior (c) and posterior (d) in MFD and CFD, at an increment of 0.5. RVFW anterior (e) and posterior (f) in MFD and CFD at an increment of 0.5. (g) Column plots indicate mean hysteresis areas in the anterior and posterior aspect of LVFW & RVFW, for MFD and CFD at an increment of 0.5 (n = 5). Error bars represent standard deviation.

Hysteresis area				
Heart regions	MFD	(SD)	CFD	(SD)
LVFW (A)	306	(104)	260	(86)
LVFW (P)	201	(17)	187	(59)
RVFW (A)	387	(87)	244	(159)
RVFW (P)	208	(117)	174	(41)

**Table 7**

Average hysteresis area ( $\text{J/m}^3$ ) of neonatal porcine LVFW and RVFW in anteroposterior directions for simple shear testing at 0.5 increments in MFD and CFD. Mean  $\pm$  SD energy dissipation values are plotted in Fig. 7 (g).

Increments	LVFW (A)				LVFW (P)			
	MFD	(SD)	CFD	(SD)	MFD	(SD)	CFD	(SD)
0.3	0.84	(0.2)	0.57	(0.3)	0.55	(0.2)	0.67	(0.2)
0.4	1.82	(0.3)	1.15	(0.4)	1.14	(0.3)	1.22	(0.4)
0.5	3.60	(0.4)	2.10	(0.5)	2.53	(0.4)	2.25	(0.5)

**Table 8**

Average peak shear stress values (KPa) for the neonatal LVFW in the anterior (A) and posterior (P) aspects for simple shear testing at 0.3, 0.4, 0.5 increments in MFD and CFD modes. Mean  $\pm$  SD stress values are plotted in Figs. 7 (c) and 7 (d).

Increments	RVFW (A)				RVFW (P)			
	MFD	(SD)	CFD	(SD)	MFD	(SD)	CFD	(SD)
0.3	0.99	(0.2)	0.82	(0.3)	0.56	(0.3)	0.45	(0.4)
0.4	2.19	(0.3)	1.69	(0.3)	1.36	(0.4)	0.85	(0.4)
0.5	4.62	(0.4)	3.38	(0.5)	3.22	(0.4)	1.84	(0.5)

**Table 9**

Average peak shear stress values (KPa) for the neonatal RVFW in the anterior (A) and posterior (P) aspects for simple shear testing at 0.3, 0.4, 0.5 increments in MFD and CFD modes. Mean  $\pm$  SD stress values are plotted in Figs. 7 (e) and 7 (f).

Configurations	LVFW (A)		LVFW (P)		RVFW (A)		RVFW (P)
	MFD	CFD	MFD	CFD	MFD	CFD	MFD
1	0.0001	0.0001	0.0001	0.0001	-	-	-
2	-	-	-	-	0.0001	0.0001	0.0001
3	0.0001	0.0001	-	-	0.002	0.01	-
4	-	-	0.86	0.86	-	-	0.12

**Table 10**

Statistical analysis (One way ANOVA along with Tukey HSD post hoc test) data for RVFW and LVFW in the anterior (A) and posterior (P) aspects represent: (1) LVFW (anterior & posterior) for MFD – CFD; (2) RVFW (anterior & posterior) for MFD – CFD; (3) LVFW (A) and RVFW (A) for MFD – CFD; and (4) LVFW (P) and RVFW (P) for MFD – CFD respectively. P – Value less than 0.05 considered statistically significant.

#### 4. Discussion

This study has identified non-linear, anisotropic, viscoelastic and heterogeneous mechanical behaviour of neonatal porcine ventricle tissue. These overall characteristics are consistent with those of other soft tissues [52-56].

Uniaxial extension testing to failure was performed following ten preconditioning cycles (Figs. 4 (b) & (c)), a method consistent with that reported elsewhere [4, 5, 7, 57-62]. Uniaxial testing for failure of the immature tissue was performed and revealed that the MFD was stiffer and more viscoelastic than the CFD (Figs. 4 (a)). Such a viscoelastic response is common in soft tissues and is due to the fluid-structure interaction within the elaborate microstructure of the cardiac samples [63-65]. At low strains, the myocardial mechanical response appears governed solely by cardiomyocytes. As the tissue was extended beyond 20% however, the CFD became stiffer than the MFD in both ventricles (Fig. 4 (a)). This phenomenon has previously been attributed to the perimysial collagen, which provides some reinforcement of the tissue as it approaches its extensibility limit. This apparent coupling between the cardiomyocytes and collagen fibrils appears to contribute to the mechanical strength of the myocardium [66-68]. A similar function of this collagen was previously reported in the adventitia of arteries [69-71]. The similar trends of the MFD and CFD uniaxial plots (Fig. 4(a)) demonstrate their similar anisotropic behaviour. Comparison with equivalent mature data indicates this variation is relatively small, probably due to the relatively few collagen fibril crosslinks, which are known to increase with age [3, 19].

Uniaxial testing also demonstrated that the LVFW had greater extensibility and viscoelasticity, though lower stiffness, than the RVFW (Figs. 4(a), (b) & (c)). This is surprising given that the LVFW has a greater proportion of collagen. Our observation, of a greater ratio of collagen to myocyte fibres in the LVFW, is consistent with previous reports of higher collagen content preserving wall thickness during diastole and systole [51, 72-74] (Table 2). Since a higher collagen content would typically be associated with greater stiffness in mature tissues, the less stiff behaviour observed here might be related to the collagen state in a 1-day neonatal heart. This is different to the intuitive mechanical contribution of collagen typical in mature tissues. It is noted that the uniaxial (LVFW – MFD) stiffness of neonatal porcine data reported here (23 kPa) is approximately one-half that of the equivalent mature porcine tissue (47 kPa) [75].

The RVFW demonstrated greater stiffness relative to the LVFW during biaxial testing which may, in part at least, be explained by the greater proportion of muscle fibres to the immature collagen than the LVFW (Fig. 5 & Table. 2). This is also the likely reason for the

greater LVFW viscoelasticity, and the RVFW's greater anisotropy, which is consistent with previous data [6]. Both ventricles demonstrated that the MFD was nearly twice as viscoelastic as the CFD (Table 5). Figure 5 (a) (Engineering stress vs stretch) demonstrated slight negative strain in the MFD and CFD. Similar, though stronger, trends have previously been reported in adult mammalian heart tissue [76] and was associated with a dense network of fine collagen fibrils linking the cardiomyocytes and large collagen fibrils. This mechanical coupling may contribute to maintaining the myocardial mechanical stiffness [10, 66]. The mechanical trends between MFD and CFD exhibited in Figs. 5 (a) & (b), is consistent with data from some canine studies [4, 5], though other adult studies report the MFD as being approximately twice as stiff than CFD [10, 60, 77]. The neonatal porcine LVFW (140 kPa) has the approximately one-third stiffness of equivalent adult porcine (400 kPa) in the MFD [78]. Biaxial extension tends to demonstrate greater stiffness than the uniaxial extension in MFD, with the RVFW exhibiting peak Engineering stress almost double the uniaxial data (Tables 4 and 6). Similarly, biaxial tests show greater anisotropy between MFD and CFD than equivalent uniaxial tests (Figs. 4 & 5), as a consequence of the collagen/muscle fibre crosslinking mechanism.

The RVFW is the stiffest tissue in simple shear, with the MFD stiffer than the CFD. Strain softening was briefly observed, perhaps caused by a disruption of perimysial collagen during cyclic shearing, as a consequence of excessive shearing between adjacent myocardial muscle layers [79-81]. The anterior walls were stiffest with greater energy dissipation, which is again consistent with the relative microstructures (Fig. 3 and Table 2). The greater magnitude of energy dissipation achieved versus biaxial tests (Tables 5 & 7) would appear indicative of the importance of shearing within the heart wall. This attribute is believed to be as a consequence of the relatively high water content of myocardium (~ 80% wet weight) and affected by the muscle presence [64]. The anterior and posterior LVFWs demonstrate similar mechanical trends in the positive and negative directions. The anterior RVFW exhibits a stiffer response in the positive direction, whilst the posterior RVFW has greater stiffness in the negative direction (Fig. 6). Fibre orientation analysis revealed orthogonal alignment of the LVFW muscle fibres, with fibres from the anterior region aligned horizontally and posterior fibres vertically (Figs. 3 (a) & (b), and Table 1). Conversely, the fibres in the anterior and posterior RVFW were aligned nearer diagonally, with the former possessing greater concentration with less intercellular space, which may in part contribute to the RVFWs asymmetric shear behaviour (Table 2 & Fig. 3). The principal or preferred fibre angles were calculated using Fourier component image analysis (Table 1). The stiffness of LVFW adult porcine data has previously been reported at 50% strain as ~ 28 kPa (MFD) and ~ 5 kPa (CFD) [9]. Compared to the equivalent data reported here for neonatal

porcine tissue (i.e.  $\sim 7.2$  kPa (MFD) and  $\sim 4.2$  kPa (CFD) at 50% strain), indicates that the neonatal tissue is approximately one-fourth the stiffness of mature tissue in the MFD. Comparing the stress-strain plots of this shear data, to the above uniaxial data, highlights a similar stress after which the MFD tissue from both ventricles stiffens dramatically (Figs. 4 (a) and 7 (c), (d), (e), (f)). This is consistent with the trend previously reported in adult porcine cardiac tissue [9].

#### 4.1. Limitations

Whilst the above results provide a valuable insight into neonatal cardiac tissue behaviour, it is acknowledged that an animal-based laboratory study differs from human, physiological reality. The porcine model was adopted as the adult organ is commonly used to simulate human performance, given their relatively similar structure and dimensions; however, there are still differences that will limit the applicability of these data. Whilst the controlled environment of a laboratory has significant advantages when investigating tissue characteristics, the need to dissect samples does create artificial boundary conditions and release residual stresses, which may alter performance. Common protocols were followed to ensure the tissues remained hydrated and in a condition similar to their *in vivo* physiology.

## **5. Conclusion**

A series of mechanical tests have been performed to characterise the behaviour of LVFW and RVFW from the neonatal porcine tissue. A strong correlation is reported between microstructure and mechanical function, whilst the tissue was found to exhibit non-linear, anisotropic, viscoelastic (hysteresis formation) and heterogeneous behaviour. The neonatal tissue is also identified as exhibiting one-half the stiffness of mature porcine tissue in uniaxial testing, one-third in biaxial testing, and one-fourth stiffness in simple shear testing. Hence, these data provide both a baseline describing the biomechanical behaviour of immature porcine cardiac tissue and an indication as to the relative change in characteristics associated with tissue maturation. This may prove valuable to researchers investigating cardiac mechanics.

## **6. Acknowledgements**

FA is grateful to the Ser Cymru NRN in Advanced Engineering & Materials for funding his PhD scholarship. JL is supported in part by NIH 1R01EB022018-01.



## References

- [1] H. Dolk, M. Loane, E. Garne, The prevalence of congenital anomalies in Europe, *Advances in experimental medicine and biology* 686 (2010) 349-64.
- [2] H. Dolk, M. Loane, E. Garne, G. European Surveillance of Congenital Anomalies Working, Congenital heart defects in Europe: prevalence and perinatal mortality, 2000 to 2005, *Circulation* 123(8) (2011) 841-9.
- [3] L.L. Demer, F.C. Yin, Passive biaxial mechanical properties of isolated canine myocardium, *The Journal of physiology* 339 (1983) 615-30.
- [4] J.D. Humphrey, R.K. Strumpf, F.C.P. Yin, Determination of a Constitutive Relation for Passive Myocardium: II.—Parameter Estimation, *Journal of biomechanical engineering* 112(3) (1990) 340-346.
- [5] V.P. Novak, F.C. Yin, J.D. Humphrey, Regional mechanical properties of passive myocardium, *Journal of biomechanics* 27(4) (1994) 403-12.
- [6] M.S. Sacks, C.J. Chuong, Biaxial Mechanical Properties of Passive Right Ventricular Free Wall Myocardium, *Journal of biomechanical engineering* 115(2) (1993) 202-205.
- [7] F.C. Yin, R.K. Strumpf, P.H. Chew, S.L. Zeger, Quantification of the mechanical properties of noncontracting canine myocardium under simultaneous biaxial loading, *Journal of biomechanics* 20(6) (1987) 577-89.
- [8] M.R. Hill, M.A. Simon, D. Valdez-Jasso, W. Zhang, H.C. Champion, M.S. Sacks, Structural and mechanical adaptations of right ventricle free wall myocardium to pressure overload, *Ann Biomed Eng* 42(12) (2014) 2451-65.
- [9] S. Dokos, B.H. Smaill, A.A. Young, I.J. LeGrice, Shear properties of passive ventricular myocardium, *American journal of physiology. Heart and circulatory physiology* 283(6) (2002) H2650-9.
- [10] G. Sommer, A.J. Schriefl, M. Andrä, M. Sacherer, C. Viertler, H. Wolinski, G.A. Holzapfel, Biomechanical properties and microstructure of human ventricular myocardium, *Acta biomaterialia* 24 (2015) 172-192.
- [11] V. Carapella, R. Bordas, P. Pathmanathan, M. Lohezic, J.E. Schneider, P. Kohl, K. Burrage, V. Grau, Quantitative study of the effect of tissue microstructure on contraction in a computational model of rat left ventricle, *PloS one* 9(4) (2014) e92792.
- [12] P. Helm, M.F. Beg, M.I. Miller, R.L. Winslow, Measuring and mapping cardiac fiber and laminar architecture using diffusion tensor MR imaging, *Annals of the New York Academy of Sciences* 1047 (2005) 296-307.
- [13] W.J. Karlon, A.D. McCulloch, J.W. Covell, J.J. Hunter, J.H. Omens, Regional dysfunction correlates with myofiber disarray in transgenic mice with ventricular expression

of ras, American journal of physiology. Heart and circulatory physiology 278(3) (2000) H898-906.

[14] A. Palit, S.K. Bhudia, T.N. Arvanitis, G.A. Turley, M.A. Williams, Computational modelling of left-ventricular diastolic mechanics: effect of fibre orientation and right-ventricle topology, Journal of biomechanics 48(4) (2015) 604-12.

[15] D.D. Streeter, Jr., H.M. Spotnitz, D.P. Patel, J. Ross, Jr., E.H. Sonnenblick, Fiber orientation in the canine left ventricle during diastole and systole, Circulation research 24(3) (1969) 339-47.

[16] C.J. Cote, A practice of anesthesia for infants and children, WB Saunders Company 1993.

[17] R.G. Cox, Smith's Anesthesia for Infants and Children - Eighth Edition, Canadian Journal of Anesthesia/Journal canadien d'anesthésie 58(10) (2011) 973.

[18] P. Anversa, J.M. Capasso, Cellular basis of aging in the mammalian heart, Scanning microscopy 5(4) (1991) 1065-73; discussion 1073-4.

[19] C.R. Gazoti Debessa, L.B. Mesiano Maifrino, R. Rodrigues de Souza, Age related changes of the collagen network of the human heart, Mechanisms of Ageing and Development 122(10) (2001) 1049-1058.

[20] C.T. Nguyen, C.S. Hall, M.J. Scott, Q. Zhu, J. Marsh, S.A. Wickline, Age-related alterations of cardiac tissue microstructure and material properties in Fischer 344 rats, Ultrasound in Medicine & Biology 27(5) (2001) 611-619.

[21] M.L. Lindsey, D.K. Goshorn, C.E. Squires, G.P. Escobar, J.W. Hendrick, J.T. Mingoia, S.E. Sweterlitsch, F.G. Spinale, Age-dependent changes in myocardial matrix metalloproteinase/tissue inhibitor of metalloproteinase profiles and fibroblast function, Cardiovascular research 66(2) (2005) 410-419.

[22] S. Giannico, F. Hammad, A. Amodeo, G. Michielon, F. Drago, A. Turchetta, R. Di Donato, S.P. Sanders, Clinical outcome of 193 extracardiac Fontan patients: the first 15 years, Journal of the American College of Cardiology 47(10) (2006) 2065-73.

[23] E. Petrossian, V.M. Reddy, D.B. McElhinney, G.P. Akkersdijk, P. Moore, A.J. Parry, L.D. Thompson, F.L. Hanley, Early results of the extracardiac conduit Fontan operation, The Journal of thoracic and cardiovascular surgery 117(4) (1999) 688-96.

[24] T. Shinoka, C. Breuer, Tissue-engineered blood vessels in pediatric cardiac surgery, The Yale journal of biology and medicine 81(4) (2008) 161-6.

[25] S. Dokos, I.J. LeGrice, B.H. Smaill, J. Kar, A.A. Young, A Triaxial-Measurement Shear-Test Device for Soft Biological Tissues, Journal of biomechanical engineering 122(5) (2000) 471-478.

- [26] T.S. Eriksson, A. Prassl, G. Plank, G.A. Holzapfel, Influence of myocardial fiber/sheet orientations on left ventricular mechanical contraction, *Mathematics and Mechanics of Solids* (2013) 1081286513485779.
- [27] T.S. Eriksson, A.J. Prassl, G. Plank, G.A. Holzapfel, Modeling the dispersion in electromechanically coupled myocardium, *International journal for numerical methods in biomedical engineering* 29(11) (2013) 1267-84.
- [28] M.P. Nash, A.V. Panfilov, Electromechanical model of excitable tissue to study reentrant cardiac arrhythmias, *Progress in biophysics and molecular biology* 85(2-3) (2004) 501-22.
- [29] S. Niederer, L. Mitchell, N. Smith, G. Plank, Simulating a human heart beat with near-real time performance, *Frontiers in Physiology* 2 (2011) 14.
- [30] T.P. Usyk, J.H. Omens, A.D. McCulloch, Regional septal dysfunction in a three-dimensional computational model of focal myofiber disarray, *American journal of physiology. Heart and circulatory physiology* 281(2) (2001) H506-14.
- [31] S.T. Wall, J.C. Walker, K.E. Healy, M.B. Ratcliffe, J.M. Guccione, Theoretical impact of the injection of material into the myocardium: a finite element model simulation, *Circulation* 114(24) (2006) 2627-35.
- [32] E. Petrossian, V.M. Reddy, K.K. Collins, C.B. Culbertson, M.J. MacDonald, J.J. Lamberti, O. Reinhartz, R.D. Mainwaring, P.D. Francis, S.P. Malhotra, D.B. Gremmels, S. Suleman, F.L. Hanley, The extracardiac conduit Fontan operation using minimal approach extracorporeal circulation: early and midterm outcomes, *The Journal of thoracic and cardiovascular surgery* 132(5) (2006) 1054-63.
- [33] C.P. Twine, A.D. McLain, Graft type for femoro-popliteal bypass surgery, *The Cochrane database of systematic reviews* (5) (2010) CD001487.
- [34] X. Wang, P. Lin, Q. Yao, C. Chen, Development of small-diameter vascular grafts, *World journal of surgery* 31(4) (2007) 682-9.
- [35] B. Wang, A. Borazjani, M. Tahai, A.L. Curry, D.T. Simionescu, J. Guan, F. To, S.H. Elder, J. Liao, Fabrication of cardiac patch with decellularized porcine myocardial scaffold and bone marrow mononuclear cells, *Journal of biomedical materials research. Part A* 94(4) (2010) 1100-10.
- [36] H. Kurobe, M.W. Maxfield, C.K. Breuer, T. Shinoka, Concise review: tissue-engineered vascular grafts for cardiac surgery: past, present, and future, *Stem cells translational medicine* 1(7) (2012) 566-71.
- [37] A. Bassols, C. Costa, P.D. Eckersall, J. Osada, J. Sabria, J. Tibau, The pig as an animal model for human pathologies: A proteomics perspective, *Proteomics. Clinical applications* 8(9-10) (2014) 715-31.

- [38] P. Vodicka, K. Smetana, Jr., B. Dvorankova, T. Emerick, Y.Z. Xu, J. Ourednik, V. Ourednik, J. Motlik, The miniature pig as an animal model in biomedical research, *Annals of the New York Academy of Sciences* 1049 (2005) 161-71.
- [39] B. Aigner, S. Renner, B. Kessler, N. Klymiuk, M. Kurome, A. Wünsch, E. Wolf, Transgenic pigs as models for translational biomedical research, *Journal of molecular medicine* 88(7) (2010) 653-664.
- [40] G.W. Almond, Research applications using pigs, *Veterinary Clinics of North America: food animal practice* 12(3) (1996) 707-716.
- [41] S.A. Book, L.K. Bustad, The fetal and neonatal pig in biomedical research, *Journal of animal science* 38(5) (1974) 997-1002.
- [42] D. Cooper, Y. Ye, L. Rolf Jr, N. Zuhdi, The pig as potential organ donor for man, *Xenotransplantation*, Springer1991, pp. 481-500.
- [43] W.R. Douglas, Of pigs and men and research, *Origins of life and evolution of biospheres* 3(3) (1972) 226-234.
- [44] Y. Luo, L. Lin, L. Bolund, T.G. Jensen, C.B. Sørensen, Genetically modified pigs for biomedical research, *Journal of inherited metabolic disease* 35(4) (2012) 695-713.
- [45] G.A. Holzapfel, R.W. Ogden, Constitutive modelling of passive myocardium: a structurally based framework for material characterization, *Philosophical transactions. Series A, Mathematical, physical, and engineering sciences* 367(1902) (2009) 3445-75.
- [46] J.S. Grashow, M.S. Sacks, J. Liao, A.P. Yoganathan, Planar biaxial creep and stress relaxation of the mitral valve anterior leaflet, *Ann Biomed Eng* 34(10) (2006) 1509-18.
- [47] J.S. Grashow, A.P. Yoganathan, M.S. Sacks, Biaxial stress-stretch behavior of the mitral valve anterior leaflet at physiologic strain rates, *Ann Biomed Eng* 34(2) (2006) 315-25.
- [48] Z.Q. Liu, Scale space approach to directional analysis of images, *Applied optics* 30(11) (1991) 1369-73.
- [49] N. Reznikov, R. Almany-Magal, R. Shahar, S. Weiner, Three-dimensional imaging of collagen fibril organization in rat circumferential lamellar bone using a dual beam electron microscope reveals ordered and disordered sub-lamellar structures, *Bone* 52(2) (2013) 676-683.
- [50] N. Reznikov, R. Shahar, S. Weiner, Three-dimensional structure of human lamellar bone: the presence of two different materials and new insights into the hierarchical organization, *Bone* 59 (2014) 93-104.
- [51] S. Javani, M. Gordon, A.N. Azadani, Biomechanical Properties and Microstructure of Heart Chambers: A Paired Comparison Study in an Ovine Model, *Annals of biomedical engineering* 44(11) (2016) 3266-3283.

- [52] G.A. Holzapfel, G. Sommer, P. Regitnig, Anisotropic mechanical properties of tissue components in human atherosclerotic plaques, *Journal of biomechanical engineering* 126(5) (2004) 657-65.
- [53] G. Sommer, P. Regitnig, L. Koltringer, G.A. Holzapfel, Biaxial mechanical properties of intact and layer-dissected human carotid arteries at physiological and supraphysiological loadings, *American journal of physiology. Heart and circulatory physiology* 298(3) (2010) H898-912.
- [54] G.A. Holzapfel, G. Sommer, C.T. Gasser, P. Regitnig, Determination of layer-specific mechanical properties of human coronary arteries with nonatherosclerotic intimal thickening and related constitutive modeling, *American journal of physiology. Heart and circulatory physiology* 289(5) (2005) H2048-58.
- [55] G. Sommer, M. Eder, L. Kovacs, H. Pathak, L. Bonitz, C. Mueller, P. Regitnig, G.A. Holzapfel, Multiaxial mechanical properties and constitutive modeling of human adipose tissue: a basis for preoperative simulations in plastic and reconstructive surgery, *Acta biomaterialia* 9(11) (2013) 9036-48.
- [56] G. Sommer, A. Schriefl, G. Zeindlinger, A. Katzensteiner, H. Ainodhofer, A. Saxena, G.A. Holzapfel, Multiaxial mechanical response and constitutive modeling of esophageal tissues: Impact on esophageal tissue engineering, *Acta biomaterialia* 9(12) (2013) 9379-91.
- [57] D.H. Lin, F.C. Yin, A multiaxial constitutive law for mammalian left ventricular myocardium in steady-state barium contracture or tetanus, *Journal of biomechanical engineering* 120(4) (1998) 504-17.
- [58] H. Ghaemi, K. Behdinan, A.D. Spence, In vitro technique in estimation of passive mechanical properties of bovine heart: Part I. Experimental techniques and data, *Medical Engineering & Physics* 31(1) (2009) 76-82.
- [59] K.B. Gupta, M.B. Ratcliffe, M.A. Fallert, L.H. Edmunds, Jr., D.K. Bogen, Changes in passive mechanical stiffness of myocardial tissue with aneurysm formation, *Circulation* 89(5) (1994) 2315-26.
- [60] M.S. Sacks, C.J. Chuong, Biaxial mechanical properties of passive right ventricular free wall myocardium, *J Biomech Eng* 115(2) (1993) 202-5.
- [61] P. Wang, F. Zhu, N.H. Lee, K. Konstantopoulos, Shear-induced interleukin-6 synthesis in chondrocytes: roles of E prostanoïd (EP) 2 and EP3 in cAMP/protein kinase A- and PI3-K/Akt-dependent NF-kappaB activation, *The Journal of biological chemistry* 285(32) (2010) 24793-804.
- [62] D. Valdez-Jasso, M.A. Simon, H.C. Champion, M.S. Sacks, A murine experimental model for the mechanical behaviour of viable right-ventricular myocardium, *The Journal of physiology* 590(18) (2012) 4571-84.
- [63] Y.-C. Fung, *Bioviscoelastic solids*, Biomechanics, Springer1993, pp. 242-320.

- [64] J.D. Humphrey, *Cardiovascular Solid Mechanics: Cells, Tissues, and Organs*, Springer New York 2013.
- [65] Y.-C. Fung, *Mechanical properties and active remodeling of blood vessels*, Biomechanics, Springer 1993, pp. 321-391.
- [66] R. Avazmohammadi, M.R. Hill, M.A. Simon, W. Zhang, M.S. Sacks, A novel constitutive model for passive right ventricular myocardium: evidence for myofiber-collagen fiber mechanical coupling, *Biomech Model Mechanobiol* 16(2) (2017) 561-581.
- [67] J.E. Bishop, G. Lindahl, Regulation of cardiovascular collagen synthesis by mechanical load, *Cardiovascular Research* 42(1) (1999) 27-44.
- [68] D.D. STREETER, H.M. SPOTNITZ, D.P. PATEL, J. ROSS, E.H. SONNENBLICK, Fiber Orientation in the Canine Left Ventricle during Diastole and Systole, *Circulation research* 24(3) (1969) 339-347.
- [69] G.A. Holzapfel, G. Sommer, C.T. Gasser, P. Regitnig, Determination of layer-specific mechanical properties of human coronary arteries with nonatherosclerotic intimal thickening and related constitutive modeling, *American Journal of Physiology - Heart and Circulatory Physiology* 289(5) (2005) H2048-H2058.
- [70] G. Sommer, P. Regitnig, L. Költringer, G.A. Holzapfel, Biaxial mechanical properties of intact and layer-dissected human carotid arteries at physiological and supraphysiological loadings, *American Journal of Physiology - Heart and Circulatory Physiology* 298(3) (2010) H898-H912.
- [71] C.A.J. Schulze-Bauer, P. Regitnig, G.A. Holzapfel, Mechanics of the human femoral adventitia including the high-pressure response, *American Journal of Physiology - Heart and Circulatory Physiology* 282(6) (2002) H2427-H2440.
- [72] T.K. Borg, J.B. Caulfield, The collagen matrix of the heart, *Fed Proc* 40(7) (1981) 2037-2041.
- [73] K.T. Weber, W.A. Clark, J.S. Janicki, S.G. Shroff, Physiologic versus pathologic hypertrophy and the pressure-overloaded myocardium, *Journal of cardiovascular pharmacology* 10 Suppl 6 (1987) S37-50.
- [74] K.T. Weber, J.S. Janicki, S.G. Shroff, R. Pick, C. Abrahams, R.M. Chen, R.I. Bashey, Collagen compartment remodeling in the pressure overloaded left ventricle, *Journal of Applied Cardiology* 3(1) (1988) 37-46.
- [75] D. Perie, N. Dahdah, A. Foudis, D. Curnier, Multi-parametric MRI as an indirect evaluation tool of the mechanical properties of in-vitro cardiac tissues, *BMC cardiovascular disorders* 13 (2013) 24.
- [76] M.S. Sirry, J.R. Butler, S.S. Patnaik, B. Brazile, R. Bertucci, A. Claude, R. McLaughlin, N.H. Davies, J. Liao, T. Franz, Characterisation of the mechanical properties of infarcted

- myocardium in the rat under biaxial tension and uniaxial compression, *Journal of the Mechanical Behavior of Biomedical Materials* 63 (2016) 252-264.
- [77] H. Ghaemi, K. Behdinan, A.D. Spence, In vitro technique in estimation of passive mechanical properties of bovine heart part I. Experimental techniques and data, *Med Eng Phys* 31(1) (2009) 76-82.
- [78] B. Wang, G. Wang, F. To, J.R. Butler, A. Claude, R.M. McLaughlin, L.N. Williams, A.L. de Jongh Curry, J. Liao, Myocardial scaffold-based cardiac tissue engineering: application of coordinated mechanical and electrical stimulations, *Langmuir : the ACS journal of surfaces and colloids* 29(35) (2013) 11109-17.
- [79] J. Emery, J. Omens, O. Mathieu-Costello, A. McCulloch, Structural mechanisms of acute ventricular strain softening, *Int J Cardiovasc Med Sci* 1 (1998) 241-250.
- [80] J.L. Emery, J.H. Omens, A.D. McCulloch, Biaxial mechanics of the passively overstretched left ventricle, *The American journal of physiology* 272(5 Pt 2) (1997) H2299-305.
- [81] J.L. Emery, J.H. Omens, A.D. McCulloch, Strain softening in rat left ventricular myocardium, *Journal of biomechanical engineering* 119(1) (1997) 6-12.